THEORY OF FROST FORMATION

by

Yatish T. Shah

B. S., University of Michigan (1964)

M. S., Massachusetts Institute of Technology (1966)

Ch. E., Massachusetts Institute of Technology (1967)

Submitted in Partial Fulfillment

of the Requirements for the

Degree of Doctor of Science

at the

Massachusetts Institute of Technology

December, 1968, *i.e. Feb., 1969*

Signature of Author _____

Department of Chemical Engineering

Certified by _____

R. C. Reid, Thesis Supervisor

_____

P. L. T. Brian, Thesis Supervisor

Accepted by _____

G. C. Williams, Chairman,
Departmental Committee on Graduate Theses

ABSTRACT

THEORY OF FROST FORMATION

by

Yatish T. Shah

Submitted to the Department of Chemical Engineering on December 30, 1968, in partial fulfillment of the requirements for the degree of Doctor of Science.

The purpose of the present research was two fold. First, the physical and thermal properties of water frost on a liquid nitrogen-cooled surface were to be measured over a wide range of deposition conditions. Secondly, the experimental results were to be analyzed and interpreted with several analytical models of varying degree of sophistication which considered processes occurring both in the gas phase and in the frost layer.

The time variation in frost density, thickness and thermal conductivity and the heat and mass fluxes were measured for the water frost deposition from a humidified stream of air onto a short copper plate, maintained at about $-315^{\circ}F$. The plate formed part of the underside of a long rectangular duct and was mounted a distance of 72 equivalent duct diameters from the entrance. The duct aspect ratio was 25:1.

The experimental results were obtained for the values of Reynolds numbers between 3,770 and 15,800, the gas humidities between dew point at $14.3^{\circ}F$ and $58^{\circ}F$, the gas temperatures between $34^{\circ}F$ and $93^{\circ}F$ and the time elapsed from the start of the frosting between 20 and 180 minutes. In all the experiments, the gas pressure over the plate was essentially atmospheric.

The experimental results for the time variation in average frost density, frost thickness and the heat and mass fluxes were successfully correlated by a simple theoretical model. This model was based on the heat and mass balances on a differential element at the frost surface. Water vapor was assumed to diffuse in the frost interior by the vapor pressure gradient at the frost surface. No consideration, however, was given to the mechanism of water transport at every layer in the frost interior. The frost density was assumed to be uniform

with depth at all times.

In order to explain a complete physical picture of the frosting process, an improved model was examined in which the heat and mass balances were taken on a differential element within the frost. The equilibrium conditions between the ice and the interstitial gas were assumed everywhere in the frost interior. This model indicated that if the equilibrium conditions exist everywhere within the frost, then the frost layer will densify non-uniformly across its depth as it accumulates on the cold surface.

For a typical set of experimental conditions, the density distributions within the frost were measured by slicing the frost layers. These measurements indicated that the density of the frost layer deposited on a liquid nitrogen-cooled surface always stays uniform with depth. Thus, the equilibrium conditions could not exist everywhere in the frost interior.

The critical evaluation of the experimental results on the density distribution within the frost indicated that the measured water flux within the frost cannot be obtained by molecular diffusion under the non-equilibrium partial pressure gradients without causing nucleation. Based on this conclusion, another 'non-equilibrium model' was postulated to explain the phenomenon of uniform densification of the frost. This model assumed that water transport in the frost interior occurs by both molecular diffusion of water vapor under a non-equilibrium partial pressure gradient and the thermal diffusion of ice nuclei. The model has been examined only qualitatively in the present research.

Thesis Supervisor: Robert C. Reid

Title: Professor of Chemical Engineering

Thesis Supervisor: P. L. Thibaut Brian

Title: Professor of Chemical Engineering

Department of Chemical
  Engineering
Massachusetts Institute
  of Technology
Cambridge, Massachusetts

December 30, 1968

Professor E. Neal Hartley
Secretary of the Faculty
Massachusetts Institute of Technology
Cambridge, Massachusetts 02139

Dear Professor Hartley:

In accordance with the regulations of the Faculty,

I herewith submit a thesis, entitled "Theory of Frost

Formation," in partial fulfillment of the requirements

for the degree of Doctor of Science in Chemical

Engineering at the Massachusetts Institute of Technology.

Respectfully submitted,

Yatish T. Shah

Acknowledgement

Some of the original ideas of this thesis were first suggested by the supervisors, Prof. P.L.T. Brian and Prof. R. C. Reid. The author wishes to acknowledge with appreciation these suggestions along with their patient and perspicacious direction during the course of the thesis. The author is particularly grateful to his supervisors for their suggestions in the theoretical aspects of this thesis.

The financial support for the author during the thesis work was made possible by fellowships from Scientific Design Co. and Arthur D. Little Co. These assistancsships are gratefully acknowledged. The fund required for the experimental as well as theoretical aspects of the work were obtained from several sources. The author very gratefully acknowledges the invaluable help of Prof. G. C. Williams, Prof. S. W. Bodman, Mr. W. Allen of American Cyanamid Co., Bound Brook, New Jersey, Mr. J. Smith of American Cyanamid Co., Willow Island, West Virginia and the personnel of Bound Brook and West Virginia plants of American Cyanamid Co. in this respect.

The author acknowledges Mr. R. C. Fulton, Mr. A. Merril and Mr. P. Bletzer for their encouraging help in constructing the apparatus. The discussion, technical and otherwise, provided by fellow graduate students Mr. J. Katzer, Mr. S. G. Kane and particularly by Dr. I. Brazinsky

are also very much appreciated. The constructive suggestions of Dr. Brazinsky in building certain pieces of the apparatus have been very helpful.

The patience and confidence demonstrated, as well as considerable material assistance performed in the form of typing a rough and a final draft of this thesis by author's wife have been, of course, most invaluable and are very gratefully acknowledged.

Table of Contents

List of Figures

List of Figures (Contd.)

List of Figures (Contd.)

List of Figures (Contd.)

List of Figures (Contd.)

List of Figures (Contd.)

List of Figures (Contd.)

List of Tables

SUMMARY

The formation of water frost on a liquid nitrogen-cooled surface from a flowing humid gas is a complex phenomenon but one which occurs with sufficient frequency in industrial practice to warrant both theoretical and experimental studies. Although some research studies have been reported on the water frosting process (3, 6, 23, 52, 89, 92, 114), only one successful preliminary attempt (14) has been made to explain the various aspects of the frosting process by means of a quantitative theory. The present research was undertaken to explore this theory in greater detail.

The present thesis first presents the results of an experimental study wherein the physical and thermal properties of water frost were measured over a wide range of deposition conditions. These results were then analysed and interpreted with various analytical models which considered processes occurring both in the gas phase and in the frost layer.

Similar Previous Studies

A. Experimental

In a similar study Brazinsky (14) obtained experimental data on the thickness, density and thermal conductivity of water frost deposited from flowing humid air onto a liquid nitrogen-cooled copper plate. The plate was a part of the under-side of a rectangular duct. The independent system parameters studied were the gas stream Reynolds number, the

humidity, and the time elapsed since the start of

frosting.   The data were taken for a Reynolds number range

of 5,600 to 14,500, a humidity range corresponding to gas

dew points of 29°F to 40°F, and for the frosting times as

high as 120 minutes.   The gas temperature was always main-

tained at about 75°F.

B.   Theoretical ('Simple Model')

Brazinsky's experimental data were generally well

correlated by a rather simple theoretical model which was

based on the following assumptions:

1.   After a smooth layer of frost is deposited on the

liquid nitrogen cooled surface, the transport of heat and

mass to the frost surface can be analysed using ordinary gas

phase correlations (i.e., no fogging is assumed to occur in

the gas phase).

2.   Water vapor is transferred from the frost surface

to the interior of the frost by a diffusional mechanism

resulting from a water vapor pressure gradient.   The rate

of transfer is proportional to the gradient at the surface.

At no time, however, is any consideration given to the

mechanism of water transport at every layer in the frost

interior.

3.   The density of the frost stays uniform with depth

at all times.

The mathematical equations applicable for this model

were obtained from heat and mass balances on a differential

layer at the frost surface.   The heat flux within the frost

was assumed to be uni-directional. The resulting equations were solved numerically to obtain the time variation in average frost density, frost thickness and heat and mass transfer characteristics of the frosting process.

Experimental Apparatus of the Present Research

A schematic of the frosting system of the present research is shown in Figure 1. This system was very similar to one used by Brazinsky. There were, however, two improvements in the present system. The gas temperature was varied by means of a heat exchanger, and the frost surface was maintained flush with the bottom of the duct during frosting. To accomplish the latter, the copper plate and calorimeter assembly, onto which the frost deposited, was rested on a jack. Thus, the plate could be lowered during an experiment to keep the frost surface and the bottom of the rectangular duct flush at all times.

Experimental and Theoretical ('Simple Model') Results and Discussion

In the present research, the properties of water frost and the heat and mass transfer characteristics of the frosting process were studied under a considerably wider range of system variables than those investigated by Brazinsky (14). The range of the independent system variables examined in the present thesis are shown in the following table.

Table 1

Ranges of System Variables

System Variables	Range
Reynolds number	3,770 - 15,800
Gas Humidity	dew point at 14.3 to 58°F
Gas Temperature	34°F - 93°F
Frosting Time	20 minutes to 180 minutes

The measurements carried out in each frosting experiment were identical to ones obtained by Brazinsky, with the exception of heat flux measurements. In the present research, the latter were determined in the transient as well as in the quasi-steady state of the frosting process.

The experimental results on the time variation in average frost density, frost thickness and heat and mass transfer rates were found to correlate well with those predicted from simple theoretical model over the entire range of system variables stated in Table 1.

The effects of Reynolds number and gas humidity on the frost properties and the rates of heat and mass transfer obtained in the present research were almost identical to ones obtained by Brazinsky (14). The Reynolds number was found to have a significant effect on the thermal resistance of the frost. The gas humidity was found to affect the mass deposition significantly.

Figures 2 and 3 show the time variation of average frost density, frost thickness and the rates of heat and mass transfer during the frosting process at various gas

tamperatures (but at constant Reynolds number and gas humidity). These data indicate that a higher gas temperature produces a frost of lower thermal resistance. As shown in the figures, the predictions of the 'simple model' were found to be in good agreement with these measured experimental facts.

If the basic assumption of the 'simple model' regarding the heat and mass transfer processes occurring in the gas during the frosting process is true, then experimentally measured frosting heat and mass transfer coefficients should agree well with ones predicted from a heat and mass transfer analysis of the frosting system. This is verified in the present research as shown in Figures 4 and 5.

The experimental heat and mass transfer coefficients were obtained from the measurements of the gas temperature, humidity, the heat and mass fluxes and the frost surface temperature. The theoretical heat transfer coefficients were obtained from Sleicher and Tribus's (105) theoretical Equation 1 shown below.

$$Nu(x) = \frac{h(x)D_H}{k_g} = \frac{\sum A_n \exp(-\lambda_n^2 X_*)}{2\sum (A_n/\lambda_n^2) \exp(-\lambda_n^2 X_*)} \tag{1}$$

where the constants A_n and λ_n are functions of Reynolds and Prandtl numbers and can be obtained from Reference 105.

The theoretical mass transfer coefficients were obtained from the Lewis analogy (39) for simultaneous heat and mass transfer, which can be mathematically described by the following Equation 2.

$$\frac{h}{K_g} = \rho_g \, c_p \, (Le)^{2/3} = \rho_g \, c_p \, (Sc/Pr)^{2/3} \qquad (2)$$

As shown in Figures 4 and 5, the arithmetic mean of the percentage deviations (percentage deviation = absolute value of ($\dfrac{\text{Experimental Value} - \text{Theoretical Value}}{\text{Experimental Value}}$) x 100) between the experimental and theoretical values of both heat and mass transfer coefficients under the frosting conditions was found to be approximately 10%. Heat transfer coefficients were also measured under non-frosting conditions. They agreed within 3% of theoretical values. It is believed that experimental errors in the frost surface temperature measurement, errors resulting from uneven transition between the duct floor and the frost surface, and errors due to the slight roughness of the frost surface were the major causes for the observed deviation between experimental and theoretical values of the heat and mass transfer coefficients. These results prove, however, that the first assumption of the simple model, as mentioned above is reasonably valid.

The mathematical solution of the equations for the simple model requires the knowledge of initial values of average frost density and frost thickness. These values may not be always available. Hence, in order to obtain these values for an arbitrary set of system conditions, the following empirical correlations were developed from the experimental data of the present research at the time of forty minutes from the start of the frosting process.

$$\rho_{f, \theta = 40\ mins.} = 1.93 \times 10^{-3}\ h^{0.933} \times T_g^{0.2062} \times P_g^{0.1511} \qquad (3)$$

and,

$$\delta_{\theta = 40\ mins.} = 6.21 \times 10^{5}\ h^{-0.1231} \times T_g^{-2.878} \times P_g^{0.779} \qquad (4)$$

The above correlations were obtained at the time of forty minutes because it was the earliest time common to all the experimentally studied system conditions for which the measurements of average frost density and frost thickness were carried out. It should be noted that Equations 3 and 4 are applicable only to the frost deposited on a liquid nitrogen-cooled metal surface from flowing humid air. The accuracy of the predictions of average frost density and frost thickness from Equations 3 and 4 is estimated to be within $\pm$ 8%.

'Improved Model' of the Frosting Process

Even though the simple model correlates well the exper- imentally measured effects of the environmental conditions on the frost properties and the heat and mass fluxes, it does not give the complete picture of the frosting process. Specifically, it neglects the mechanism by which every layer in the frost interior densifies with time. Hence a further theoretical study was carried out to develop a more improved model which could take into account the physical processes occurring in the frost interior along with those occurring in the gas phase.

The 'simple model' assumed that water vapor is transported in to the frost interior due to a vapor pressure gradient at the frost surface. This vapor pressure gradient is caused by the temperature gradient. Since this assumption leads to successful predictions of the water transport past the frost surface, it appears logical to assume that the same mechanism would cause the water transport at every layer in the frost interior. Thus, the first attempt towards the attainment of an improved model was carried out with the help of this assumption. The mathematical equations were obtained by taking the heat and mass balances on a differential element in the frost interior. The transport processes occurring at the frost surface were one set of boundary conditions for the theoretical equations. The other set of boundary conditions were taken at the cold wall. The final mathematical equations with appropriate boundary conditions can be summarized as follows. The schematic of the frosting process as visualized by this model is shown in Figure 5.

Mass Balance

$$\frac{\partial}{\partial x}\left(\frac{D_B}{RT}\frac{(1-\rho_f/\rho_{ice})}{\tau}\frac{\partial P_{vp}}{\partial x}\right) = \frac{\partial \rho_f}{\partial \theta} \qquad (5)$$

also,

$$\frac{\partial P_{vp}}{\partial x} = \frac{\partial P_{vp}}{\partial T}\frac{\partial T}{\partial x} \qquad (6)$$

from Clausius-Clapeyron equation (80)

$$\frac{\partial P_{vp}}{\partial T} = \frac{M\,\Delta H\,P_{vp}}{RT^2} \qquad (7)$$

hence,

$$\frac{\partial}{\partial x}\left(\frac{D_B}{RT}\frac{(1-\rho_f/\rho_{ice})}{\tau}\left(\frac{M\,\Delta H\,P_{vp}}{RT^2}\right)\left(\frac{dT}{dx}\right)\right) = \frac{\partial \rho_f}{\partial \theta} \qquad (8)$$

Heat Balance

$$q = k_f \frac{dT}{dx} \qquad (9)$$

Boundary Conditions

At Cold Wall

$$T(o) = T_w \qquad (10)$$

$$J_o = 0 \qquad (11)$$

At the Frost Surface

$$h(T_g - T_s) + K_g(P_g - P_s) \cdot \Delta H = k_f \frac{dT}{dx}\bigg|_{x=\delta} \qquad (12)$$

(neglecting sensible cooling of condensible component)

$$K_g(P_g - P_s) = \rho_{f,s} \frac{d\delta}{d\theta} + \frac{D_B}{RT} \frac{(1 - \rho_f/\rho_{ice})}{\tau} \frac{\partial P_{vp}}{\partial x}\bigg|_{x=\delta} \qquad (13)$$

With the knowledge of independent system parameters, the initial values for $\rho_f(x,0)$ and $\delta(0)$ and the correlation for the frost thermal conductivity (which was obtained experimentally as shown in Figure 7), the above equations were solved numerically to obtain $\rho_f(x,\theta)$, $T(x,\theta)$ and $\delta(\theta)$.

The predictions of the above equations for $\rho_f(x,\theta)$ and $\delta(\theta)$ under a typical set of system conditions of Re = 5,600, humidity = gas dew point at 29.2 $^{\circ}$F and T_g = 70 $^{\circ}$F are shown in Figure 8. The initial values of density were assumed to be constant everywhere in the frost interior. As shown in the figure, the model predicts that if water transport at every layer in the frost interior is caused by the prevailing vapor pressure gradient, then the entire frost layer will densify non-uniformly. The layer at the frost surface (where the ice vapor pressure is high) densifies at a considerably higher rate than one near the

cold wall. As a matter of fact, in eighteen minutes of the frosting process the density of a thin layer at the frost surface attains a value three times larger than one near the cold wall.

Experimental Measurement of a Density Gradient in the Frost Interior

The validity of the predictions of density distribution within the frost by the above described improved theoretical analysis was investigated by means of experimental measurements. These measurements were made on frost deposited at Re=15,800, a humidity corresponding to a dew point at $30^\circ F$, and with $T_g = 71^\circ F$.

The frost was sampled with a polystyrene tube which was made by glueing 0.0625 inch thick equal diameter rings. Frost samples were then cut with a cold razor. Several slices could be obtained. The slicing process was carried out in a cold room (temperature = $-20^\circ F$). The density of each slice was then calculated from the measurements of mass and volume.

Figure 9 shows the results of these measurements for the various frosting experiments. These results indicate that the density of the bottom 0.0625 inch thick layer was at all times almost the same as that of the entire frost layer, whose thickness varied from 0.091 inch at 26 minutes to 0.256 inch at 144 minutes. The density values shown in Figure 9 are estimated to be accurate within $\pm 12\%$. Thus, it was concluded from all these results that, unlike

the predictions of the improved theoretical analysis,
the density of the frost deposited on a liquid nitrogen-
cooled surface always stays uniform with depth.

Discussion on the Above Described Experimental and
Theoretical Results

The experimental fact that the density of the frost
is always uniform with depth indicates that the assumption
of equilibrium conditions between the interstitial gas
and ice everywhere in the frost interior is not valid.

Further proof for the invalidity of the existence
of equilibrium conditions in the frost interior can be
shown by comparing the predictions of the improved and
simple models for the time variation in average frost
density, frost thickness and heat flux. This is shown
in Figure 10. For a short duration of the frosting process,
the agreement between their predictions is found to be
fairly good. However, as shown in the figure, the deviation
between the predictions increases with time. This should
be expected because as the improved model predicts a
higher and higher density gradient, the temperature
distribution in the frost interior predicted by both the
models would differ more and more (see Figure 11). Hence
the predictions of the improved model will not agree
with those of the simple model over a long period. Since
the predictions of the simple model agree well with the
experimental results, the improved theoretical analysis
will fail to explain any observed effect in the frosting

process for a long period.

It should be noted that the predictions of the improved and the simple models also indicate that even though the experimentally observed rate of mass transport in the frost interior cannot be explained with the assumption that at every layer water vapor is in equilibrium with ice at the prevailing temperature, there could be only a very slight deviation from equilibrium between the gas and ice at the frost surface. Otherwise, the non-equilibrium partial pressure gradient and the vapor pressure gradient would just have to coincide with each other at the frost surface under all diverse gas phase conditions.

In the absence of equilibrium conditions within the frost, the true mechanism of water transport at every layer in the frost interior may be molecular diffusion of water vapor under a non-euqilibrium partial pressure gradient. The validity of this hypothesis can br examined from an analysis of the experimental results of Figure 9. This analysis is briefly described below.

If the water transport at every layer in the frost interior occurs by the diffusional mechanism under a non-equilibrium partial pressure gradient, one can write

$$\frac{\partial}{\partial x}\left(\frac{D_B}{RT}\frac{(1-\rho_f/\rho_{ice})}{\tau}\frac{\partial p}{\partial x}\right) = \frac{\partial \rho_f}{\partial \theta} \qquad (14)$$

Integrating the above equation for the uniform (with depth) rate of frost densification and substituting the boundary condition that at $x=0$, $J=0$, one obtains

$$\frac{\partial p}{\partial x} = x \frac{d\rho_f}{d\theta} \frac{\tau}{(1-\rho_f/\rho_{ice})} \frac{RT}{D_B} \tag{15}$$

The above Equation 15 can be integrated to obtain

the partial pressure at x=0.0625 inch by either setting

the boundary condition for p at x=0 (at the cold wall)

or at x= δ (at the cold surface). Both of these cases

can be examined as follows.

If the boundary condition for partial pressure is

taken at x=0, one can write.

$$\int_{p_{x=0}}^{p_{x=x}} dp = \int_{x=0}^{x=x} x \frac{d\rho_f}{d\theta} \frac{\tau RT}{(1-\rho_f/\rho_{ice}) D_B} dx \tag{16}$$

$$\therefore \ p_{x=x} - p_{x=0} = \int_{x=0}^{x=x} x \frac{d\rho_f}{d\theta} \frac{\tau RT}{(1-\rho_f/\rho_{ice})} dx \tag{17}$$

Assuming $p_{x=0} = P_{vp\ x=0}$ (vapor pressure of ice at

-320°F), using the data of Figures 9 and 12 at a time of

79 mins. and taking the values of τ and D_B from the following.

Equations 18 and 19.

$$\tau = 1.10 \qquad\qquad (\underline{94}) \qquad\qquad (18)$$

$$D_B = 3.3 \times 10^{-6} T^{2.0087} \qquad (\underline{94}) \qquad\qquad (19)$$

where D_B is in ft^2/hr and T is in °R, the integral on the

right hand side of Equation 17 for the bottom 0.0625 inch

thick frost layer can be calculated to be 1.485 mm. of Hg.

Hence, $p_{x=0.0625"} = 1.485$ mm. of Hg.

It should be noted that the assumption of $p_{x=0} = 0$

makes the above calculated value of $p_{x=0.0625"}$ the most

conservative one. Also, at time of 79 mins. $P_{vp,x=0.0625"}$

= 5.2 x 10^{-4} mm. of Hg. Hence, the required partial pressure at x=0.0625 inch indicate the existence of super-saturation ratio of $\frac{1.485}{5.2 \times 10^{-4}}$ = 2.86 x 10^3. Such a high value of supersaturation ratio, of course, indicates a strong possibility for occurrence of nucleation.

The strong possibility for nucleation indicates that Equation 14 may not be a valid representation of the true physical processes occurring in the frost interior. This indication can be verified by examing the realistic nature of the partial pressure value at the frost surface calculated from Equation 16. By setting the upper limits on the integrals of Equation 16 at x=δ, and using the data of Figures 9 and 12 and Equations 18 and 19, the partial pressure at the frost surface can be calculated to be 16.86 mm. of Hg. Since the experimental results of Figures 9 and 12 were obtained with the partial pressure of water vapor in the bulk gas at the value of 4.14 mm. of Hg., the above calcul-ated value of partial pressure at the frost surface is very unrealistic. Hence, Equation 14 could not be the true representation of the frost densification process.

It should be obvious to note that if the boundary condition for p in Equation 15 is set at the frost surface, then the partial pressure at x=0.0625 inch can be calculated from the following Equation 20

$$p_{x=\delta} - p_{x=0.0625"} = \int_{x=0.0625"}^{x=\delta} x \frac{d\rho_f}{d\theta} \frac{\tau RT}{(1-\rho_f/\rho_{ice})D_B} dx \tag{20}$$

Assuming $p_{x=\delta} = P_{vp}|_{x=\delta} = 1.632$ mm. of Hg. (note that this

assumption is quite realistic as indicated by simple model)

and calculating the right hand side of above Equation 20

from the data of Figures 9 and 12 and Equation 18 and 19

$P\mid_{x=0.0625"}$ was found to be -13.65 mm. of Hg. This

absurd value of partial pressure at x=0.0625 inch indicates,

once again, that Equation 14 does not represent the true

physics of the frost densification process.

Densification of Frost under Non-Equilibrium Conditions

(Non-Equilibrium Model')

Based on the results described above, a new model was

postulated to represent the true mechanism of water

transport in the frost interior. This model has only been

examined qualitatively in the present research. It can be

briefly described as follows.

The model postulates that the frost interior can be

divided into three sections on the basis of state of water

existing in the bulk interstitial gas. Near the frost

surface (region 1), where the vapor pressures of ice are

high, all the vapor exists in the vapor form. Near the cold

wall (region 3), where the vapor pressures of ice are

extremely small, all the water exists in the form of ice

nuclei. In between these two regions, there is a so-called

transition region (region 2), where the water exists both

in the form of ice nuclei as well as vapor.

As water vapor reaches the frost surface from the bulk

gas by diffusional mechanisms, it penetrates in the frost

interior due to a partial pressure gradient caused by a
temperature gradient at the frost surface. Since the 'simple
model' has been found to predict the water vapor transport
past the frost surface fairly successfully, it can be
assumed that at the frost surface water vapor is almost
in equilibrium with ice at the existing temperature. The
postulation regarding the state of water implies that the
supersaturation of water vapor (p/P_{vp}) in the interstitial
bulk gas should be considerably high at the interface of
regions 1 and 2, so that nucleation can occur. Thus, as
water vapor diffuses from the frost surface to the interior,
the supersaturation ratio increases from the value of
approximately 1 at the frost surface to a considerably high
value at the interface of regions 1 and 2.

The ice crystals in region 1 grow by the condensation
of water vapor. Hence, the crystal growth in this region
is controlled by the rate at which water vapor arrives at
the crystal surfacefrom the bulk interstitial gas. The
present model visualizes the uniform growth of the ice
crystals over the entire region 1 as a result of counter-
balancing effects of increase in driving force $(p-P_{vp})$
for the mass transfer between interstitial gas and the
crystal surface and the decrease in the molecular
diffusivity of water vapor in air (due to decrease in
temperature) with the increase in depth from the frost
surface.

As water continues to move deeper in the region 2,

water vapor is now not only used up due to the growth of
ice crystals by vapor condensation but also by the
generation of ice nuclei. At every layer, the generated
ice nuclei are kicked towards the cold wall by a thermal
force caused by the existing temperature gradient. While
moving, some of these nuclei are impinged (or trapped)
on the existing crystals. Thus, the crystals in this region
grow by deposition of ice nuclei on the existing crystals
as well as by vapor condensation. The model visualizes the
uniform growth of ice crystals in region 2 as a result
of a complex combination of these two separate mechanisms
of the growth.

The continuous depletion of the water vapor will result
in the existence of water only in the form of ice nuclei
at the interface of regions 2 and 3. Thus, water is
transported in region 3 only in the form of ice nuclei.
Since the temperature decreases with depth in this region,
nuclei will remain in the solid form as they move towards
the cold wall.

The ice crystals in region 3 can be expected to grow
uniformly due to a constant rate of trapping of the nuclei
on the existing crystals at every layer as the nuclei move
towards the cold wall. This is because for a given frost
structure the probability for the rate of nuclei impingement
can be visualized as a direct function of nuclei
concentration and the momentum of each nuclei. Brock's
equation (15) for thermal diffusive velocity indicate that

this velocity for the ice nuclei of a given size in the
frost interiorwould vary approximately linearly with
temperature gradient. Since the temperature gradient
increases with depth (see Figure 12), the thermal diffusive
velocity would also increase with depth. Thus, the constant
rate of trapping at every layer in region 3 could be caused
by the counterbalancing effect of increase in velocity
of the nuclei but decrease in nuclei concentration with
increase in depth from the frost surface.

The mathematical formulation of this 'non-equilibrium'
model is possible. However, due to extreme difficulty
involved in the accurate predictions of the nucleation rate
and the trapping rate of ice nuclei, the solution of the
mathematical equations is, at present, not possible.

Conclusions

From the results of the present research the following
conclusions are made regarding the deposition of water
frost on a cryogenically cooled surface.

1. The 'simple model' can be successfully used for the
design of cryogenically cooled equipment under a wide range
of frosting conditions.

2. At every layer in the frost interior, the bulk
interstitial gas and the ice crystals do not exist under
equilibrium conditions at the prevailing temperatures.
Thus, even though the water transport past the frost-gas
interface can be successfully predicted with the assumption
of an equilibrium between ice and gas at the frost surface,

the complete picture of the frosting process can only be
successfully modelled with the assumption that water
transport at every layer in the frost interior occurs by
diffusional mechanism under a non-equilibrium partial
pressure gradient as well as by the transfer of ice nuclei.

3.   The density of the frost deposited on a liquid nitrogen
-cooled surface stays always uniform with depth. The
'non-equilibrium model' appears to explain the true
mechanism for uniform densification of the frost.
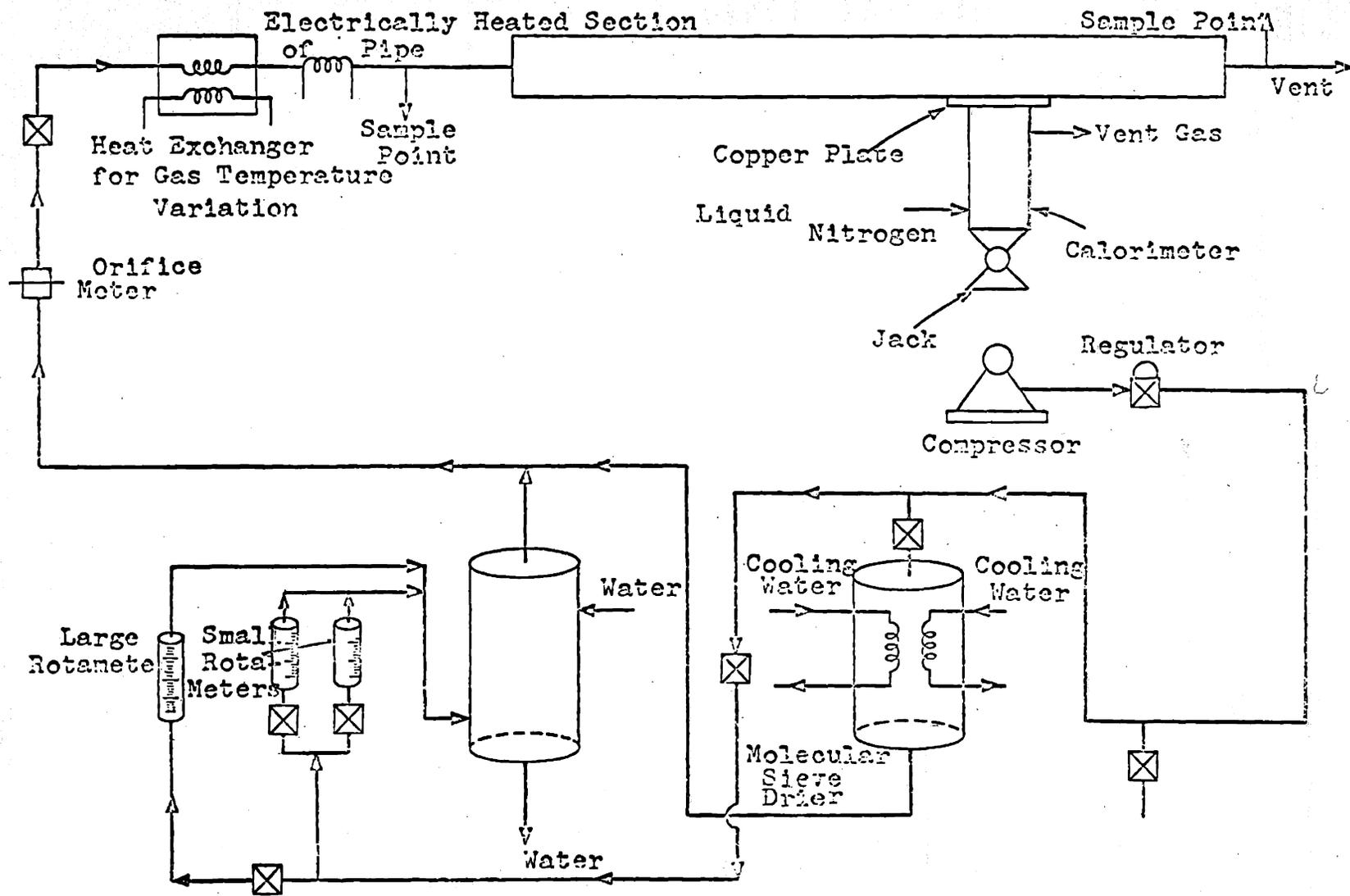
Figure 1   Flowsheet of Equipment

Experimental Data

○ Re=5,790·Humidity=Gas dew point at 27.2°F.
$T_g = 34°F$

△ Re=5,100·Humidity=Gas dew
point at 27.2°F·T_g=93°F

– – – Theoretical
Curves

Frost Thickness (inches)

0.40

0.30

0.20

0.10

0

40 60 80 100 120 140
Time (mins.)

Mass Deposition (lbm/ft^2)

0.07

0.06

0.05

0.04

0.03

0.02

0.01

20 40 60 80 100 120 140
Time (mins.)

Average Frost Density(gms./cc.)

0.10

0.09

0.08

0.07

0.06

0.05

0.04

0.03

40 60 80 100 120 140
Time (mins.)

Heat Flux(BTU/hr ft^2)

1,000

900

800

700

600

500

400

300

20 40 60 80 100 120 140
Time (mins.)

Figure 2   Experimental Facts and Theoretical
Predictions on Effect of Gas Temp-
erature on the Time Variation of Frost
Properties and Heat and Mass Fluxes
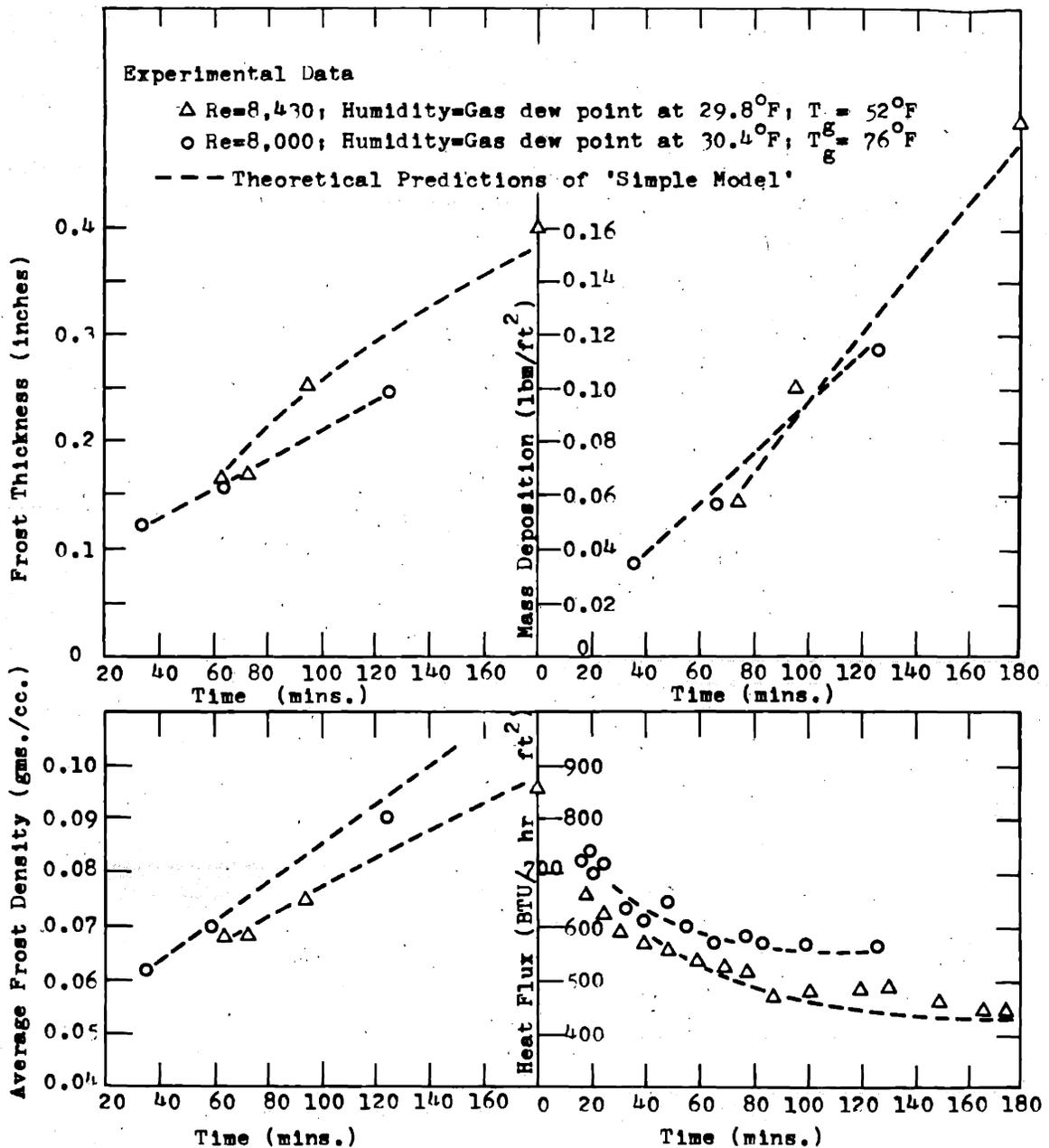
Figure 3   Experimental Facts and Theoretical Predictions on
Effect of Gas Temperature (at Constant Humidity and
Reynolds Number) on Variation of the Frost Properties
and Heat and Mass Fluxes with Time

Figure 4

Experimental Data:

	Gas Temperature	Cold Surface Temperature	System Conditions
□	93°F	15°F	Frosting
○	75°F	8°F	Frosting
△	50°F	5°F	Frosting
⬡	34°F	2°F	Frosting
●	82°F	-11.5°F	Non-Frosting

—— Theoretical Predictions under Non-Frosting Conditions (105)

① $T_g = 93°F$, $T_s = 15°F$
② $T_g = 75°F$, $T_s = 8°F$
③ $T_g = 50°F$, $T_s = 5°F$
④ $T_g = 34°F$, $T_s = 2°F$

Heat Transfer Coefficient (B'U/hr ft² °F)
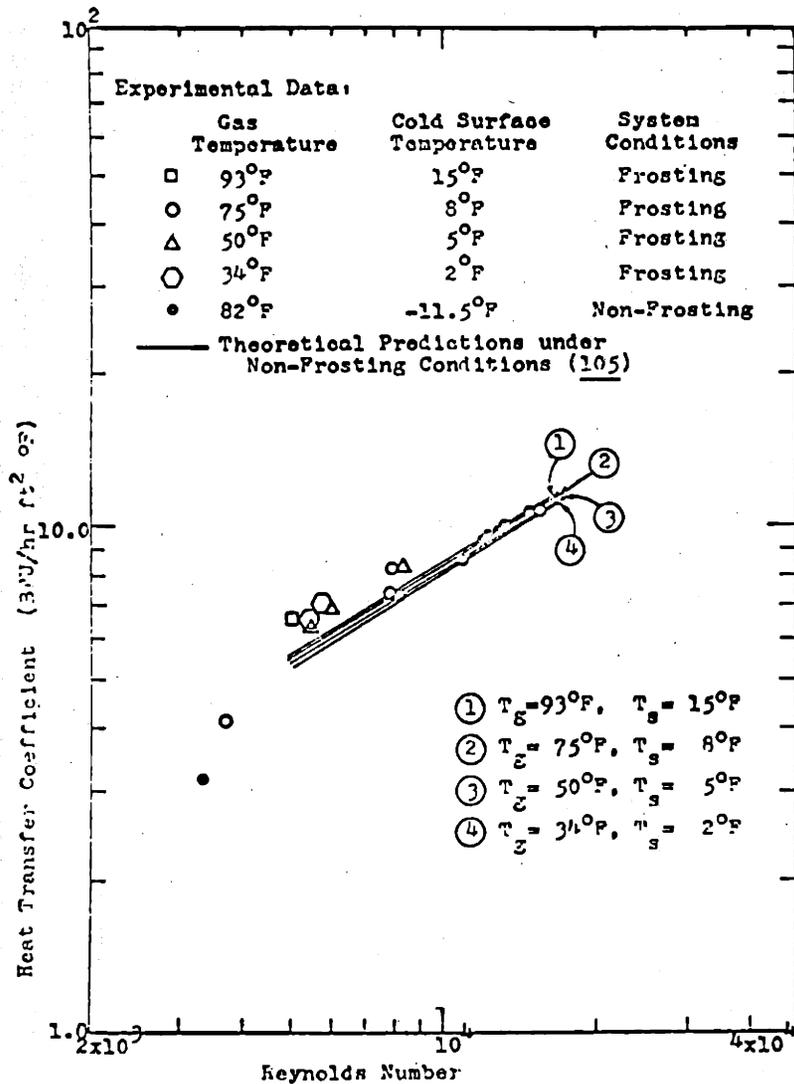
Reynolds Number

Figure 4 Heat Transfer Coefficient versus Reynolds Number (at Various Gas Temperatures) under Frosting and Non-Frosting Conditions

Figure 5

Experimental Data:

	Gas Temperature	Cold Surface Temperature
□	93°F	+ 15°F
○	75°F	+ 8°F
△	50°F	+ 5°F
⬡	34°F	+ 2°F

—— Theoretical Predictions from Lewis Analogy (104)

① $T_g = 93°F$, $T_s = 15°F$
② $T_g = 75°F$, $T_s = 8°F$
③ $T_g = 50°F$, $T_s = 5°F$
④ $T_g = 34°F$, $T_s = 2°F$

Mass Transfer Coefficient (ft/hr)
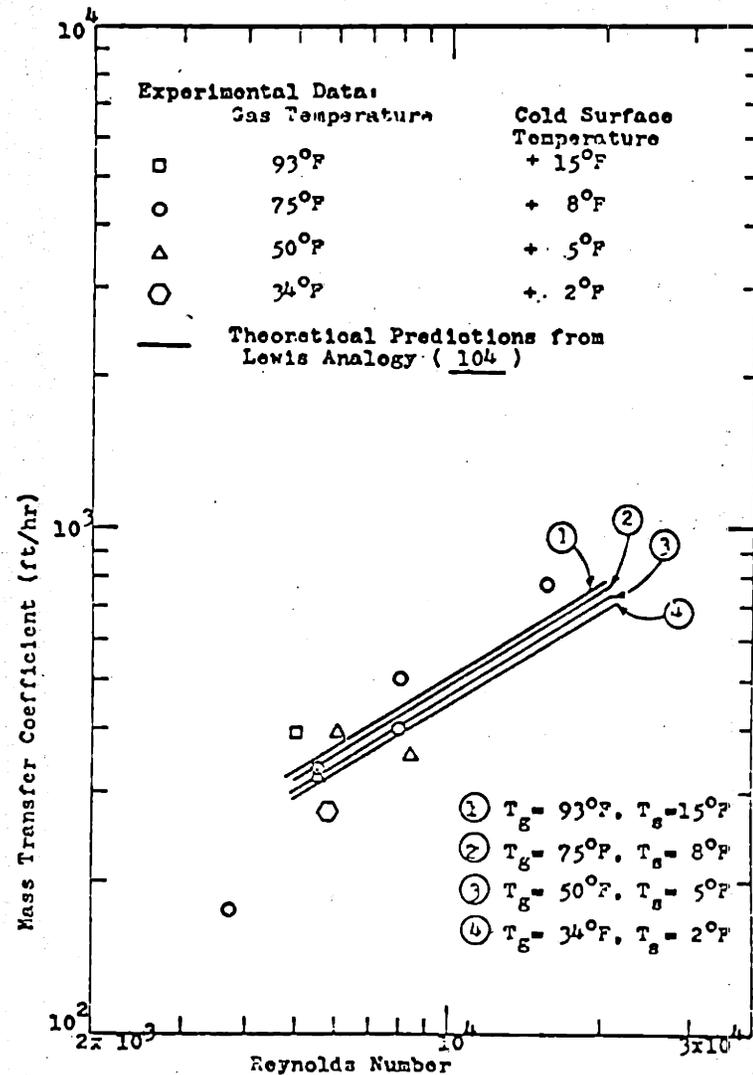
Reynolds Number

Figure 5 Mass Transfer Coefficient versus Reynolds Number (at Various Gas Temperatures) under Frosting Conditions

42

Heat Transfer Coefficient = h
Mass Transfer Coefficient
$= K_g$

Reynolds Number = Re
Gas Temperature = T_g
Humidity = p_g

←———————Gas Flow

Direction of Heat and Mass
Transfer

Heat Flux = $h(T_g - T_s) + K_g(p_g - p_s)\Delta H$
Mass Flux = $K_g(p_g - p_s)$

(T_g, p_g)

(T_s, p_s)

Thermal Boundary Layer

Heat Flux $= J|_{x+\Delta x}$

←—— Frost Surface
(Temperature = T_s)

$x + \Delta x$
x

Frost   Layer

$J|_x$

x

(T_w, p_w)

Temperature Profile

←—— Cold Wall
(Temperature = T_w)

$J|_{x=0} = 0$
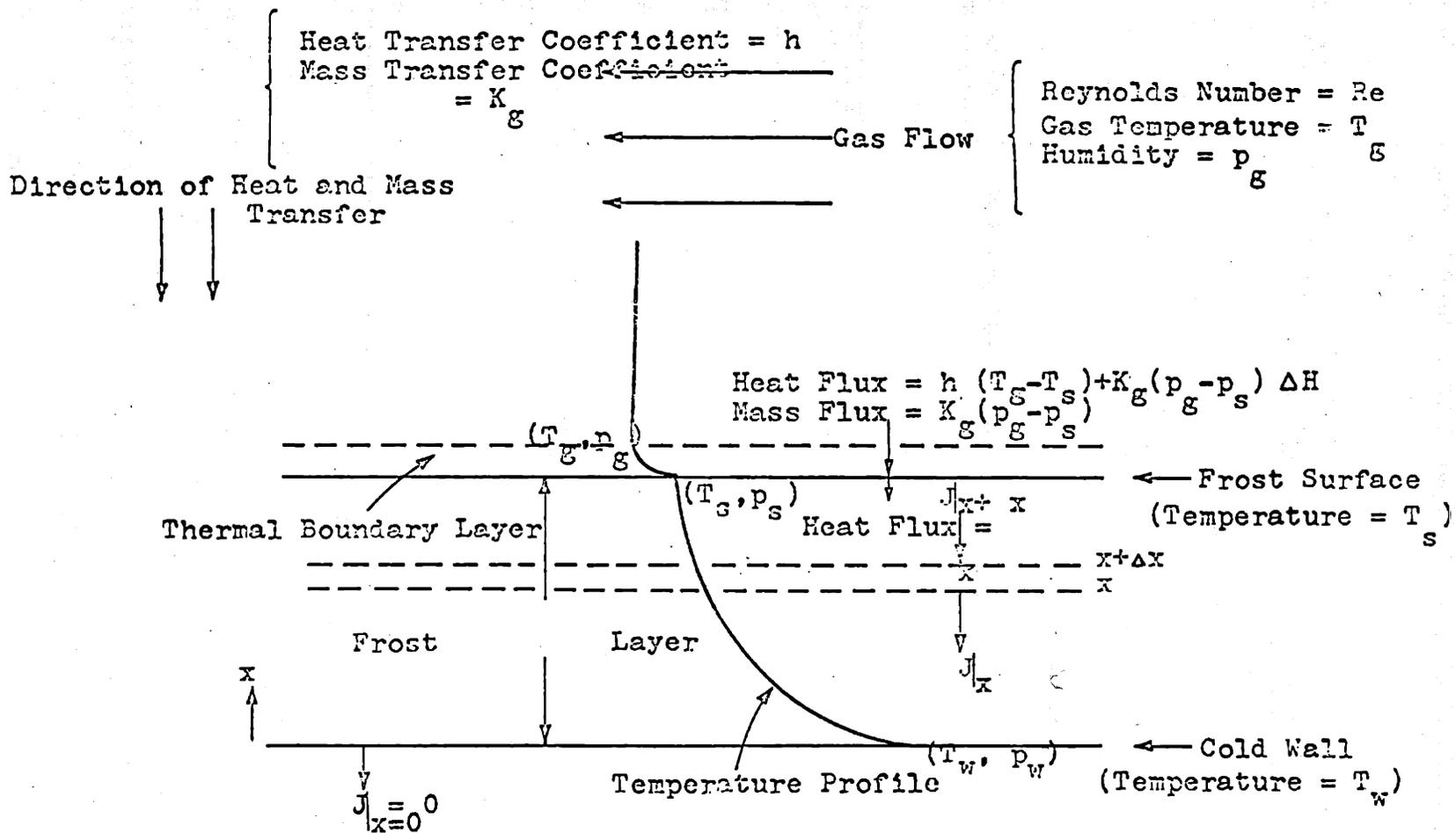
Figure 6   Schematic of Frosting Process as Visualized by
Improved   Model

43
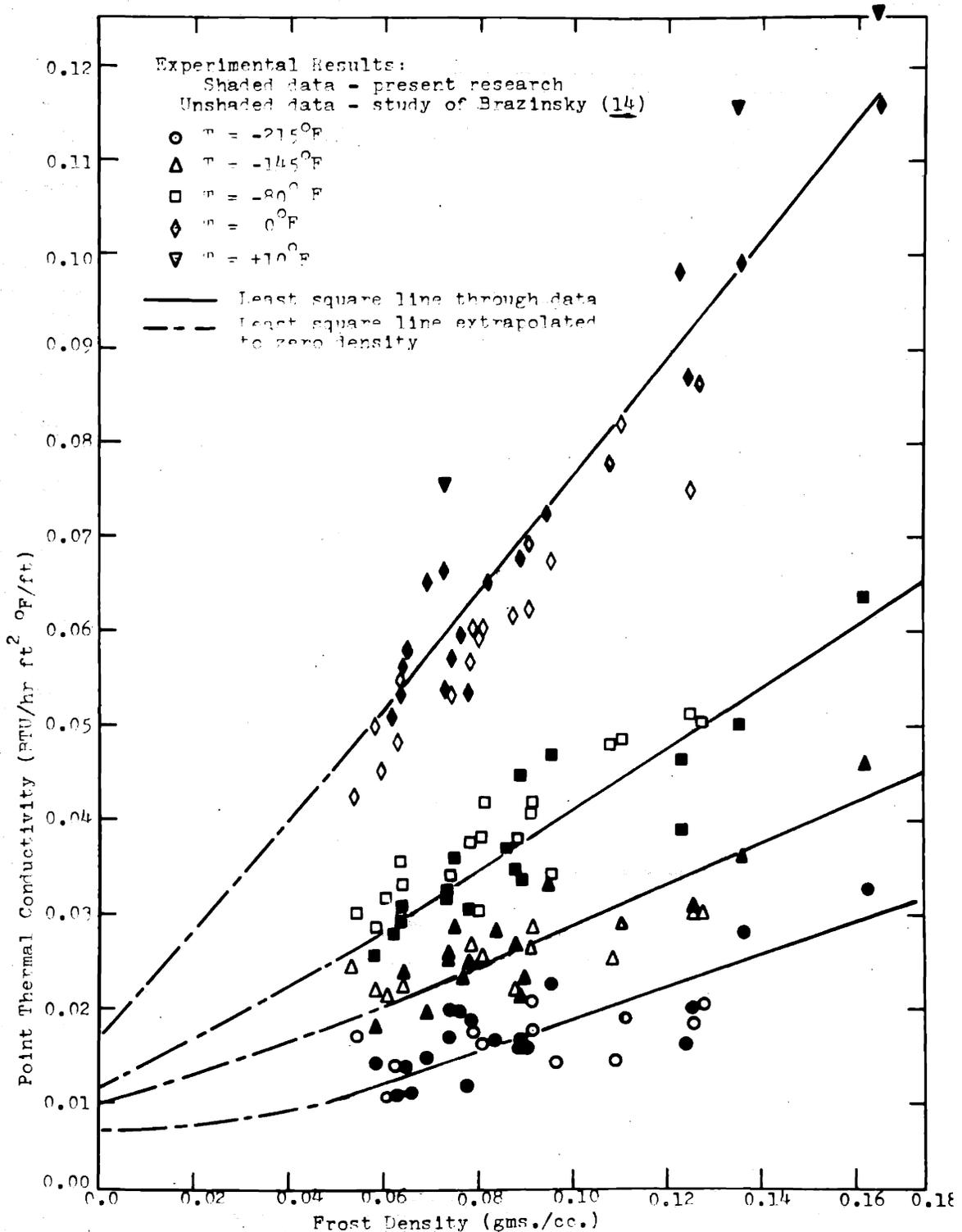
Figure 7   Point Thermal Conductivity as a Function of Density
with Temperature as a Parameter

θ = 20 mins.

θ = 17 mins.

θ = 12 mins.

θ = 2 mins.

θ = 7 mins.

Frost Density (gms./cc.)

0.10
0.09
0.08
0.07
0.06
0.05
0.04
0.03
0.02
0.01
0

0   0.02   0.04   0.06   0.08   0.10   0.12
Distance from Cold Wall (inches)
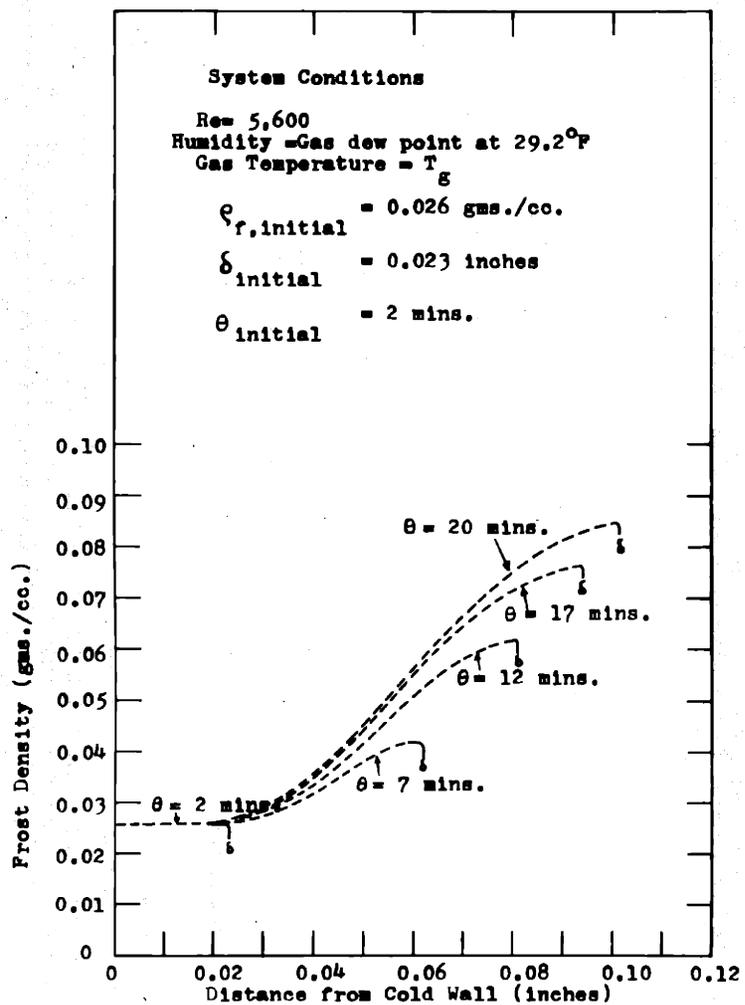
Figure 8   Predictions of 'Improved
Model' for Time Variation in Frost
Density and Thickness

● Average Density of the Entire Frost Layer
▲ Density of the Bottom 0.0625" Thick Frost Layer
■ Density of the Bottom 0.125" Thick Frost Layer

Experimental Conditions

Re = 15,800
Humidity = Gas dew point at 29.8°F
T_g = 71°F

Frost Density (gms./cc.)

0.17
0.16
0.15
0.14
0.13
0.12
0.11
0.10
0.09
0.08
0.07
0.06
0.05
0.04

0   50   100   150
Time (mins.)
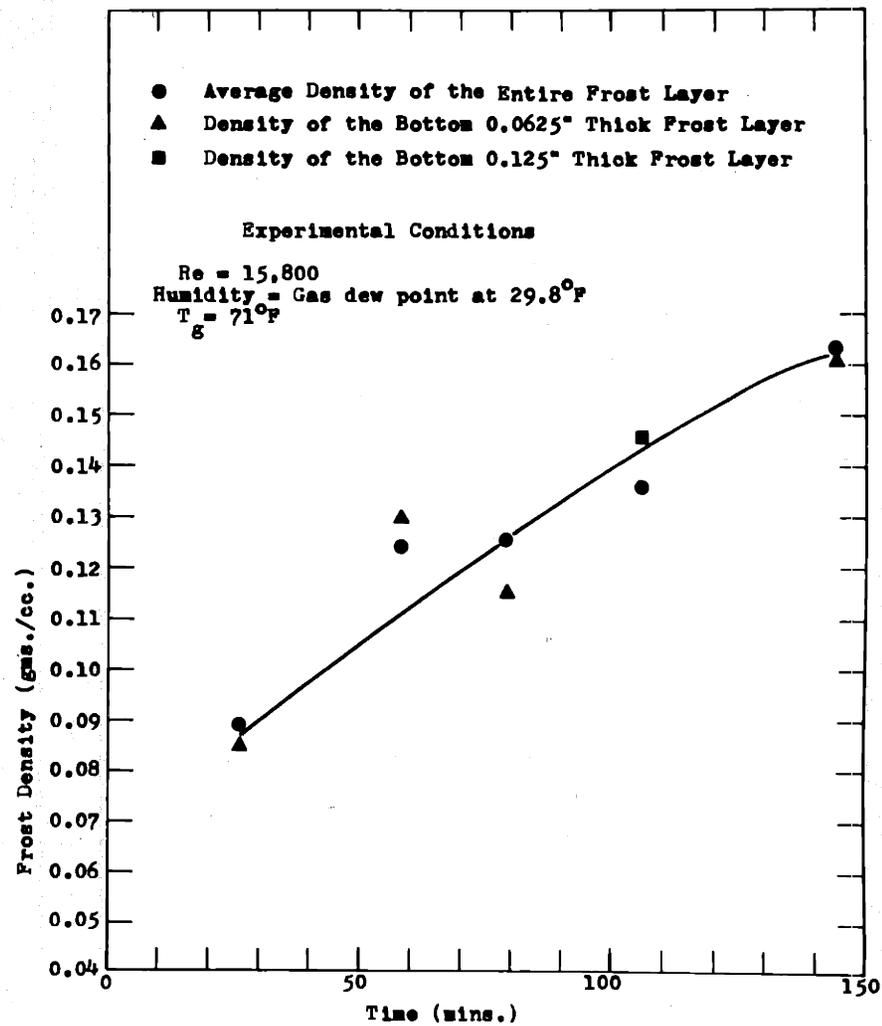
Figure 9   Density Distribution within the Frost as a
Function of Time

Heat Flux (BTU/hr ft²)

—— Curve generated by 'Simple Model'
—·—·— Curve generated by 'Improved Model'

1,300
1,100
900
700
500

2   10   20
Time (mins.)

Prost Thickness (inches)

0.10
0.075
0.05
0.025
0

System Conditions

Re= 5,600
Humidity=Gas dew point at 29.2°F
T_g= 70°F

0   10   20
Time (mins.)

Average Frost Density ($\frac{gms.}{cc.}$)

0.05
0.04
0.03
0.02
0.01
0

0   10   20
Time (mins.)
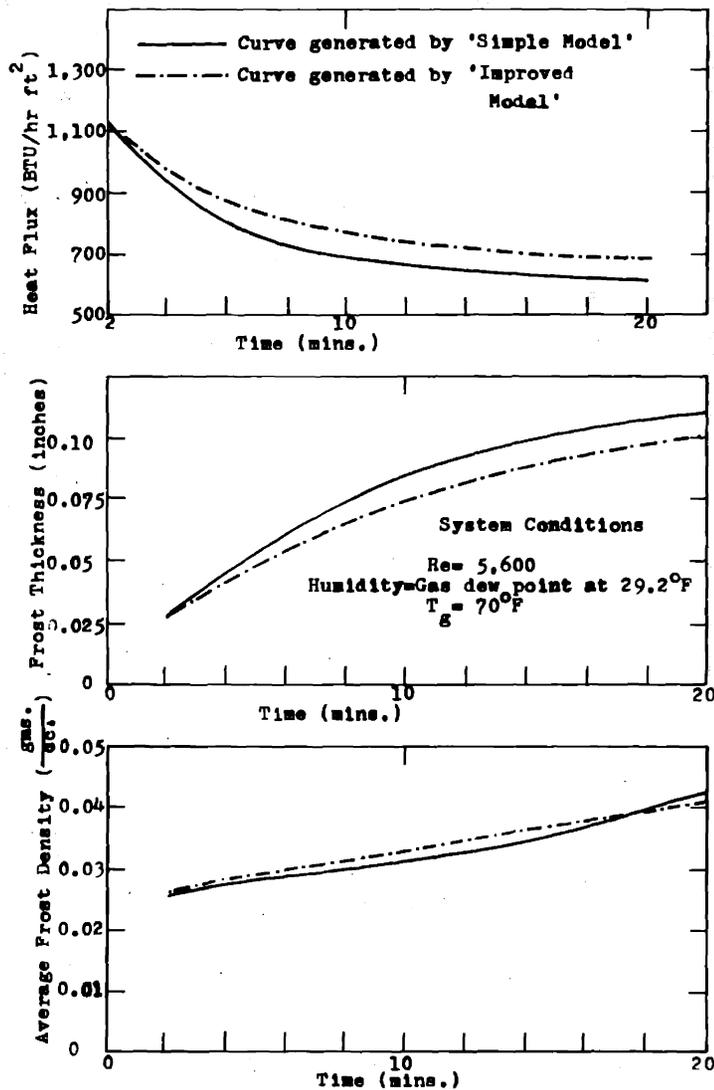
Figure 10   Comparison between Predictions of 'Simple' and 'Improved' Models

—— — Predictions of 'Improved Model'
—— Predictions of 'Simple Model'

System Conditions

Re=5,600; Humidity=Gas dew point at 29.2°F;
T_g= 70°F

Starting Time for Theoretical
Predictions = 2 mins.

θ = 7 mins.

θ = 20 mins.

θ = 2 mins.

Temperature (°F)

+20
0
-20
-40
-60
-80
-100
-120
-140
-160
-180
-200
-220
-240
-260
-280
-300
-320

0   0.05   0.10
Distance from Cold Wall (inches)
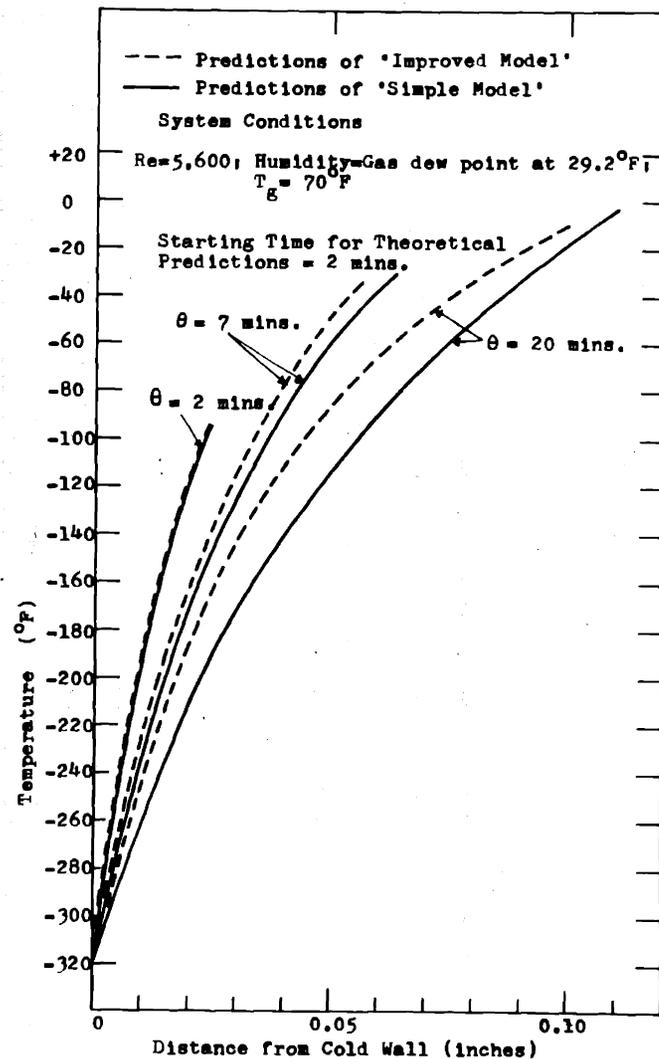
Figure 11   Predictions of Time Variation in
Temperature Distribution within
the Frost by 'Simple' and
'Improved' Models
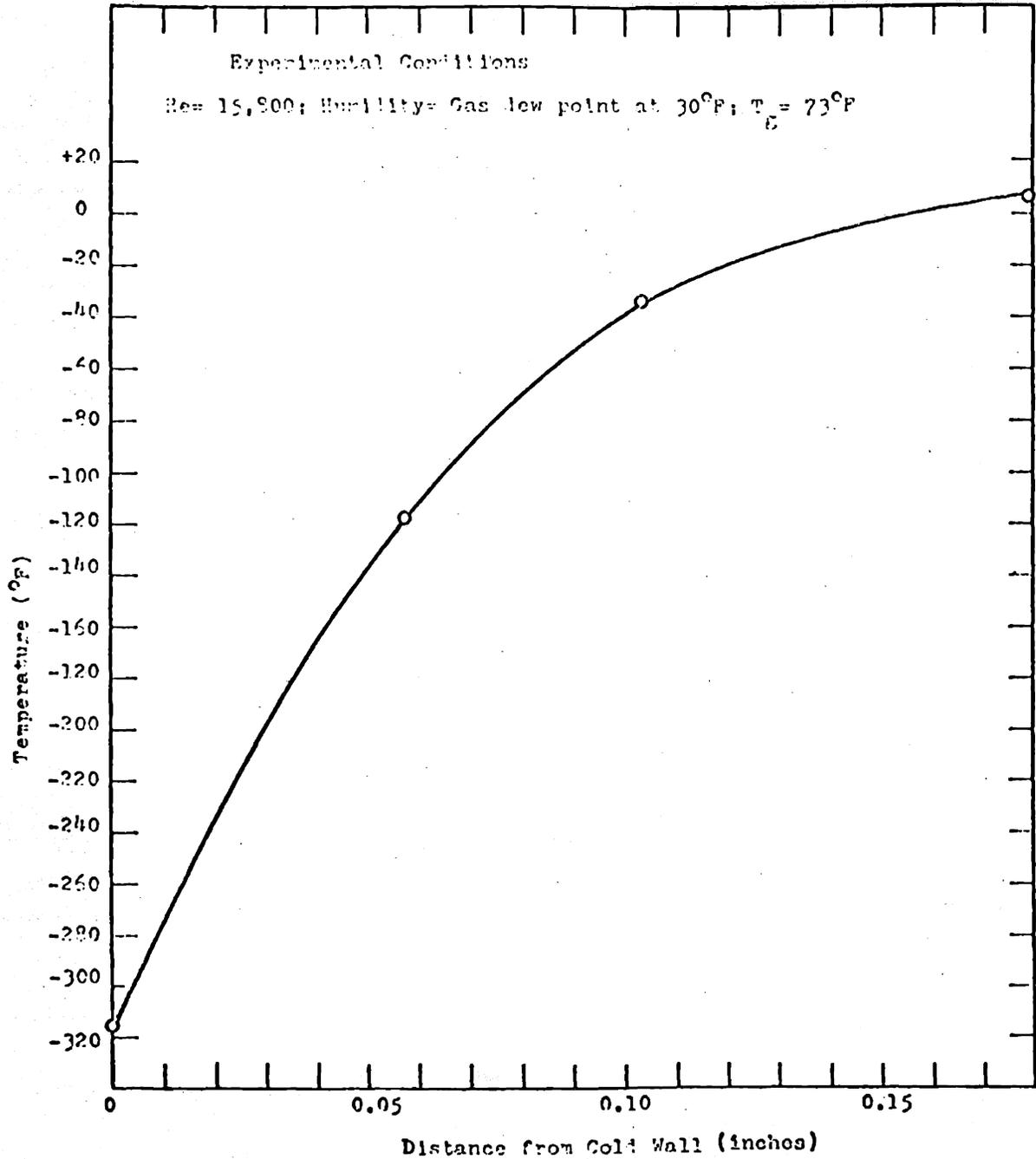
Figure 12   End of Run Temperature Profile within the Frost

S E C T I O N   I

INTRODUCTION

Summary

Although there are some data reported in the literature
on the structure and properties of water frost as well as
for the heat transfer under frosting conditions, there is
as yet no completely satisfactory quantitative theory for
the frosting process.

The frosting process with both small and large wall-gas
temperature differences have been investigated. The frosting
heat transfer studies have dealt with both natural and forced
convection. In all the studies heat flux through the frost
has been found to reach a nearly steady value after a short
duration of frosting.

For small wall-gas temperature differences diffusional
mechanisms control the transport of water vapor from gas to
cold surface. For the frost deposition on a surface at
cryogenic temperatures, diffusional mechanisms control the
water vapor transport after a smooth layer of frost is formed.

The formation of a smooth frost layer on a surface cooled
by liquid nitrogen appears to occur in a very complex manner.
It seems that at first, frost deposits are formed in the forms
of clumps and then very soon these clumps are "filled in".
Due to the fluffy nature of the frost, a small deposit of it
creates significant insulation on the cold surface; and
hence a smooth thin layer of this frost raises the surface

temperature to the extent that fogging in the gas phase
boundary layer becomes highly improbable. The time for the
formation of a smooth frost layer has been found to depend
upon the gas phase turbulence.

The quasi-steady state heat flux during the frosting
process is achieved by simultaneous increase in frost
conductivity and thickness such that the thermal resistance
of the frost remains almost constant. The frost conductivity
is increased by increase in density. The density of the
frost increases by the diffusion of water vapor in the frost
interior which is caused by the vapor pressure gradient at
the frost surface.

It is the objective of this research to obtain a quant-
itative model of the frosting process which could enable
one to explain the experimentally observed effects of the
various system variables on the frost properties. Both
experimental as well as theoretical studies are planned.
Some light will also be shed upon the physical processes
occurring in the frost interior.

I-A Practical Application of the Frosting Phenomenon

Process in which heat is transferred to a refrigerated
surface with the simultaneous deposition of a frost layer
are important in gas coolers, refrigeration, regenerators,
freeze-out purification of gases, cryopumping and the
storage of cryogenic liquids. In these processes, frost
deposition may be required for successful operation of a
process or it may be an undesirable side effect.

The practical application of the frosting process can be well illustrated by its effect on the aerospace industry. In this industry frost deposits are found to be of mixed blessings. Frost accumulates on the walls of uninsulated missile fuel tanks. These frost layers partially insulate the Oxygen supply from external heat leak, thus reducing the amount of liquid required for 'topping' before firing. However, the accumulated frost adds an undesirable (and unknown) weight to the missile. These effects of frost depositions on the aerospace industry are typical examples of the industrial occurrences of the frosting phenomenon.

Even though there has been research work in each of the above mentioned industries, the data, when available, are widely scattered through out the literature. Most of the published work is directed toward refrigeration and freeze-out purification. Frosting process under natural convection has been studied somewhat extensively by missile industries. Forced convection frosting has also been reported recently by several investigators (7,14,23,24,26,50,51,58,86,89,90, 114). The final results of all these investigations are, however, correlated empirically and are applied specifically to the system conditions taken under examination. For these reasons, a generalized theory for the frosting process is of significant practical interest.

I-B Description of the Frosting Process

Frost deposits form when a gas mixture comes in contact

with a surface whose temperature is below the dew point of the gas and the freezing point of the vapor. As the mixture flows over the cold surface a concentration gradient is established normal to the surface, resulting in a mass flux towards the cold wall. Simultaneously, a temperature gradient is established causing a heat flux which cools the gas.

For small temperature differences between the bulk gas and the cold surface, the condensible component in the gas phase will move towards the wall by molecular and turbulent diffusional processes. If these temperatures are known, the heat and mass fluxes can be predicted with the usual heat and mass transfer correlations.

As the cold surface temperature is decreased and the temperature difference between the surface and the gas is increased, the diffusion mass flux at first increases rapidly and then levels off because the equilibrium concentration of the condensible component at the surface is approximately an exponential function of the surface temperature as shown in Equation I-B1.

$$\ln p_w = \frac{a}{T_s} + b \qquad (I\text{-}B1)$$

The heat flux, however, continues to increase almost linearly according to Equation I-B2

$$q = h \, (\, T_g - T_s \,) \qquad (I\text{-}B2)$$

Thus, the gas stream may be cooled below the dew point for low surface temperatures. This may cause sufficient

supersaturation in the gas phase thermal boundary layer to
form fog particles or ice nuclei. Particle impingement or
trapping of the particles on the surface then becomes the
dominant mechanism of frost deposition. Therefore, the
difference in deposition mechanism for large and small
temperature differences depends on the formation of fog in
the gas stream.

The limits for fog formation within the gas film adjacent
to a cold surface have been derived by Johnstone and
co-workers (57). The derivation assumed that a gas vapor
mixture flowed in fully developed pipe flow. It was also
assumed that the film theory adequately described the flow
(i.e. a turbulent core without concentration and temperature
variation normal to the surface, and a stagnant film where
heat and mass transfer resistances are concentrated). Bulk
temperatures and humidities were found for which the film
remained everywhere unsaturated. A plot of fog formation
limits for the water-air system is shown in Figure I-B1.
The plot shows water vapor concentration as a function of
gas phase dry bulb temperature at various surface temperatures.
For any surface isotherm, operating points below this curve
show regions where no fogging can occur anywhere in the gas
phase. Fog may form for all bulk gas conditions lying above
the curve for a particular surface temperature. The plot shows
that, for a given bulk gas temperature, the maximum humidity
without fog formation is a strong function of the surface
temperature. Thus, this plot indicates approximately the

regions of high and low temperature differences. The theories
for fog formation limits in various other systems are described
by Amelin (2).

The deposition of the frost on a very cold surface (about
-315°F) with a large temperature difference between the
cold surface and the gas appears to be a very complex process.
Initially, fog or ice nuclei are formed in the gas phase (92,
116). These nuclei probably grow by diffusion of water vapor
and by collisional processes. The nucleated particles are
quite small and most likely follow the motion of the flutuating
eddies in the turbulent gas stream. Some particles deposit
on the cold wall; others are apparently swept away from the
cold surface and sublime. The initial deposit is an irregular
patchy frost and could be resulted from the formation of a
few micro-islands of frost which acted as traps for additional
ice particles. A good discussion of phenomenon of particle
transfer from the gas phase is given by Weber (114). During
this initial phase, temperatures in the frost are probably
not significantly different from the cold surface temperature.
However, as the clumps of frost grow and the space between
these clumps is filled in, a layer of frost, which now has
significant insulative effect, builds up. This type of
deposition is usually of short duration, and the time depends
upon the conditions of the system variables such as Reynolds
number, humidity and gas temperature (14). Thus, after a
short while, a smooth layer of frost insulates the cold
surface and, in effect, imposes a thermal resistance which

results in a sufficient increase in the frost surface
temperature so that diffusional mechanisms of frost
formation predominates.

Since the formation of fog in the gas boundary layer
is usually of short duration for the frost deposition by
forced convection, these mechanisms are neglected in the
theoretical study of the present research.

I-C Previous Studies

The key original ideas for the development of those
theoretical models studied in the present research evolved
from the logical explanation of the experimentally observed
phenomena by previous investigators.   Hence, in this section
a brief survey of the important previous studies in the
present research area is made.

A.   NATURAL CONVECTION:

a.   Frosting with Small Temperature Differences:

Experimental data for natural convection on horizontal
cylinders with a small temperature difference between the
gas and the cold surface (18, 41, 102) show that the total
heat flux through the frost at first increased, then decreased
to a steady value, smaller than the initial value.   This
increase of about 20% is believed to be caused by the
increased roughness of the frost deposit.   Alternatively,
the increase may be viewed as due to the fin effect of the
individual frost elements.   The true reason, however, is
not known as yet.

Frost formation in natural convection over a vertical plate two feet high has been investigated by Whitehurst (115, 117). His measurements showed that the total heat flux for the plate decreased fairly rapidly at first and then reached a steady value. Higher gas humidities gave a higher initial heat flux and a lower steady state heat flux than the lower humidity. The initial heat flux value was found to be higher at lower plate temperatures but the steady state value of heat flux was found to be independent of plate temperature.

Whitehurst (115, 117) as well as Stoecker (109) found that the frost thickness increased even after the asymptotic heat flux had been reached. Since the thermal resistance of the frost layer must remain constant after the steady state heat flux has been reached, they concluded that the frost thermal conductivity increased to compensate for the increased thickness. Schropp (102) found that the average frost conductivity increased right from the beginning of frost accumulation. He found that both frost density and thermal conductivity increased as frosting proceeded. This simultaneous increase in frost density and thermal conductivity agrees with the work of other investigators who have found that frost or snow thermal conductivity increases with density (25, 38, 120). Schropp (102) and Stoecker (109) found that for natural convection with small temperature differences frost density values ranged from

about 0.091 gms./cc. to nearly 0.917 gms./cc. depending

upon the system conditions.

b.   Frosting with Large Temperature Differences:

    Natural convection frosting with temperature differences

greater than 100°F have been studied for various geometries

such as vertical cylinders (92), vertical plates (117) and

spheres (52).   In these studies, a constant heat flux

through the frost was reached after a short time of frosting.

The rate of frost accumulation on the cold surface, at first

increased slightly, then decreased and levelled off, while

the density increased from a very small value to within 5

per cent of that of solid ice.   The mass of frost adhering

to the cold surface was only 10 to 30 per cent of that

predicted by the Lewis relation or the Chilton and Colburn

analogy.   Ruccia and Mohr (92) obtained the frosting heat

flux correlation based on the data for a cylindrical liquid

oxygen tank 18 inches in diameter.   This correlation predicts

that higher humidities yield lower steady state over-all

heat transfer coefficients.   The data of Holten (52),

however, show no humidity effect.   The reason for this

discrepancy is not known.

B.   FORCED CONVECTION

a.   Small Temperature Differences:

    Forced convection has been investigated in a number of

geometries.   Frosts were deposited inside tubes (23, 51, 90)

and on the inner surface of an annulus in a double pipe

exchanger (59) for counter current flow of coolant and
air. Frosts were also formed on a flat plate in a wind
tunnel (26) and on the inner surface of an annulus (7)
with constant surface temperature. Single cylinders in
cross flow (24) as well as staggered (50, 86) and in-line
(50) tube banks have been used. In all the cases the total
heat flux and the convective heat flux for the frosted
surface attained a steady state value lower than the unfrosted
flux. For internal frosting (i.e. inside tubes and annular
passages) the over-all heat transfer coefficient increased
at first and then decreased, as in natural convection.
The effect of frost roughness was investigated by Coles and
Ruggieri (26). Their frost layers were formed by diffusion
and convection from a high velocity gas stream.

Chen (23) was the first to propose a mechanism for
frost growth. He postulated a two step mechanism; the
layer first grows towards a stable roughness height and then,
as deposition proceeds, it remains at the stable height.
The stable roughness height is reached when the rate of mass
transfer to the top of the element equals that to the "valleys"
between rough height decreases as Reynolds number increases
and that, as deposition proceeds, the stable roughness height
decreases due to area blockage. The net effect of these
two steps is to raise the gas side coefficients (78) and
thus the over-all coefficient. However, as frost continues
to accumulate, the insulation effect takes over and the heat
flux decreases. The pressure drop increases rapidly as

the roughness builds up to its stable value, then
increases more slowly as frost accumulation blocks the
flow area. Fair agreement was obtained between Chen's
data and the prediction of this theory. However, he did
not account for the increased temperature difference in the
unfrosted portions of the exchanger, and frost thermal
conductivity and density were taken as adjustable constants.

Chung and Algren (24), Hardy, et al. (50) and Prins (86)
found that frost continued to accumulate after the steady
state heat flux had been reached. Rische (90) measured the
density of beniene frosts formed inside a tube over a range
of Reynolds number. His data show that the density increased
with time and approached that of solid benzene for long times
and high gas velocities (Reynolds numbers). Higher velocities
yielded higher density at any given time. Extropolation of
his density time curve back to zero time indicated that
higher velocity formed denser layers initially.

b. Large Temperature Differences:

Very few investigations have been done on the formation
of the frost on liquid nitrogen cooled surfaces in forced
convection. Richards et al. (89) studied the frost deposited
outside of the liwuid nitrogen cooled cylinder. Liquid
nitrogen was continually circulated through the cylinder by
natural convection due to the heat flow to the cylinder.
The vapor was separated from the liquid and measured to
determine the total heat flux. In these tests the heat

flux attained a steady state value which was a function

of the velocity and humidity of the air stream. For water

contents greater than about one percent by volume the steady

state heat flux was greater than the initial flux. For

humidities about 2 mole per cent water the heat flux

fluctuated around the steady value. This fluctuation was

believed to be due to the condensation of liquid water on

the frost surface. This water soaked into the frost causing

it to shrink and pack together forming a layer of ice at

the frost surface. Snow-like frost was then deposited on

the layer of ice until the surface again reached 32°F and

water droplets formed. The cycle was then repeated. The

heat flux decreased during frost deposition but increased

when the layer froze.

Figure I-C1 shows typical values of the heat flux from

Reference 89 for a Reynolds Number of 132,000 (velocity of

80 ft/sec.), gas temperature 100°F and three humidities.

No fluctuations appeared for the lowest humidities, but they

were very pronounced for the highest water vapor content.

Frost layer thermal conductivities also showed fluctuations

as shown in Figure I-C2.

Weber (114) studied the heat transfer and the frost

accumulation rates for flow through a tube when the tube was

cooled externally by liquid nitrogen. He found that as

frosting began the frictional pressure drop increased and

the over all heat transfer coefficient decreased. After

some time, however, the heat flux reached a constant value
even though frost thickness continued to increase. As the
inlet humidity increased (at a given flow rate) these
changes occurred more rapidly and the steady state over-
all heat transfer coefficient decreased.

A typical plot of the apparent overall heat transfer
coefficient versus time for a given Reynolds number at
three different humidities as obtained by Weber (114) is
shown in Figure I-C3. The effect of Reynolds number at a
given humidity on the apparent overall heat transfer
coefficient versus time profile is shown in Figure I-C4.
The apparent overall heat transfer coefficient was defined
by the following Equation I-C3.

$$\overline{U}_a = \frac{Wc_p}{D_o L} \ln \left(\frac{T_1 - T_w}{T_2 - T_w} \right) \qquad (I-C3)$$

Weber explained his results by saying that during the
steady state heat transfer both frost density and thermal
conductivity increased when more frost accumulated to yield
the constant overall heat transfer coefficients. He postulated
that the increase in frost density was caused by the
diffusion of water vapor towards the cold wall due to
temperature gradient across the frost layer. The increased
frost density gave an increased frost thermal conductivity.
The steady state heat transfer coefficients were lower for
the higher inlet humidities because less time was available

for frost densification by diffusion. Therefore, at the
heat transfer steady state the higher humidities gave
frosts with lower densities and thus lower thermal
conductivities. Weber's postulation for the internal
diffusion is the basis for the first two theoretical models
studied in the present thesis. It is described in more
detail in Section I-D.

Initially Weber (114), and later Brazinsky (14),
determined the thermal conductivity of the frost deposited
on a liquid nitrogen cooled surface. Frosts were formed
on a liquid nitrogen cooled copper plate which was part
of the underside of a rectangular duct. Their system was
very similar to the one used in the present thesis. Their
results showed that the thermal conductivity of the low
temperature frosts increased with density. However, for
a given frost density the thermal conductivity was lower
for the lower frost surface temperature.

Brazinsky (14) also found that frost density increased
with time and at any time density increased with the Reynolds
number. The steady state value of heat flux was found to
be increased with Reynolds number and decreased with increase
in humidity. These results are shown in Figure I-C5. In
quasi-steady state heat transfer region, the frost surface
temperature was found to remain constant and almost
independent of system conditions. The values of the frost
surface temperatures for typical experimental conditions

are shown in Table I-C1. Brazinsky (14) also obtained

thermal conductivity of frost as a function of density

and temperature from the measurement of temperature

distribution in the frost interior. A typical temperature

profile in the frost interior is shown in Figure I-C6.

C. Heat and Mass Transfer Analogies for Frosting

The applicability of the heat and mass transfer analogies

to the process of frost formation has been tested

experimentally by Chung and Algren (24) and Coles and

Ruggieri (26). Two simple analogies are the Chilton and

Colburn analogy and the Lewis analogy. The Chilton-Colburn

analogy is

$$j_H \quad = \quad j_D \qquad\qquad (I\text{-}C4)$$

For small vapor concentration the analogy becomes

$$\frac{h}{c_p G} \ (\ Pr\ )^{2/3} \quad = \quad \frac{K_g \rho_g}{G} \ (\ Sc\ )^{2/3} \qquad (I\text{-}C5)$$

The Lewis analogy for small vapor concentration may

be written as (104)

$$\frac{h}{K_g \rho_g c_p} \quad = \quad (\ Le\ )^{2/3} \qquad\qquad (I\text{-}C6)$$

Hence, from definition of the j-factors, the Lewis

analogy in terms of j-factors is

$$j_H \ / \ j_D \quad = (\ Pr/Sc\ )^{2/3} \quad = \ (\ Le\ )^{2/3} \qquad (I\text{-}C7)$$

The j-factors for frosted surface from the experimental

data of References 24 and 26 were calculated. The results

are summarized in the following Table I-C2.

Table   I-C2

Verification of Heat and Mass Transfer Analogies

	Coles (26)	Chung (24)
Geometry	plate	cylinder
Mass Transfer By	sublimation	deposition
Reynolds number	$0.8\text{-}4 \quad 10^{6}$	$0.2\text{-}1 \quad 10^{4}$
$j_H\ /\ j_D$	1.25	1.18

The data of Table I-C2 are within 12% of the simple Lewis relation (Equation I-C7). The Chilton and Colburn analogy was well verified when the frost surface temperature reached $32^{\circ}F$ and liquid water condensed (59).

D. Properties of Cryogenic Frosts

The density of the cryogenic frost has been found to be much lower than those of the frost deposits formed at high temperatures (14). Until now, the variables which significantly affect the frost density are found to be Reynolds number (or gas velocity), humidity and time elapsed since the start of frosting (14).

The thermal conductivity of the frost deposited on a cryogenically cooled surface has been studied by few investigators (6,14,52,114,115). Holten (52) obtained the average thermal conductivity from the calculated temperature differences across the frost, and measured

values of the heat flux and frost thickness. He observed

that average frost layer thermal conductivity was a strong

function of the average frost temperature. Barron (6) and

Whitehurst (115) also calculated thermal conductivity of

the frost from the measurements of heat flux, frost thickness

and temperature difference across the frost. Their frosting

system was a vertical flat plate. Although, their conductivity

values show considerable scatter, the trend of their data

showed that the frost thermal conductivity increased with

increasing density and temperature. All these investigators

have indicated that there is a large temperature gradient

existing in the frost interior (10^4 to 10^5 °F/ft.).

The measurements of point thermal conductivity as a

function of density and the temperature in the frost interior

were first reported by Weber and Brazinsky (114). They

measured the temperature distribution in the frost interior

along with heat flux, density and thickness measurements.

A correlation between point thermal conductivity, density

and temperature obtained by Brazinsky (14) is shown in

Figure I-C7. Both Weber and Brazinsky concluded from their

measurements that point thermal conductivity of the frost

increases with density and temperature.

As yet, the microstructure of the cryogenic frosts

has not been studied extensively. Weber (114) and

Brazinsky (14) correlated their point thermal conductivity

data by modelling the frost microstructure. Their models

predicted the variation of thermal conductivity with density and temperature in fair agreement with the data. Brazinsky (14) has also reported some data on the mocroscopic observations of the frost structure.

I-D Background of this Thesis

The original physical ideas involved in the development of the theoretical models of the present thesis were first suggested by Prof. P.L.T. Brian and Prof. R.C. Reid. These ideas were logically deduced from the Weber's (114) postulation for the explanation of the quasi-steady state heat transfer condition in the frosting process. In this section, they are briefly described.

As described previously, a smooth layer of frost formed on a liquid nitrogen cooled surface imposes a thermal resistance which results in a marked increase in the frost surface temperature. Hence, after a smooth layer of frost is formed, the rate of frost deposition is governed by the diffusional mechanisms in the gas phase thermal boundary layer.

As additional frost deposits upon this cold surface, the rate of heat transfer from the warm gas to the cold surface decreases. However, as described in Section I-C, numerous investigators observed (3,6,14,23,52,76,77,89, 114,115) that after an initial transient period (in which heat flux decreases), the heat flux levels off and becomes essentially constant with time.

Weber (114) explained this "steady state" heat transfer
rate by postulating that the frost layer upon the cold
surface densifies with time. During densification, the
frost thermal conductivity increases very substantially,
presumably because of greater inter-particle contact. This
density increase was visualized as occurring by the diffusion
of water vapor within the frost layer. This diffusion is
produced by the ice vapor pressure gradient perpendicular
to the cold surface. Mathematically, the rate of diffusion
within the frost may be written as,

$$J = \frac{D_B \; c_T}{(1-Y)} \quad \frac{(1- \rho_f / \rho_{ice})}{\tau} \quad \frac{dY}{dx} \qquad \text{(I-D1)}$$

where the term $(1- \rho_f / \rho_{ice})$ is the void fraction in the frost
interior and τ is the tortuosity. The partial pressure
gradient is produced in the frost when heat is transferred
across the layer. Bader et al. (5) have found that a
snow layer is saturated with water at local temperature.
Assuming this would be also the case for cryogenic frost,
the temperature gradient through the frost would produce
an ice vapor pressure gradient. Therefore, the
concentration gradient in Equation I-D1 can be replaced by

$$\frac{dY}{dx} = \frac{dY^S}{dx} = \frac{dY^S}{dT} \frac{dT}{dx} = \frac{1}{P} \frac{dP_{vp}}{dT} \frac{dT}{dx} \qquad \text{(I-D2)}$$

where the superscript s denotes a saturation value.
Therefore, as heat is transferred to the wall, water vapor

diffuses in the same direction, increasing the density
of the frost layer.

From Equations I-D1 and I-D2 and using the ideal gas
law and the Clausius-Clapeyron equation (80) gives

$$JM_v = -D_B M_v c_T \frac{(1- \rho_f / \rho_{ice})}{\tau} \quad \frac{Y^s}{1- Y^s} \quad \frac{M_v \Delta H}{R T^2} \frac{dT}{dx} \qquad (I-D3)$$

Examination of Equation I-D3 shows that the rate of
vapor diffusion within the frost is a function of the
local temperature gradient in the frost. Therefore, the
amount of water vapor that has diffused and thus the "ageing"
of the frost layer depends on the time lapse since the
start of deposition, the temperature level within the frost
and the temperature gradient (or heat flux).

The above described mathematical explanation for the
frost densification is used in the mathematical formulation
of the several models for the frosting process studied in the
present thesis.

After postulating this mechanism for the frost
densification, Weber (114) concluded that this frost
densification resulted in an increase in thermal conductivity
of the frost layer which just balanced the increasing mass
of frost layer as frost continued to deposit and thus
stabilized the heat transfer rate at a steady value.

Compensating effects such as this are often observed
in nature, but the existence of a steady state heat transfer
rate even while frost continues to deposit on a cold surface

is a wide-spread observation common to all investigations
of the subject. It seems highly improbable, considering
such a diversity of experimental situations, that the
increase in frost thermal conductivity due to frost
densification would just happen by chance to counterbalance
the increasing frost accumulation and keep the heat transfer
rate constant.

Brazinsky (14) shed considerable light upon this
phenomenon. He conducted frosting heat transfer studies
in a wind tunnel with a cryoginically cooled copper plate.
Along with the heat transfer rates, he also measured the
temperature profiles within the depositing frost layer
and thus the thermal conductivity of the frost deposit
and the frost surface temperature were monitored through
out the run.

Furthermore the increase of frost layer density with
time was measured. These results confirmed the postulate
that the frost layer does densify and that this densification
does indeed result in an increase in the thermal
conductivity of the frost layer which just compensates
for the increased mass of frost to keep the heat transfer
rate steady. The results also show, as would be expected,
that the frost surface temperature is essentially constant
during this steady state heat transfer phase. Furthermore,
the frost surface temperature is essentially independent
of gas phase Reynolds number and the humidity of the bulk

gas stream.

The fact that the frost surface temperature varied only slightly over a wide range of experimental conditions suggested the presence of a high-gain feed-back effect tending to keep it constant and confirms the suspicion that the compensating effects which result in a steady state heat transfer rate are by no means compensating simply by chance. The rate of internal diffusion of water vapor within the frost layer is a strong function of frost temperature. The partial gradient which forces the water vapor diffusion can be thought of as the product of a temperature gradient and the slope of the curve of water vapor pressure versus temperature. This latter quantity increases exponentially as the frost temperature increases, and thus the importance of water vapor diffusion in the frost layer is strongly dependent upon temperature level.

As the insulating frost layer builds up on the cold plate, the heat flux decreases and the frost surface temperature rises. Finally, however, the frost surface temperature reaches a value at which internal water vapor diffusion within the frost layer becomes very substantial, and the frost layer begins to densify. As more frost accumlates and the frost layer gets thicker, there is a tendency for the frost layer to insulate the surface even more, causing a further increase in the frost surface temperature. But because of the very high sensitivity

of internal diffusion to the frost surface temperature,
a very small increase in the surface temperature results
in a sufficiently great increase in the rate of diffusion
of water vapor that the thermal conductivity and density
of the frost layer are increased to the point where the
heat flux falls off only very slightly and the surface
temperature rises only very slightly as additional frost
is deposited. Thus the frost surface temperature and the
heat transfer rate are stabilized by a very high-gain
negative feed-back effect of frost surface temperature upon
the rate of densification of the frost layer. Since the
frost surface temperature will vary but little, the thermal
resistance of the frost layer is automatically adjusted
to be in a given ratio with the thermal resistance of the
gas phase boundary layer. For example, increasing the gas
phase Reynolds number will decrease the thermal resistance
of the gas phase and thus will force the frost to become
denser in order that it too will have a decreased thermal
resistance. This is exactly the effect of gas phase
Reynolds number upon frost density found by Brazinsky (14).

The concept of the high-gain feed-back effect regulating
the frost density leads to the conclusion that the frost
density would vary substantially with the bulk gas phase
temperature. For example, if the gas phase temperature
were increased the rate of heat transfer through the gas

phase boundary layer to the frost could be increased.

Therefore, either the frost surface temperature would

rise substantially or the thermal resistance of the frost

layer would be decreased.   The above physical ideas indicate

that a rather small increase in frost surface temperature

would result and that this would be sufficient to increase

greatly the rate of internal water vapor transfer so as to

increase the frost density and decrease the thermal

resistance of the frost layer sufficiently.   Therefore

the concept in these physical ideas is that of a frost

layer responding to thermal forces upon it and to the

high-gain feed-back effect of internal diffusion so that

its density and, therefore, its thermal conductivity adjust

themselves and keep the frost surface temperature almost

invariant.

The physical ideas described above are used to obtain

quantitative theoretical models of the frosting process as

described in Sections II-A and II-B.

I-E   Scope of this Thesis

It is the purpose of this thesis to obtain a theoretical

model or models to explain quantitatively the effect of

various system variables on the frost properties such as

density and thermal conductivity and on the heat and mass

transfer rates in the frosting process.   The experimental,

as well as theoretical studies, will be carried out.   The

water frost will be deposited by forced convection over a

liquid nitrogen cooled surface. Some specific comments
and recommendations will also be made for the application
of the results of the present thesis to other system
geometries and the formation of other kinds of frost.

Experimental work is undertaken for a system in which
humid air is flown through infinitely parallel plates.
The frost will be deposited on a liquid nitrogen cooled
copper section which will form part of the lower plate.
The following significant studies will be carried out.
A.   The frost density, thickness, heat flux through the
frost and the temperature distribution in the entire frost
layer as a function of time will be measured for the various
ranges of the system variables. The system variables that
will be considered in the present research are Reynolds
number, gas temperature and humidity.
B.   The density gradient in the frost interior is to be
measured for several frosting experiments.

Theoretical models will be developed to correlate all
the experimental facts and to understand the mechanisms of
the frosting process.

Two other short experimental programs will also be
undertaken.   The first one is undertaken to verify the
validity of the postulated mechanism of internal diffusion
as described in Section I-E.

The second one involves the experimental measurements
of heat transfer coefficient in non-frosting conditions
when the cold surface temperature is kept at about $-15^\circ F$.

These data will be used to evaluate the theoretical models. The details of these experimental programs are shown in Section III-B and III-D.

I-F Possible Contribution of this Thesis

It is hoped to make the following contributions with this thesis.

I. Obtain a theoretical model for the frosting process which could be used for the quantitative prediction of the frost properties and the heat and mass transfer characteristics of the water frosting process under a given set of enviromental conditions.

II. Some qualitative or quantitative, if possible, evidences showing the applicability of the theoretical results of the present thesis to a wide variety of system geometries and to other kinds of frost (e.g. carbon dioxide frost).

III. Discuss microscopic process occuring inside the frost to account for densification.

Table I-C1

Experimentally Measured Surface Temperatures in
Quasi-steady State Heat Transfer Region
As a Function of Reynolds Number
and Humidity (14)

Reynolds Number	Humidity (dew point °F)	Steady Value of Frost Surface Temperature (°F)
14,500	40.0	+24
9,300	40.1	+25
5,600	39.9	+20
9,300	28.7	+12
5,600	29.1	+12
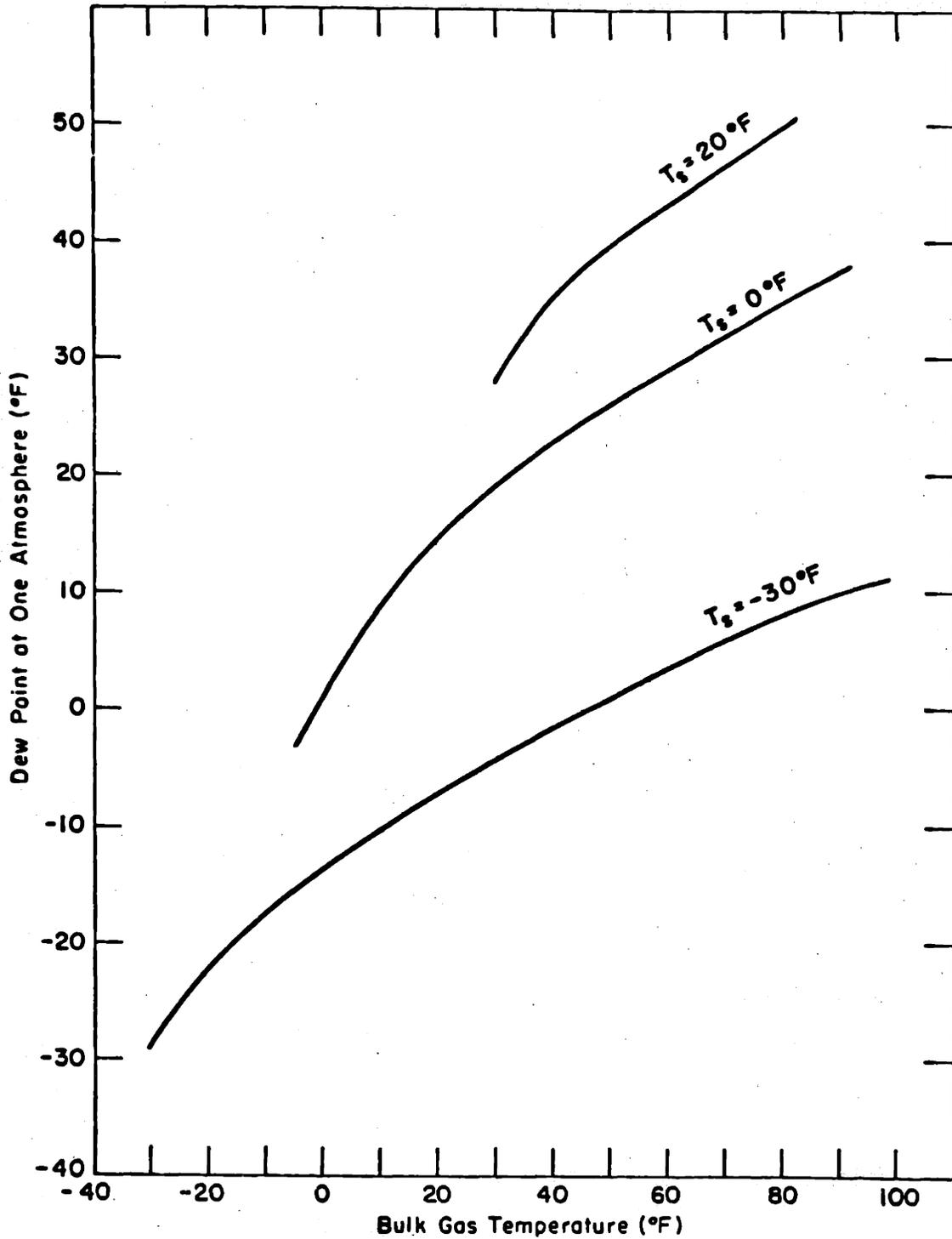
Figure I-B1 Fog Formation Limits at One Atmosphere

FIGURE I-C1

Data: Ref. 89
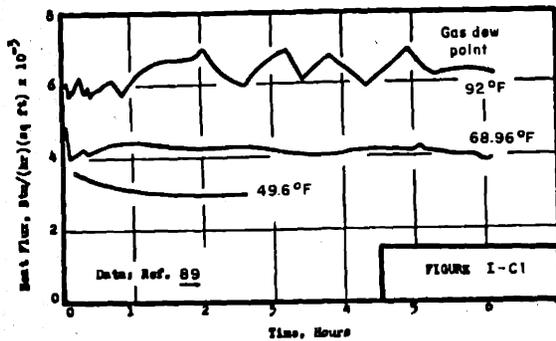
FIGURES I-C1 and I-C2   Low Temperature Horizontal
Cylinder in Crossflow

                         Reynolds Number: 152,000
                         Air Velocity: 80 ft/sec
                         Air Temperature: 100°F
                         Cylinder Temperature: -320°F

Data: Ref. 89

FIGURE I-C2

FIGURE I-C3

Heat Transfer
Coefficients

$Re_{f,0} \sim 37,600$

Inlet
Humidity
Gas

Symbol	dew point (°F)
O	-11.5
□	-10.5
△	8.9

Data of Ref. (114)

Inlet Humidity ~ gas dew
                 point of
                 8.9°F

FIGURE I-C4

Heat Transfer
Coefficients

Symbol	$Re_{f,0}$
□	37,900
▽	27,200
△	17,500
O	8,700

Data of Ref. (114)
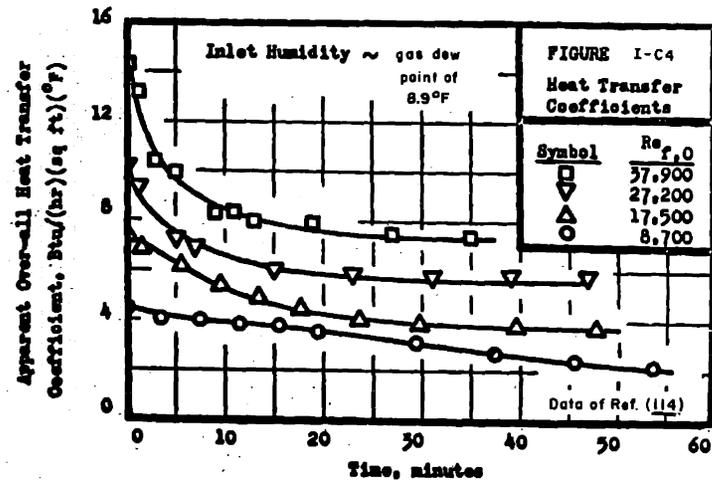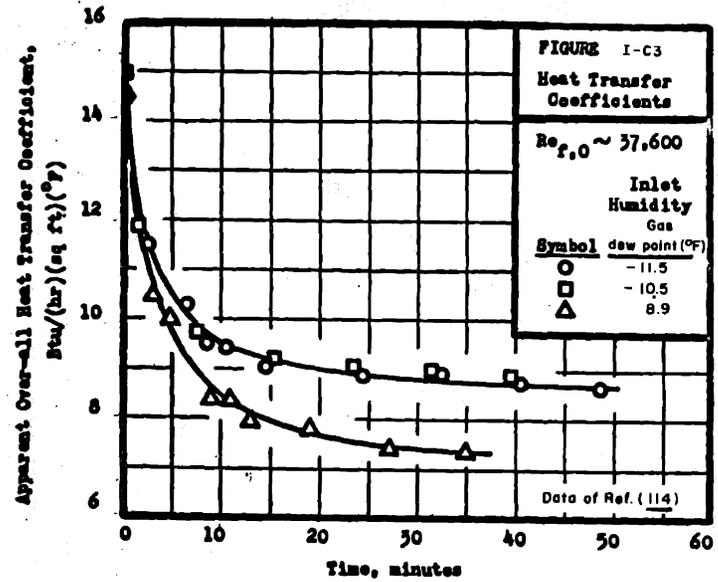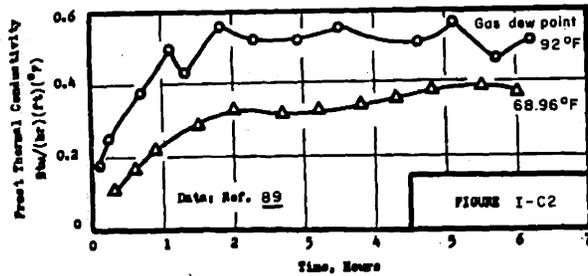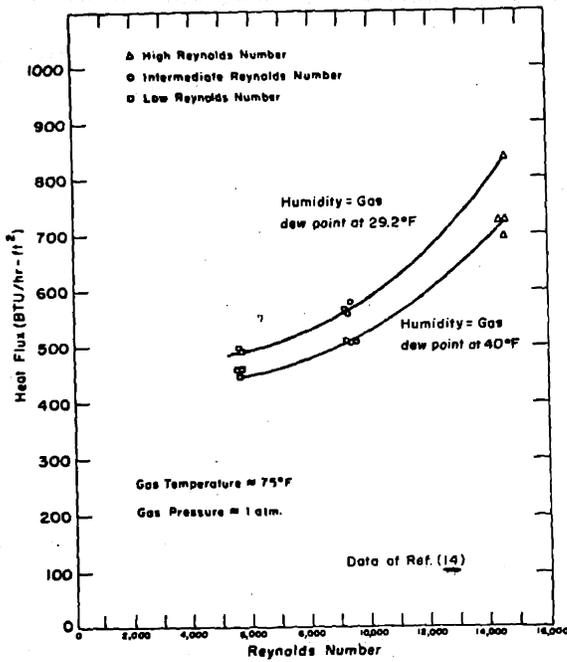
Figure I-C5 Quasi-Steady State Heat Flux as a Function of
Reynolds Number and Humidity
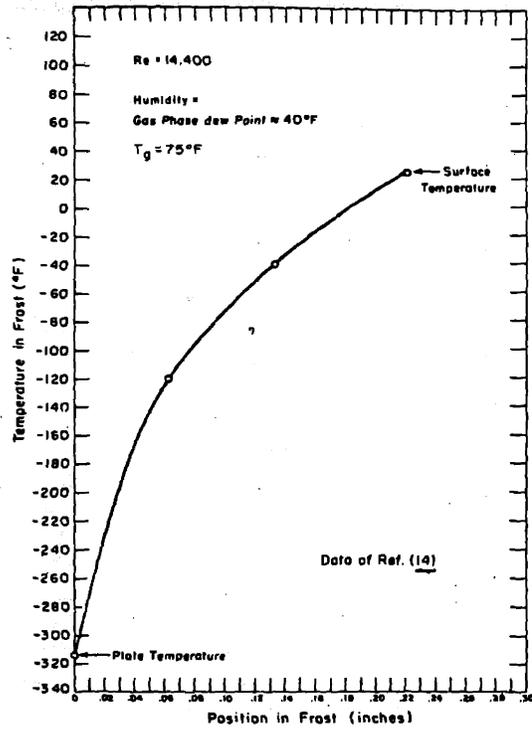
Figure I-C6 End of Run Temperature Profile in Frost
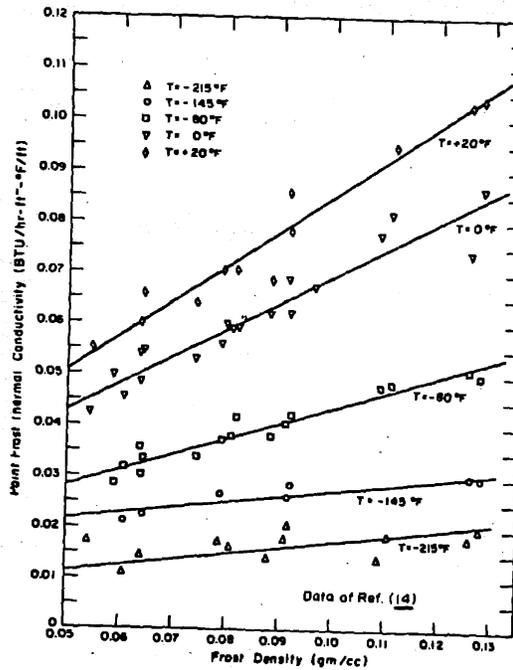
Figure I-C7 Frost Thermal Conductivity as a Function of Density,
with Temperature as a Parameter

S E C T I O N   II

Development of Theoretical Models for the Frosting Process

Several models, of varying sophistication, are examined critically in this section to interpret the complex phenomena of frosting.

II-A Simple Model of the Frosting Process

Postulations and Assumptions of Simple Model

1.   After a smooth layer of frost is formed, the transport of heat and mass to the frost surface can be analyzed using ordinary gas phase correlations.   That is, no nucleation of water vapor occurs anywhere in the gas phase.

2.   Water vapor is transferred from the frost surface to the interior by a diffusional mechanism resulting from a vapor pressure gradient.   The rate of transfer is proportional to the gradient at the surface.   No consideration is given to the water transport within the frost except to assume that the entire frost layer densifies uniformly..... there is no density gradient present in the frost.

3.   Heat is transferred through the frost by a combined mechanism of conduction in the solid and gas phase and by the enthalpy transport of water vapor.   This heat transfer in the frost interior is assumed to be one dimensional only.

4.   The point thermal conductivity of the frost assumed

to be a function of temperature and frost density. The

average frost layer thermal conductivity, on the other

hand, assumed to be only a function of <u>average</u> frost

density.

<u>Qualitative Description of the Model</u>

As postulated before, for the frost deposition on a

liquid nitrogen cooled surface, this model is applied

only after a smooth layer of frost is formed. The schematic

of the frosting process as visualized by this model is

shown in Figure II-AO.

Qualitatively, according to this model, one visualizes

the frosting process as one in which water vapor from the

gas phase is transferred to the frost surface by a

simultaneous heat and mass transfer processes. Once

water vapor deposits on the existing frost, part of it

resublimes and diffuses in the frost interior and the rest

of it increases the frost thickness. Thus both frost

density and thickness increase with time. The model

assumes that the internal diffusion of water vapor is

proportional to the vapor pressure gradient existing at

the frost surface and hence it is a very strong function

of frost surface temperature.

Although this model postulates the internal diffusion

as the cause for frost densification, it is important to

note that it ignores the explanation for the mechanism

by which diffused water vapor spreads itself in the frost

interior, after it leaves the frost surface. Thus it

considers only a differential element at the frost
surface for explanation of the effects of various
independent system parameters on the frosting process and
on the variation of the frost properties with time.

Previous experimental studies (14,23,25,114,116) have
indicated that after an initial short duration of the
frosting process, the rate of heat transfer through the
frost attains a quasi-steady state, even though the frost
continues to accumulate on the cold surface. The simple
model explains this phenomenon on the basis of a high gain
negative feed-back effect of the frost surface temperature
on the internal diffusion.

In the quasi-steady state heat transfer condition,
as frost accumulates and as frost layer gets thicker, there
is a tendency for the frost layer to insulate the surface,
causing an increase in the frost surface temperature. But,
because of the very high sensitivity of internal diffusion
to the frost surface temperature, a very small increase
in the surface temperature results in a sufficiently great
increase in the rate of diffusion of water vapor that the
thermal conductivity and density of the frost layer are
increased to the point where the heat flux falls off only
very slightly as additional frost is deposited. Thus
this high gain negative feed back effect of frost surface
temperature on internal diffusion causes the frost surface
temperature and hence the heat transfer through the frost
to remain almost constant. One can also deduce from the

above discussion that the model predicts that frost

responses to the thermal forces acting upon it, because at

constant frost surface temperature, the thermal resistance

of the frost is adjusted to be in a given ratio with the

thermal resistance of the gas phase boundary layer.

The basic mathematical equations of this model predict

the variation of frost density, thickness, mass deposition

and heat transfer rate through the frost with them. The

knowledge of the independent system variables such as

Reynolds number, humidity, gas temperature and cold wall

temperature are required to obtain these predictions.

For a well defined system (i.e., one in which heat

and mass transfer coefficients can be characterized), if

one knows thermal conductivity of frost as a function of

density and temperature (note that this can be obtained

experimentally or can be obtained from a frost structure

model as shown in Appendix F), one can predict the frost

surface temperature from the mathematical formulation of

the model. Knowledge of frost surface temperature then

allows one to predict the variation in frost density,

thickness, rate of frost formation and heat transfer

through the frost as it deposits on the cold surface.

Mathematical Formulation of Simple Model

The average frost density, thickness, surface

temperature of the frost, and heat transfer through the

frost are obtained from heat and mass balance at the

frost surface.

The principal equations resulting from the heat and mass balances at the frost surface can be obtained as follows.

Heat Transfer from the Gas to Frost Surface

Heat is transferred from the gas to the frost both by convection and by material transport of the condensible component. This rate of heat transfer may be written as,

$$q = h \ (T_g - T_s) + N_s \Delta H + N_s \ C_p \ (T_g - T_s) \qquad \text{(II-A1)}$$

The sensible cooling of the condensible component in Equation II-A1 is usually small and can be safely neglected. Equation II-A1, hence, can be rewritten as,

$$q = h \ (T_g - T_s) + N_s \ \Delta H \qquad \text{(II-A2)}$$

At the frost surface, there is energy transfer to the frost layer by two mechanisms. First there is the usual conduction process. Secondly, there is an internal mass flux caused by the temperature gradient in the frost layer. Both are proportional to the surface temperature gradient. Thus, one may write,

$$q = k_{f,s} \ (\frac{dT}{dx})_s \ = (k_{fi} + k_{excess})_s \ (\frac{dT}{dx})_s \qquad \text{(II-A3)}$$

where $k_{f,s}$ is an effective conductivity including both the intrinsic conductivity, k_{fi}, and the excess conductivity due to evaporative mass transport, k_{excess}, is evaluated at the frost surface temperature and density. The detailed description of k_{excess} is given in Appendix F.

Mass Balance over Frost Layer

The total mass of frost at some specified time is,

$$m_f = A \int_0^\delta \rho_f \, dx \qquad\qquad\qquad (II\text{-}A4)$$

The frost thickness is time dependent. The variation of m_f with time is abtained by differentiating Equation II-A4, i.e.,

$$N_s = \frac{dm_f}{A \, d\theta} = \frac{d}{d\theta} \int_0^\delta \rho_f \, dx = \int_0^\delta \frac{d\rho_f}{d\theta} \, dx + \rho_{f,s} \frac{d\delta}{d\theta} \qquad (II\text{-}A5)$$

Also the mass flux, N_s, can be expressed by a gas phase mass transfer coefficient and partial pressure driving force as,

$$N_s = K_g \, (p_g - p_s) \qquad\qquad\qquad (II\text{-}A6)$$

where K_g is presumable determined by the gas phase fluid dynamics, p_g by the concentration of condensible component in the gas phase and p_s by the frost surface temperature.

Returning to Equation II-A5, the rate of increase in frost mass has been broken down into two parts. The first represents the rate of densification of the existing layer while the second allows for an increase in frost thickness with time. The densification results from internal diffusion of the condensible as there is a temperature gradient within the frost layer. The term

$$\left(\frac{d\rho_f}{d\theta} \right) dx = \left(\frac{dN_s}{dx} \right)_s dx = N_{si} \qquad\qquad (II\text{-}A7)$$

is equal to the mass flux from the frost surface, N_{si}. It should be noted that in Equation II-A7, $\left(\frac{dN_s}{dx}\right)_s$ is not a function of x.

N_{si} is assumed to be limited by ordinary diffusional

processes.

$$N_{s1} = - M_v \ D'_{eff} \ (\frac{dP_{vp}}{dx})_s \qquad \text{(II-A8)}$$

D'_{eff} is related to the usual diffusion coefficient as,

$$D'_{eff} = \frac{D_B \epsilon}{\tau} \left(\frac{P}{P - P_{vp}} \times \frac{1}{RT} \right) \qquad \text{(II-A9)}$$

in which τ is the tortuosity and ϵ is the void fraction

i.e., $\epsilon = (1 - \rho_f / \rho_{ice})$

The vapor pressure gradient can also be written as

$$\left(\frac{dP_{vp}}{dx} \right) = \left(\frac{dP_{vp}}{dT} \right) \left(\frac{dT}{dx} \right) \qquad \text{(II-A10)}$$

Using Clausius-Clapeyron equation (80) one can write,

$$\frac{dP_{vp}}{dx} = \left(\frac{M_v \Delta H \ P_{vp}}{RT^2} \right) \left(\frac{dT}{dx} \right) \qquad \text{(II-A11)}$$

Combining Equations II-A9 and II-A11, and assuming P_{vp} to be small so that $(P-P_{vp})$ is approximately equal to the system pressure P, then Equation II-A9 becomes

$$N_{si} = -\beta(T_s) \left(\frac{\epsilon}{\tau} \right) \left(\frac{dT}{dx} \right)_s \qquad \text{(II-A12)}$$

where,

$$\beta(T_s) = D_B M_v \Delta H \ P_{vp} / R^2 T_s^3 \qquad \text{(II-A13)}$$

Hence,

$$\frac{d\rho_f}{d\theta} = -\beta(T_s) \frac{(1 - \rho_f / \rho_{ice})}{\tau} \left(\frac{dT}{dx} \right)_s \qquad \text{(II-A14)}$$

The function $\beta(T_s)$ has the units of mass/length-time temperature and is a strong function of T_s.

From Equations II-A5, II-A6, II-A8 and II-A11

$$N_G = K_g (P_g - P_s) = \rho_f \frac{d\delta}{d\theta} - \beta(T_s) \left(\frac{\epsilon}{\tau} \right) \left(\frac{dT}{dx} \right)_s \qquad \text{(II-A15)}$$

and heat balance equation can be written as

$$q = h(T_g - T_s) + K_g(P_g - P_s) \cdot \Delta H = R_{f,s} \left(\frac{dT}{dx} \right)_s$$

$$= k_{f,x} \left(\frac{dT}{dx} \right)_{f,x} = \frac{(\int_{T_w}^{T_s} k_f \ dT)}{\delta} \qquad \text{(II-A16)}$$

Computer Solution of Mathematical Equations

The equations derived above were solved by numerical methods. A computer program was written to obtain frost density, thickness, and heat transfer through the frost versus time profiles from numerical solution of the equations. The functional relation $k_f = f\ (\rho_f, T)$ was obtained by an empirical correlation of the experimental data of Brazinsky (14). The details of the computer program is described in Appendix D.

Computer Results

The computer solution was used to study the following aspects of the simple model.

1. Comparison between the predictions of the model and experimental results for time variation of the frost density and thickness as well as the rate of heat transfer through the frost.

2. The effect of the initial values (os frost density and thickness) on the model's predictions for the frost density and thickness as a function of time.

3. Predictions of the model for the effect of step changes in the environmental conditions on the frost density, thickness and heat transfer through the frost.

Figures II-A1 to IIA10 compare the predictions of the simple model for the frost density, thickness, heat transfer through the frost and mass deposition of the frost versus time profiles for ten different experimental conditions studied in the present research. In all the

cases, the first experimental data points of the frost density and thickness were taken as the starting values for the theoretical predictions. The heat transfer coefficients used in the model were obtained from the Sleicher and Tribus's (105) theoretical heat transfer analysis (see Appendix L) of the present system under non frosting conditions.

The results of the Figures II-A1 to II-A10 show surprisingly good agreement between the experimental facts and the predictions of the model. The maximum deviation between the theoretical and experimental frost density values was about 8% and that for the frost thickness values was approximately within 10%. The mean average deviations for all the results was less than 3% both for frost density and thickness values. The slightly poor agreement between the experimental and theoretical heat fluxes in some of the cases (Figure II-A8, II-A9, and II-A10) was due to the difference in the values of the theoretical and experimental heat transfer coefficients.

Figures II-A11 and II-A12 show the comparison between the predictions of the simple model and the experimental data of Brazinsky (14). Although the starting values were once again chosen to be the first experimental data points of the frost density and thickness, the theoretical calculations were carried out using the experimentally determined heat transfer coefficients. It can be seen from these figures that the agreement between the predictions

of the model and the experimental facts was quite good.

In order to obtain frost density and thickness versus time profiles from the solution of the mathematical equations of the simple model, initial frost density and thickness values have to be known. In most real situations, these values at any arbitrary time may not be known. In order to increase the range of application of the theoretical model, it is important to study the effect of the starting values on the predictions of the model for the time variation of the frost density and thickness.

Figure II-A13 shows the theoretical results (for a set of experimental conditions) of the time variation of the frost density and thickness obtained from the various assumed starting values. Two different starting values of the thickness (0.0015 inch and 0.015 inch) and three different starting frost density values (0.026 gms./cc., 0.035 gms./cc., 0.046 gms./cc.) were examined. The starting time was assumed to be one minute (from the start of frosting) for the lower initial thickness and two minutes for the higher initial thickness. The results indicate that the time variation of the frost density in the quasi-steady state region is slightly dependent on the initial values. The time variation of the frost thickness in the quasi-steady state heat transfer region is, however, almost independent of the initial values. It should be noted, that the theoretical predictions for the comparison of the Figures II-A1 to II-A12

were carried out with the first experimental data points of the frost density and thickness as the starting values because erroneously assumed initial values will introduce additional deviation between the experimental facts and the theoretical predictions.

It can also be observed from the results of the Figures II-A13 and II-A14 that assumed initial values of the frost density and thickness affect the frost densification rate only in the transient heat transfer state.

As postulated before, the simple model can be applied to the process of frost formation on a liquid nitrogen cooled surface only after a smooth layer of frost is formed (i.e. when no fogging occurs). It has been experimentally found in the present research as well as in the investigation of Brazinsky (14) that time for the formation of a smooth layer of frost is a strong function of Reynolds number (i.e. heat and mass transfer coefficients) and a weak function of gas temperature and humidity. Table II-A1 shows the experimentally observed relationship between the time for the formation of a smooth layer of frost and the heat transfer coefficient.

The results of Figures II-A13 and II-A14 and of Table II-A1 indicate that if the initial values for the frost density and thickness are taken at the time for the formation of a smooth layer of frost, any reasonable values of the frost density and thickness (see discussion of the results in this section)   will be

sufficient for the good predictions of the time variation
of the frost density and thickness in a quasi-steady
state region.

Since in the real frosting process the chances for
a step change in the environmental conditions are quite
high, the predictions of the simple model for the effects
of the step changes in the environmental conditions on
the frosting process and frost properties are of practical
significance.

For a set of experimental conditions (Re=5,600, humidity
= dew point at 29.2°F, T_g=530°R and T_w=144°R), at time
of seventy five minutes from the start of frosting, when
the cold wall temperature increased from about 144°R to
350°R (keeping all other system conditions unchanged), the
model predicted that the frost surface temperature would
increase from about 9°F to about 32°F. Hence, it predicted
erroneous results for the time variation of the frost
density and the thickness at T_w=350°R. The results of
this test is shown in Table II-A2.

One can deduce from the above-mentioned results that
in general, the model predicts increase in frost surface
temperature with the increase in the cold wall temperature.
The frost densification rate will be increased and the
heat and mass fluxes and the time variation of the frost
thickness will be decreased by this increase in the frost
surface temperature.

Figure II-A15 shows the model's predictions for a

step change in Reynolds number on the frost properties
and heat transfer through the frost. The step variation
in Reynolds number was carried out at eighty five minutes
from the start of frosting (all other system conditions
were kept unchanged). The model predicted that the step
increase in Reynolds number (from 8,000 to 15,800), would
cause faster rate of change of density, slower rate of
change of thickness and faster rate of mass deposition
with time. The step increase in Reynolds number would
cause the heat flux and the frost surface temperature to
be increased initially sharply, but heat flux levels out,
later, at another (but higher) and the frost surface
temperature at another (but lower) quasi-steady state
values. The step decrease in Reynolds number (from 8,000
to 5,600) would have an opposite effect on the frost
properties, surface temperature and the heat transfer
through the frost.

The predictions of the model for the effects of a
step change of gas temperature on the frost properties
and heat transfer through the frost are described in
Figure II-A16. The step increase (from 75°F to 110°F)
and step decrease (from 75°F to 30°F) in gas temperature
(at all other system conditions unchanged) would have the
similar effects of the frost density, thickness, surface
temperature and heat transfer through the frost as those
obtained for the step variation in Reynolds number.

Figure II-A17 shows the predictions of the simple

model regarding the effects of a step change in humidity
on the frost properties and heat transfer through the
frost (all other system conditions were kept unchanged).
The step variation in humidity (from dew point of 33.2°F
to dew point of 40.3°F and to dew point of 14.3°F) will
change the rate of frost densification only slightly
but significantly change the frost surface temperature
and the time variation of frost thickness. Both frost
thickness and the surface temperature will increase with
a step increase in humidity. The heat transfer through
the frost will be only slightly affected by a step
variation in humidity.

Discussion of Computer Results

The results of Figures II-A1 to II-A12 reveals the
surprising success of the simple model in representing the
complex frosting process. Even though the simple model
ignores the explanation for a mechanism by which water
vapor penetrates the interior of the frost, its significant
contribution lies in a simple quantitative explanation
for the time variation of the frost density, thickness
and heat transfer through the frost for the wide variety
of the system conditions.

In general, all the experimental data on the frost
density, thickness and heat transfer through the frost
agree well with the predictions of the simple model. The
large deviation between the experimental and the predicted
values for the heat transfer through the frost for

certain experimental conditions (Figure II-A8, II-A10) are mainly due to the large difference in the values of the experimental and the theoretical heat transfer coefficients. Some deviation between the experimental and the theoretical values of the frost density in Figure II-A7 and of the frost thickness in Figure II-A9 can be accounted by the difference in the theoretical and experimental values of the mass deposition at a later time.

Qualitative explanation for the occurrences of the experimental facts and the effects of various independent system parameters such as Reynolds number, humidity and gas temperature on the frost properties and the frosting process predicted by the model can be given as follows.

Physically, the process of frost formation essentially involves the transfer of heat and mass of a condensible component from the gas to the cold surface. This occurs because as soon as warm gas comes into contact with the cold surface, temperature and the concentration gradients are established in the gas boundary layer. Thus, the condensible component is transported towards the cold surface by the concentration driving force, and similarly heat is transferred from gas to the cold surface by the temperature driving force. The intrinsic constants which control the rate of mass and heat transfer at the given driving forces are, of course, the usual mass and heat transfer coefficients respectively.

If the cold surface temperature is very low (for

example, liquid nitrogen temperature), then as seen
previously (see Section I), the above described
mechanisms control the frosting process only after a
smooth layer of frost is ust formed on the cold
surface.

It should be noted that the various independent
system parameters involve in the frosting process should
affect either the various driving forces or the intrinsic
constants described previously. In fact, bulk gas
humidity and temperature will affect the driving forces
for the mass and heat transfer (i.e., $\Delta p = p_g - p_s$
and $\Delta T = T_g - T_s$) respectively and Reynolds number
will affect the intrinsic constants for the heat and
mass transfer (i. e., h and K_g).

If Reynolds number (or gas velocity) is increased,
the gas phase turbulence will be increased. This will
increase the thermal and mass momentum in the gas
particles and as a result the heat and mass transfer
coefficients will be increased. The physics of the
frosting process indicate that an incraese in Reynolds
number (at constant Gas temperature and humidity) will
increase the heat and mass transfer rates due to increase
in heat and mass transfer coefficients. Also, a higher
thermal momentum will cause the ice particles to pack
more tightly so that the frost of a higher density and
hence of a higher thermal conductivity will be formed.

Thus, the key concepts of the simple model that the
frost responses to the thermal forces acting upon it and
that the effect of Reynold number is to increase the
thermal and mass momentum are in agreement with the
physics of the frosting process. The results shown in
the Figures II-A , II-A7, and II-A10 substantiate the
above discussion quantitatively with the help of
experimental facts and the theoretical predictions.

It should be noted that in several investigations
(89, 114), in which the fog particles were formed in the
gas phase, the density variation with Reynolds number
was explained by saying that since the fluctuating
velocity component normal to the main gas flow increases
with Reynolds number, the impact velocity of the fog
particles with the frost layer is graeter at the higher
Reynolds number. Greater impact velocities cause the
particles to pack more tightly and hence a frost layer
of higher density results.

The above explanation is erroneous for three reasons.
First, the statement that higher particle impact velocities
lead to more tightly packed arrays has not been proven so
far. Secondly, the explanation for the frost density beha-
vior based on the particle impact velocities is not applicable
for the cases where fog particles do not form in the gas
phase (i.e. frost formation at high temperatures). Lastly,
it does not explain the experimental facts regarding the
effects of Reynolds number on the heat and mass transfer

processes during the frost deposition.

The increase in humidity will, of course, increase the mass transfer rate from gas to the cold surface due to an increase in the concentration driving force ($\Delta p = p_g - p_s$). Since the thermal forces imposed on the frost are not changed by varying the humidity, the density of the frost will not be significantly affected by the variation in humidity. Frost thickness, however, will increase significantly with increase in humidity because of increase in mass flux. Thicker frost at a higher humidity will insulate the cold surface better. Hence, the frost surface temperature will be a little higher and the quasi-steady state heat flux from gas to the frost surface will be lower at a higher humidity. All these effects of the variation in humidity, as dictated from the physics of the frosting process, are in agreement with the experimental facts and the theoretical predictions of the Figures II-A2, II-A8 and II-A1, II-A3.

The increase in gas temperature will increase the driving force for the heat transfer ($\Delta T = T_g - T_s$). This will, of course increase the heat flux from gas to the frost surface. In order to achieve the thermal balance on the system, increase in the gas temperature should also increase the heat flux through the frost. This can occur either by increase in the frost surface temperature or by increase in the frost density. Increase in the frost surface temperature, however, will decrease the mass

flux. Hence, the tendency of the frost layer will be to decrease its thermal resistance such that the thermal balance is regained. The experimental facts and the theoretical predictions of the Figures II-A5, II-A6 and II-A7, II-A9 are in agreement with these physical expectations.

The initial values of the frost density and thickness for the theoretical calculations of the Figures II-A1 to II-A12 were taken to be the first experimental data points. In order to expand the range of application of the model and to eliminate the need for the experimental data points for the theoretical calculations, a study was made to determine a judicious choice of the initial values for a wide variety of the system conditions. The important results of this study are shown in Figures II-A13, II-A14 and in Table II-A1.

There are three parameters to be fixed at the initial conditions; frost density, thickness and the starting time. Since the model applies only after a smooth layer of frost is formed, the time for formation of a smooth layer of frost should be taken as the starting time. The approximate value of this for given system conditions can be obtained from the data of Table II-A1.

It has been found experimentally in the present research as well as in the study of Brazinsky (14) that the density of the frost clumps formed in the initial phase of the frosting process at the low temperature lies between 0.02 gms./cc. to 0.03 gms./cc. for all experimental

conditions.   Hence, 0.025 gms/cc. would be a reasonable value for the frost density at the time when smooth layer of frost is just formed.

The results of the Figure II-A13 indicate that the time variation of the frost thickness in the quasi-steady state heat transfer region is very weakly dependent upon its initial values.   However, since thickness is a continuously increasing function of time, the initial value of the frost thickness should be lower than a true value at a little later time.   A very approximate but reasonable guess for the frost thickness value at the time when a smooth layer of frost is just formed can be obtained as follows.

A very approximate value for the mass deposition on the cold surface at the time for the formation of a smooth thin frost layer can be given by the following Equation II-A17.

$$\rho_f \times \delta = \int_0^t K_{gi} (p_g - p_s) d\theta$$

(II-A17)

Neglecting p_s (since the frost surface temperature is extremely low during this time), one can write

$$\delta = K_{gi} p_g t / \rho_f$$

(II-A18)

In Equation II-A18, K_{gi} and p_g are the known experimental variables. An approximate value of 't' can be obtained from the data of Table II-A1. Finally, ρ_f can be obtained from the following experimentally measured correlation between average frost density and the heat transfer coefficient

$$\rho_f = 0.025 \left(\frac{h}{2.5}\right) \qquad \text{(II-A19)}$$

Thus, an approximate value of the frost thickness at the time when a smooth layer of frost is just formed can be calculated from Equation II-A18.

Just to demonstrate the usefulness of the above-mentioned procedure, theoretical predictions for the system conditions of the Figure II-A13 will be obtained with the starting values dictated by it. Thus, the starting time will be 12.5 minutes (from the data of Table II-A1) and the initial frost density will be 0.025 gms./cc. The initial value of the frost thickness can be calculated using Equation (II-A18) as follows.

$$K_{gi} = 0.016 \text{ lb}_m/\text{hr ft}^2 \text{ mm.Hg.}$$

$$p_g = 6.34 \text{ mm.Hg}$$

$$t = 12.5 \text{ minutes (from Table II-A1)}$$

$$\rho_f = 0.090 \text{ gms./cc.}$$

$$\delta = \frac{0.016 \times 6.34 \times 12 \times 12.5}{0.09 \times 62.5 \times 60}$$

$$= 0.044 \text{ inches}$$

The theoretical predictions for the time variation of the frost density and thickness with the starting values of ρ_f = 0.025 gms./cc. and δ = 0.044 inches at the time of 12.5 minutes, are shown in the Figure II-A13. It can be seen that the theoretical predictions with these starting values agree well with the experimental results.

There are two other attempts made to obtain a judicious choice for the initial values at an arbitrary time.

In the first attempt, available frost density and
thickness versus time profiles in the quasi-steady state
heat transfer region are extrapolated backwards by using
the computer solution with negative time increment. The
results of this attempt is shown in Table II-A2. The
results show that this method for obtaining the frost
density and thickness at an earlier time is not successful
because of the erroneous calculation of the frost surface
temperature during backward extrapolation. The frost
surface temperature is found to be increased as time is
moved backwards.

It appears, from the results, that a slight error in
the calculation of the frost surface temperature (by Newton
Raphson's method) at the starting time is propagated and
expanded at a subsequent time. If, however, the
transcendental equation for the surface temperature is
solved by an analytical method, it will be possible to
avoid this error in the calculation of the frost surface
temperature. Unfortunately, a closed form analytical
solution of the transcendental equation is not possible
because it contains fifth and the higher order terms in
unknown T_s (according to Abbel's law). Further efforts
to obtain a correct solution for the frost surface
temperature are not carried out.

In the second attempt to obtain a judicious chocie
for the initial values, a correlation between the frost
density, thickness and the system variables is obtained.

The correlation is obtained forty minutes from the start

of frosting. The experimental data of the present

research are used for this purpose. The following results

are obtained.

$$\rho_f = 1.930 \times 10^{-3}\ h^{0.933}\ T_g^{0.2062}\ P_g^{0.1511} \qquad \text{(II-A20)}$$

and,

$$\delta = 6.21 \times 10^{5}\ h^{-0.1231}\ T_g^{-2.878}\ P_g^{0.779} \qquad \text{(II-A21)}$$

All the nomenclatures of Equations II-A20 and II-A21

are described in Appendix R.

The details of the correlation procedure is described

in Appendix G.

In the real frosting process, constant environmental

conditions are rare. Hence the effect of a step change in

environmental conditions on the frosting process is of

considerable practical significance. The predictions of

the model in this regard are described in Figures II-A15

to II-A17. The results are in qualitative agreement with

the physics of the frosting process.

If the cold wall temperature is suddenly increased

then ΔT across the frost is decreased and the heat flux

through the frost will be decreased. In order to achieve

a thermal balance on the system, heat flux from the gas

to the frost surface should also go down and hence the

frost surface temperature will increase up to the point

that the heat transfer through the frost is equalled to

that from gas to the frost surface. Thus physics of the frosting process dictates the increase in the frost surface temperature with a step increase in the cold wall temperature.

Figure II-A15 shows that the step increase in Reynolds number will cause an initial sharp increase in the heat flux through the frost followed by the frost growth under the transient heat transfer situation and finally attainment of a new quasi-steady state heat transfer condition. The results of the Figure II-A15 also indicate that the decrease in Reynolds number will have the converse effects on the frost properties. Since, physics of the frosting process indicates that the frost will respond to the thermal forces acting upon it, the behavior of the frosting process under a step change in the Reynolds number will be in qualitative agreement with the results of Figure II-A15.

A step variation in the gas temperature also changes the thermal force acting upon the frost. Hence, it will have a similar effect on the heat flux and frost thermal resistance as obtained for a step change in Reynolds number. The mass flux will also be affected by a step variation in the gas temperature because of the variation in the frost surface temperature. These deductions which are based on the physics of the frosting process are in qualitative agreement with the results of Figure II-A16.

It has been found experimentally that a step variation in humidity affects the frost thickness much more significantly than the frost density and the heat transfer through the frost. It is expected that a step variation in humidity will also have a similar effect on the frosting process. The results of Figure II-A17 are in qualitative agreement with these physical expectations.

Conclusions

As a result of the theoretical analysis of the simple model, the following conclusions can be made.

1. The model predicts frost density, thickness and heat transfer through the frost versus time profiles which are in agreement with the experimental facts for a wide range of experimental conditions.

2. The theoretical calculations for time variation of the frost density and thickness can be started at the time when a smooth layer of frost is just formed. The frost density of 0.025 gms./cc. and the thickness calculated from the Equation II-A18 can be used as the initial values for the calculations. The initial values calculated in this manner can be used only when the frost is deposited by forced convection on a cryogenically cooled surface.

3. The values of the frost density and thickness at forty minutes from the start of frosting on a liquid nitrogen cooled surface by forced convection can be obtained from the Equations II-A20 and II-A21.

4.   The model predicts the effects of a step variation
in environmental conditions on frost properties in
agreement with the physics of the frosting process.

II-B Speculations of Processes Occuring within the Frost

    As seen in Section II-A, the simple model correlates
the effects of various independent system parameters
on the frost properties and the frosting process. This
correlation is obtained by considering the energy and
mass balances on a differential element at the frost
surface.   The simple model, however, ignores the explanation
for the mechanisms by which water vapor spreads itself in
the frost interior once it leaves the frost surface.   In
order to understand the mechanism by which every layer of
the frost interior densifies with time, an 'improved model'
(or `sophisticated model) of the frosting process was
made.   This section describes in detail this first attempt
to understand the microscopic phenomena in the frost interior.

    The basic postulations and the assumptions of the new
model considered here are as follows:

1.   The partial pressure of water vapor at every point in
the frost interior is assumed to be the equilibrium vapor
pressure at existing temperatures.

2.   Every layer of the frost interior densifies with time
because of the water vapor transport in the frost interior.
The vapor pressure gradient due to temperature gradient
causes this transport of water vapor.

3. The thermal conductivity of the frost can be represented as a function of the frost density, temperature and frost structure.

4. Heat conduction in the frost interior is one dimensional only.

5. On the gas side of the gas-frost interface, the heat and mass transfer characteristics of the boundary layer control the frosting process.

Qualitative Description of the "Sophisticated" Model

Like the "simple model" this model is applied only after a smooth layer of frost is formed. The schematic of the frosting process as visualized by this model is shown in Figure II-BO.

Qualitatively, this model is based on the same physical ideas as those used in the simple model. However, some of the physical ideas are extended to explain the microscopic occurrences in the frost interior.

It was assumed in the simple model that water vapor diffuses in the frost interior by vapor pressure gradient existing at the frost surface. The "sophisticated" model extends this physical idea to explain the processes occuring in the frost interior. It assumes that at every layer in the frost interior the bulk gas is in equilibrium with the ice at the prevailing temperature and thus there is a vapor pressure gradient exist at every point. During a frosting process, each layer of the frost interior densifies under the prevailing equilibrium conditions.

The mathematical formulation of this model is obtained by writing the heat and mass balances on a differential element of the frost. The frost surface conditions, which were the basis for the complete mathematical formulation of the 'simple model', are taken as only one set of boundary conditions. The other set of boundary conditions is taken at the cold wall. This model describes the development of the density distribution within the frost on the basis of the mechanism of water transport in the frost interior postulated above. Thus, it attempts to seek an explanation for the mechanism by which water vapor can diffuse through every layer of the frost interior. The principal mathematical equations of this model can be obtained as follows.

Mass Balance

Mass balance on a differential element of the frost can be written as

$$A \left. J \right|_{x+\Delta x} - A \left. J \right|_{x} = A \Delta x \frac{\partial \rho_f}{\partial \theta} \qquad \text{(II-B1)}$$

The mass flux, J, by the vapor pressure gradient can be written as

$$J = \frac{D_{eff}}{RT} \frac{1}{(1-P_{vp}/P)} \frac{\partial P_{vp}}{\partial x} \qquad \text{(II-B2)}$$

where,

$$D_{eff} = \frac{D_B (1-\rho_f/\rho_{ice})}{\tau}$$

All the nomenclatures of Equations II-B2 and II-B3 are described in Appendix R.

Substituting Equations II-B2 and II-B3 into II-B1, one

obtains,

$$\frac{\dfrac{D_B(1-\rho_f/\rho_{ice})}{RT\,\tau\,(1-P_{vp}/P)}\left.\dfrac{\partial P_{vp}}{\partial x}\right|_{x+\Delta x} - \dfrac{D_B(1-\rho_f/\rho_{ice})}{RT\,\tau\,(1-P_{vp}/P)}\left.\dfrac{\partial P_{vp}}{\partial x}\right|_{x}}{\Delta x} = \frac{\partial \rho_f}{\partial \theta} \qquad \text{(II-B4)}$$

or,

$$\frac{\partial}{\partial x}\left[\frac{D_B(1-\rho_f/\rho_{ice})}{RT\,\tau\,(1-P_{vp}/P)}\,\frac{\partial P_{vp}}{\partial x}\right] = \frac{\partial \rho_f}{\partial \theta} \qquad \text{(II-B5)}$$

Also,

$$\frac{\partial P_{vp}}{\partial x} = \left(\frac{\partial P_{vp}}{\partial T}\right)\left(\frac{\partial T}{\partial x}\right) \qquad \text{(II-B6)}$$

Using Clausius-Clapeyron equation (80), one can write

$$\frac{\partial P_{vp}}{\partial x} = \left(\frac{M\,\Delta H\,P_{vp}}{RT^2}\right)\left(\frac{\partial T}{\partial x}\right) \qquad \text{(II-B7)}$$

Combining Equations II-B5 and II-B7, one can write

$$\frac{\partial}{\partial x}\left[\frac{D_B(1-\rho_f/\rho_{ice})}{RT\,\tau\,(1-P_{vp}/P)}\left(\frac{M\,\Delta H\,P_{vp}}{RT^2}\right)\left(\frac{\partial T}{\partial x}\right)\right] = \frac{\partial \rho_f}{\partial \theta} \qquad \text{(II-B8)}$$

Heat Balance

One dimensional steady state heat conduction in the frost interior can be written as,

$$q = k_f \frac{dT}{dx} \qquad \text{(II-B9)}$$

where,

$$k_f = k_{fi} + k_{excess} \qquad \text{(II-B10)}$$

The excess thermal conductivity, k_{excess}, can be represented as (see Appendix F)

$$k_{excess} = \frac{D_B\,\Delta H^2\,P_{vp}\,M^2}{R^2\,T^3} \qquad \text{(II-B11)}$$

Physically, k_{excess} is the additional component of

the conductivity caused by evaporative mass transport in the frost interior.

Boundary Conditions

1. At Cold Wall

The schematic of the boundary conditions at the cold wall is shown in Figure II-B1.
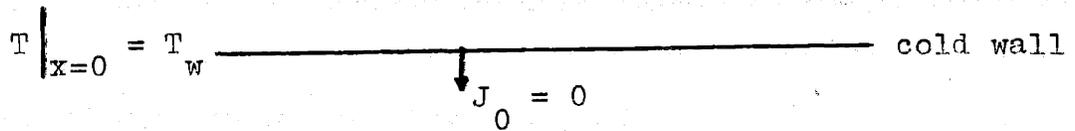
$$T\Big|_{x=0} = T_w \text{ ———————————— cold wall}$$
$$\downarrow J_0 = 0$$

Figure II-B1   Schematic of the boundary conditions
at the cold wall

A. Heat Boundary Condition

Temperature at the cold wall remains constant at all time. Hence,

$$T\Big|_{x=0} = T_w \qquad \text{at all time} \qquad \text{(II-B12)}$$

B. Mass Boundary Condition

There is no mass flux past the cold wall. Hence,

$$J\Big|_{x=0} = \frac{D_e\left(1 - \rho_f/\rho_{ice}\right)}{RT\tau\left(1 - P_{vp}/P\right)} \frac{\partial P_{vp}}{\partial x}\Big|_{x=0} = 0 \qquad \text{(II-B13)}$$

2. At the Frost Surface

The schematic of the boundary conditions at the frost surface is shown in Figure II-B2.

Gas Flow ⇄

Heat Flux $= h(T_g - T_s) + K_g(P_g - P_s)\cdot\Delta H$
Mass Flux $= K_g(P_g - P_s)$

Mass allocated to ————————————— ← FROST SURFACE
increase the frost thickness

$$= \rho_{f,s}\frac{d\delta}{d\theta}$$

Heat Flux $= k_f\dfrac{dT}{dx}$

Mass Flux $= \dfrac{D_e\left(1 - \rho_f/\rho_{ice}\right)}{RT\tau\left(1 - P_{vp}/P\right)}\dfrac{\partial P_{vp}}{\partial x}\Big|_{x=\delta}$
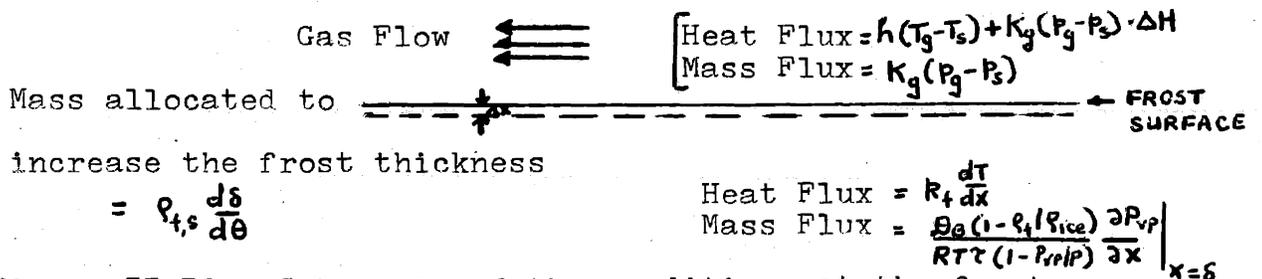
Figure II-B2   Schematic of the conditions at the frost
surface

A. Heat Boundary Condition

Heat is transferred from the gas to the frost both by convection and by material transport of the condensible component. This rate of heat transfer can be written as

$$q = h\ (T_g - T_s) + K_g\ (p_g - p_s) \Delta H \qquad (II-B14)$$

It should be noted that in above equation, the heat required for the sensible cooling of the condensible component is neglected.

On the frost side (at the frost surface), there is energy transfer through the frost layer by two mechanisms. First, there is the usual conduction process. Secondly, there is an internal mass flux caused by the temperature gradient. Both are proportional to the surface temperature gradient. Thus, one may write

$$q = k_{f,s}\left(\frac{dT}{dx}\right)_s = (k_{fi} + k_{excess})_s \left(\frac{dT}{dx}\right)_s \qquad (II-B15)$$

Thus, the heat balance at the frost surface can be written as

$$h\ (T_g - T_s) + K_g\ (p_g - p_s) \Delta H = k_{f,s}\left(\frac{dT}{dx}\right)_s \qquad (II-B16)$$

B. Mass Boundary Condition

The total mass that comes to the frost surface is given by Equation II-B17.

$$J_s = K_g\ (p_g - p_s) \qquad (II-B17)$$

Part of this mass diffuses in the frost interior due

to vapor pressure gradient existing at the frost surface. The rest of it increases the frost thickness.

The mass flux which diffuses in the frost interior can be written as

$$J_{si} = \frac{D_B}{RT\,\tau} \frac{(1-\rho_f/\rho_{ice})}{(1-P_{vp}/P)} \left.\frac{\partial P_{vp}}{\partial x}\right|_{x=\delta} \qquad \text{(II-B18)}$$

and the mass allocated to increase the frost thickness can be written as

$$J_{so} = \rho_{f,s}\frac{d\delta}{d\theta} \qquad \text{(II-B19)}$$

Combining Equations II-B17, II-B18 and II-B19, the mass boundary condition at the frost surface can be written as

$$J_s = J_{si} + J_{so} \qquad \text{(II-B20)}$$

or,

$$K_g(P_g - P_s) = \rho_{f,s}\frac{d\delta}{d\theta} + \frac{D_B}{RT\,\tau}\frac{(1-\rho_f/\rho_{ice})}{(1-P_{vp}/P)}\left.\frac{\partial P_{vp}}{\partial x}\right|_{x=\delta} \qquad \text{(II-B21)}$$

or,

$$K_g(P_g - P_s) = \rho_{f,s}\frac{d\delta}{d\theta} + \frac{D_B}{RT\,\tau}\frac{(1-\rho_f/\rho_{ice})}{(1-P_{vp}/P)}\left.\left(\frac{M\cdot\Delta H\, P_{vp}}{RT^2}\right)\left(\frac{\partial T}{\partial x}\right)\right|_{x=\delta} \qquad \text{(II-B22)}$$

Dimensionless Form of the Equations

The equations described above can be dedimensionlized as follows.

Let $z = x/\delta$ \qquad (II-B23)

then,

$$\rho_f = \rho_f\,(z,\theta)$$

$$\partial \rho_f = \frac{\partial \rho_f}{\partial \theta}\bigg|_z \partial \theta + \frac{\partial \rho_f}{\partial z}\bigg|_\theta \partial z \qquad \text{(II-B24)}$$

$$\frac{\partial \rho_f}{\partial \theta} = \frac{\partial \rho_f}{\partial \theta}\bigg|_z + \frac{\partial \rho_f}{\partial z}\bigg|_\theta \frac{\partial z}{\partial \theta} \qquad \text{(II-B25)}$$

Since, $\quad z = x/\delta$ $\qquad\qquad\qquad$ (II-B26)

then $\qquad \dfrac{\partial z}{\partial \theta} = - z \dfrac{\dot{\delta}}{\delta}$ $\qquad\qquad$ (II-B27)

where $\qquad \dot{\delta} = \dfrac{d\delta}{d\theta}$

therefore, $\qquad \dfrac{\partial \rho_f}{\partial \theta} = \dfrac{\partial \rho_f}{\partial \theta}\bigg|_z - z \dfrac{\dot{\delta}}{\delta} \dfrac{\partial \rho_f}{\partial z}\bigg|_\theta$ $\quad$ (II-B28)

Hence, Equation II-B8 can be written in the dimensionless form as

$$\frac{1}{\delta} \frac{\partial}{\partial z}\left[\frac{D_B (1-\rho_f/\rho_{ice})}{RT\,\tau\,(1-\rho_{vf}/P)}\left(\frac{M\,\Delta H\,\rho_{vp}}{RT^2}\right)\frac{1}{\delta}\frac{\partial T}{\partial z}\right] = \frac{\partial \rho_F}{\partial \theta}\bigg|_z - z \frac{\dot{\delta}}{\delta}\frac{\partial \rho_F}{\partial z}\bigg|_\theta \quad \text{(II-B29)}$$

Similarly, Equation II-B9 can be written in the dimensionless form as

$$q = \frac{k_f}{\delta} \frac{\partial T}{\partial z} \qquad\qquad \text{(II-B30)}$$

Dimensionless Form of the Boundary Conditions

The boundary conditions can take the following dimensionless form

1. At Cold Wall

A. Heat Boundary Condition

$$T\bigg|_{z=0} = T_w \qquad \text{at all time} \qquad \text{(II-B31)}$$

B. Mass Boundary Condition

$$J\bigg|_{z=0} = \frac{D_B (1-\rho_f/\rho_{ice})}{RT\,\tau\,(1-\rho_{vp}/P)\,\delta}\frac{\partial \rho_{vp}}{\partial z}\bigg|_{z=0} = 0 \qquad \text{(II-B32)}$$

2. At the Frost Surface

A. Heat Boundary Condition

$$q\Big|_{z=1} = h\,(T_g - T\big|_{z=1}) + K_g(p_g - p\big|_{z=1})\,\Delta H = \frac{k_f}{\delta}\frac{\partial T}{\partial z}\Big|_{z=1} \quad (II\text{-}B33)$$

B. Mass Boundary Condition

$$J_s\Big|_{z=1} = K_g(p_g - p\big|_{z=1}) = \rho_{f,s}\frac{d\delta}{d\theta} + \frac{D_B(1 - \rho_f/\rho_{ice})}{RT\gamma(1 - P_{vr}/P)\,\delta}\frac{\partial P_{vP}}{\partial z}\Big|_{z=1} \quad (II\text{-}B34)$$

Computer Solution of the Equations

The finite difference solution of the above equations was obtained with the help of a computer. The solution involves the following steps.

1. Starting with an initial value of uniform (with depth) frost density and thickness, Equation II-B30 along with boundary conditions Equations II-B31 and II-B33 are used to obtain the temperature distribution in the frost interior at the starting time. The fourth order Runga-Kutta method is used to solve Equation II-B30.

2. Equations II-B29 along with the boundary conditions Equations II-B32 and II-B34 are then solved by a six point finite difference technique to obtain the density distribution within the frost and the frost thickness at new time.

3. Step 1 is repeated to obtain the temperature distribution within the frost at new time, and thus the calculation process is iterated.

The details of the computer solution is described in Appendix E.

Computer Results

The computer solution of the mathematical equations

of the 'sophisticated model' gives a density and a
temperature distribution within the frost and the frost
thickness as a function of time. Figures II-B3 to II-B6
show the results of this solution for two typical sets of
system conditions. Figure II-B3 describes the predictions
of the density distribution in the frost interior when it
is deposited under the system conditions of Reynolds number
= 5,600, humidity = gas dew point at 29.2^{O}F and gas
temperature = 70°F. The predictions for the variation in
temperature distribution within the frost with time for
the same experimental conditions (in the transient state
of heat transfer) is shown in Figure II-B4. The theoretical
curves shown in Figures II-B3 and II-B4 are obtained with
an assumed starting value of frost density= 0.026 gms./cc.,
uniform with depth and a thickness of 0.023 inches. The
initial values are taken at the time of 2 minutes from the
start of the frosting process.

Figure II-B5 describes the similar results for another
set of experimental conditions (Re=14,700, humidity= dew
point at 40°F, T_g= 70°F) in which the starting values are
taken in the quasi-steady state heat transfer region (at
the time of 30 minutes from the start of the frosting
process). The values of the initial uniform (with depth)
frost density and frost thickness in this case are 0.076
gms./cc. and 0.144 inches respectively. The predictions
for the variation in temperature distribution within the
frost with time in this quasi-steady state heat transfer

region is shown in Figure II-B6.

The results shown in Figures II-B3 and II-B4 indicate
that the model predicts a large difference in the rate of
frost densification at various points in the frost interior.
The rate being the highest at the frost surface (where the
vapor pressures of ice are the highest). Figure II-B4 shows
that the temperature distribution in the frost interior
changes significantly in the transient heat transfer state
of the frosting process. On the other hand, as shown in
Figure II-B6, the variation in the temperature distribution
within the frost with time is very slow in the quasi-steady
state of heat transfer in the frosting process.

Since mathematical formulations of both 'simple' and
'sophisticated' models are based on the very similar physical
ideas, one would expect a good agreement between the values
of the average frost density (average frost density $= \dfrac{\int_0^{\delta} \rho_f(x)\,dx}{\delta}$),
frost thickness and heat transfer through the frost as a
function of time predicted by the them for the identical
system conditions. The comparison between the average frost
density, frost thickness and heat transfer through the frost
predicted by the models at various times is described in
Figures II-B7 and II-B8 for two different sets of system
conditions. Figure II-B7 shows the comparison for a case
in which the initial values of frost density and frost
thickness are taken in the transient state of heat transfer.
Figure II-B8, on the other hand, shows the comparison for
a case in which the starting values of frost density and

and thickness are taken in the quasi-steady state of heat
transfer. The results of Figures II-B7 and II-B8 indicate
that even though there is reasonably good agreement between
the results predicted by both the models, the deviation
between their predictions increases with time. Since, as
seen in Section II-A, the predictions of 'simple model'
agree well with the experimental results, the above described
results also indicate that the predictions of 'sophisticated
model' (for the time variation in average frost density,
frost thickness and heat transfer through the frost) will
not agree with the experimental results for a long period
of the frosting process.

The predictions of the 'sophisticated model' for the
density distribution in the frost interior are not agreement
with the experimental results shown in Figure II-B9. Figure
II-B9 shows the experimental data for the density of the
various frost slices at different depths and at different
times deposited under a typical set of system conditions.
One can conclude from these results that the frost density
remains essentially uniform (with depth) at all time. The
theoretical predictions shown in Figures II-B3 and II-B5,
on the other hand, indicates the existence of a large density
gradient in the frost interior after a short duration
from the start of frosting. Thus, it can be concluded that
the 'sophisticated model' does not speculate well, the
microscopic occurrences in the frost interior.

Discussion of Computer Results

The computer results of Figures II-B3 and II-B5 indicate that the sophisticated model shows that the assumption of equilibrium conditions between interstitial gas and ice within the frost is not valid.

The predicted density gradient can be explained on the basis of the driving force which causes it. The development of a large density gradient indicates that the driving force for the rate of frost densification, namely $\frac{\partial}{\partial x}\left(\frac{D_{eff}}{T}\frac{\partial P_{vp}}{\partial x}\right)$ varies significantly across the frost layer. Since an empirical correlation between molecular diffusivity and temperature (see Figure II-B10) shows that D_B/T is approximately proportional to T, it is in fact $\frac{\partial}{\partial x}\left(T\frac{\partial P_{vp}}{\partial x}\right)$ that varies significantly across the frost layer.

The reason for a significant variation of $\frac{\partial}{\partial x}\left(T\frac{\partial P_{vp}}{\partial x}\right)$ in the frost interior is the extremely sharp drop of vapor pressure of ice at low temperatures. The vapor pressure profile in the frost interior for a typical set of experimental conditions is shown in Figure II-C3.

The deviation between the predictions of the simple and sophisticated models for the time variation in average frost density, frost thickness and heat transfer rate (see Figures II-B7 and II-B8) should be expected to increase with time elapsed from the start of the calculations. This is because, as sophisticated model predicts higher and higher density gradient in the frost interior, the temperature distribution within the frost predicted by both the models would differ more and more. This is shown in Figures II-B4

and II-B6. This increasing deviation between the predicted

temperature distributions would obviously cause the other

predictions (see Figures II-B7 and II-B8) of the models

to deviate more and more. This, of course, means that the

predictions of the sophisticated model for the time variation

in average frost density, frost thickness and the rate of

heat and mass transfer would not agree with the experimental

results for a long period.

Conclusions

Two important conclusions can be drawn from the

analysis of the sophisticated theoretical model.

1.   The sophisticated model will not predict the time

variation in average frost density, frost thickness and

heat transfer through the frost well in agreement with

the experimental results over a long period.

2.   The driving force for the rate of frost densification

assumed in the sophisticated model, namely $\frac{\partial}{\partial x}\left(\frac{D_{eff}}{T}\frac{\partial P_{vf}}{\partial x}\right)$

varies significantly across the frost layer and this causes

a significant build-up of density gradient within the frost

as it accumulates on the cold surface. Since the experimental

facts indicate that the density of the frost stays uniform

(with depth) at all time, the sophisticated model does not

speculate the true physical processes occurring in the

frost interior.

II-C Critical Evaluation of the Speculated Physical Processes

(by "Sophisticated" Model) Occurring in the Frost Interior

The resuls of the sophisticated model indicated that if

at every layer in the frost interior, an equilibrium

between the gas and ice exists then the frost densifies

non uniformly (with depth) with time.   The non uniform

frost densification is caused by the significant

variation in the driving force $\frac{\partial}{\partial x}\left[\frac{D_{eff}}{T}\frac{\partial P_{vp}}{\partial x}\right]$ for it.   The

experimental data in Figure II-B9, on the other hand,

indicate that the frost density stays almost uniform

(with depth) at all time.   This experimental fact demands

a critical evaluation of the speculated physical processes

occurring in the frost interior.

The sophisticated model assumed that the partial

pressure of water vapor at every point in the frost interior

was the vapor pressure at that point i.e. at the temperature

prevailing there.   Since this assumption governs the

mechanism under which every layer in the frost interior

densifies with time, it is examined critically, in this

section, with the help of some experimental data as follows.

Quantitative Verification of Equilibrium Situation in the

Frost Interior

If every layer of the frost interior densifies uniformly

(i.e. frost density remains uniform with depth at all time),

the mass balance Equation II-B4 on the differential

element of the frost can be written as

$$\frac{\partial}{\partial x}\left[\frac{D_B(1-\rho_f/\rho_{ice})}{RT\tau(1-p/P)}\frac{\partial p}{\partial x}\right] = \frac{d\rho_f}{d\theta}$$ (II-C1)

Assuming $(1-p/P) \approx 1.0$, Equation II-C1 can be written as

$$\frac{\partial}{\partial x}\left[\frac{D_\theta\,(1-\rho_f/\rho_{ice})}{RT\,\tau}\,\frac{\overline{\partial p}}{\partial x}\right] = \frac{d\rho_f}{d\theta} \qquad \text{(II-C2)}$$

integrating Equation II-C2, one obtains

$$N_x = \frac{D_\theta\,(1-\rho_f/\rho_{ice})}{RT\,\tau}\,\frac{\partial p}{\partial x} = x\,\frac{d\rho_f}{d\theta} + c_1 \qquad \text{(II-C3)}$$

substituting Boundary Condition at $x = 0$, $N_x=0$ in Equation II-C3, one obtains that $c_1 = 0$ hence Equation II-C3 becomes

$$\frac{D_\theta}{T}\,\frac{\partial p}{\partial x} = x\,\frac{d\rho_f}{d\theta}\,\frac{R\,\tau}{(1-\rho_f/\rho_{ice})} \qquad \text{(II-C4)}$$

A typical experimental condition of Brazinsky (**14**) is used to obtain $p(x)$ curve in the frost interior from Equation II-C4. It should be noted that similar results can be obtained from the experimental data of the present research.

From Figure II-C1 of ρ_f versus time profile at $\rho_f = 0.111$ gms./cc.

$$1-\rho_f/\rho_{ice} = 1-(0.111/0.917) = 0.879 \qquad \text{(II-C5)}$$

and

$$\left.\frac{d\rho_f}{d\theta}\right|_{\rho_f=0.111} = 2.925 \text{ lbm./ft}^3\text{hr.} \qquad \text{(II-C6)}$$

substituting the values of the Equation II-C5 and II-C6 into the Equation II-C4, one obtains

$$\frac{\partial p}{\partial x} = \frac{T}{D_\theta} \times \frac{(2.925)\times 85.85 \times 1.10\ x}{0.879} = 315\,\frac{Tx}{D_\theta} \qquad \text{(II-C7)}$$

The molecular diffusivity of water vapor in nitrogen can be correlated with temperature by the following correlation (**94**).

$$D_B = 3.30 \times 10^{-6} \, T^{2.0087} \tag{II-C8}$$

where T is in °R and D_B is in ft^2/hr

The details of this correlation are shown in Figure II-B10.

Substituting the Equation II-C8 into II-C7 and integrating,

$$\int_{x=0}^{x=x} dp = \int_{x=0}^{x=x} \frac{9.54 \times 10^7 \, x}{T^{1.0087}} \, dx \tag{II-C9}$$

$$\therefore \quad P\Big|_{x=x} = P\Big|_{x=0} + 9.54 \times 10^7 \int_{x=0}^{x=x} \frac{x}{T^{1.0087}} \, dx \tag{II-C10}$$

where p is in lb$_f$/ft^2

or

$$p\Big|_{x=x} = p\Big|_{x=0} + 3.41 \times 10^7 \int_{x=0}^{x=x} \frac{x}{T} \, dx \tag{II-C11}$$

where p is in mm. Hg.

Assuming partial pressure of the water vapor at the cold wall is an equilibrium vapor pressure at the cold wall temperature and using the experimental data for the temperature versus x profile in the frost interior the results of Table II-C1 can be obtained. The deviation from the equilibrium at every point in the frost interior can be seen from the listed values of vapor pressure and the supersaturation ratio in Table II-C1.

The results of Table II-C1 are plotted in Figures II-C3 and II-C4.

Discussion of Results ——

The results of the above analysis, as described in the Figures II-C3 and II-C4, show that there is a large deviation from the equilibrium at every point in the frost interior.   If no nucleation is assumed then the true water vapor pressure exceeds the local vapor pressure by a large amount.   Hence, a realistic model of the physical processes occurring in the frost interior should take into account a possibility of nucleation and should consider the transport of water vapor under a true partial pressure gradient.

It should be noted that since the theoretical results of the sophisticated model Section II-B indicate that ice particles can not grow under their own vapor pressure at cryogenic temperatures, the results of Figure II-B9, for the uniform densification of the frost can be explained only if the ice particles near the cold wall (at liquid nitrogen temperature) grow in non-equilibrium situation.   The strong possibility of nucleation in the frost interior as shown by the theoretical analysis of this section indicate that ice at that temperature will grow by both impingement of ice nuclei on the existing crystals and by the molecular diffusional mechanisms under non-equilibrium situation.

Conclusions

The principal conclusions of the above calculations can be stated as follows.   ——

1. If no nucleation is assumed, the calculated water vapor pressure exceeds the local vapor pressure by a large amount.

2. In the colder region of the frost, ice crystals will grow by the impingement of the ice nuclei on the already existing crystal as well as by the molecular diffusional mechanisms under non-equilibrium situation.

II-D Summary of the Available Literature Information on the Possible Physical Processes Occurring in the Frost Interior

The results described in Sections II-B and II-C indicate that in order to obtain a model which can explain the uniform densification of the entire frost layer, a critical evaluation of the possible physical processes occurring in the frost interior is needed. This section briefly summarizes the significant and useful available literature information on the various possible physical processes which might be taking place within the frost.

Numerous physical processes can take place in the heterogeneous structure of the frost interior. In the 'sophisticated model' it was assumed that at every layer in the frost interior, the interstitial gas is in equilibrium with ice at the prevailing temperature. However, the analysis described in Section II-C indicate that in actual fact there will be a large deviation from equilibrium at every layer in the frost interior. Under the non-equilibrium conditions, the significant physical processes which could occur within

the frost are as follows.

1. Nucleation of liquid or solid particles of water from the vapor phase.

2. Non-equilibrium growth of ice crystals from the vapor phase.

3. Thermal diffusion of fog or ice nuclei in the interstitial gas.

Several effects or occurrences which assumed to have negligible effect on the densification of the frost are stated below.

1. Gravitational effect.

2. Electrostatic forces on ice nuclei.

3. Thermal diffusion of water vapor in air.

All the above stated occurrences are neglected for the following reasons.

1. Gravitational Effect

The bottom layer of the frost could densify by the gravitational force exerted by the top layer. This gravitational force, however, could not be important when the frost is deposited in a vertical tube. Also, it varies from layer to layer. Thus, the significance of gravitational force for the explanation of the uniform densification of the frost (with depth) deposited on a surface with an arbitrary geometrical shape does not appear very promising. For the present purpose, therefore, this effect is neglected.

2. Electrostatic Forces on Ice Nuclei

If nucleation occurs predominantly in the frost interior,

then the possible electrostatic charges on these nuclei could cause the transfer of these particles from layer to layer. At present, however, it is difficult to conceive the cause for the development of the possible electrostatic charges on the nuclei. Hence, this effect is neglected in the present thesis.

3. Thermal Diffusion of Water Vapor in Air

Since there is a large temperature gradient existing within the frost (see Section IV-A), one would expect that the diffusion of water vapor by the thermal gradient could be equally important as one due to the concentration (or vapor pressure) gradient. Contrary to the expectations, however, the following calculations indicate that the thermal diffusion of water vapor in air within the frost is negligible compare to the diffusion of water vapor under concentration gradient.

Comparison of Mass Fluxes under Concentration (Vapor Pressure) and Temperature Gradient

The total flux of water vapor within the frost due to both thermal and concentration gradient can be given by the following Equation II-D1.

$$N_W = \text{total flux of water vapor} = \frac{D_{W-A}}{c_W c_A} \left(\frac{dc_W}{dx} + \frac{k_T}{T} \frac{dT}{dx} \right) \qquad (\text{II-D1})$$

where, the term $\dfrac{D_{W-A}}{c_W c_A} \dfrac{dc_W}{dx}$ represents the mass flux of water vapor due to ordinary concentration gradient and the term $\dfrac{D_{W-A}}{c_W c_A} \dfrac{k_T}{T} \dfrac{dT}{dx}$ represents the water flux due to

thermal diffusion.

Grew and ibbs (49) define k_T, the thermal diffusion coefficient, to be equal to $\alpha n_1 n_2$, where α denotes the thermal diffusion factor. Various methods for evaluating α are presented in Reference 49. In the present calculation maximum value of α is chosen, in order to obtain the value for maximum mass flux by thermal diffusion. From the graph on page 29 of Reference 49, it can be found that $\alpha \approx 0.180$ for very low water vapor concentrations of air-water vapor mixture. This value is assumed to be applicable at all positions in the frost interior.

From Equation II-D1, it is obvious, that contribution of thermal diffusion to the total mass flux can be evaluated by comparing the values of $\frac{dc_W}{dx}$ and $\frac{k_T}{T} \frac{dT}{dx}$ at various points in the frost interior.

Also, $\frac{dc_W}{dx} = \frac{dc_W}{dT} \frac{dT}{dx}$ and so a comparison between $\frac{dc_W}{dT}$ and $\frac{k_T}{T}$ or between $\frac{dc_W}{dT}$ and $\frac{\alpha c_W c_A}{T}$ should be made.

Values of $\frac{dc_W}{dT}$ and $0.18\, c_W\, c_A/T$ at different temperatures are shown in Table II-D1. At any given temperature $\frac{dc_W}{dT}$ can be obtained from the slope of the vapor pressure curve. At all temperatures between $-300°F$ and $+20°F$ the value of $0.18\, c_W c_A/T$ found to be less than 1.32% of $\frac{dc_W}{dT}$. It can be therefore concluded that at all positions within the frost the mass flux due to thermal diffusion is small compared with the flux due to concentration gradient. Hence, the effects of thermal diffusion on the

frost densification can be ignored for the present purpose.

Available Literature Information on the Physical Processes
Occurring within the Frost

1. Nucleation from the Vapor Phase

There are three kinds of nucleation that can occur in
the frost interior; homogeneous, heterogeneous and secondary.

The secondary nucleation is, at present, a very poorly
understood phenomenon. It can either occur by shearing off
the dendrites of the existing crystal by thermal forces or
due to mere presence of ice crystals. Both of these are
possible to occur in the frost interior. The occurrence of
this phenomenon may not required a considerably high
supersaturation. There are, as yet, no significant
experimental as well as theoretical studies done in this
area.

The heterogeneous nucleation is a very complex process
because of its diverse relationships to the amount, size
and nature of the impurities present in the gas. For the
purpose of finding an explanation for the uniform
densification of the frost under an arbitrary set of system
conditions, however, this phenomenon could not play a
significant role for the following reason.

It appears highly probable that uniform densification
of the entire frost layer will be observed if frost is
deposited from a mixture of ultra pure air and water vapor.
Both Brazinsky (14) and Weber (114) used purified Nitrogen
from Nitrogen Bottle (purity of over 99%) as a carrier

gas for water vapor in the frosting experiments, and they
still observed the same amount of frost densification as
observed in the present research.   In the present studies
ordinary air is used as a carrier gas which is expected to
have a little higher amount of impurity than nitrogen from
nitrogen bottle.   These results indicate that heterogeneous
nucleation can not be used to explain the uniform densifica-
tion of the frost under an arbitrary set of system condit-
ions.   Hence, it is neglected for the present purpose.

The homogeneous nucleation has been studied somewhat
extensively both experimentally as well as theoretically.
The detailed survey of the available literature for this
phenomenon is described in Appendix H.   The occurrence of
homogeneous nucleation requires a significant amount of
supersaturation of water vapor in the gas.   If secondary
nucleation is not a predominant mechanism, then it is
possible, as seen in Section II-C, to achieve a sufficiently
high supersaturation in the gas for homogeneous nucleation.
The important studies done for this process can be summar-
ized as follows.

1.   The experimental data on homogeneous nucleation rate
are obtained only for temperatures above $-73^{o}C$.   These
data are obtained in Wilson Chamber or in sonnic nozzles.
The data agree well with the theoretical relationship of
Becker and Doring ($\underline{8}$).

2.   Volmer ($\underline{112}$), Becker and Doring ($\underline{8}$) and Frankel
($\underline{9}$, $\underline{40}$, $\underline{42}$) equations are the three most significant

theoretical relationships for the homogeneous nucleation rate. The predictions of nucleation rate by Becker and Doring (8) and by Frankel (9,40,42) equations have been found to agree well with the experimental data (12,43,111).

2. Non-Equilibrium Growth of Ice Crystals from the Vapor Phase

The frost densification is essentially a result of growth of ice crystals network. The ice crystals can grow either by particle impingement of ice nuclei which are formed either in bulk interstitial gas or near the crystal surfaces, or by condensation of the water vapor which is transported from the bulk gas to the crystal surface. The detailed survey of available literature for the latter kind of growth is described in Appendix J.

The study of crystal growth by particle impingement is an extremely difficult task, particularly for the ice network in the frost interior. It requires the knowledge of frost structure, the position of the particles in the bulk interstitial gas and the possible forces acting upon the particles. There is, as yet, no significant study done to be able to predict all these requirements.

Usually, the phenomenon of particle impingement can be handled by assuming a value for so called 'sticking coefficient'. If no ice particles stick to the existing crystal then sticking coefficient has a zero value. On the other hand, if all the ice nuclei formed in the gas stick to the existing crystal, then sticking coefficient

will have a value of unity. There is, as yet, no systematic

guidelines developed to obtain a value of sticking

coefficient under a given set of system conditions.

The research work that has been done to study the

crystla growth from vapor phase by diffusional mechanisms

can be summarized as follows.

A.   The experimental data for the growth of ice crystals

from vapor phase have been obtained only at temperatures

above -30°C. In initial part of the growth these data found

to agree well with a model (68) which assumed that growth

process is controlled by simultaneous heat and mass transfer

from bulk to the crystal surface. After an initial short

duration, the growth process has been found to occur in

the dendritic manner.

B.   The growth studies have been made with the crystals

of various shapes.

C.   So far, no significant theoretical as well as

experimental studies of dendritic crystal growth process

have been carried out.

3. Thermal Diffusion of Aerosols in Air

The existence of a large temperature gradient (see

Section IV-A) and the possibility for an existence of a

large number of water or ice nuclei indicate the probability

for a significant flux of water or ice by thermal diffusion

of these aerosols in the colder region of the frost. There

has been a significant amount of theoretical as well as

experimental work done in this area. None of these studies

however, have been dealt with ice particles or with low temperature conditions (below room temperature). The detailed available literature information for this phenomenon is described in Appendix K. The important information can be summarized as follows.

A.   The thermal force on a solid particle of size greater than 4 microns is usually very small in magnitude.

B.   The guidelines for the development of theoretical equations for this process depend upon the flow regimes (i.e. on the value of ratio λ/r_p; where λ is mean free path of molecules and r_p is the radius of liquid or solid particles). The theoretical equations for both $\lambda/r_p \ll 1.0$ and $\lambda/r_p \gg 1.0$ have been reported extensively by several investigators (15,16,22,35,95,113). The theoretical analysis of the process for $\lambda/r_p \approx 1.0$ (transition regime) is extremely difficult task and no quantitative theoretical relationships have been obtained so far. For the present purpose, Brock's equation for the thermal force (15) is used for the calculation of thermal diffusive velocity of ice or water nuclei in the interstitial gas within the frost (see Section II-E). The details of Brock's equation as well as the brief descriptions of all other theoretical relationships are shown in Appendix K.

C.   The experimental measurements of the thermal force on the aerosol particles of wide range of thermal conductivity (10^{-4} cal./cm. sec. $^{\circ}$C to 0.1 cal./sec. cm. $^{\circ}$C) have been studied. The experimental data have been found to be in

fair agreement with the theoretical predictions. As yet,
no experimental data for thermal force on aerosols have
been taken at low temperatures (i.e. below room temperature).

II-E Model for Frost Densification ('Non-Equilibrium Model')

As seen in Section II-B, the 'improved model' (or
'sophisticated model') for the frosting process predicts
that if every layer of the frost densifies under the
prevailing equilibrium conditions then the frost will densify
non-uniformly across its depth. The experimental
measurements on the density gradient within the frost, on
the other hand, indicated that the frost density remains
uniform (with depth) at all times.

The discrepancy between the experimental facts and
the theoretical predictions for the uniformity of the
frost density was examined theoretically in Section II-C.
It was concluded that the uniform densification of the
frost could be obtained if the ice crystals grew in a
non-equilibrium situation. The calculations also indicat-
ed that in the colder region of the frost (near the cold
wall) a significant amount of water could exist only in
the form of ice nuclei.

With the results of Section II-B and II-C along with
the available literature information on the possible
phenomena occurring in the frost interior (as described
in Section II-D), a new model for the frost densification
was developed. In this section, the new model is describ-
ed in detail and discussed qualitatively as an explanation

for the uniformity of the frost densification.

The basic postulations and the assumptions of the new model are as follows.

1. At the frost surface, water vapor is in equilibrium with ice at the prevailing temperature. The partial pressure gradient due to the temperature gradient at the frost surface causes the transport of water vapor within the frost. (It should be noted that the 'simple model' was also based on this assumption).

2. The interior of the frost is divided into three regions for convenience of discussion and calculation. Near the frost surface, where the vapor pressure of ice is large (probably above $-40°F$), all the water is transported as vapor. Near the cold wall, on the other hand, where the vapor pressure of water is extremely small, water is transported through the frost only in the form of ice nuclei. In between these two regions, there is a so called 'transition' region in which water is transported in the form of both ice nuclei and vapor.

3. The transport of water near the frost-gas interface (region 1) is believed to be caused by the partial pressure gradient due to a temperature gradient. Near the cold wall (region 3) water is transported through every layer by thermal diffusion of ice nuclei. Both thermal diffusion of ice nuclei and molecular diffusion of water vapor contribute to the water transport in the 'transition' region (region 2).

4. Thermal diffusion of water vapor is assumed to be negligible compared to diffusion by concentration gradient.

5. At each layer in regions $\underline{2}$ and $\underline{3}$ the mass the mass of the ice nuclei present is small compare to the mass of the existing crystalline phase.

6. The nuclei concentration at each layer in the regions $\underline{2}$ and $\underline{3}$ remains constant with time.

7. In regions $\underline{2}$ and $\underline{3}$ the thermal diffusive velocity of an ice nuclei is sufficiently high so that the nuclei will impinge (or be trapped) on the existing crystals before they can grow appreciably.

8. In region $\underline{1}$, ice crystals grow by condensation of water vapor. In region $\underline{3}$, ice crystals grow by the impingement (or trapping) of ice nuclei as they are driven towards the cold wall by a thermal force. Both particle trapping and vapor condensation contribute to the ice crystal growth in region $\underline{2}$.

Qualitative Description of the Model

As water reaches the frost surface from the bulk gas, it diffuses into the frost interior due to partial pressure gradient caused by the temperature gradient. Since the simple model predicts the water transport past the frost surface well in agreement with the experimental facts, it can be assumed that at the frost surface, ice and the gas are in equilibrium with each other.

The postulations regarding the state of water imply that the supersaturation of water vapor (p/P_{vp}) in the

interstitial bulk gas should be high at the interface
of regions 1 and 2 so that nucleation can occur. Thus,
as water vapor moves from the frost surface to the inter-
ior, the supersaturation ratio increases from the value
of about 1 at the frost surface to a considerably higher
value at the interface of region 1 and 2.

The ice crystals in region 1 grow by the condensation
of water vapor. Hence, the crystal growth in this region
is controlled by the rate at which water vapor arrives at
the crystal surface from the bulk interstitial gas. The
present model visualizes a uniform growth of an ice
crystal over the entire region as the result of counter-
balancing effects of an increase in driving force for the
mass transfer $(p/P_{vp} - 1)$ and the decrease in molecular
diffusivity of water vapor in air with increase in depth
from the frost surface.

As water penetrates deeper into region 2 water vapor
is now not only used up due to the growth of ice crystals
by diffusional mechanisms but also by the generation of ice
nuclei. The crystal growth by vapor condensation in this
region will be controlled by the same mechanisms as
described above.

The ice nuclei generated at every layer in the region
2 are directed towards the cold wall by a thermal force.
The force results from the temperature gradient. While
moving, some of these nuclei are impinged (or trapped) on the
existing crystals. Thus, the crystals in this region also

grow by deposition of ice nuclei on the existing crystals.

The model visualizes the uniform growth of ice crystals in region 2 as a result of the complex combination of the two separate mechanisms of growth (growth by vapor condensation and the growth by particle impingement). As seen previously, growth by vapor condensation is controlled by $p(x)$ and $T(x)$ distributions. It can also be expected that the crystal growth by impingement or trapping would be governed by the concentration of nuclei and the valocity at which each nuclei is moving towards the cold wall. This is because the probability for the rate of nuclei impingement can be visualized as a direct function of number of nuclei and the momentum of each nuclei. As shown in Section II-E-1, it has been found that the thermal diffusive valocity in the frost interior varies approximately linearly with temperature gradient. Thus, just like crystal growth by vapor condensation, the frost densification by impingement of nuclei is also expected to be governed by water content (i.e. nuclei concentration) and temperature distribution.

The continuous depletion of water vapor will result in the existence of water only in the form of ice nuclei at the interface of region 2 and 3. Thus, water is transported in the region 3 only in the form of ice nuclei. Since the temperature decreases with depth in this region, nuclei will remain in the solid form as they move towards the cold wall.

The ice crystals in region 3 will grow uniformly by impingement of the nuclei on the existing crystals at a

constant rate as the nuclei move towards the cold wall.
As discussed above, this growth will be controlled by the
water content and the temperature distribution at each
layer in the region.

Mathematical Formulation of the Model

Region 1

The mass balance on a differential element of frost
in region 1 can be given by the following equation.

$$\frac{\partial}{\partial x}\left(\frac{D_B}{RT}\ \frac{(1-\rho_f/\rho_{ice})}{\tau}\ \frac{\partial p}{\partial x}\right) = \frac{\partial \rho_f}{\partial \theta} \qquad \text{(II-E1)}$$

All the terms in Equation II-E1 are defined in
Appendix R.

It should be noted that D_B decreases as x decreases,
i.e., the depth from the frost surface increases.   If N
is the number of large ice crystals in each differential
element of frost, then rate of frost densification can also
be written by Equation II-E2

$$\frac{\partial \rho_f}{\partial \theta} = N\ \frac{dm}{d\theta} \qquad \text{(II-E2)}$$

where $\frac{dm}{d\theta}$ = growth rate of a single ice crystal

Mass Boundary Conditions at the Frost Surface

$$N\bigg|_{x=\delta} = \frac{D_B}{RT}\ \frac{(1-\rho_f/\rho_{ice})}{\tau}\ \frac{\partial p}{\partial x}\bigg|_{x=\delta} \approx \frac{D_B}{RT}\ \frac{(1-\rho_f/\rho_{ice})}{\tau}\ \frac{\partial P_{vp}}{\partial x}\bigg|_{x=\delta} \qquad \text{(II-E3)}$$

and,

$$K_g\,(P_g - P_s) = \rho_{f,s}\ \frac{d\delta}{d\theta} + N\bigg|_{x=\delta} \qquad \text{(II-E4)}$$

Region 2

The mass balance on a differential element of the

frost in this region can be given by the following equation.

$$\frac{\partial}{\partial x}\left[\frac{D_B}{RT}\frac{(1-\rho_f/\rho_{ice})}{\tau}\frac{\partial p}{\partial x}+nV_t\right]=\frac{\partial \rho_f}{\partial \theta} \qquad (II\text{-}E5)$$

Nuclei Balance

If nuclei concentration remains constant with time, the nuclei balance on a differential element of the frost can be given by the following equation.

$$\frac{\partial}{\partial x}(nV_t)+\dot{N}_r-\dot{N}_d=0 \qquad (II\text{-}E6)$$

where $\dot{N}_r$ is the rate of formation of nuclei and $\dot{N}_d$ is the depletion rate of nuclei from the interstitial gas. All other terms in Equations II-E5 and II-E6 are defined in Appendix R.

It is easy to see that Equation II-E5 can be divided into two parts as follows.

The frost densification due to diffusional mechanism can be written as

$$\frac{\partial \rho_f'}{\partial \theta}=\frac{\partial}{\partial x}\left[\frac{D_B}{RT}\frac{(1-\rho_f/\rho_{ice})}{\tau}\frac{\partial p}{\partial x}\right] \qquad (II\text{-}E7)$$

On the other hand, the frost densification by the particle impingement can be written as

$$\frac{\partial \rho_f''}{\partial \theta}=\frac{\partial}{\partial x}(nV_t)=f(n,V_t) \qquad (II\text{-}E8)$$

Also, from Equation II-E5

$$\frac{\partial \rho_f}{\partial \theta}=\frac{\partial \rho_f'}{\partial \theta}+\frac{\partial \rho_f''}{\partial \theta} \qquad (II\text{-}E9)$$

Region 3

In this region, water transport occurs solely by

thermal diffusion of ice nuclei. Thus,

$$\frac{\partial \rho_f}{\partial \theta} = \frac{\partial}{\partial x} (n V_t) = \dot{N}_d = f(n, V_t) \qquad \text{(II-E10)}$$

The nuclei balance can be written as

$$\frac{\partial}{\partial x} (n V_t) - \dot{N}_d = 0 \qquad \text{(II-E11)}$$

Mass Boundary Condition at the Cold Wall

Since no mass passes the cold wall,

$$N_x \Big|_{x=0} = n V_t \Big|_{x=0} = 0 \qquad \text{(II-E12)}$$

Heat Balance

An energy balance in all three regions at the quasi-steady state of heat transfer can be written as

$$q = k_f \frac{dT}{dx} = (k_f' + k_{excess}) \frac{dT}{dx} \qquad \text{(II-E13)}$$

where, k_f' = intrinsic thermal conductivity of frost

k_{excess} = excess thermal conductivity due to water transport.

Heat Boundary Conditions

1. At the frost surface

$$h (T_g - T_s) + K_g (P_g - P_s) \cdot \Delta H = K_f \frac{dT}{dx} \qquad \text{(II-E14)}$$

(note that this is the same as one used in the 'sophisticated' model)

2. At the cold wall

$$T(0) = T_w \qquad \text{(II-E15)}$$

Qualitative Discussion on the Model

Due to the extreme difficulties involved in obtaining the values of $\dot{N}_r$ and $\dot{N}_d$, the mathematical equations derived above are not solved quantitatively in the present thesis. However, in the discussion that follows the new model is evaluated qualitatively to examine whether it can explain the phenomenon of uniform densification of the frost. For the sake of clarity, each region (as shown in Figure II-E1) will be treated separately.

Since the simple model of the frosting process (see Section II-A) has been found to predict the effects of the independent system parameters on the frost properties fairly successfully, the heat and mass boundary conditions at the frost surface in this model are taken to be ident- ical to those in the 'simple model'.

The mathematical formulation of the 'simple model' indicated that the amount of water vapor that diffuses into the frost interior from the frost-gas interface can be well predicted from the following equation.

$$N\big|_{x=\delta} = \frac{D_B}{RT} \frac{(1-\rho_f/\rho_{ice})}{\tau} \frac{\partial P_{vp}}{\partial x}\bigg|_{x=\delta} \tag{II-E16}$$

It should be noted that, since the equilibrium conditions can not exist within the frost, the true mech- anism of water transport past the frost surface could be molecular diffusion under a non-equilibrium partial pressure gradient. Thus, a general equation for the internal diffusion of water vapor at the frost surface can be written as,

$$N\Big|_{x=\delta} = \frac{D_B}{RT} \frac{(1 - \rho_f/\rho_{ice})}{\tau} \frac{\partial p}{\partial x}\Big|_{x=\delta} \simeq \frac{D_B}{RT} \frac{(1 - \rho_f/\rho_{ice})}{\tau} \frac{\partial P_{vp}}{\partial x}\Big|_{x=\delta} \quad \text{(II-E17)}$$

Since nucleation is assumed to be negligible in region 1 (note that this assumption is based on the literature information on nucleation phenomenon as described in Section II-D and Appendix H), the ice crystals in this region will grow by the condensation of water vapor which is transported from the bulk interstitial gas to the crystal surface. At the frost-gas interface equilibrium is assumed to exist between ice and gas. At the interface of regions 1 and 2, on the other hand, nucleation first occurs. Thus, it is obvious that the postulations of the model imply that the deviations from equilibrium would be increased with depth (or distance from the frost surface) in this region. The ice crystals in this region will, thus, grow under non-equilibrium conditions.

The non-equilibrium heat and mass transfer controlled growth of the crystals in the region 1 can be mathematically correlated from the following equation. The details for the derivation of this equation is shown in Appendix J

$$\frac{dm}{d\theta} = \frac{4\pi C (p/P_{vp} - 1)}{\dfrac{\Delta H^2 M}{k_g RT^2} + \dfrac{RT}{D_\theta M P_{vp}}} \quad \text{(II-E18)}$$

$$= \frac{4\pi C (p/P_{vp} - 1)}{f(T)} \quad \text{(II-E19)}$$

All the nomenclatures of Equations II-E18 and II-E19 are described in Appendix R.

Since k_g and D_B decreases with temperature, $f(T)$, in Equation II-E19, would decrease with increase in temperature. The relation between $f(T)$ and temperature is shown in Table II-E1.

Table II-E1

f(T) as a Function of Temperature

T ($^\circ$R)	$f(T)$ ($\frac{ft-hr}{lb_m}$)
460	2.474×10^4
450	4.114×10^4
440	7.069×10^4
430	1.275×10^5
420	2.274×10^5
400	9.066×10^5
360	2.165×10^7

Since, both $(p/P_{vp}-1)$ and $f(T)$ increases with depth from the frost surface, the model visualizes that uniform densification of the frost in region 1 could be achieved by the proper adjustment between water vapor content (partial pressure) and the temperature at every layer such that the ratio of $(p/P_{vp}-1)$ and $f(T)$ remains constant over the entire region.

In order to illustrate the above discussed point more

clearly, a sample calculation was carried out. For a typical set of experimental conditions (Run number 29), a p(x) distribution in region 1 was obtained with the assumption that $(p/P_{vp}-1)/f(T)$ remains constant at all x's (note that f(T)'s at various x's can be calculated from experimentally measured T(x) profile). Table II-E2 shows the calculated p(x) distribution.

Table II-E2

Partial pressure as a function of x

$T(^{o}R)$	$f(T)$ $\left(\dfrac{ft-hr}{lbm}\right)$	Calculated p(x) mm. of Hg.	x (inches)	$P_{vp}(x)$ mm. of Hg.
462	2.12×10^{4}	1.080	0.202	1.080
460	2.474×10^{4}	1.048	0.200	0.984
450	4.114×10^{4}	0.610	0.184	0.569
440	7.0695×10^{4}	0.358	0.173	0.330
430	1.275×10^{5}	0.2115	0.163	0.174
420	2.274×10^{5}	0.134	0.153	0.100

From the values of p(x) distribution shown in Table II-E2, $\dfrac{d\rho_f}{d\theta}$ of the frost slice between x=0.158 inch and x=0.2010 inch is calculated using Equation II-E1 . Thus,

$$\frac{d\rho_f}{d\theta} = \frac{\dfrac{D_B}{RT}\dfrac{(1-\rho_f/\rho_{1ce})}{\tau}\dfrac{\partial p}{\partial x}\Big|_{x=0.201"} - \dfrac{D_B}{RT}\dfrac{(1-\rho_f/\rho_{1ce})}{\tau}\dfrac{\partial p}{\partial x}\Big|_{x=0.158"}}{0.043/12}$$

$$= \frac{0.0629-0.02995}{.043/12}$$

$$= 0.897 \quad \frac{lbm}{hr\ ft^3}$$

The experimentally measured $\frac{d\rho_f}{d\theta}$ under the same conditions of the system has been found to be $0.95\frac{lbm}{hr\ ft^3}$ (see Figure IV-A1). It should be noted that the data shown in Table II-E2 indicate that the value of C in Equation II-E26 for the investigated experimental conditions would be 17 microns. This value is comparable with 20 microns which is calculated from the assumed dimensions of an ice needle.

The above calculations indicate that there exists a p(x) distribution (for a typical set of experimental conditions) which could cause the experimentally measured densification of the frost at every layer in region 1 by the heat and mass transfer controlled growth process. The calculated p(x) distribution indicate that supersaturation ratio (p/P_{vp}) increases as x decreases.

In summary, it can be said that the present model for the frost densification suggests that the uniform densification of the frost in region 1 would be controlled by T(x) and p(x) distributions.

As postulated previously, the transfer of water in region 3 occurs due to thermal diffusion of ice nuclei. The validity of this postulation can be examined as follows.

For typical experimental mass flux of 0.05 lbm/hr ft^2, assuming nucleus diameter of 50°A (see Appendix H) and taking the value of thermal diffusive velocity of 93.10 ft/hr from Brock's equation (see Section II-E-1) at temperature of -135°F, the nuclei concentration required for the mass flux of 0.05 lbm/hr ft^2 would be,

$$n' = \frac{N_x}{V \times \rho_{ice} \times \frac{4}{3}\pi r_p^3} = \frac{0.05 \times 454}{93.10 \times 6 \times 10^{-20}} = 4.07 \times 10^{18} \frac{molecules}{cu. ft.}$$

$$= 1.432 \times 10^{14} \frac{Molecules}{cc.}$$

If it is assumed that the residence time for these nuclei is 10^{-3} secs. (note that there is no basic ground for this assumption except that it might give a conservative value for nucleation rate), then $\dot{N}_r$ required for this much nuclei concentration at all time would be 1.432×10^{17} molecules/cc. sec.

If homogeneous nucleation is a predominant mechanism for nuclei generation (it should be noted that this is the worst kind of nucleation mechanism), then partial pressure required for the $\dot{N}_r = 1.432 \times 10^{17} \frac{molecules}{cc. sec.}$ at temperature od $-135^\circ F$ would be $250 \times .00001 = .0025$ mm. Hg. (from Figure H-4).

The partial pressure at the frost surface typically varies between 1 to 3 mm. of Hg. Thus, the magnitude of partial pressure at the temperature level of $-135^\circ F$ compared to one at the frost surface indicate that the postulation that mass flux in region 3 occurs by thermal diffusion of ice nuclei appears physically realistic.

At every layer in region 3 some nuclei are expected to be impinged (or trapped) in the existing structure. Thus, mathematically, frost densification process can be defined by the following equation.

$$\frac{d\rho_f}{d\theta} = \frac{\partial}{\partial x}(n V_t) \qquad (II-E20)$$

There are three possible forces that could cause the movement of ice nuclei in the colder region. They are thermal, gravitational and the force due to electrostatic charges on the ice nuclei. The reasons for possible development of electrostatic charges on the ice nuclei are, at present, unknown and hence in the present thesis possible force due to electrostatic charge is neglected. The preliminary calculations indicated that thermal force is considerably higher than gravitational force on the ice nuclei. Thus, the movement of ice nuclei mainly occurs by thermal force. As shown in Section II-E-1, the thermal diffusive velocity has been found to be an approximate function of only the temperature gradient in the frost interior. In fact, the following approximate correlation for thermal diffusive velocity in the frost interior was obtained from Brock's equation (see Section II-E-1)

$$V_t = \alpha \frac{dT}{dx} \qquad\qquad (II-E21)$$

where α = constant.

Since it has been found experimentally that $\frac{dT}{dx}$ increases with depth from the frost surface, V_t would be increased with depth. Since the ice crystals in region 3 grow by impingement (or trapping) of ice nuclei on the existing crystals, nuclei concentration or water content has to decrease with increase in depth from the frost surface. Thus, n decreases and V_t increases with depth from the frost surface.

The ice crystals in region $\underline{3}$ grow by the impingement
(or trapping) of nuclei on the crystal network as they
move towards the cold wall. This is an analogous
situation to one in which a bunch of ping pong balls are
thrown through a network. At every point (along its
depth), the ping pong balls may or may not collide or get
trapped in the network. It can be easily visualized that
the probability for the ping pong balls to collide on solid
wall in the network would be higher at higher concentration
of balls and higher velocity. Similarly, the rate of
collision (or trapping) of ice nuclei on the ice crystals
is expected to be higher at higher nuclei concentration
and the thermal diffusive velocity. Thus, in general,
the rate of depletion of ice nuclei from the bulk interstitial
gas would be proportional to n, V_t and 'a'. Where 'a'. is
the effective surface area to volume ratio for the collision.
For constant 'a', $\dot{N}_d$ would be an increasing function of n
and V_t.

It is an extremely difficult task to obtain an accurate
quantitative relation between $\dot{N}_d$, n and V_t. However, from
the qualitative description shown above, it can be predicted
that the crystal growth by nuclei impingement in region $\underline{3}$
would be constant at each layer because continuous increase
in V_t but decrease in n with increase in depth.

In summary, it can be said that the model visualizes
that water content and temperature distribution would govern
the uniform densification of the frost in region $\underline{3}$.

The evaluation of frost densification process in region 2 is quite difficult.   The frost in this region will densify by both vapor condensation as well as by impingement of ice nuclei on the existing crystal.   Since, region 2 is the transition between regions 1 and 3 and since regions 1 and 3 are expected to densify uniformly, it is more than likely that region 2 would also densify uniformly. It should be noted that physically, region 2 is one in which particle impingement takes over the control for frost densification from the process of vapor condensation.

II-E-1 Determination of a Correlation for Thermal Diffusive Velocity in the Frost Interior

As discussed in Appendix K, there are two significant correlations for evaluation of thermal force exerted on an aerosol particle in slip region ($\lambda/r_p < 1.0$, where λ, mean free path and r_p, radius of the particle).   Epstein (95) initially derived a correlation for thermal force by a simple treatment of the process of thermal diffusion.   The predictions of the thermal force from Epstein equation, however, found to agree well with the experimental facts only for solid particles with low thermal conductivity (10^{-4} cal/gm. cm. $^{\circ}F$).   For the particle of large thermal conductivity, Epstein equation has been found to predict much lower value of thermal force than the actual (experimental) one.   This is because the thermal conductivity of solid has been believed to give undue importance in the correlation

for thermal force. It should be noted that the thermal conductivity of ice is approximately 10^{-2} cal/gm. cm$^{\circ}$C at low temperatures. Also thermal conductivity of ice increases with decrease in temperature. Thus, it is expected that Epstein equation would predict low thermal force on ice nuclei than the actual ones.

Realizing the shortsomings of the Epstein equation, Brock (15) carried out more rigorous first order slip flow continum analysis of the thermal diffusion process. Brock's correlation for the thermal force has been found to predict the values of thermal forces well in agreement with the experimental facts for all the values of thermal conductivity of solid particles. The value of λ/r_p, however, has been found to affect the validity of Brock's equation. It is found to be accurate for $\lambda/r_p < 0.25$, but only approximately valid for $\lambda/r_p > 0.25$. For $\lambda/r_p > 0.25$, Brock's equation has been found to predict thermal force as low as 50 to 100% of experimental ones. For the present purpose, since λ/r_p is as high as 0.50 at high temperature, it is expected that the values of thermal force at high temperatures calculated by Brock's equation could be as low as 30 to 50% of experimental ones.

In this short section, the thermal diffusive force and the valocity for an ice nuclei (of 25°A radius) in the frost interior are calculated using both Epstein's and Brock's theoretical analysis. The required temperature gradients at various points were obtained from a typical

T(x) (experimental) profile in the frost interior. The
results of these calculations are shown in Table II-E3.
The equations used for the calculations are shown below.

<u>Epstein equation (95)</u>

A. <u>Thermal Force</u>

$$F_t = -9\pi r_p \left(\frac{\eta^2}{\rho T}\right) \left(\frac{K_f}{2K_f + K_{ice}}\right) \left(\frac{dT}{dx}\right) \qquad \text{(II-E22)}$$

B. <u>Thermal Diffusive Velocity</u>

$$V_t = \frac{3}{2}\left(1 + \frac{0.82 \times 10^{-5}}{r_p}\right) \left(\frac{K_f}{2K_f + K_{ice}}\right) \left(\frac{\eta}{\rho T}\right) \left(\frac{dT}{dx}\right) \qquad \text{(II-E23)}$$

<u>Brock equation (15)</u>

A. <u>Thermal Force</u>

$$F_t = 9\pi \frac{\eta^2}{\rho T} r_p^2 \left(\frac{1}{1 + 6\frac{\lambda}{r_p}}\right) \left(\frac{\frac{R_f}{R_{ice}} + \frac{15}{4}\frac{\lambda}{r_p}}{1 + \frac{2R_f}{R_{ice}} + \frac{15}{2}\frac{\lambda}{r_p}}\right) \left(\frac{dT}{dX}\right) \qquad \text{(II-E24)}$$

B. <u>Thermal Diffusive Velocity</u>

$$V_t = \frac{3}{2}\left(\frac{\eta}{\rho T}\right) \left(\frac{1}{1 + 6\frac{\lambda}{r_p}}\right) \left(1 + \frac{0.82 \times 10^{-5}}{r_p}\right) \left(\frac{\frac{R_f}{R_{ice}} + \frac{15}{4}\frac{\lambda}{r_p}}{1 + \frac{2R_f}{R_{ice}} + \frac{15}{2}\frac{\lambda}{r_p}}\right) \left(\frac{dT}{dx}\right) \qquad \text{(II-E25)}$$

where,

$$\eta = 0.499\,\bar{v}\,\rho\,\lambda \qquad \text{(II-E26)}$$

All the nomenclature in Equation II-E22 to II-E26 are
described in Appendix R.

From the results of Table II-E3, it can be seen that
Epstein equation predicts that velocity due to thermal
force would decrease (more sharply near the cold wall) with
decrease in the temperature in the frost interior.   As seen
previously, however, these predictions may be erroneous due

to high thermal conductivity values of ice at low temp-
eratures.   Brock's equation, on the other hand, predicted
that thermal diffusive velocity would be increased with
depth in the frost interior and would be approximately
proportional to the prevailing temperature gradient.   Since
Brock's equation has been found to predict thermal force
and thermal diffusive velocity well in agreement with the
experimental results of many other materials (whose thermal
conductivities are in the range of those of ice), its
predictions are taken to be more valid that the predictions
of Epstein's equations, for the present purpose.   Thus, in
summary, it is concluded that the thermal diffusive valocity
in the frost interior would be increased with depth from the
frost surface and would approximately vary as dT/dx.

Table II-Al

Correlation between Heat Transfer Coefficient and Time
for the Formation of a Smooth Layer of Frost

Heat Transfer Coefficient $(Btu/ hr\ ft^2\ {}^oF)$ h	Time to Form Smooth Layer of Frost (minutes) t
5.62	39
7.25	28
11.08	13

The above data fits the equation

for $h \geq 13$ Btu/hr ft^2 ^oF

$$t = (13 - h)/0.19$$

and,

for $h \leq 13$ Btu/hr ft^2 ^oF

$$t = 0$$

Table II-A2

Effect of Negative Time Increment on the Computer Solution
of 'Simple Model'

System Conditions: Reynolds number = 9,300
Humidity = dew point at 29.3°F
Gas temperature = 70°F
Wall temperature = -315°F

Time (minutes)	Frost Surface Temperature (°F)	Frost Density (gms./cc.)	Frost Thickness (inches)
75	13.0940	0.0685	0.176040
73	13.1736	0.066947	0.174092
71	13.2842	0.0653462	0.172198
69	13.4285	0.0636945	0.170376
67	13.6125	0.0619888	0.168644
65	13.8435	0.0602257	0.167026
63	14.1311	0.0584016	0.165553
61	14.4841	0.0565129	0.164264
59	14.9148	0.0545561	0.163205
57	15.4368	0.0525278	0.162438
55	16.0664	0.0504250	0.162040
53	16.8213	0.0482455	0.162112
51	17.7209	0.0459885	0.162783
49	18.7844	0.0436556	0.164221
47	20.0300	0.0412520	0.166645
45	21.4702	0.0387878	0.170335
43	23.1089	0.0362807	0.175652
41	24.9333	0.0337574	0.183044
39	26.9109	0.0312549	0.193055
37	28.9849	0.0288208	0.206309
35	31.0806	0.0265090	0.223467
33	33.1125	0.0243726	0.245158
31	35.0054	0.0224546	0.271883
29	36.7048	0.0207798	0.303928
27	38.1838	0.0193517	0.341332

Table II-C1

Calculated Distribution of Supersaturation Ratio within

the Frost

X (inches) distance from cold wall	P(mm Hg) partial pressure of water vapor	P_{vp} (mm Hg) Vapor pressure of water vapor	P/P_{vp}
0	0	0	1
0.01	0.0711	3.59×10^{-35}	1.980×10^{33}
0.02	0.2630	3.98×10^{-25}	6.610×10^{23}
0.04	0.8275	7.14×10^{-7}	1.115×10^{6}
0.06	1.558	0.0001	15,580
0.08	2.515	0.00134	1,872
0.10	3.670	0.00350	1,045
0.12	5.000	0.043	116.20
0.14	6.500	0.130	50.0
0.16	8.1400	0.364	22.35
0.18	9.930	0.870	11.40
0.20	11.850	1.750	6.775
0.22	13.900	3.10	4.49

Table II-D1

Comparison Between Molecular and Thermal Diffusion

in the Frost Interior

Temperature ($^\circ$F)	dc_w/dT	$\frac{0.180}{T} c_w c_A$
+20	1.70×10^{-4}	$.0131 \times 10^{-4}$
-80	7.65×10^{-7}	$.0352 \times 10^{-7}$
-145	2.27×10^{-9}	$.0138 \times 10^{-9}$
-215	2.61×10^{-12}	$.0199 \times 10^{-12}$
-300	6.98×10^{-16}	$.0742 \times 10^{-16}$

$\frac{dc_w}{dT}$ = Term proportional to the driving force gradient
for ordinary molecular diffusion

$\frac{0.180}{T} c_w c_A$ = Term proportional to the driving force
gradient for thermal diffusion.

Table II-E3
Thermal Force and Velocity at various Positions in the Frost
Interior Calculated from Epstein(95) and Brock(15) Equations

Temp. (°F)	Position from Cold Wall (inches)	$\dfrac{(F_t)_E}{(\frac{dT}{dx})}$	$\dfrac{(F_t)_B}{(\frac{dT}{dx})}$	$(\frac{dT}{dx})$ (°R/ft)	$\dfrac{(V_t)_E}{(\frac{dT}{dx})}$ (ft²°R hr)	$\dfrac{(V_t)_B}{\frac{dT}{dx}}$ (ft²°R hr)	$(V_t)_E$ (ft/hr)	$(V_t)_B$ (ft/hr)
-270	0.01	9.35×10^{-14}	$.948 \times 10^{-11}$	5.0×10^{4}	3.35×10^{-5}	3.40×10^{-3}	1.673	170.0
-214	0.025	2.76×10^{-13}	1.29×10^{-11}	4.02×10^{4}	8.12×10^{-5}	3.78×10^{-3}	3.260	152.0
-135	0.055	8.10×10^{-12}	1.711×10^{-11}	2.315×10^{4}	1.90×10^{-4}	4.03×10^{-3}	4.395	93.10
-80	0.095	1.326×10^{-12}	1.92×10^{-11}	1.585×10^{4}	2.72×10^{-4}	4.035×10^{-3}	4.310	64.0
-30	0.145	1.999×10^{-12}	2.082×10^{-11}	1.098×10^{4}	3.847×10^{-4}	4.01×10^{-3}	4.220	43.9

Heat Transfer Coefficient = h
Mass Transfer Coefficient = K_g

Direction of Heat and
Mass Transfer

Reynolds Number = Re
Gas Temperature = T_g
Humidity = p_g

Gas Flow

$J_{total} = K_g (p_g - p_s)$

(T_g, p_g)

Frost Surface
(Temp. = T_s)

(T_s, p_s)

Frost   Layer $J_s = \frac{D_e}{RT} \frac{(1 - \rho_f/\rho_{ice})}{\tau} \frac{\partial p_f}{\partial x}\Big|_{x=\delta}$ Thermal Boundary Layer

Temperature Profile

Cold Wall (Temp.
= T_w)

(T_w, p_w)

Total Driving Force for Heat Transfer in the Frost
Interior

Driving Force for Heat
and Mass Transfer in the
Gas Phase

Figure II-A0   Schematic of Frosting Process as Visualized by
'Simple Model'
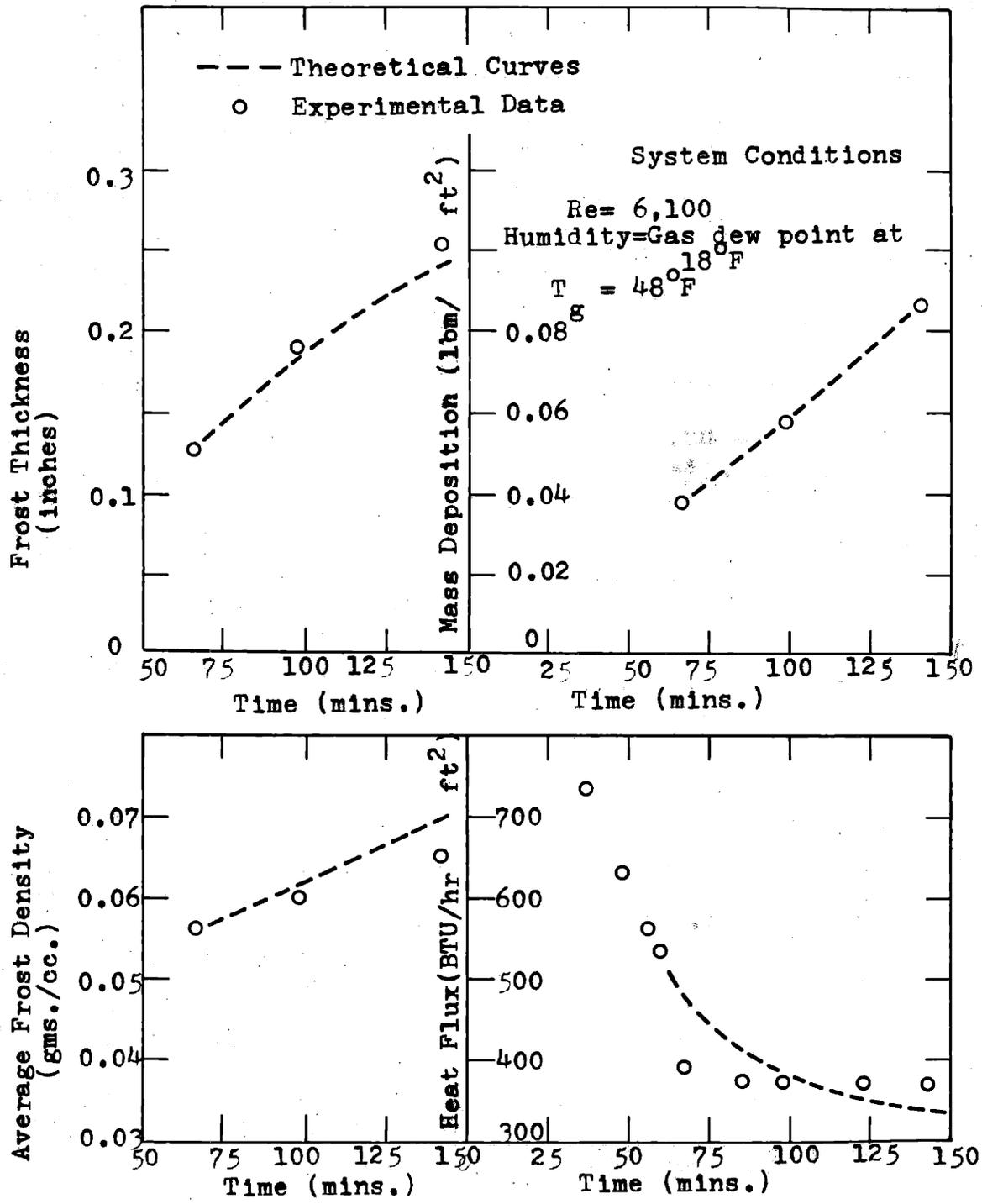
Figure II-Al   Comparison between Experimental
Facts and Theoretical Predictions
of 'Simple Model'
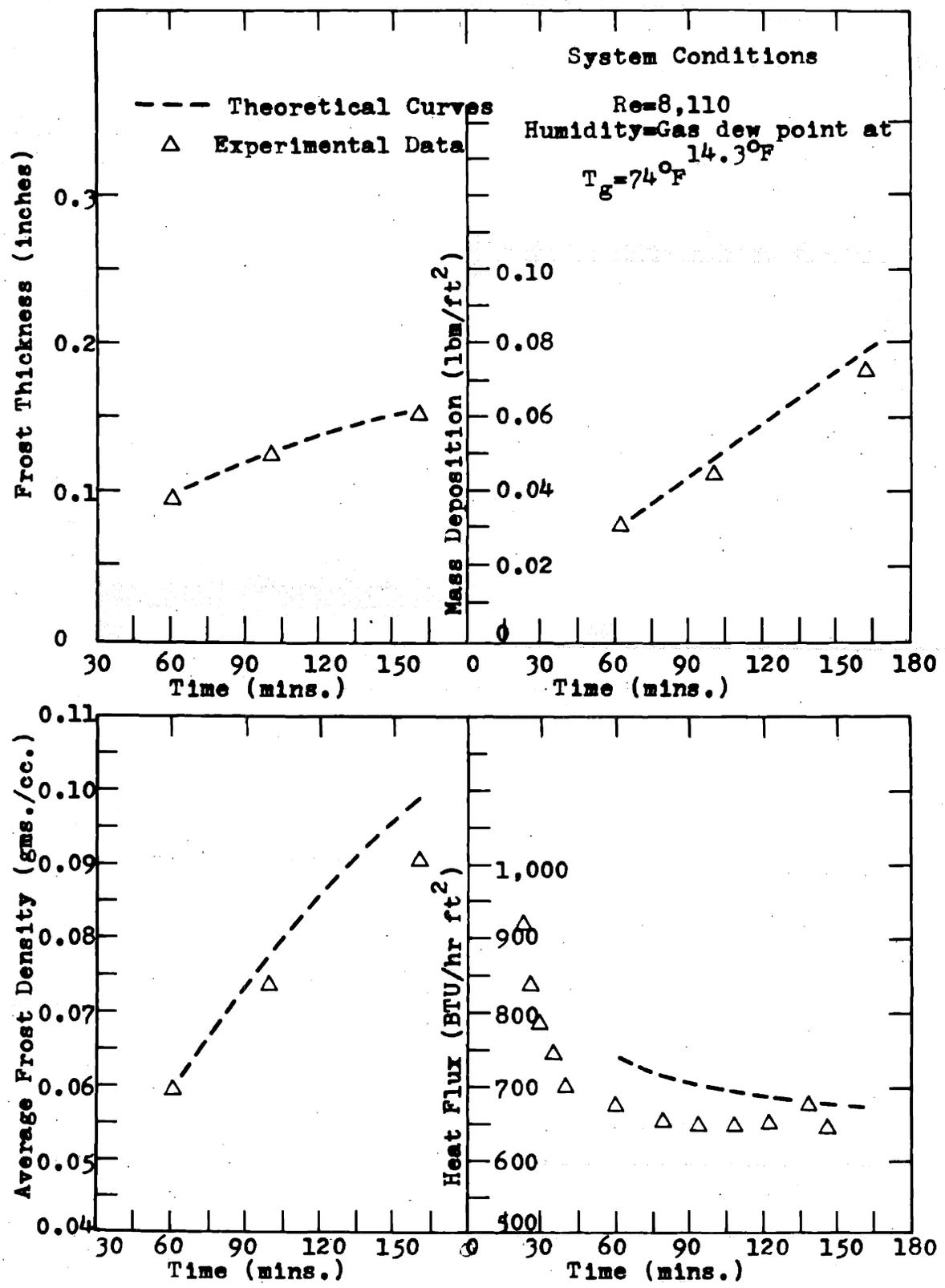
Figure II-A2   Comparison between Experimental Facts and
Theoretical Predictions of 'Simple Model'
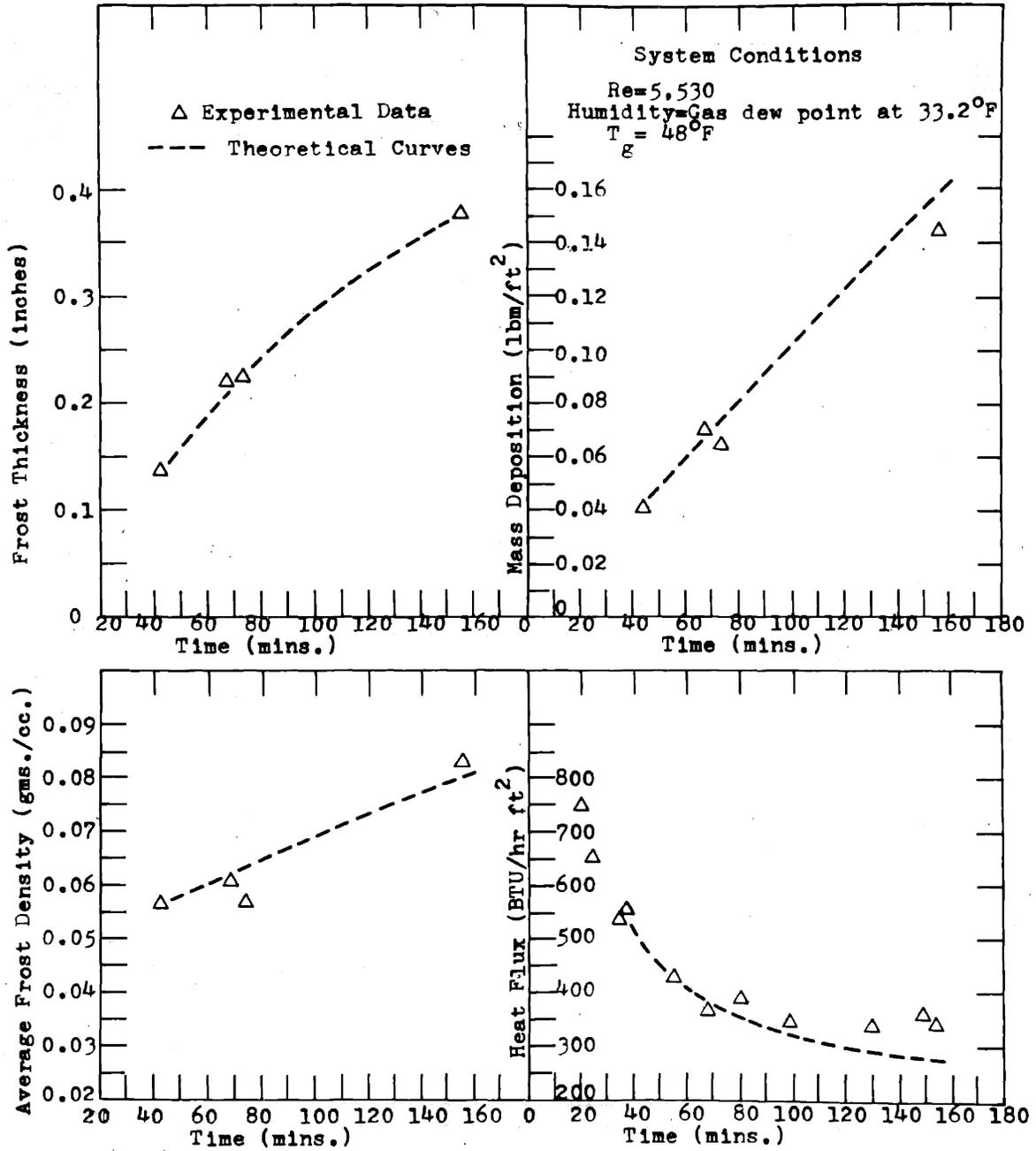
Figure II-A3   Comparison between Experimental Facts and
                Theoretical Predictions of 'Simple Model'
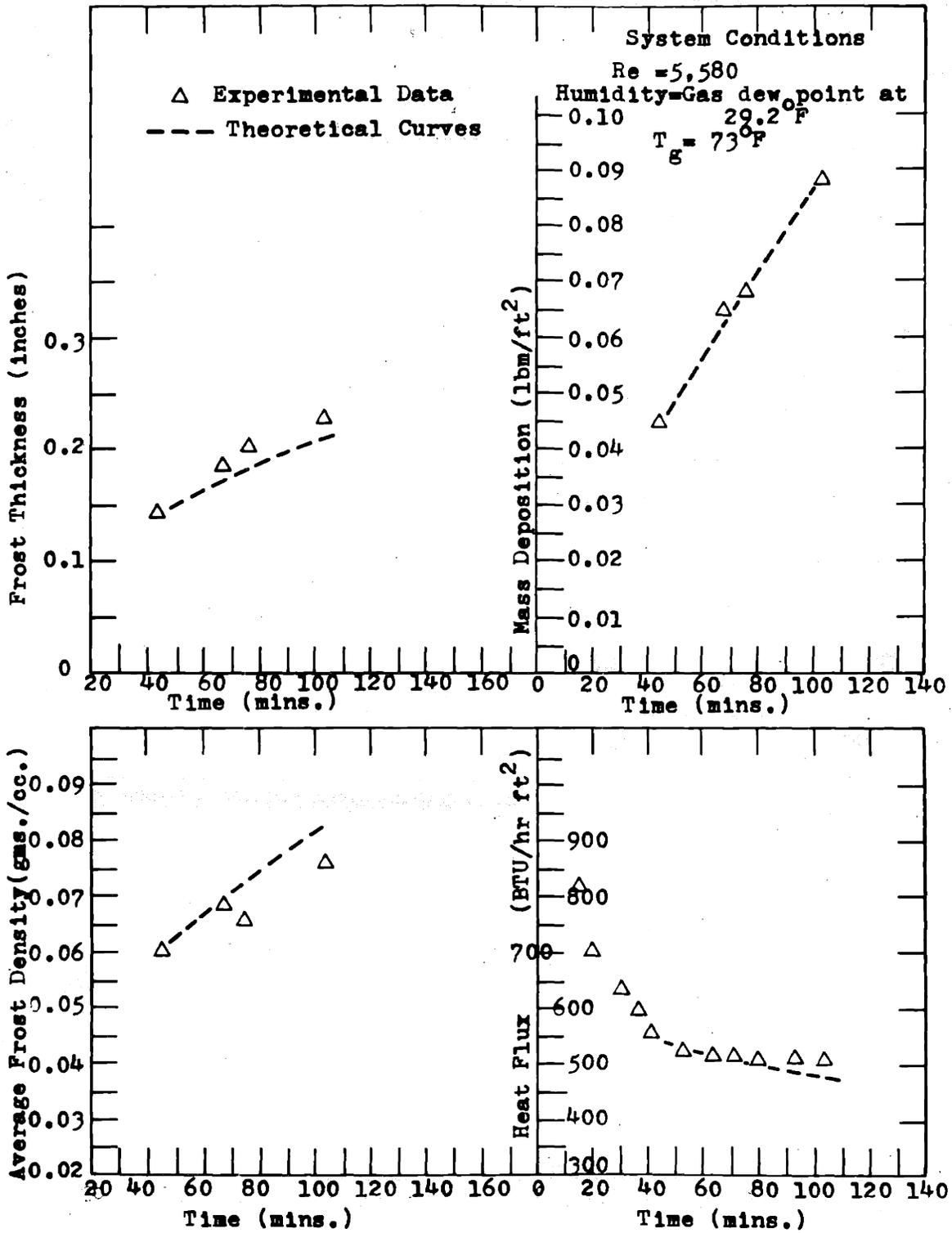
Figure II-A4   Comparison between Experimental Facts and
Theoretical Predictions of 'Simple Model'
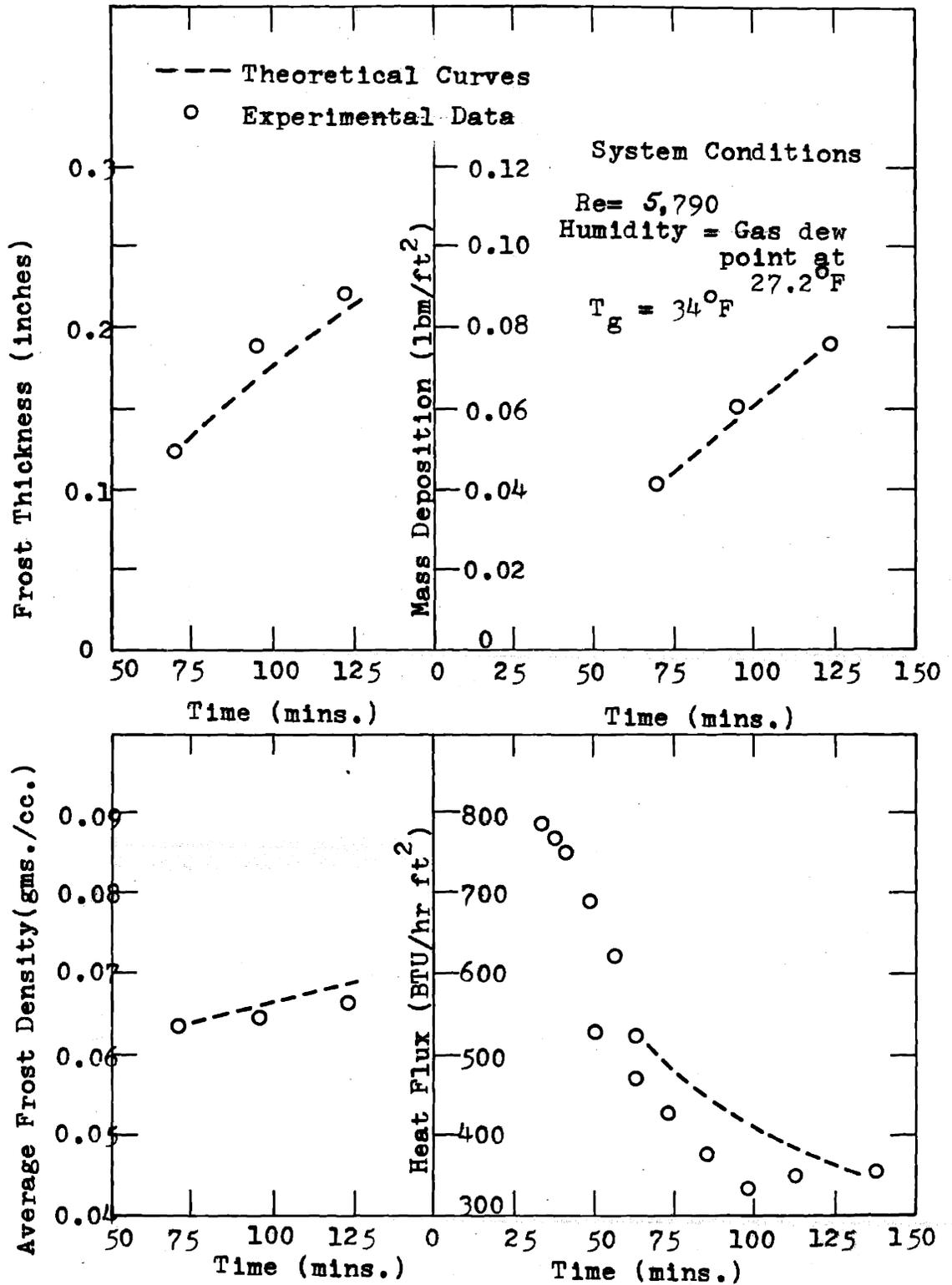
Figure II-A5   Comparison between Experimental
Facts and Theoretical Predictions
of 'Simple Model'
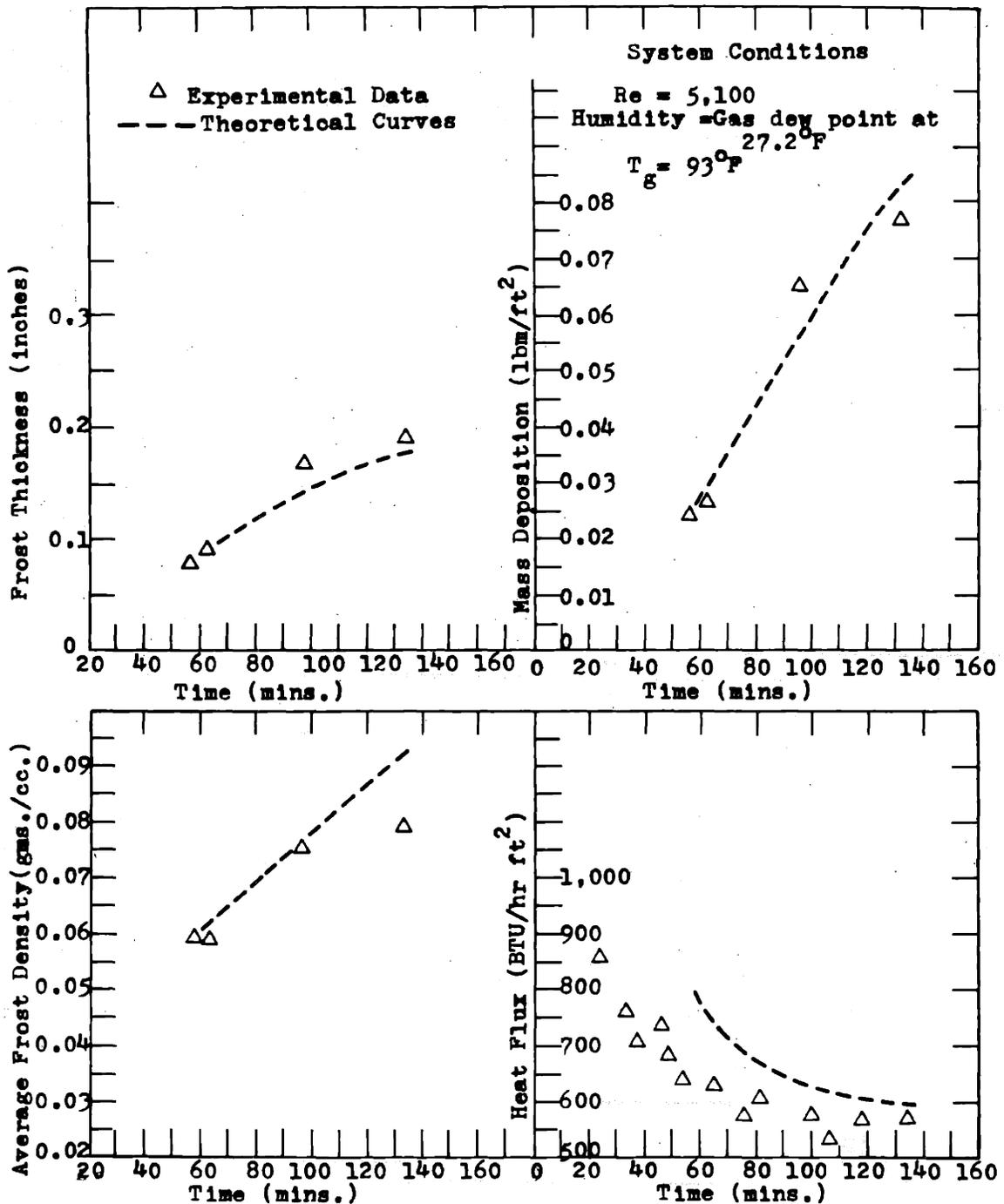
Figure II-A6   Comparison between Experimental Facts and
Theoretical Predictions of 'Simple Model'
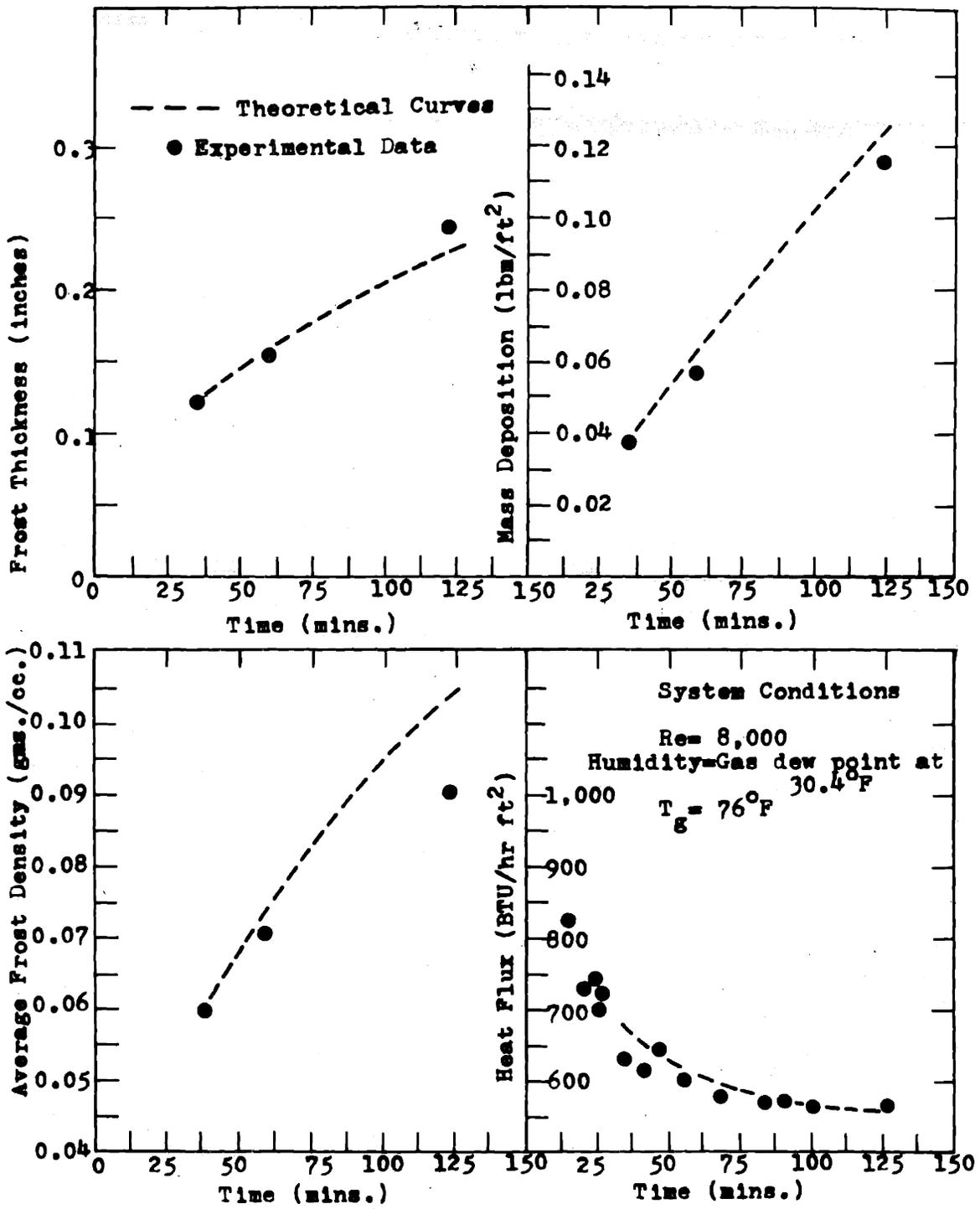
Figure II-A7   Comparison between Experimental Facts and
Theoretical Predictions of 'Simple Model'
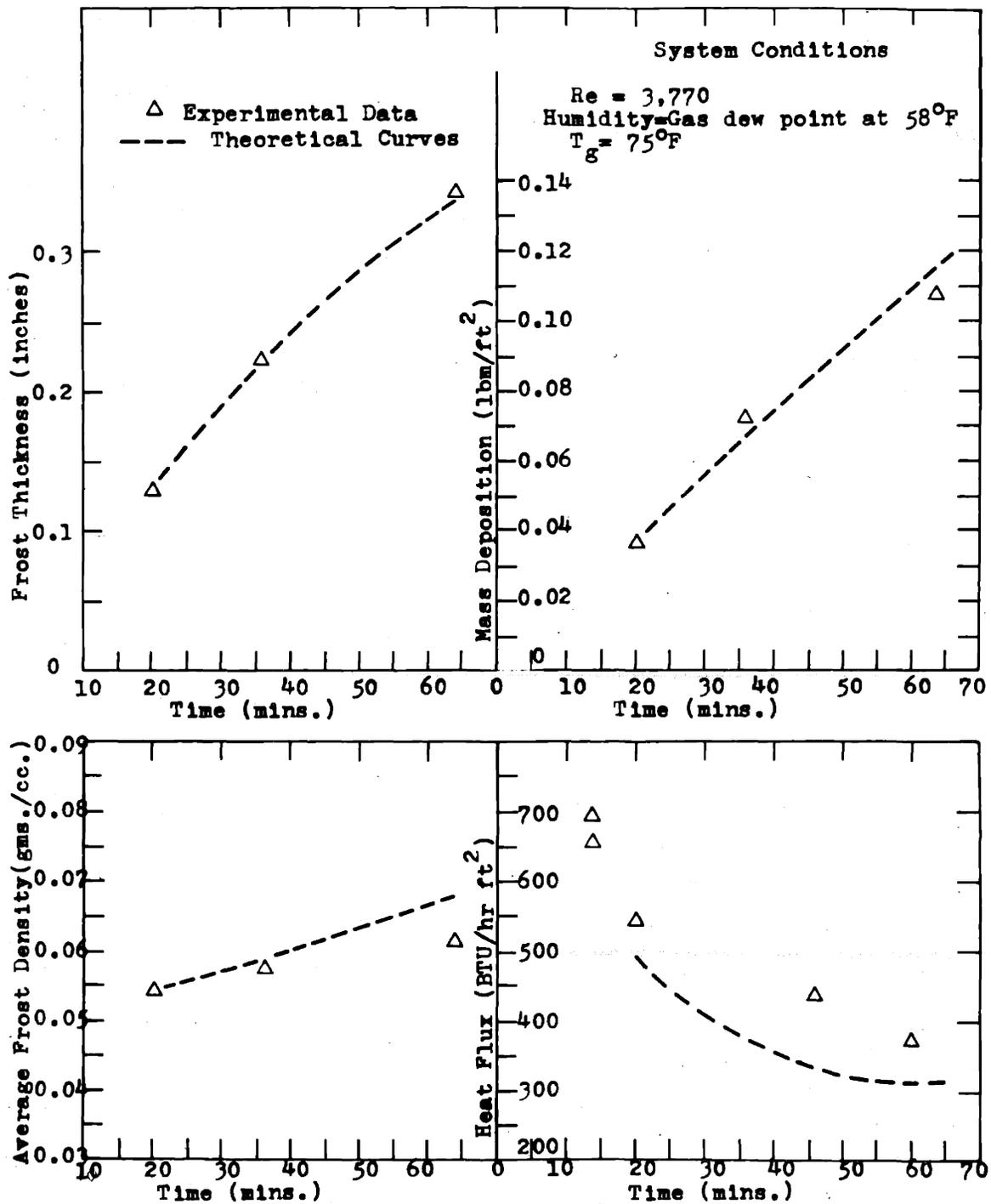
Figure II-A8   Comparison between Experimental Facts and
Theoretical Predictions of 'Simple Model'
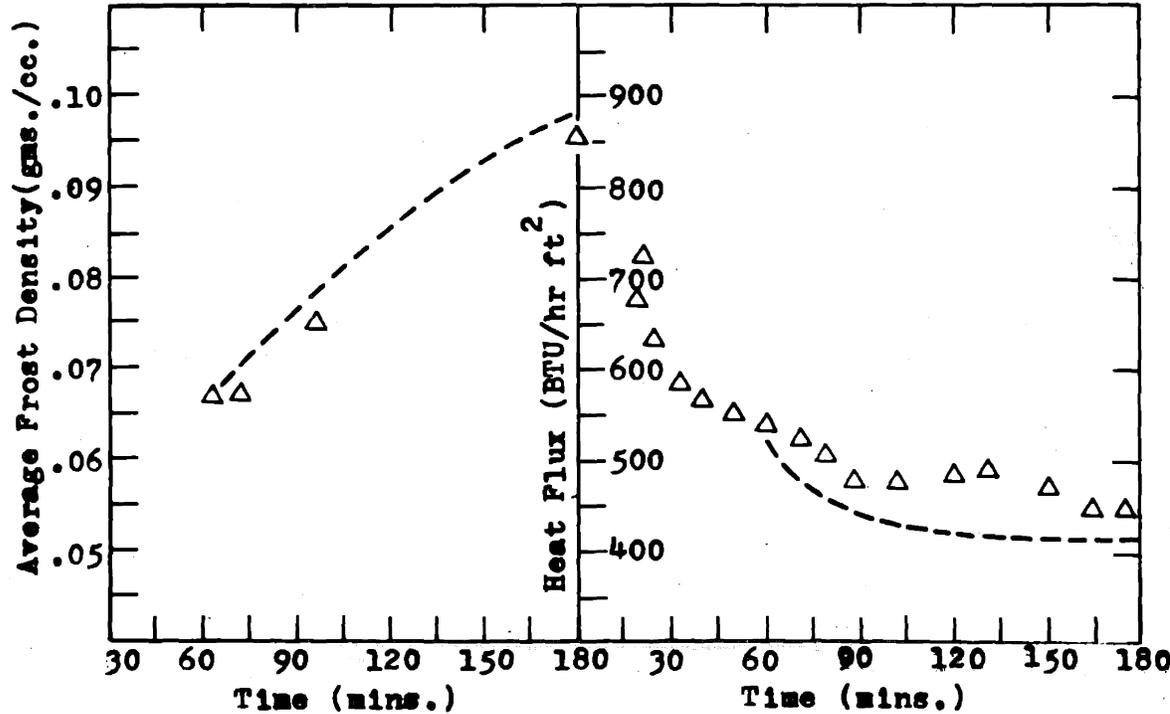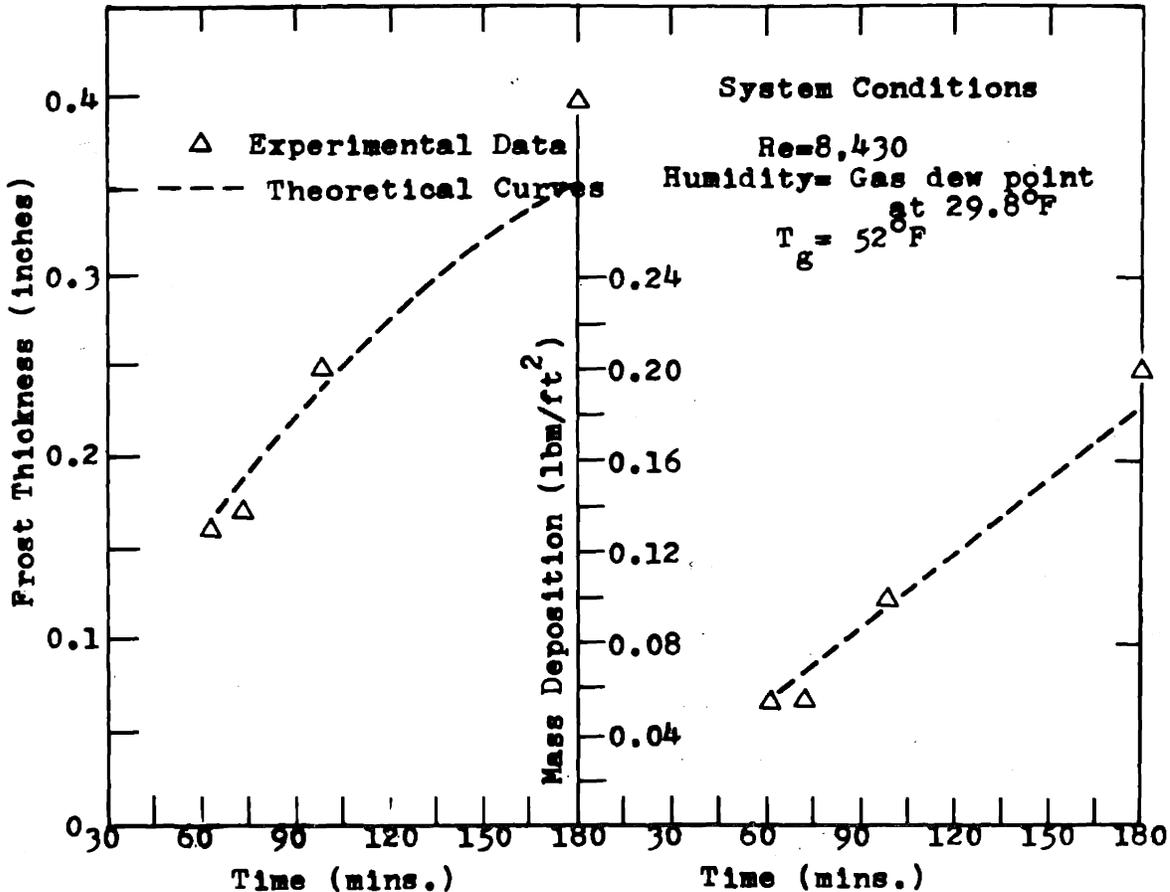
Figure II-A9   Comparison between Experimental Facts and
               Theoretical Predictions of 'Simple Model'
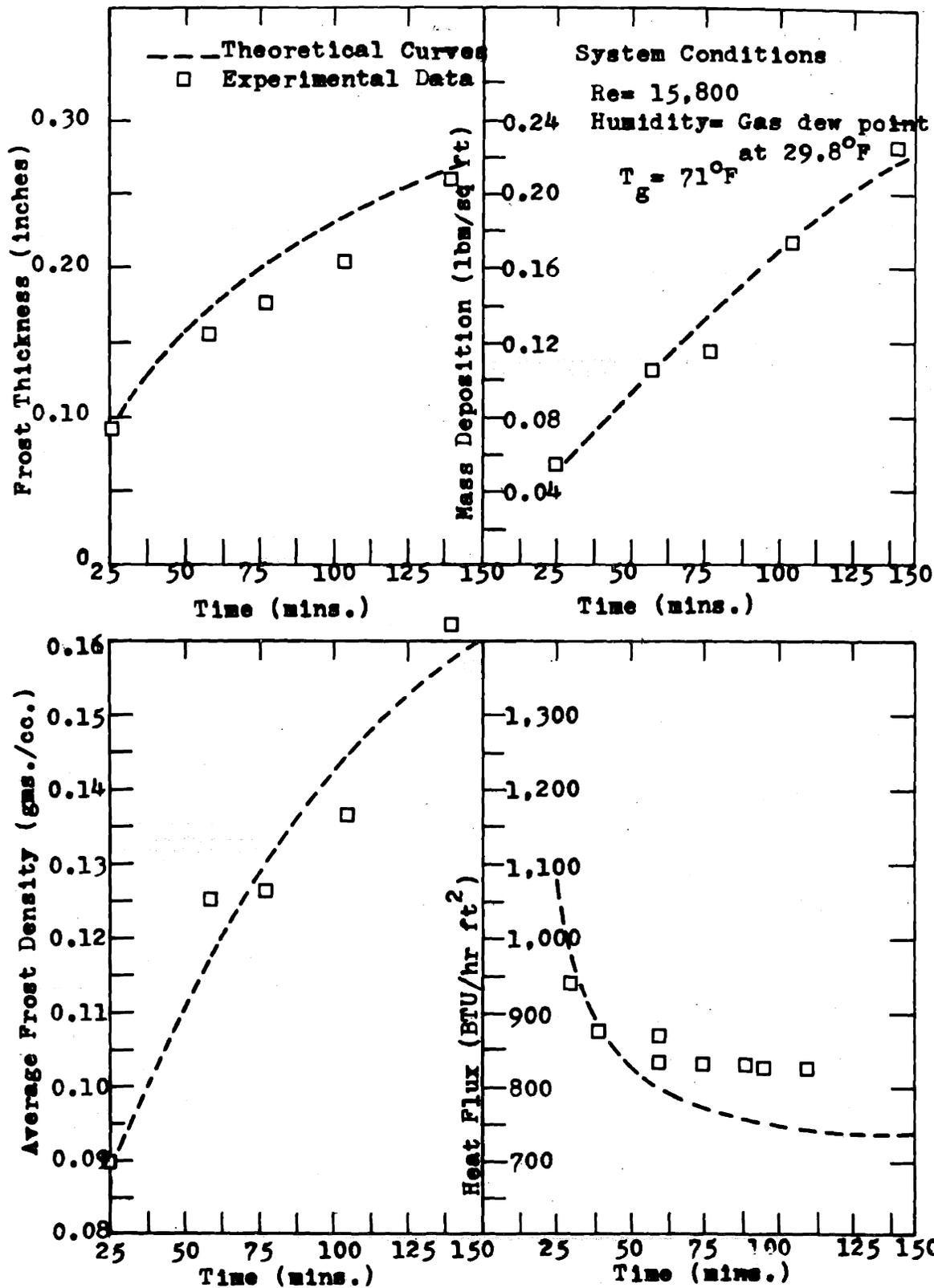
Figuer II-A10 Comparison between Experimental Facts and
Theoretical Predictions of 'Simple Model'

Figure II-A11

Experimental Conditions

△ Re=14,500; Humidity=Gas dew point at 29°F; T_g = 70°F

◯ Re=5,600; Humidity=Gas dew point at 29.2°F; T_g= 70°F

○ Re=9,300; Humidity=Gas dew point at 29.2°F; T_g= 70°F

● Re=9,300; Humidity=Gas dew point at 40°F; T_g= 70°F

⬢ Re=5,600; Humidity=Gas dew point at 40°F; T_g= 70°F

▲ Re=14,500; Humidity=Gas dew point at 40°F; T_g= 70°F

— — — Computer Results of 'Simple Model'
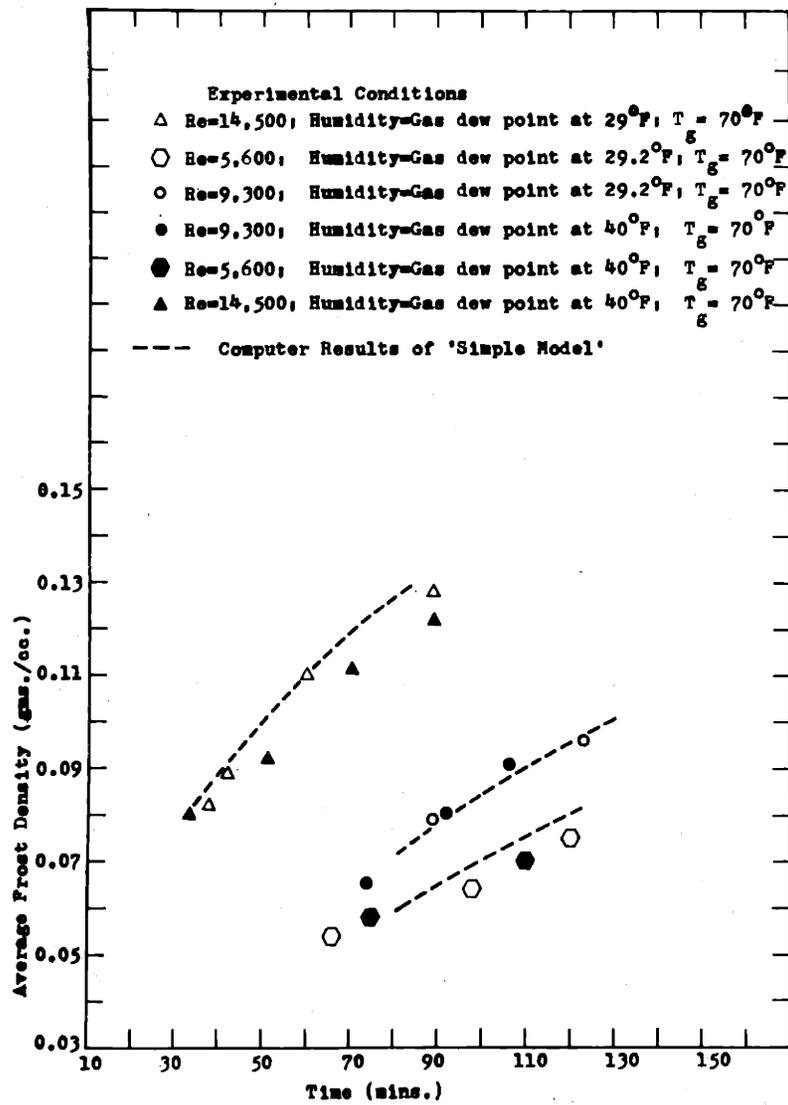
Figure II-A11   Comparison Between 'Simple Model' Predictions
and Experimental Data of Brazinsky (14)

Figure II-A12

— — — Predictions of 'simple model'
Experimental Data

△ Re=14,500; Humidity=Gas dew point at 40°F; T_g= 70°F

□ Re=5,600; Humidity= Gas dew point at 29.2°F; T_g= 70°F

○ Re=9,300; Humidity=Gas dew point at 29.2°F; T_g= 70°F
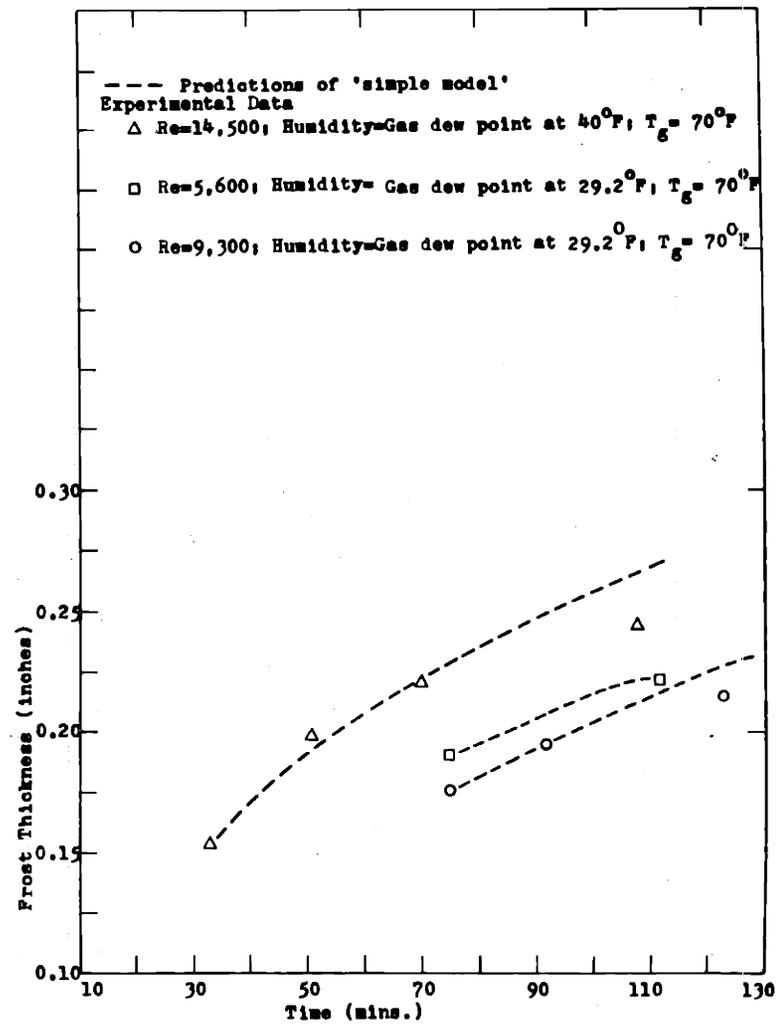
Figure II-A12   Comparison between Predictions of 'Simple
Model' and Experimental Data of Brazinsky (14)

Figure II-A13

Effect of Initial Values of Average Frost Density
and Frost Thickness on the Predictions of
'Simple Model'

Figure II-A14

Effect of Starting Values on the 'Simple
Model' Predictions for Time Variation in
Average Frost Density and Frost Thickness
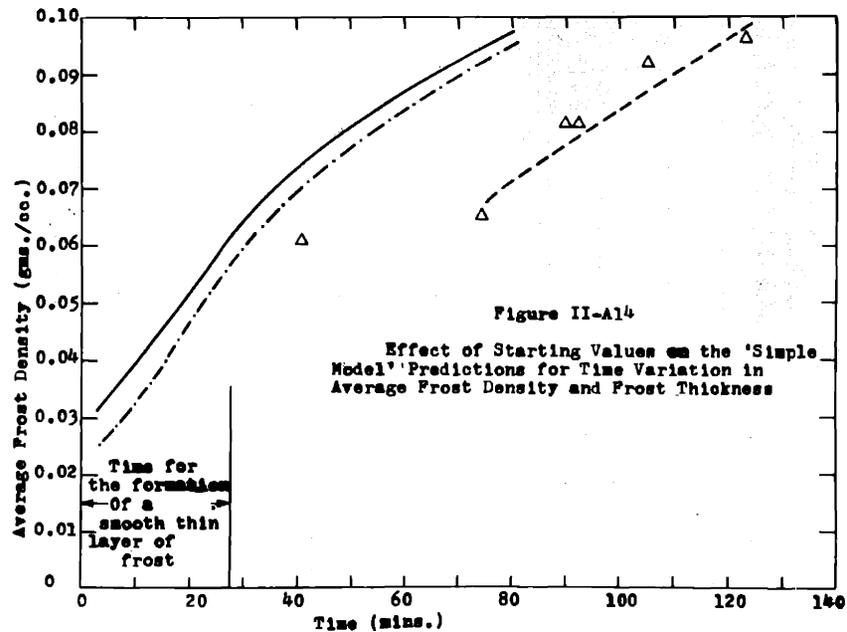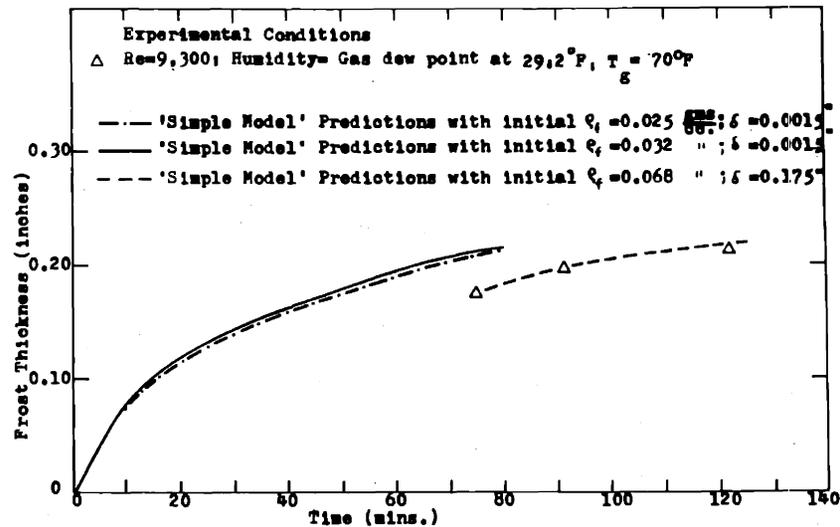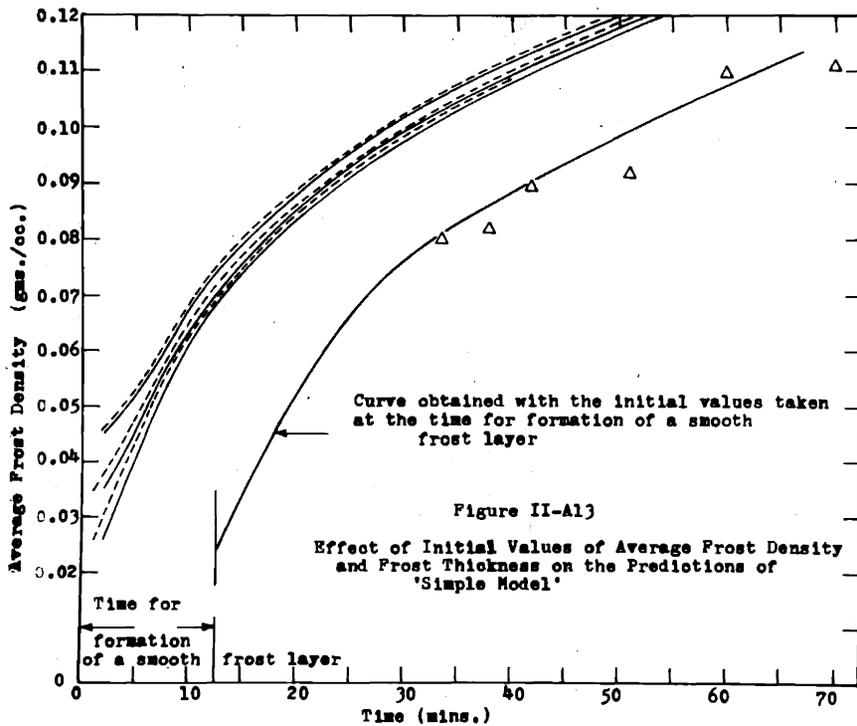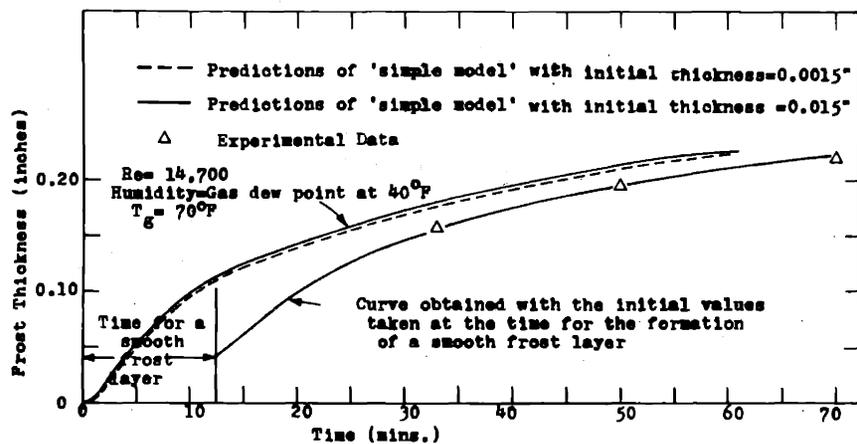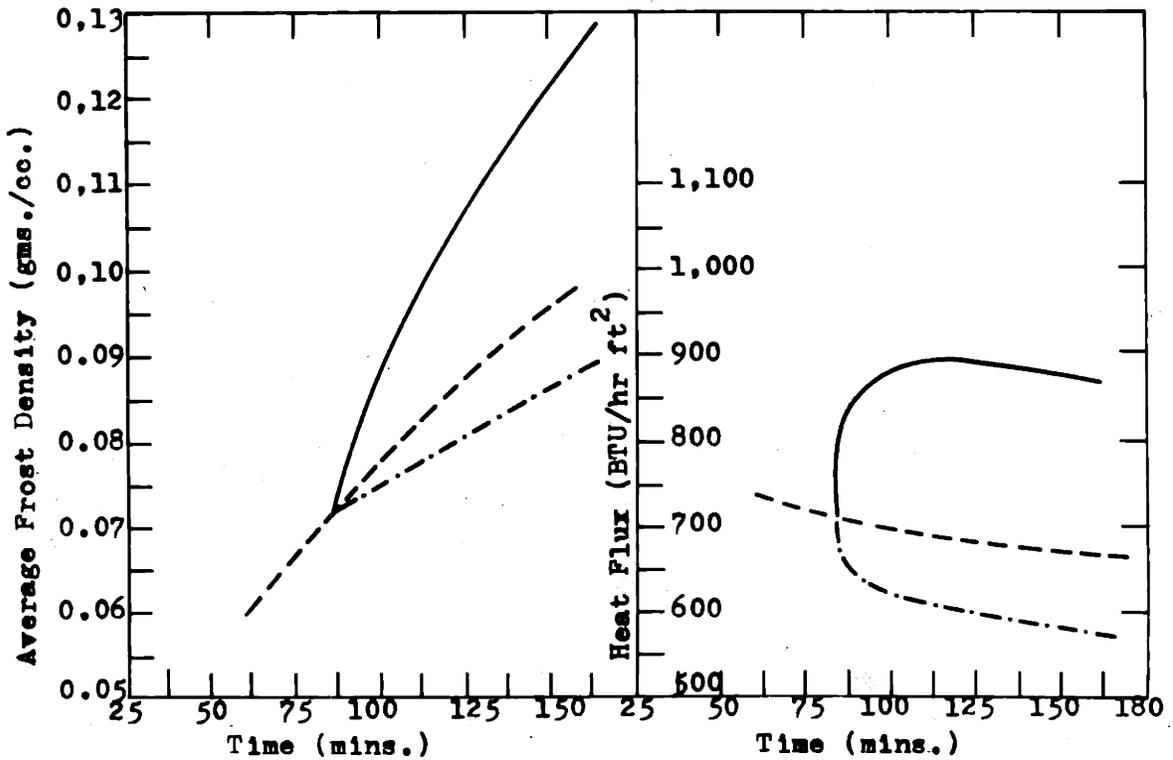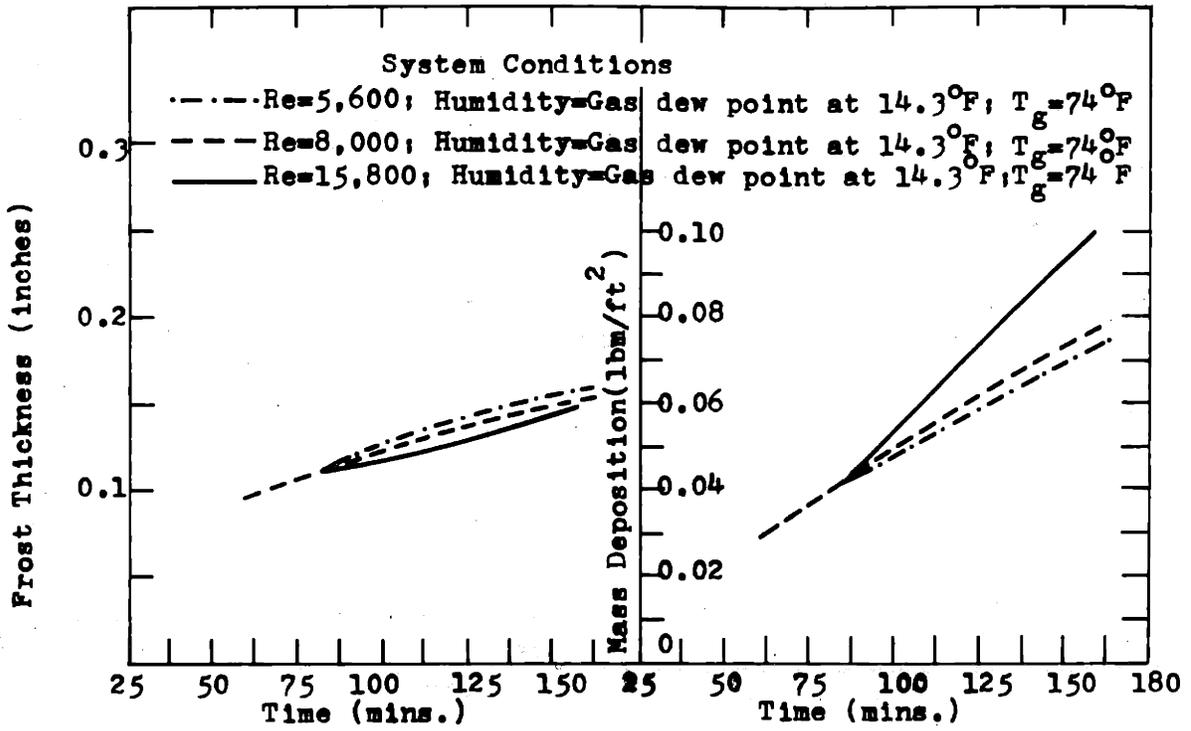
Figure II-A15   'Simple Model' Predictions for Effect of a Step Change in Reynolds Number on Frost Properties
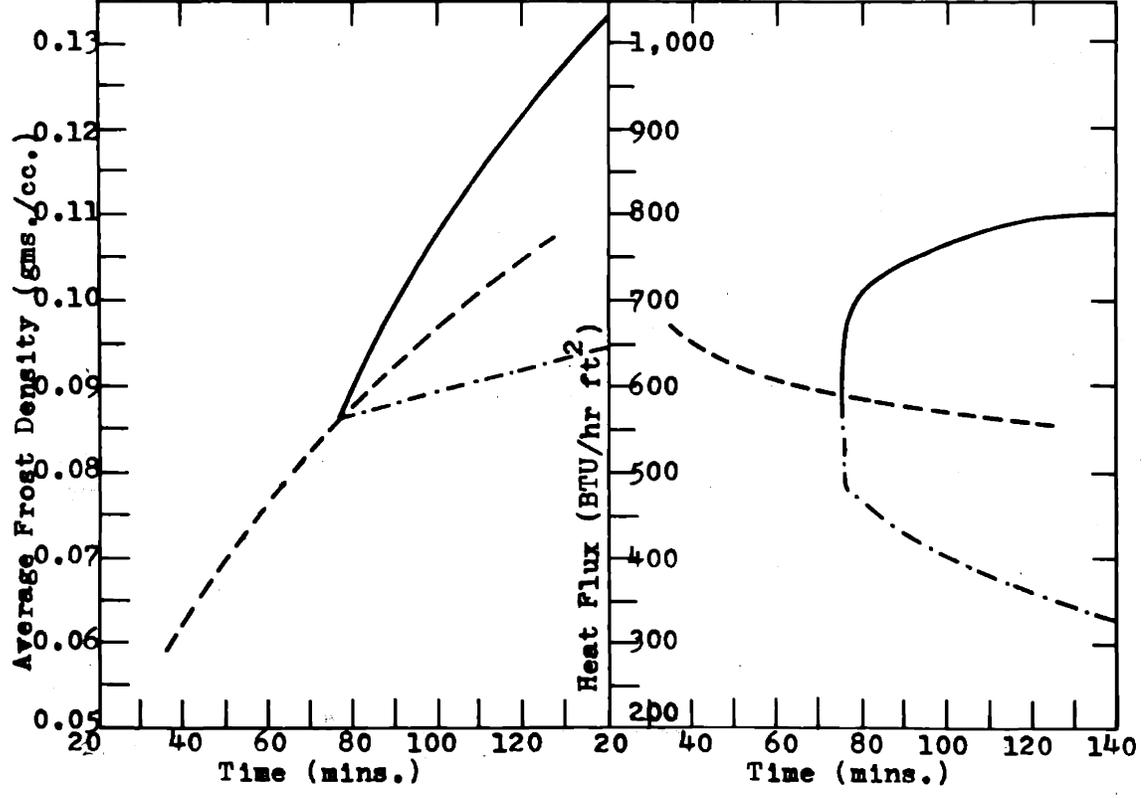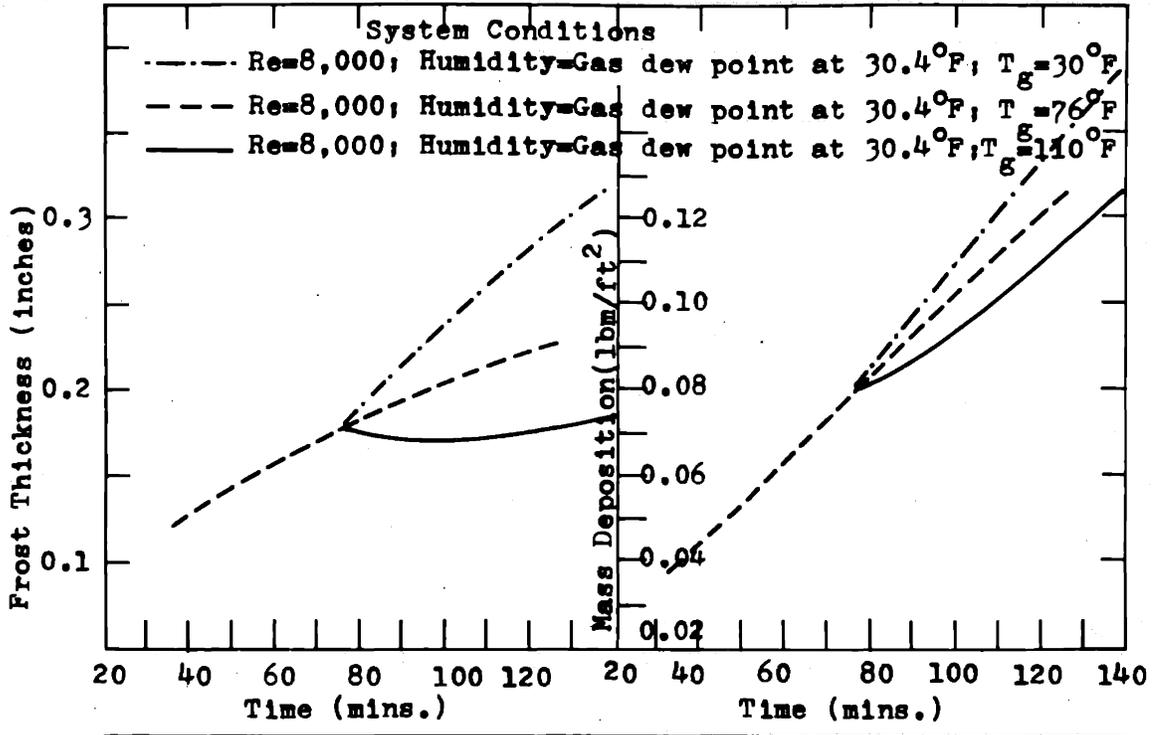
Figure II-A16   'Simple Model' Predictions for Effect of a
                 Step Change in Gas Temperature on Frost
                 Properties
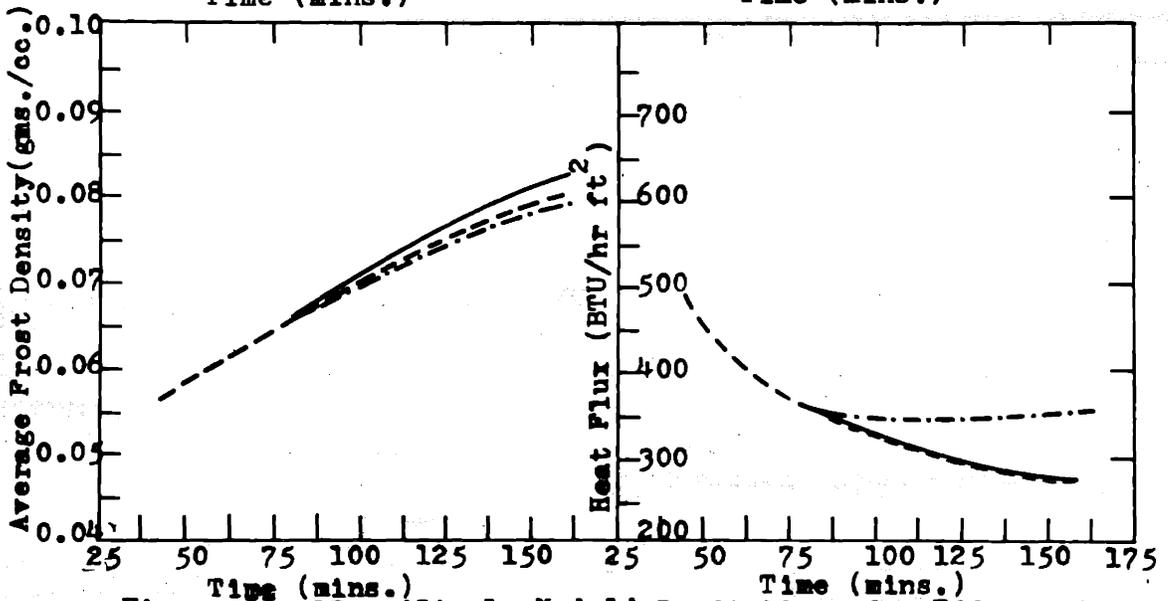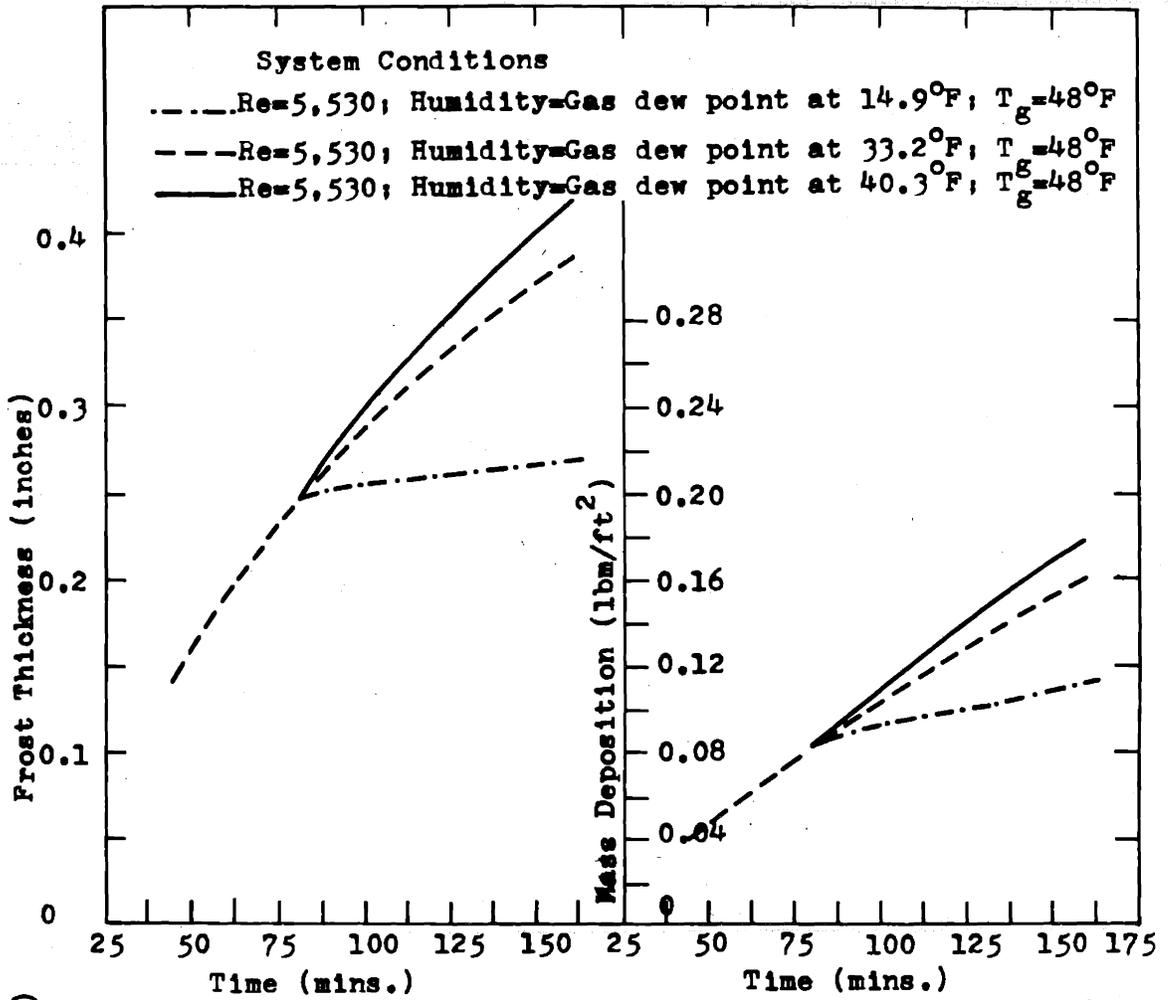
Figure II-A17   'Simple Model' Predictions for Effect of a
                  Step change in Humidity on Frost Properties.

Heat Transfer Coefficient = h

Mass Transfer Coefficient
= K_g

Direction of Heat and Mass
Transfer

Gas Flow

Reynolds Number = Re
Gas Temperature = T_g
Humidity = p_g

Heat Flux = $h (T_g - T_s) + K_g (p_g - p_s) \Delta H$
Mass Flux = $K_g (p_g - p_s)$

(T_g, p_g)

(T_s, p_s) $J|_{x+x}$

Thermal Boundary Layer   Heat Flux =

Frost Surface
(Temperature = T_s)

$x + \Delta x$
x

Frost   Layer

$J|_x$

x

(T_w, p_w)

Cold Wall
(Temperature = T_w)

$J|_{x=0} = 0$

Temperature Profile

Figure II-BO   Schematic of Frosting Process as Visualized by
' Improved   Model'

System Conditions

Re= 5,600
Humidity =Gas dew point at 29.2°F
Gas Temperature = T_g

$\rho_{f,initial}$ = 0.026 gms./cc.

$\delta_{initial}$ = 0.023 inches

$\theta_{initial}$ = 2 mins.

θ = 20 mins.

θ = 17 mins.

θ = 12 mins.

θ = 7 mins.

θ = 2 mins.

Frost Density (gms./cc.)

Distance from Cold Wall (inches)

Figure II-B3   Predictions of 'Sophisticated Model' for Time Variation in Frost Density and Thickness

——— Predictions of 'Sophisticated Model'
——— Predictions of 'Simple Model'

System Conditions

Re=5,600; Humidity=Gas dew point at 29.2°F;
T_g = 70°F

Starting Time for Theoretical
Predictions = 2 mins.

θ = 7 mins.

θ = 20 mins.

θ = 2 mins.

Temperature (°F)

Distance from Cold Wall (inches)
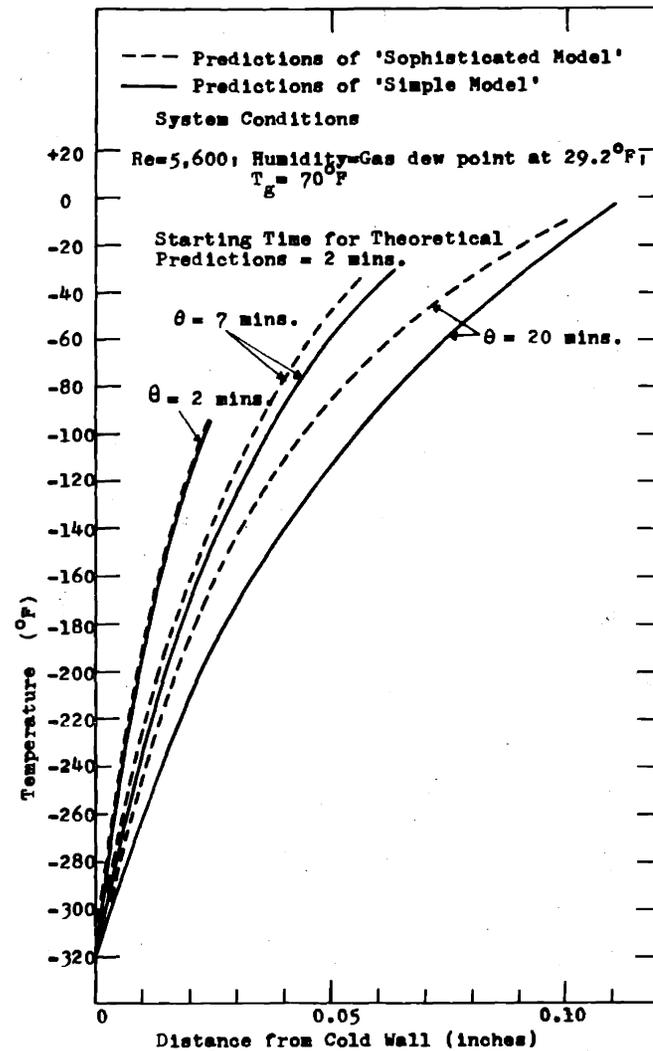
Figure II-B4   Predictions of Time Variation in Temperature Distribution within the Frost by 'Simple' and 'Sophisticated' Models
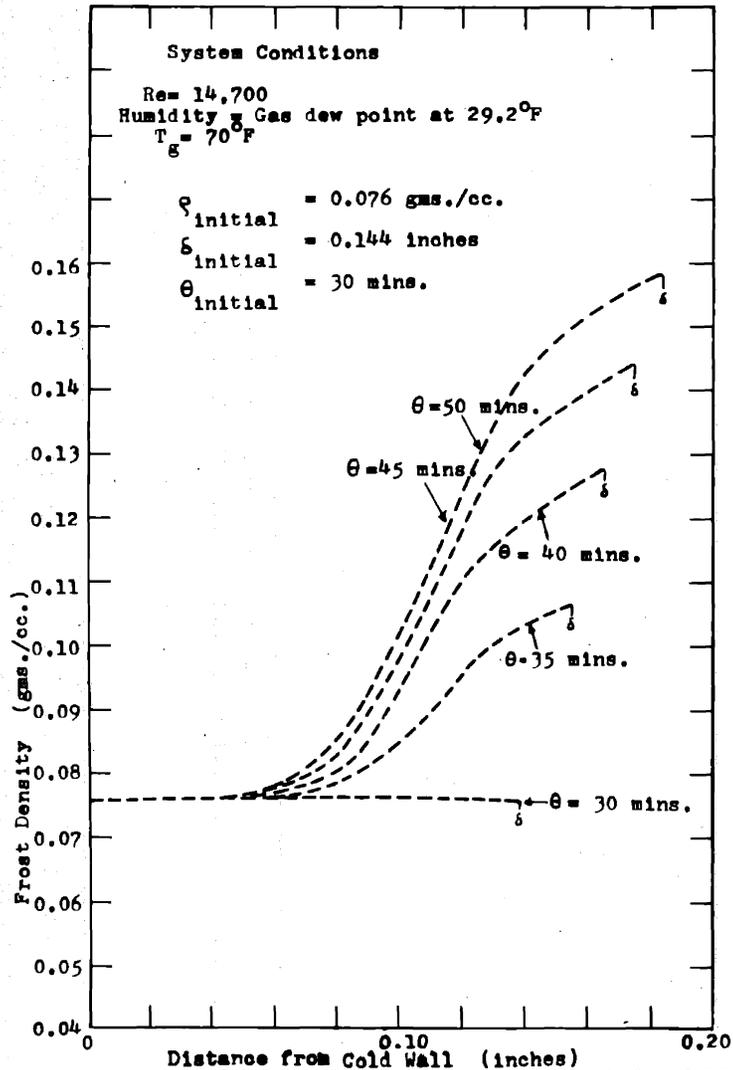
Figure II-B5   Predictions of 'Sophisticated Model'
                for Time Variation in Frost Density
                and Thickness
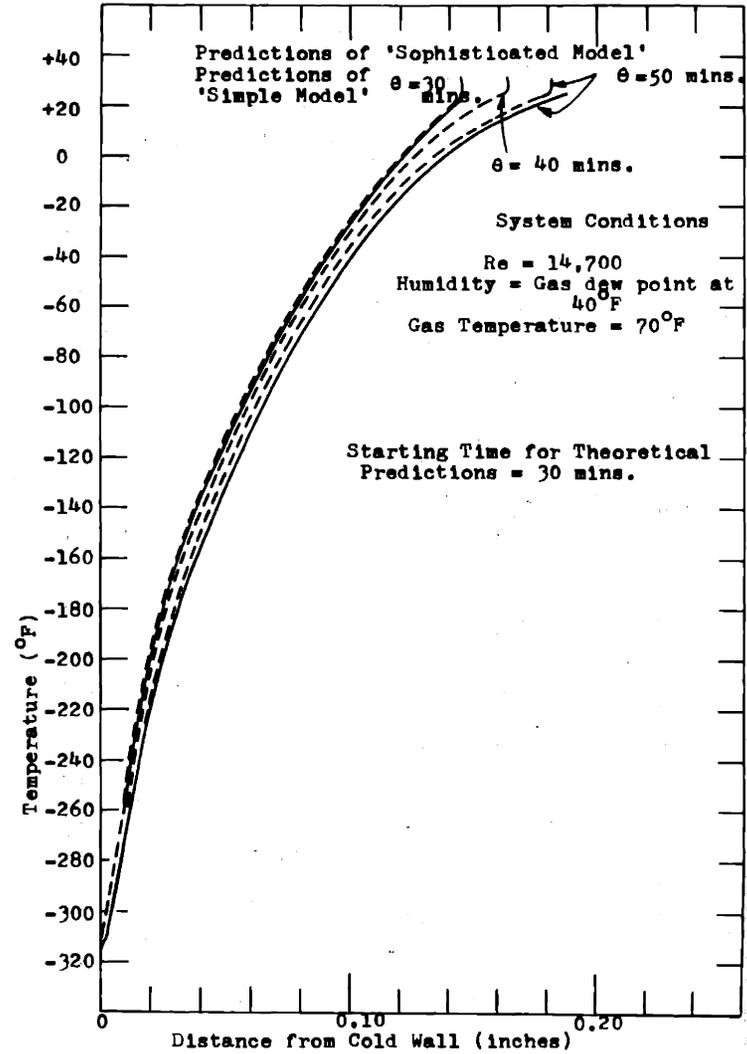
Figure II-B6   Predictions of Time Variation in
                Temperature Distribution within
                the Frost by 'Simple and
                'Sophisticated' Models
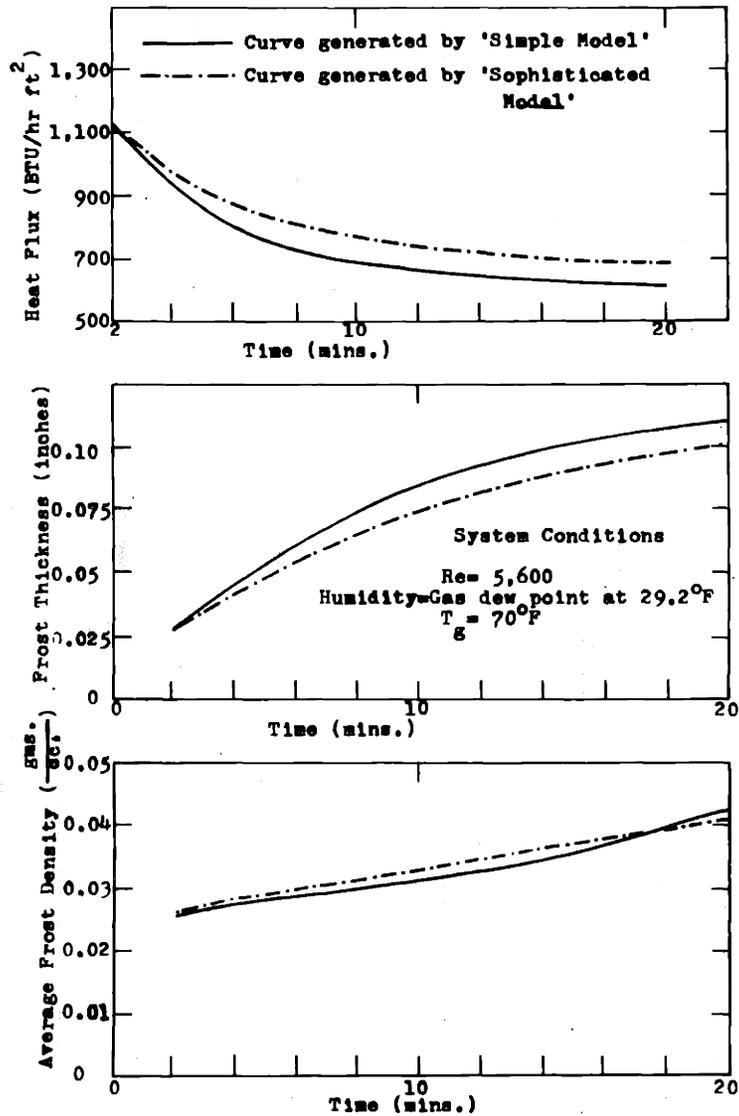
Figure II-B7 Comparison between Predictions of
'Simple' and 'Sophisticated' Models
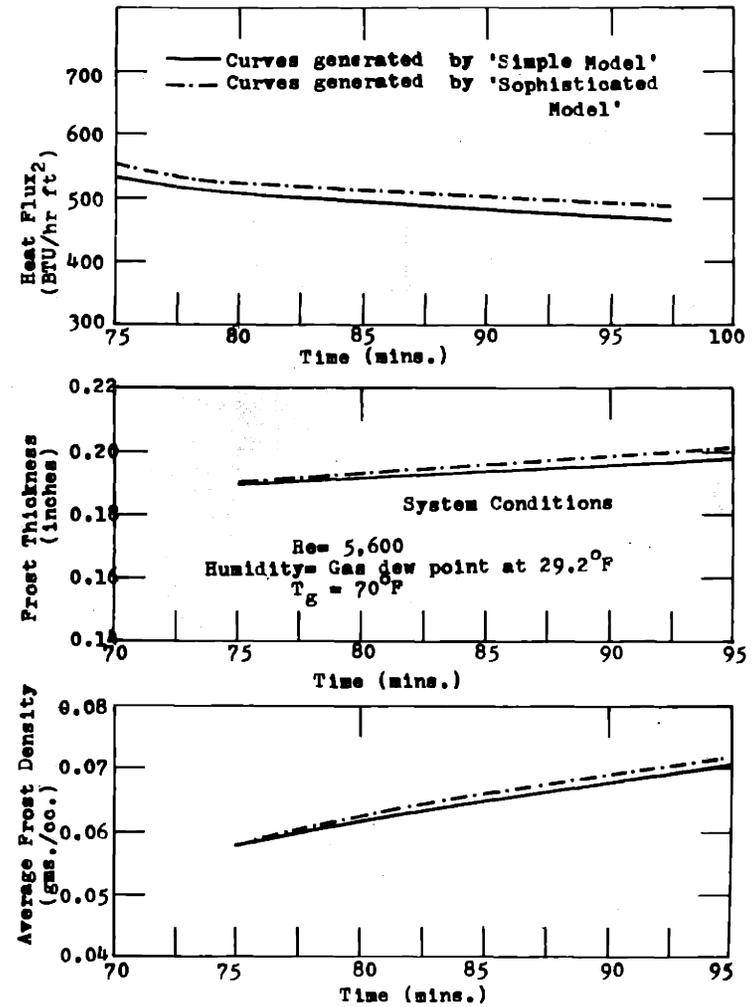
Figure II-B8 Comparison between Theoretical
Predictions of 'Simple' and
'Sophisticated' Models

- Average Density of the Entire Frost Layer
- Density of the Bottom 0.0625" Thick Frost Layer
- Density of the Bottom 0.125" Thick Frost Layer

Experimental Conditions

Re = 15,800
Humidity = Gas dew point at 29.8°F
T_g = 71°F
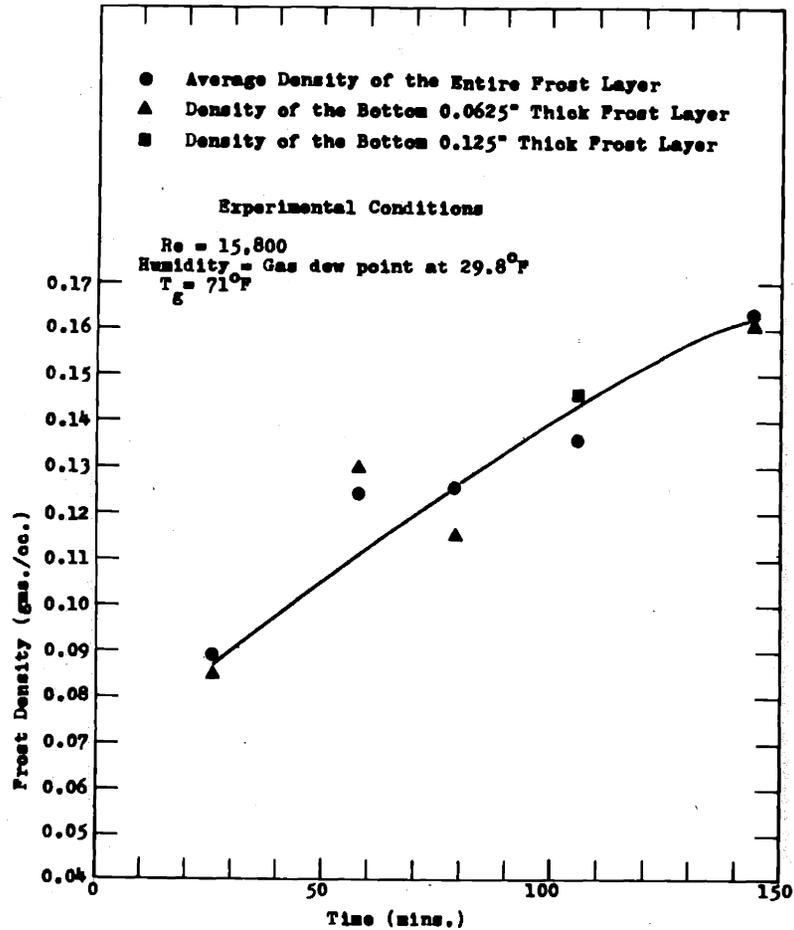
Figure II-B9   Density Distribution within the Frost as a Function of Time

$$D_{1-2} = \frac{0.001858 \times T^{1.5} \times (M_1+M_2/M_1M_2)}{\sigma_{12}^2 P \Omega_D}$$

σ_{12} = 3.165 (from Reference 94)

M_1 = 18
M_2 = 29

Ω_D = 1.449 $(\frac{kT}{\epsilon_{12}})^{-0.50877}$
(from $\frac{kT}{\epsilon_{12}}$ this Figure)

$\frac{\epsilon_{12}}{R}$ = 180.5   (94)

D_{1-2} = 2.6795 x 10^{-6} $T^{2.00877}$

where, T is in °K and D_{1-2}
is in cm^2/sec

Ω_D= 1.449 $(\frac{kT}{\epsilon_{12}})^{-0.50877}$

Data of
Reference 94

Figre II-B10

Correlation for Diffusion
Coefficient of Water Vapor
in Air
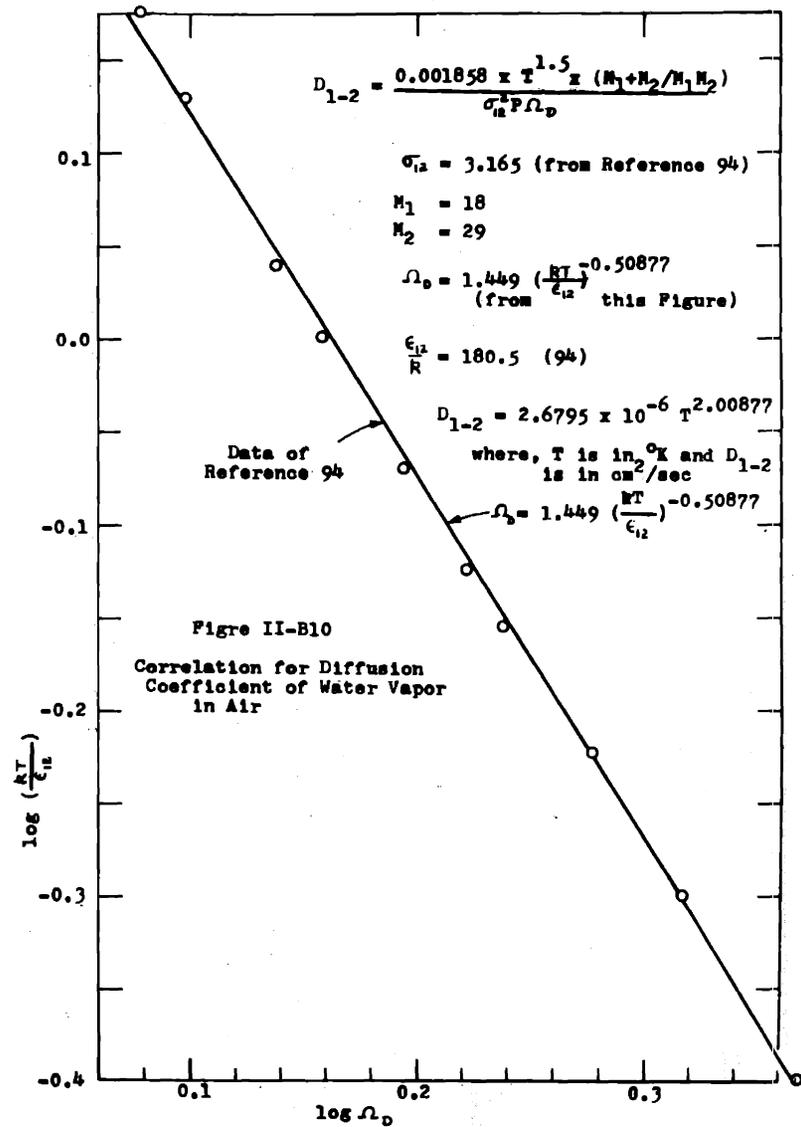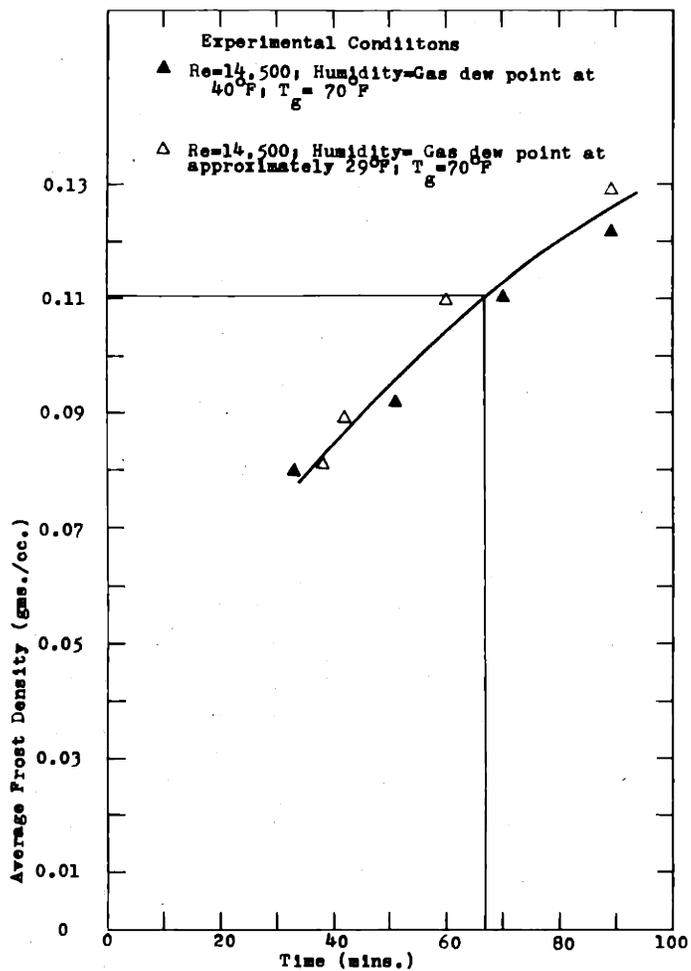
Figure II-C1   Experimental Data of Brazinsky (14)
                for Average Frost Density as a
                Function of time
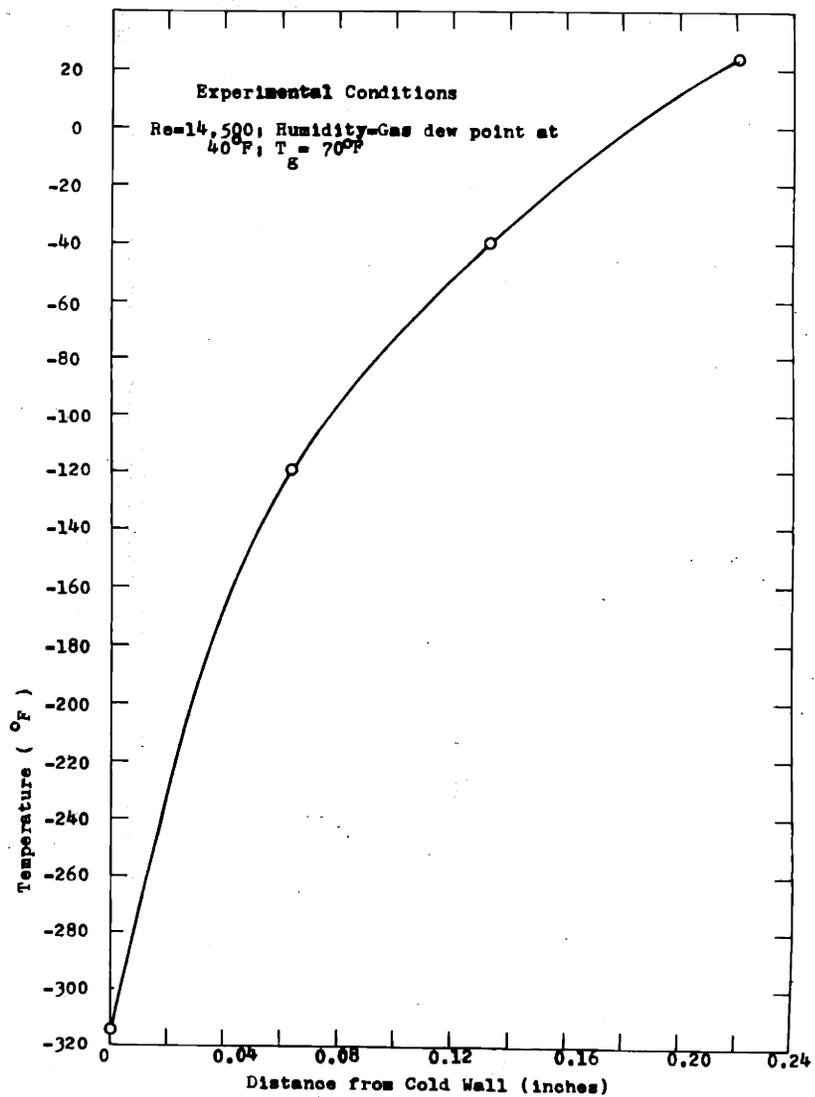
Figure II-C2   End of Run Temperature Profile within the
               Frost Measured by Brazinsky (14)
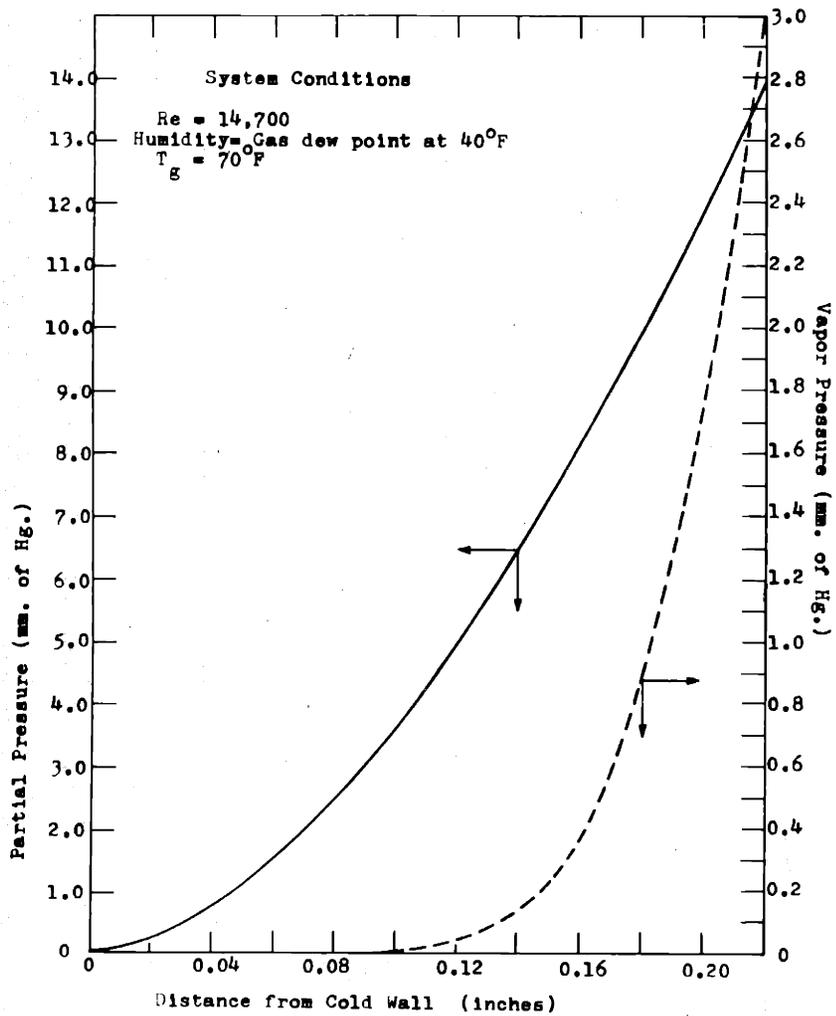
Figure II-C3 Partial Pressure and Vapor Pressure as
a Function of Position in the Frost Interior
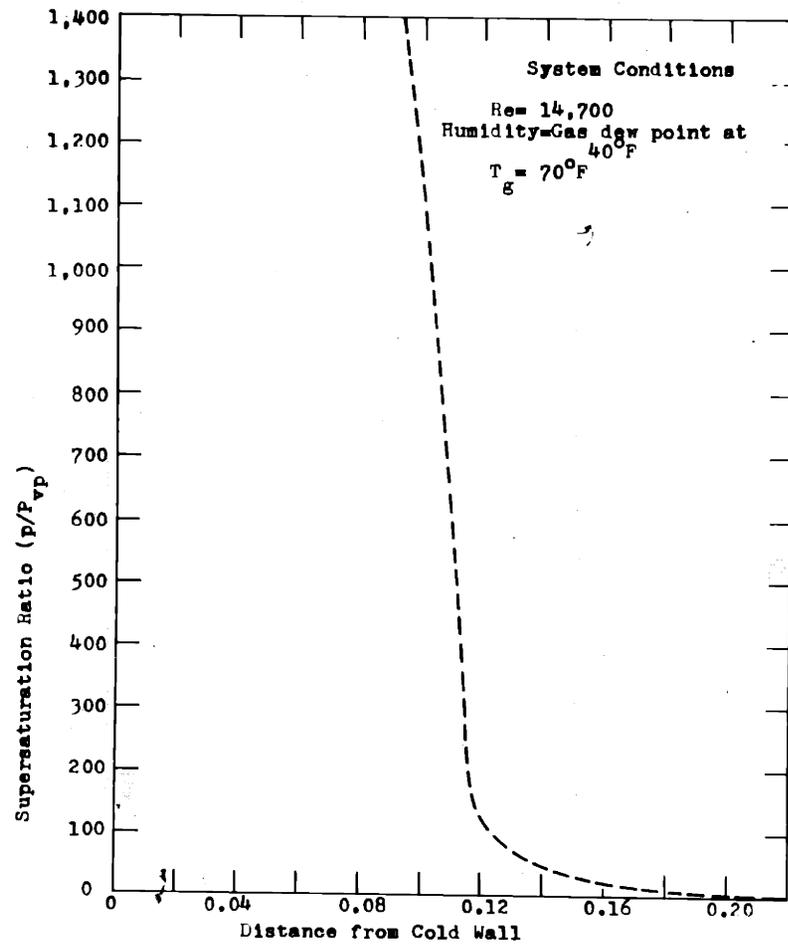
Figure II-C4 Supersaturation Ratio (p/P_{vp}) as a function
of Position in the Frost Interior
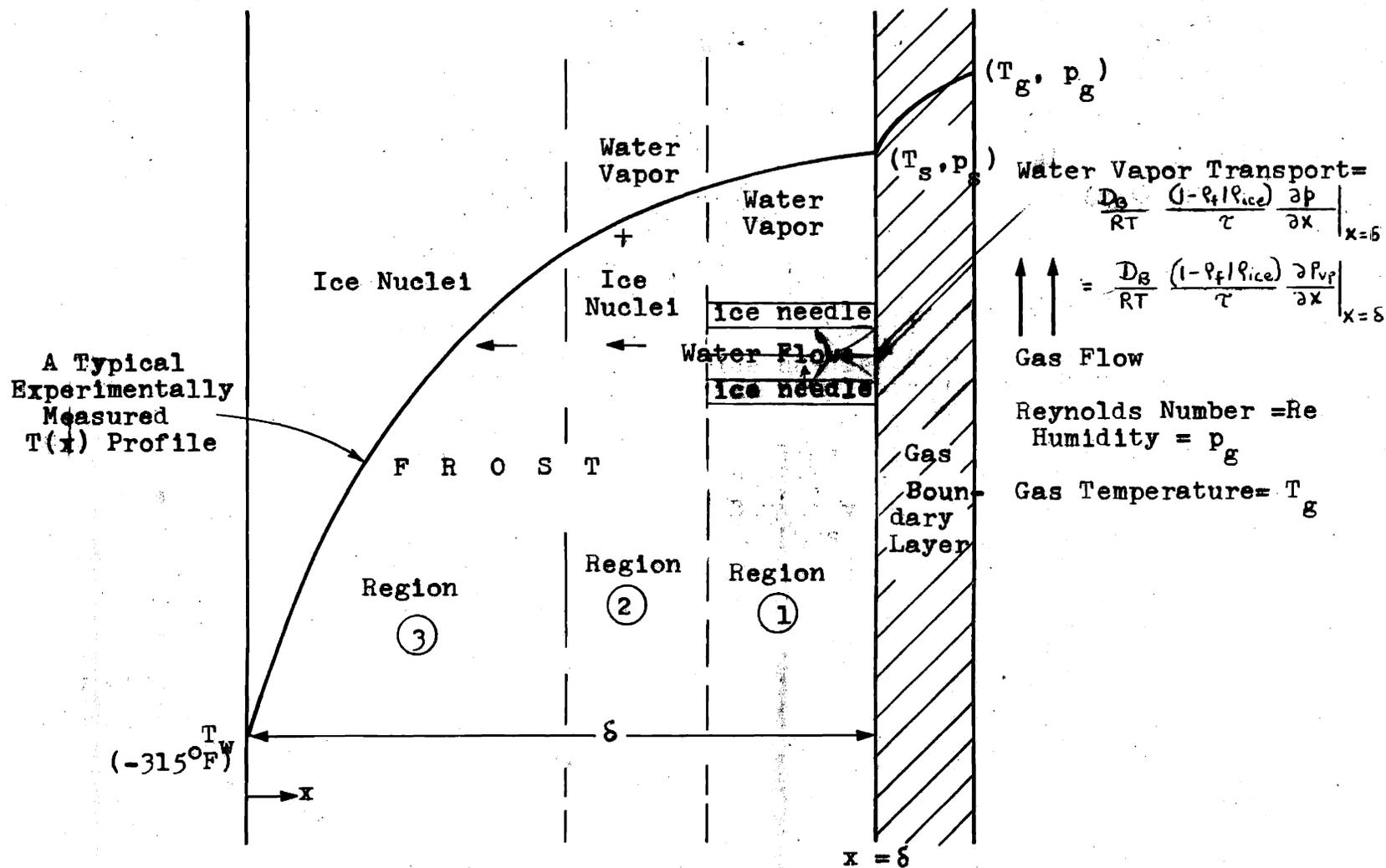
Figure II-E1 Schematic of Frosting Process as Visualized by 'Non-Equilibrium Model'

S E C T I O N   III

APPARATUS AND PROCEDURE

III-A Experimental Measurement of Effect of Independent System Parameters on Frost Properties

I. Apparatus

1. Flow Sheet

A diagram of flow system is shown in Figure III-A1. The most important feature of the equipment was the cold plate onto which the frost was deposited. As shown, it is a small circular copper plate, which formed part of the underside of a long rectangular duct and was mounted at a distance of 72 equivalent duct diameters from the duct entrance. The air from a compressor was filtered and divided into two streams. One was dried with 4-A molecular sieve while the other was saturated with water vapor by passing it counter-current to water in a humidifier packed with one-inch raschig rings. The two streams when remixed produced a gas with the desired humidity. The humidified air was then metered with an orifice passed through a heat exchanger to vary the gas temperature and then through a mixer to obtain a well-mixed stream.

Before entering the duct, the air was passed through a diverging nozzle, an aluminum box containing 2 inch thick honeycomb and two 16 mesh screens and finally through a converging nozzle. The purpose of this inlet section of the duct was to obtain a uniform velocity profile in the flowing gas. The schematic of this section is shown in Figure III-A3.

The gas which was now at the desired temperature and

humidity, flowed through five feet of duct (see Figure III-A3) before it passed over a cold circular copper plate. The purpose of this five feet duct length was to obtain fully developed velocity profile in the gas before it passed over the cold plate. The air leaving the duct was purged out to the atmosphere. The pipings of the system were made of one inch diameter or smaller polyvinyl chloride, metal and rubber tubings. The instrumentation used in this system is described in Appendix A.

The three independent system parameters studied in the present research work were Reynolds number (based on the hydrolic diameter of the duct), gas temperature and humidity. The Reynolds number was varied by changing the flowrate of air. The gas temperature was varied by submerging the heat exchanger in an ice and brine cold bath for low gas temperature experiments and by heating the gas by means of an electrical heating tape would around the heat exchanger for high gas temperature experiments. The gas humidity was varied by adjusting the air flow rate through the drier and the humidifier.

2. <u>Copper Plate and Associated Boil-off Calorimeter.</u>

The copper plate onto which the frost deposited was a circular plate of 5.54 inch diameter and ¼ of an inch thick. The plate actually consisted of two sections; an inner section which served as the heat transfer test section and an outer annular "ring" which served as a guard section. The inner section was 2.235 inches in diameter.

A 0.02 inch thick epoxy ring separated the two sections of

the plate.   The primary purpose of the epoxy ring was
to reduce heat conduction from the outer annular section
into the inner section.   This ring also bonded the two
sections of the plate together and supported the weight
of the stainless steel liquid nitrogen calorimeter vessels,
the inner section of copper plate and the 17 copper
equilibrator rods silver soldered to the bottom of this
inner section.   A detailed sketch of the plate arrangement
is shown in Figure III-A2.   Ninety-one copper equilibrator
rods were silver soldered to the bottom of the outer annular
section.   (Before soldering the rods to the plate, each rod
was inserted in a hole, $\frac{1}{4}$ of an inch in diameter by 1/8 inch
deep). The rods provided a low thermal resistance path
between the copper plate and the liquid nitrogen in the
calorimeter, thus maintaining the plate at a temperature
within several degrees of the normal boiling point of liquid
nitrogen.

An outer brass cylinder filled with liquid nitrogen
served as a heat transfer guard chamber for the inner stain-
less steel test vessel.   The outer annular section of the
copper plate was fitted into the brasschamber by means of a
1/8 inch deep groove, machined in the outer copper plate.
The connection between the copper plate and the brass chamber
was sealed by epoxy resin.   All the 91 rods were contained
within the brass chamber (see Figure III-A2).   The entire
calorimeter assembly could be jacked up-and-down whenever
desired.

The copper plate was surrounded by $\frac{1}{2}$ inch thick styroform plate. This assembly is shown in Figure III-A4. The two ends of the styroform plate were flush with the bottom of the duct. The purpose of the styroform plate was to insulate the copper plate from the bottom of the aluminum duct. The frost growth during an experiment was viewed through the Lucite "windows" which formed part of the sides of the duct.

The brass chamber was insulated with four layers of fiberglass aircraft insulation. Each layer was separated by aluminum foil to reduce radiation to the chamber.

Four lines were silver soldered to the brass cylinder (see Figure III-A2). Line I provided continuous ventilation of the liquid nitrogen boil-off. Thermocouples measuring the temperature of the outer plate and temperature of the vapor space in the outer cylinder were inserted through Line II. Line III served as the liquid inlet, and Line IV was the liquid nitrogen overflow line. After each run the liquid nitrogen was drained from the calorimeter through Line III.

3. Rectangular Duct.

The rectangular duct was 7 feet long, 10.25 inches wide and 0.4 inch high. Five feet of warm duct preceeded the cold copper plate and surrounding styroform plate assembly to ensure that the turbulent velocity profile in the gas passing over the cold plate was fully developed.

A large aspect ratio (width/height $=25$) was used in order to simulate the case of flow between infinitely wide parallel

plates.   It should be noted that for this geometry, the
clearance between the parallel plates does not affect the
Reynolds number (since Re = $\frac{2\rho q'}{L\mu}$).

The top of the duct above the plate was made of 0.25
inch thick Lucite.   This Lucite section was easily removed,
allowing the frost to be sampled at the end of each run.
The movable thermocouple probe, which was used to measure the
frost surface temperature, was mounted in this Lucite section
(see Figure III-A2).   The entire inside of the duct was
lined with aluminum foil in order to minimize radiant heat
transfer to the frost surface.

The duct was made of No. 14 guage aluminum.   Before
each run, the copper plate was jacked up flush with the bottom
of the duct.   During a run, as frost deposited on the copper
plate, the calorimeter assembly was lowered almost continuously
such that the frost surface always remained flushed with the
floor of the duct.

4.   Humidity Control System.

A drier with 4-A molecular sieves (see Section III-A5)
and a humidifier packed with one-inch Raschig rings (see
Section III-A6) arranged in parallel were used to control the
gas stream humidity (Figure III-A1).   The desired humidity
was obtained by controlling gas flow through both the humidifier
and drier, and subsequently remixing these separate streams.
The gas flowing through the humidifier could be saturated
at any temperature between 40°F and 75°F depending upon the
temperature of the water circulating through the tower.   The

drier was designed such that the completely dried and
fresh 4-A molecular sieve would lower the dew point of
flowing gas up to approximately -90°F.   Thus, with this
arrangement, a very wide range of humidities could be obtained.
In the present thesis, however, the humidity was varied from
a dew point of about 14°F to a dew point of about 33°F except
for a few experiments in which flowing air was at dew point
of approximately 58°F.   The water for the humidifier and
cooling coils in the drier was supplied from the building
high pressure main.

5. Drier.

The drier containing about 50lbs. of 4-A molecular
sieve was made of No. 14 guage aluminum sheet.   It was a
cylindrical tank 3 feet high and 14 inches in outside diameter.
The molecular sieve was supported by a perforated plate
fastened to the walls.   A filter cloth was laid on top of
the plate to filter the gas leaving the drier and a thin
layer of glass wool was placed on the top of the molecular
sieve to filter the gas before it came into contact with the
sieve.

The top of the drier was equipped with two circular
Eisenglass windows.   If silica-gel were to be used for
drying water vapor, its color change due to adsorption of
water could be visualized from these windows.   Moist gas
entered the top and exited at the bottom of the drier.
For safety reasons, the drier was equipped with a safety
valve.

Heat is evolved when water vapor is adsorbed by molecular sieve. In fact, if the temperature of the bed is allowed to rise significantly, water vapor adsorption capacity is drastically reduced. The bed of molecular sieve was therefore cooled with water flowing through a coil imbedded in the sieve. Four thermocouples were inserted to measure the temperatures of the bed (see Figure III-A5). The bed was kept essentially at room temperature.

When the dew point of the air coming out of the drier exceeded 10°F, the molecular sieve was regenerated. The regeneration procedure consisted essentially of maintaining the sieve at a temperature of about 350°F for approximately 24 hours while dry nitrogen gas was being bled through the bed. The sieve was maintained at this temperature by high pressure steam which was passed through the imbedded stainless steel coil and by an electrical heater wrapped around the outside of the drier. The drier was insulated from its surroundings only during the regeneration period.

The insulation was removed before each experiment. Figure III-A5 shows the schematic of the regeneration process.

6. **Humidifier.**

The humidifier was a cylindrical tank made of No.14 guage aluminum. It was $3\frac{1}{2}$ feet high and 14 inches in outside diameter. It was packed with 1 inch Raschig rings which were supported by a $\frac{1}{2}$ inch mesh aluminum screen attached to the wall of the tank. Water was sprayed onto the packing

from an aluminum coil whose end was closed off and which contained holes on its underside. Water was supplied to it from a high pressure main. The schematic of the humidifier is shown in Figure III-A6.

As shown in the Figure III-A6, the gas entered at the bottom and exited at the top of the humidifier. During operation of the tower, a constant liquid seal of about $3\frac{1}{2}$ inches was maintained over the liquid outlet in order to prevent gas from escaping by this route. The water level was viewed through a sight glass.

At the gas exit end, a baffle was placed 1 inch in front of the outlet to prevent the gas from jetting into the outlet tube. Glass wool and a filter cloth trapped entrained water droplets and large dust particles which would have been carried along with the exiting gas stream.

The humidifier was designed such that for a sufficiently large ratio of liquid to gas flow rate, the gas stream became saturated at all gas flow rates. For safety reasons, the packed tower was equipped with a safety valve.

7.   Gas Temperature Control.

The mixed gas stream from the humidifier-drier parallel combination was heated (cooled) in a heat exchanger. The heat exchanger was a 0.5 inch i.d. coiled copper tubing with an equivalent straight length of about 20 feet. The coiled heat exchanger had ten turns.

For experiments in which the gas temperature was below room temperature, the copper coil heat exchanger was

immersed in an ice or ice and brine bath. The gas temperature above room temperature was obtained by winding an electrical heating tape around the heat exchanger. The gas temperature for these experiments was controlled by adjusting the electrical power input to the heater. The heated section in these experiments was surrounded by fiberglass insulation in order to prevent significant heat loss to the surroundings.

The gas temperature was measured at three locations in the system, at the entrance of the duct, just above the copper plate, and at the downstream end of the duct.

8. Flow Control and Measurement.

The gas flow rate was controlled by the needle values placed at various locations in the system as shown in Figure III-Al.

The gas flow rate was measured with an orifice meter. Details of the calibration and construction are presented in Appendices B and A respectively.

9. Duct Inlet and Outlet Chambers.

Before the gas entered the duct, it flowed through a diverging nozzle, a rectangular box containing a 2 inches thick honeycomb and two 16 mesh aluminum screens, and finally through a converging nozzle. All these sections were made of No. 14 gauge aluminum sheet and were connected by No.8 gauge aluminum flanges. The dimensions of each piece are shown in Figure III-A3.

The purpose of the nozzles, honeycomb and the screens was to provide the gas with a uniform velocity profile at the entrance to the duct. The five feet of warm duct preceeding the copper plate was used (**39**, **72**) to obtain the fully developed velocity profile gas flow.

After leaving the cold plate and surrounding styroform assembly, the gas passed through a ten inch long duct and then through a converging nozzle before it was purged out to the atmosphere. The outlet end of the duct was made of No. 14 gauge aluminum sheet. The detailed dimensions of which are shown in Figure III-A3.

II. <u>Experimental Procedure</u>

1. <u>Preliminaries Before a Run</u>

Before each run was started, it was necessary to determine the appropriate settings for the flow control valves in order that the gas entering the duct would have the desired humidity, flow rate and temperature. The pre-run procedure for finding these appropriate valve settings is described below.

The knowledge of the humidities of the gas which would leave the drier and the humidifier was obtained by making two experiments. In the first experiment, no gas was flown through the humidifier and the humidity of the gas leaving the drier was measured by the method described in Appendix A. In the second experiment, no gas was flown through the drier and the humidity of the gas leaving the humidifier was measured by the same method. In the second experiment, the

maximum attainable humidity of the exit gas was obtained
by measuring the temperature of the water circulating
through the tower. From these information, the necessary
flow rates through the drier and the humidifier for the
required gas humidity were calculated. A non-frosting run
at the desired gas flow rate was then made to adjust the
valve settings for the required humidity. Once the settings
of the flow control valves were detrmined during the
preliminaries, it was generally not necessary to change them
during the actual run.

A second step in the preliminary procedure involved
adjusting the temperature of the gas entering the duct. For
low gas temperature experiments, this was accomplished by
adjusting the temperature of the ice and brine bath and the
length of the heat exchanger immersed in the bath. For high
gas temperature experiments, the required temperature was
accomplished by changing the electrical power input to the
heater. The variac setting determined during the preliminary
procedure was then used for the actual run.

2. Start-up

Once the preliminaries described above were completed,
the over-all system was purged with dry nitrogen gas. After
about 5 to 10 minutes of purging, liquid nitrogen was supplied
to the calorimeter from a 25 litre dewar. The liquid filled
the inner and outer cylinders of the calorimeter and then
flowed out through the overflow line (see Figure III-A2).
This overflow was collected in an empty dewar. (During the

run, the liquid overflow rate was maintained as constant as possible). The frosting experiment was not started, until the temperature of the inner and outer sections of the copper plate became constant at approximately -320°F.

Before the run actually started, (i.e. before the gas was allowed to flow over the cold copper plate), the variac in the heater circuit was set to the desired values for high temperature experiments and for low temperature experiments the known heat transfer area of the heat exchanger was immersed in the prepared ice or ice and brine bath. The thermocouples used to measure the temperature distribution within the frost were fastened to the copper plate by two metal poles .003 inches thick and about 0.3 inches high. The distances between the thermocouples and the copper plate were measured by a depth micrometer. The calorimeter was rested on a jack, such that during a run it could be lowered. The copper plate was flushed with the bottom of the duct and the removable portion of the duct right above the plate was sealed with the taps.

Finally the water was circulated in the humidifier and the gas flow was started using the regulating value on the compressor. The opening of the regulating value on the compressor.corresponded to the actual start of the run and hence to time zero.

3. Procedure During the Actual Experiment.

During an experiment the following measurements were carried out at various time intervals.

A.   The liquid nitrogen boil-off rate from the inner cylinder
was measured with a calibrated rotameter. In some experiments
this reading was checked with a wet test meter connected in
series with the rotameter.   The boil-off measurement was
used to calculate the heat flux into the heat transfer test
section (inner cylinder of the calorimeter; see Appendix H).
The boiled-off vapor was superheated as it flowed from the
calorimeter to the measuring rotameter.

B.   The pressures in the inner and outer chamber of the
calorimeter and on the orifice meters were measured with the
water manometers.

C.   The various thermocouple readings were measured period-
ically. Thermocouple locations in the system were as follows:

     a.   Under the inner and outer copper plates.

     b.   In the inner and outer chamber of the calorimeter.

     c.   In the frost interior.

     d.   In the gas flow passage, as shown in Figure III-A3.

D.   As frost was deposited, the calorimeter assembly was
slowly but almost continuously lowered so as to keep the frost
surface flushed with the bottom of the duct.   This was
necessary for maintaining the velocity profile in the gas
flowing over the cold plate well developed and to keep heat
and mass transfer coefficients between gas and frost surface
constant during the run.   The smooth transition between the
floor of the duct and the frost surface was verified by
visual examination through the Lucite "windows". By this
method, the smooth transition could be obtained only within

0.04 inches.

E.   In most of the experiments, it was necessary to
switch liquid nitrogen supply dewars as the first dewar
was depleted.   The switch was accomplished by shutting the
valve on the liquid nitrogen inlet line, lifting the liquid
transfer tube out of the first dewar by means of a hot
blower and inserting it into the second one.   After the new
connection was made leak tight, the valve on the liquid line
was re-opened, allowing liquid nitrogen to flow again from
the supply dewar to the calorimeter.

F.   Towards the end of an experiment, the frost surface
temperature was measured with a "movable" thermocouple probe.
In making the measurement the probe assembly was lowered
towards the frost surface.   The millivolt output of this
thermocouple was read on a potentromater.   The output was
read and plotted as a function of distance from the centre
of the duct.   Figure III-A7 shows a typical plot of this
output.   The sharp change of the slope of the above plot
determines the position of the frost surface.   The location
of the frost surface by this method can be obtained only
within 0.02 inches.   The visual observation of the movement
of the thermocouple was done through the Lucite windows.

In general, care had to be exercised to prevent the
thermocouple wire from causing any disturbances to the frost
surface when it was moved in and out of the frost.   If large
chunks were torn out of the frost layer while retracting the
thermocouple from the frost interior, the experiment was

discontinued.   This type of accident was generally prevented
by lowering the thermocouple wire slowly towards the frost
surface.   The wire would therefore cool significantly before
contact.   When a warm wire contacts the frost, localized
melting results.   The molten frost subsequently refreezes
and bonds other parts of the frost to the wire.   Retraction
of the wire, of course, results in large chunks of frost
being ripped out.

4.   Shutdown.

At a predetermined time, the gas flow was stopped.   The
following operations were performed just after the shutdown
in the cronological order:

A.   The water flow rate through the humidifier was turned off.

B.   The Lucite section of the duct (i.e., the short section
just above the copper plate) was removed.   Several frost
samples at various locations on the copper plate were taken
with the glass vials of known cross section.

C.   The frost thickness was measured with a depth micrometer
at various locations on the copper plate.

D.   In some experiments, several samples of the frost were
taken with the polystyerene tubes (see Section III-C) to
determine the density gradient within the frost.   These
samples were immediately stored in a small closed container
which was kept in a liquid nitrogen bath.

E.   The frost was cleared away from the areas adjacent to
the thermocouples without disturbing the probes.   The
heights of these thermocouples above the plate were then

measured with a depth micrometer.

F.   If step (D) had been carried out then the samples of

the various frost slices were obtained by the method

described in Section III-C.

G.   The glass vials containing the frost collected by

step (B) and (F) were weighed.   (By the time the vials

were weighed, the frost had melted to liquid water).   The

actual frost weight was determined by subtracting the weight

of the dry vials (in case of step (B)) or dry vial and

polystyrene ring (in case of step (F)) from the tare weight.

Densities were calculated from the measured frost weights

and the volumes of the collected frost samples.

III-B Experimental Measurement of the Effect of a Temperature Gradient across the Frost on its Density.

1.   Apparatus

       To determine the effect of a temperature gradient on

the frost density, an apparatus was constructed as shown in

Figure III-B1.

       Two hollow cylinders were mounted vertically end-to-end

and the frost under investigation was placed in the measured

space between the ends (see Figure III-B1).   The sandwiched

frost was divided into several slices by inserting 200 mesh,

0.002 inch thick phos-bronze screens.   The frost was

insulated from the surroundings by two inch thick fibre

glass insulation.   During a run, the two ends of the cylind-

ers were maintained at different but constant temperatures.

Experiments were made with both large and small temperature

differences across the frost. The complete experimental set-up was placed in a cold room whose temperature can be varied between +20°F to -20°F.

In the experiments with a large temperature difference across the frost, the copper plate of the lower hollow cylinder was maintained at liquid nitrogen temperature (-310°F). In order to reduce the heat loss, this cylinder was insulated with two inch thick asbestos. The top hollow cylinder, in these runs, was filled with Nujol (oil) and an electrical heater was inserted in this oil bath. With the help of this heat reservoir of oil bath, the copper plate of the top cylinder was maintained at approximately 15°F. The temperatures of both the lower and the upper copper plates were measured by copper-constantan thermocouples. The experimental set-up for these experiments is shown in Figure III-B1.

In the experiments with a small temperature difference across the frost, the upper copper plate was kept once again at approximately 15°F. The lower copper plate, however, was kept at approximately -4°F by blowing cold air under the plate. The temperature of the cold room was maintained at approximately -4°F. The rest of the set-up was identical to the previous one. Figure III-B2 shows the set-up for these experiments.

2. Procedure.

The frost for these experiments was obtained from natural snow. The frost was sprinkled over the lower

copper plate. During this process of sprinkling, the phos bronze screens were inserted in the frost as shown in Figure III-B1. In order to determine the uniformity of the laid frost, the thickness and density of each slice of the frost were measured by the methods described in Section III-A. The top cylinder was then adjusted such that the top copper plate just touched the frost surface (see Figure III-B1). Thus, the frost was sandwiched between the plates. The sandwiched frost was then insulated on its sides by fibre glass insulation.

During all the experimental runs the temperature of both the copper plates was measured at intervals of ten minutes and a good contact between the top copper plate and the frost surface was assured by visual observation.

At the end of each experiment, density and thickness of each slice of the frost was again measured, taking a few samples on each screen and on the lower copper plate.

Experiment number R-7 was carried out to measure the density gradient in the frost deposited by natural convection on liquid nitrogen cooled copper plate. In this experiment liquid nitrogen was circulated in the lower cylinder. As soon as a certain thickness of frost was deposited, a phos bronze screen was placed over it. This phos bronze screen was supported by four small wooden supports such that the screen touched the frost without crushing it down. More frost was then allowed to accumulate on this screen and then the above process was repeated. Thus, several slices of

the frost were obtained.   The density and thickness of each

slice was then measured by the method described previously.

III-C Experimental Measurement of Density Gradient Within

the Frost.

Apparatus and Procedure.

     To determine if the frost deposited early in a run was

of a different density from that deposited at a later stage,

some frost cores were sliced horizontally to separate discrete

portions identified by being formed at different times. This

slicing was not easily done.   After numerous attampts, a

simple technique was developed using a small polystyrene tube.

The tube was itself sliced into several rings 0.0625 inch

thick.   These rings were glued together to form the original

tube.   However they could be easily separated with a knife.

The tube was cooled in liquid nitrogen.   The frost at the

end of an experiment was then sampled with the cold poly-

styrene tube and placed into a cold box at liquid nitrogen

temperature.   The whole assembly was then carried to the

-20°F cold room.   The tube made of rings was cut with a

cold razor.   The density of the frost contained in each

ring was measured by the method described previously.

III-D Measurement of Heat Transfer Coefficient in Non-Frost-

ing Conditions

     As seen in Section II, a theoretical evaluation of the

frosting process requires an accurate knowledge of heat

transfer coefficient.   Hence, the heat transfer coefficients

under non-frosting conditions were measured in the experimental set-up of Figure III-Al.

In these experiments, the copper plate was maintained at a temperature of approximately -12°F by circulating liquid Freon -12 through the calorimeter. A corrigated aluminum foil was cemented over the copper plate in order to obtain frost like curface conditions. The measurements of heat flux were carried out in exactly the same manner as done in the frosting experiments (see Section III-A). The plate temperature was measured by imbedding a thermocouple in the cement.

The dried air was obtained by allowing all the air to flow through a drier containing 4-A molecular sieve. The dew point of the gas coming out of the drier was sufficiently low so that no frost was deposited on the cold plate during an experiment.

The heat transfer coefficients at various Reynolds numbers were obtained in this manner. In all the experiments the temperature of air was maintained at room temperature.
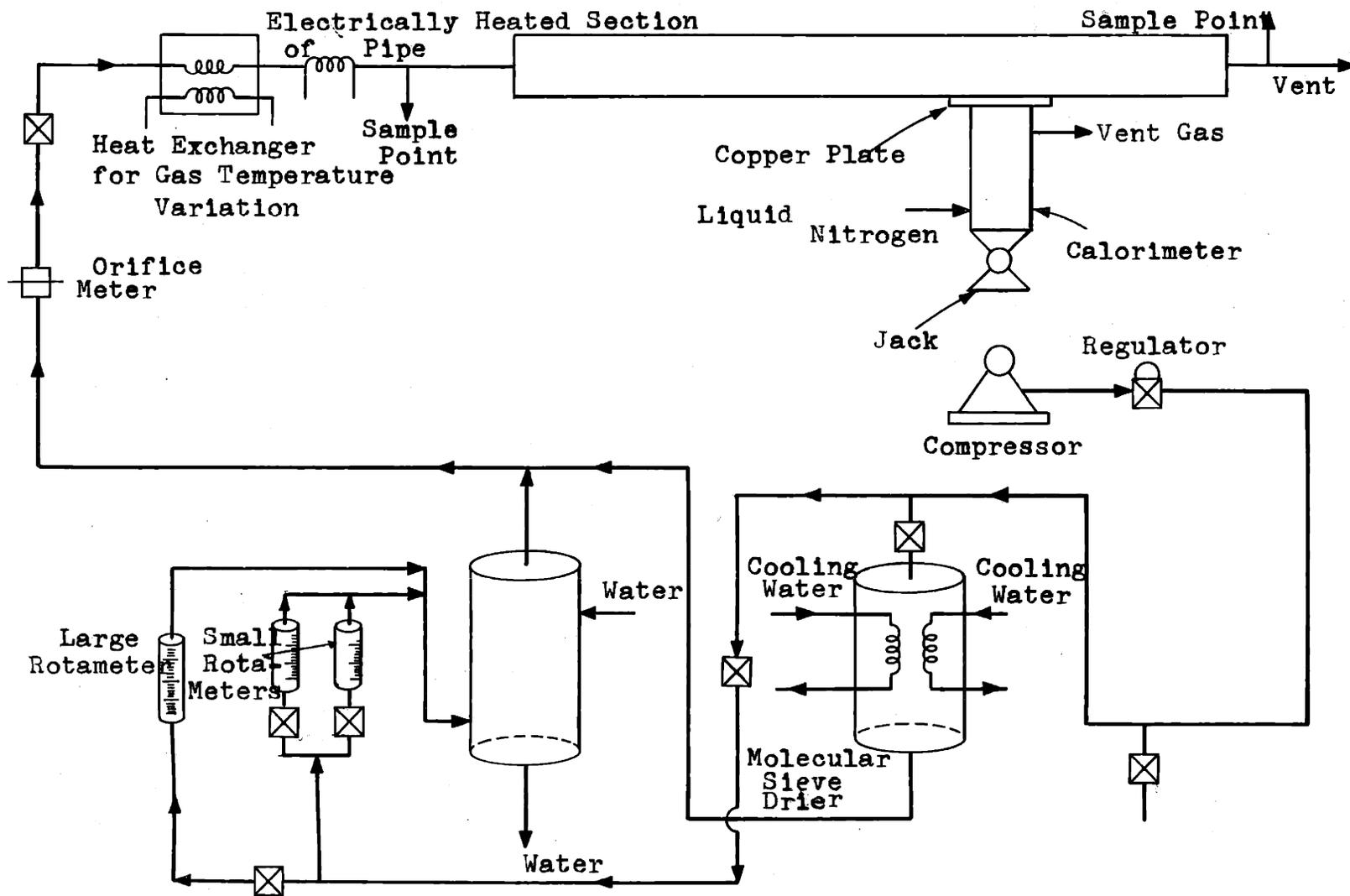
Figure III-Al   Flowsheet of Equipment
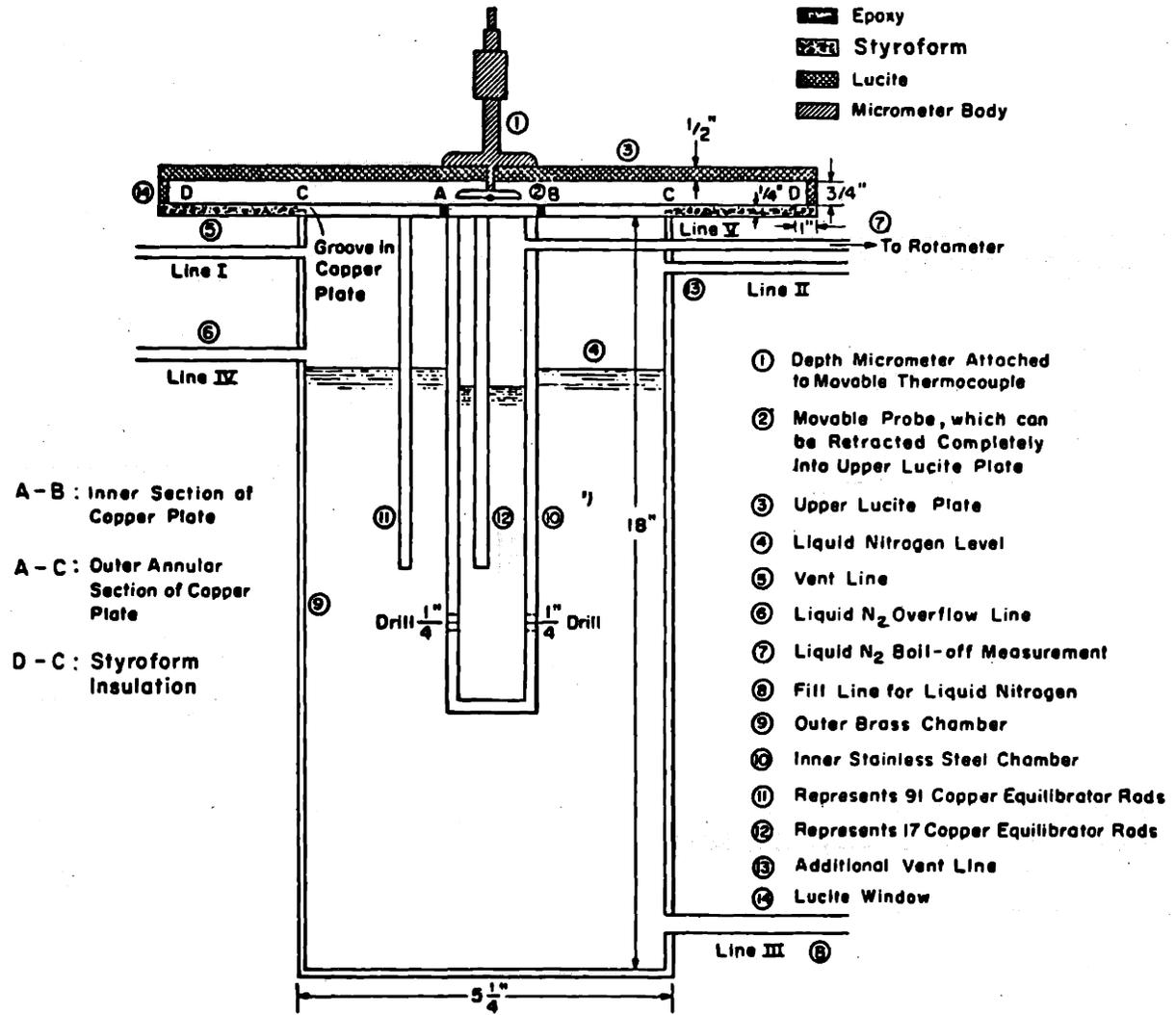
Figure III-A2   Copper Plate and Associated Boil-off Calorimeter
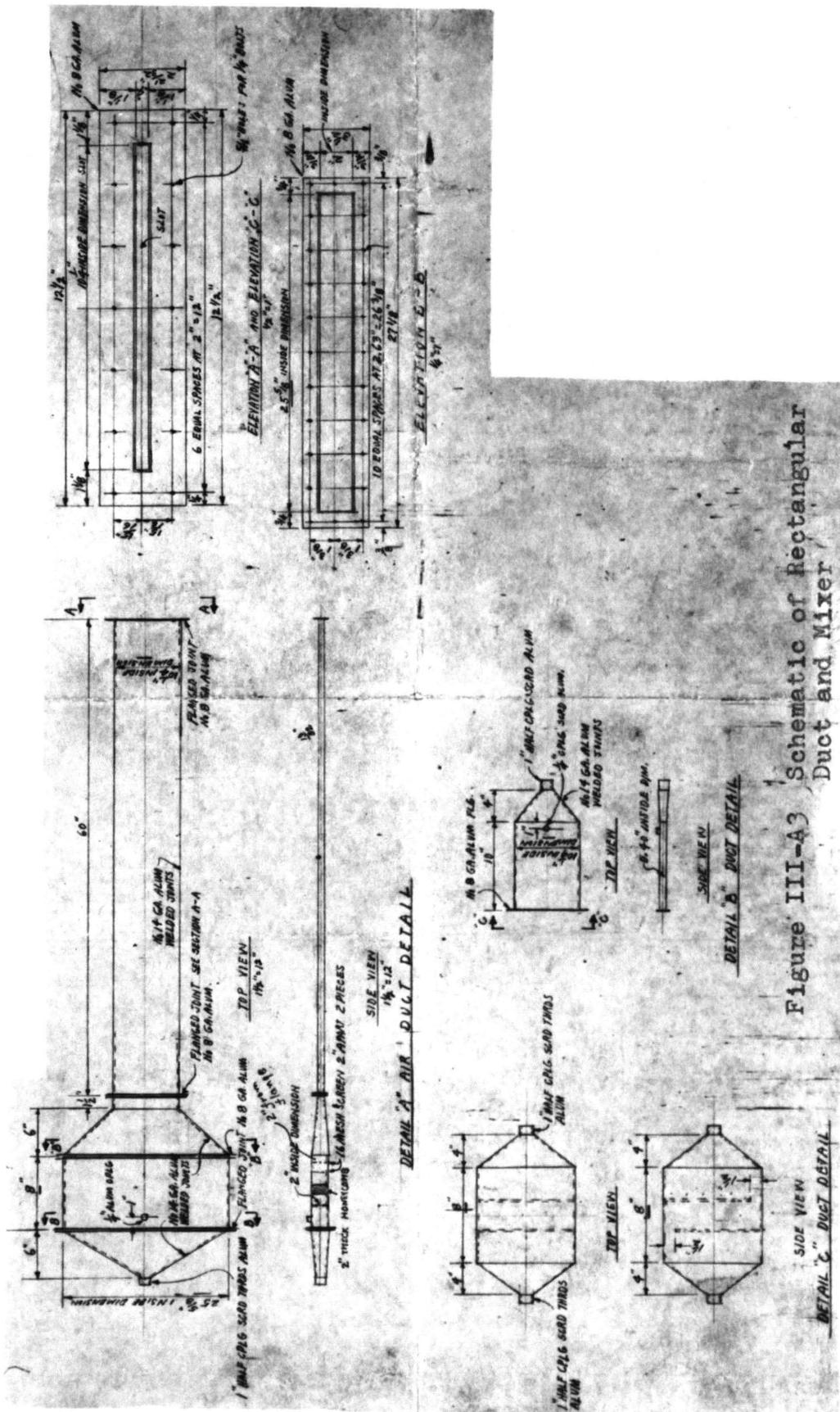
Figure III-A3 Schematic of Rectangular Duct and Mixer
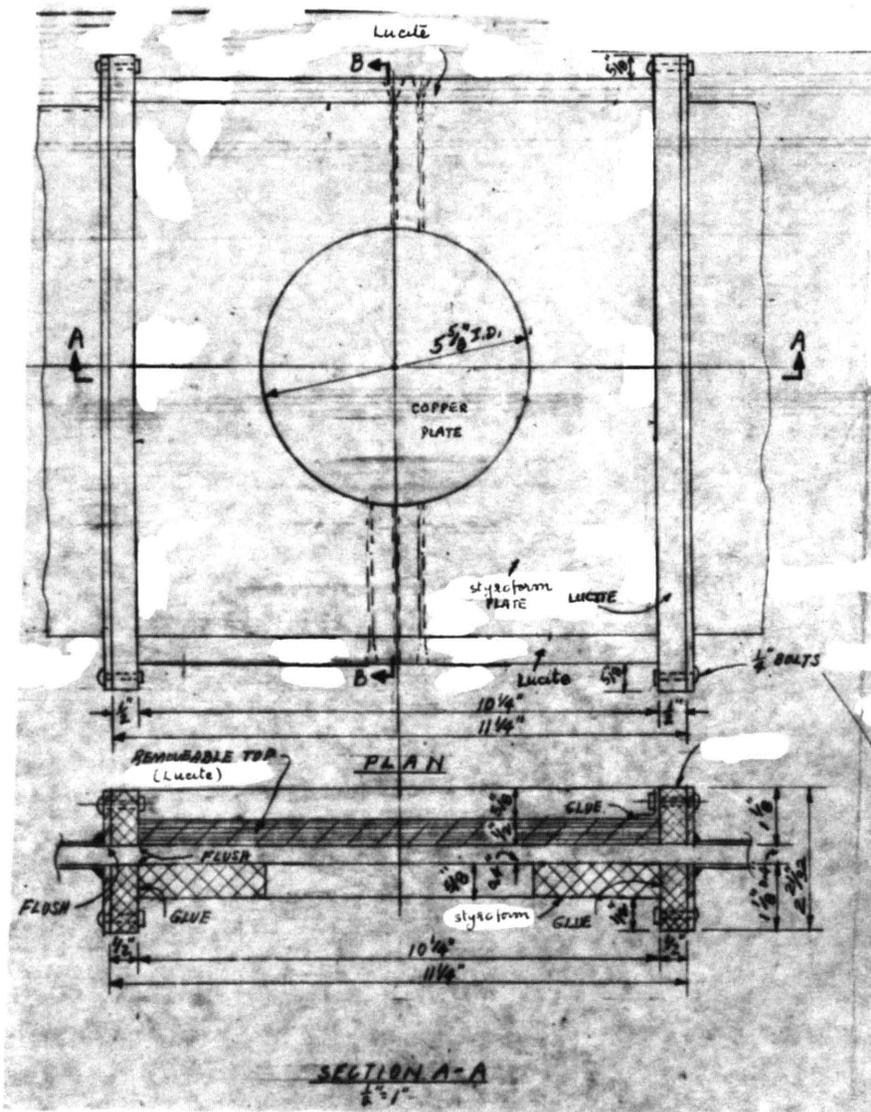
Figure III-A4 Schematic of Styroform Assembly Surrounding Copper Plate

Figure III-A5   Schematic of Drier Unit
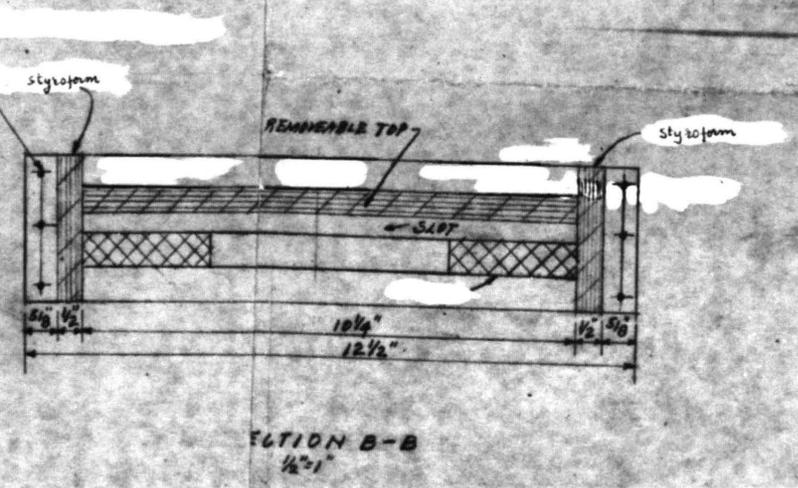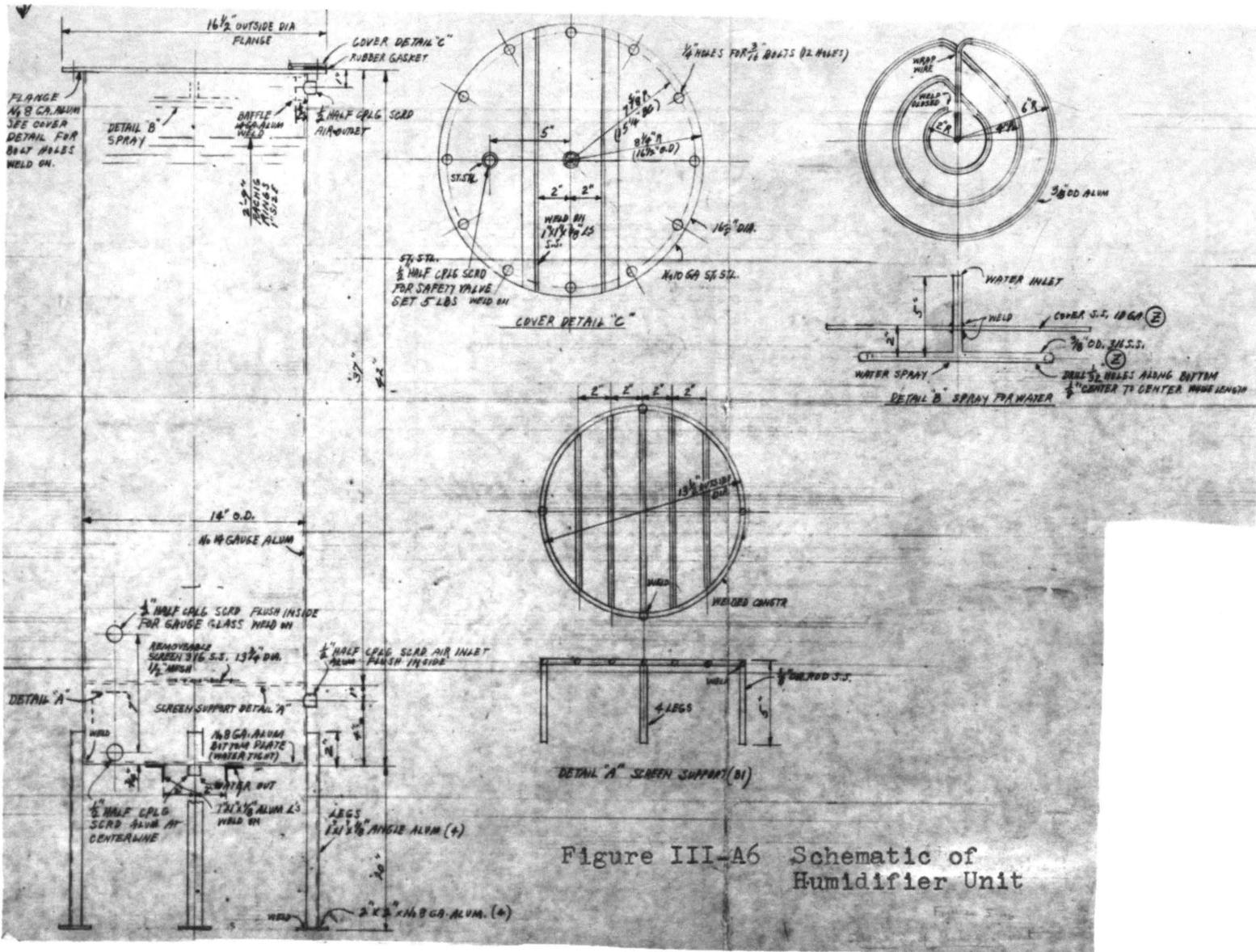
Figure III-A6 Schematic of Humidifier Unit
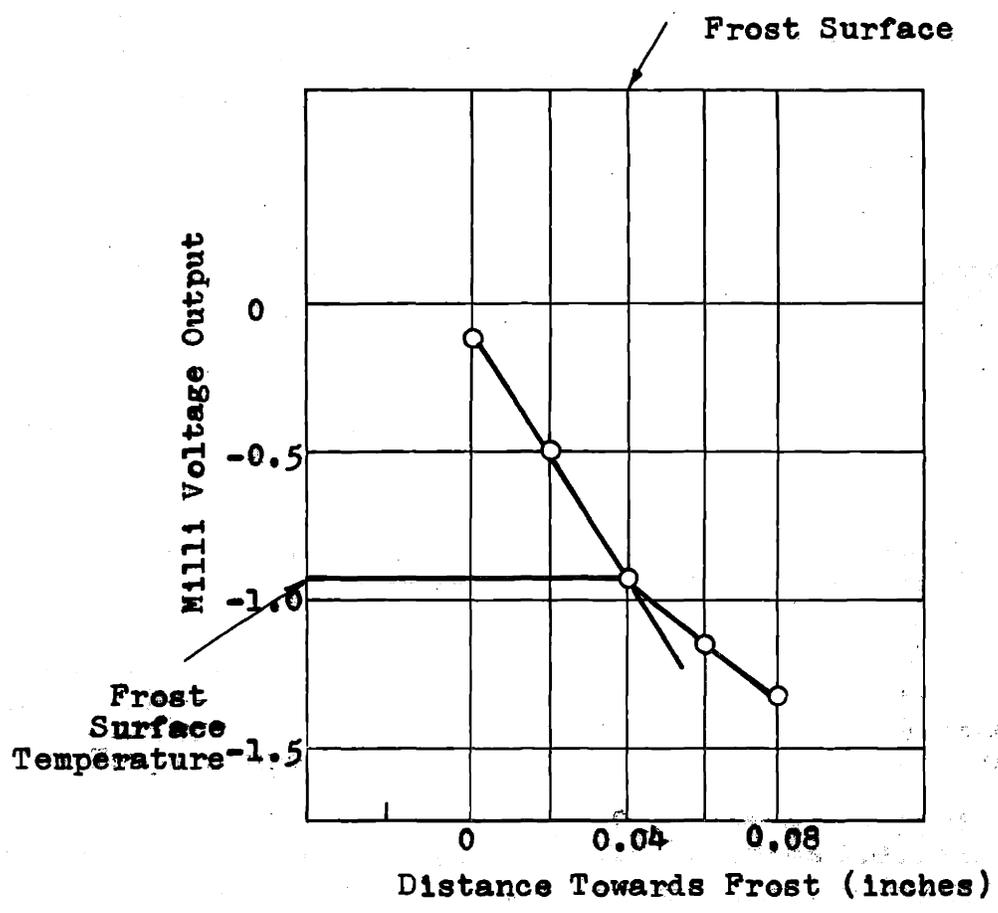
Figure III-A7   Millivoltage Output versus
Distance to Determine the
Frost Surface Temperature

Stirrer   Immersion Heater
                                              } Supp-
                                                orting
                                              Rods

Top Hollow Cylinder

Nujol

Thermocouples

200 Mesh Phos-Bronze
       Screens
Asbestos Fibre Glass
       Insulator

Bottom
Hollow
Cylinder

Overflow
Trap

Table

Notrogen   Liquid
Gas   Nitrogen
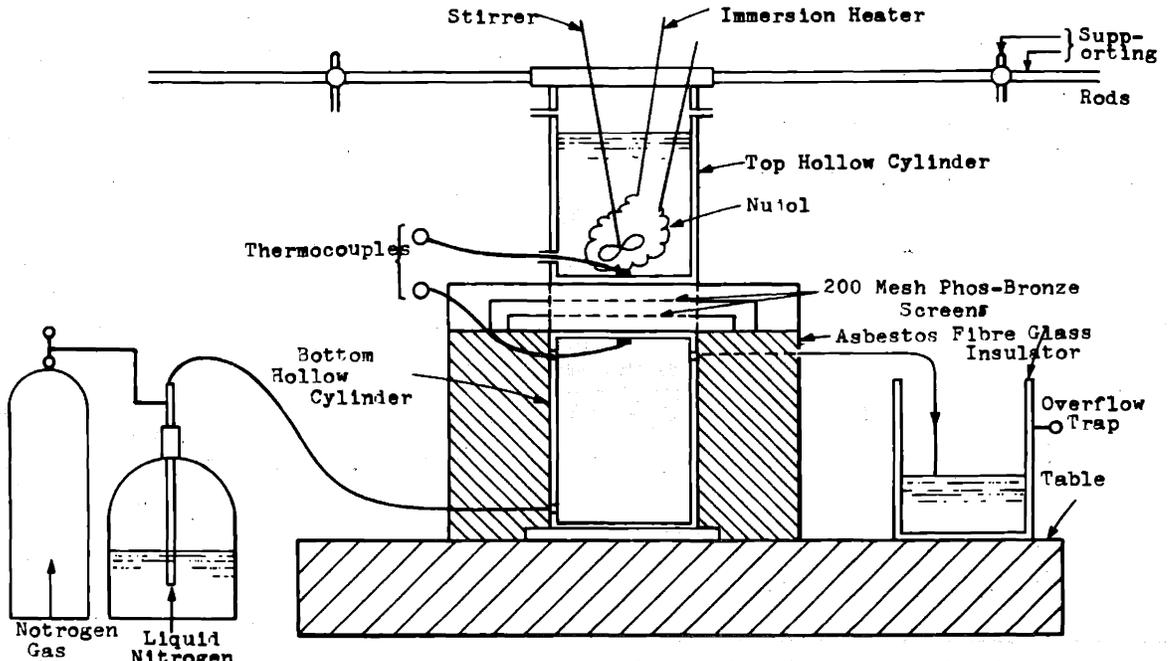
Figure III-B1   Experimental Set-up for Measurement of Effect of a
                Large Temperature Difference on the Frost Density

Stirrer   Immersion Heater
                                              Support-
                                           } ing
                                              Rods

Fibre Glass Insulation

Top Hollow
Cylinder

Nujol   Surrounding
           Temperature = -5°F

Thermocouples

Fibre Glass Insulation

200 Mesh Phos-Bronze Screen

Supporter

Supporter

Bottom Hollow Cylinder

Blower   Table
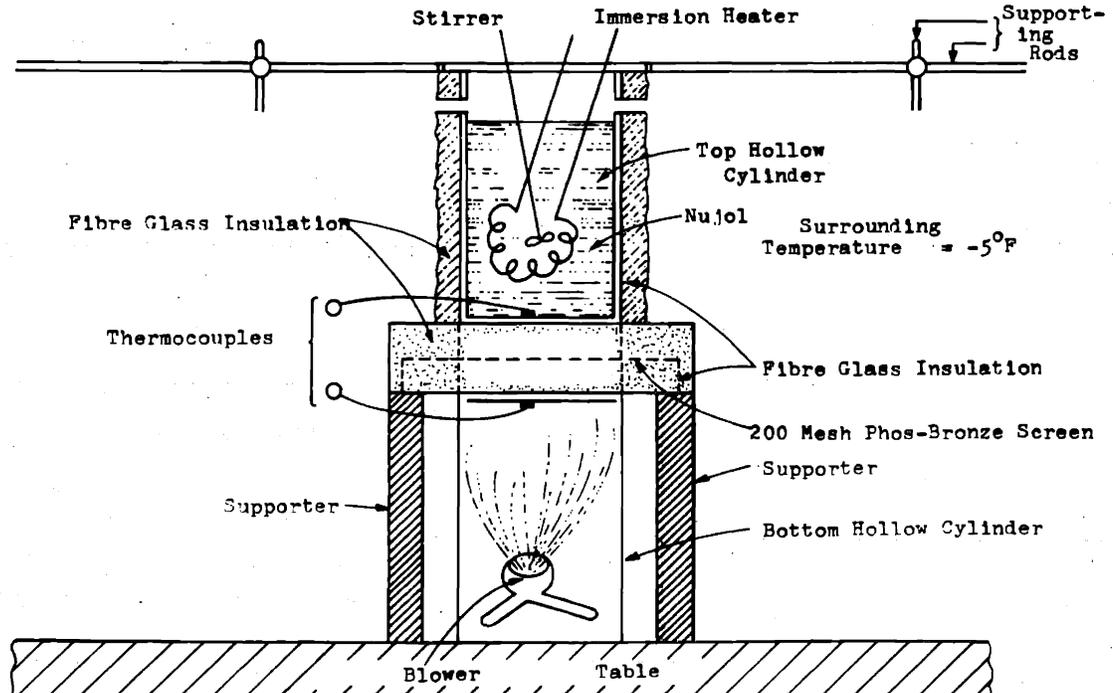
Figure III-B2   Experimental Set-up for Measurement of a Temperature
                Difference (Small) on the Frost Density

S E C T I O N IV

EXPERIMENTAL RESULTS

The experimental results of this thesis are separated into four catagories as follows.

A.   The effect of the independent system parameters, Reynolds number, humidity and gas temperature on the average frost density, frost thickness, thermal conductivity, and rate of heat transfer through the frost.

B.   The effect of a temperature gradient in the frost on its density.

C.   The measurement of density gradients in the bulk of the frost.

D.   The measurement of heat transfer coefficients for forced flow through a rectangular duct under the non-frosting conditions.

IV-A Effects of Various Independent System Parameters on Frost Properties

Summary

Average frost densities (densities of the entire frost layer), frost thicknesses and mass deposition rates were measured only after a smooth layer of frost was formed on the cold plate. The heat flux measurements were made over most of the frosting time (except for about the first ten minutes).

The range of independent system variables studied were: Reynolds number from 3,770 to 15,800, humidity

from a dew point at 14.3°F to a dew point at 58°F; and
gas temperature from 34°F to 93°F.

The most important measurements made in all the
frosting experiments are shown in Tables IV-A1 to IV-A5.

Average frost densities ranged from 0.053 gms./cc
to 0.163 gms./cc. Frost thickness varied from 0.08
inches to 0.40 inches. The total elapsed time for an
experiment was from 20 minutes to 180 minutes. The
quasi-steady state value of heat fluxes ran from
338 Btu/hr ft^2 to 830 Btu/hr ft^2.

The calculations of average thermal conductivity
of the frost (defined by Equation IV-A1) indicate that
over the average frost density range of 0.055 gms/cc to
0.163 gms./cc, the conductivity value varied from
0.0190 Btu/hr ft°F to 0.0534 Btu/hr ft°F. The point
thermal conductivity values of the frost (defined by
Equation IV-A2) increased both with density and temperature
and it ranged from approximately 0.01 Btu/hr ft°F to
0.1257 Btu/hr ft°F over the density range from 0.055
gms./cc to 0.163 gms./cc and temperature range from
-215°F to +10°F.

1.   Initial Phases of a Frosting Experiment

In the initial stage of the frosting experiments,
before a significant amount of frost was deposited, a
fog was observed in the gas space immediately adjacent
to the plate. The amount of fog increased with humidity
and gas temperature. Shortly thereafter, islands of

frost began to form. Initially, the heights of the individual islands increased. Before long, however, the spaces between them began to fill in and very soon a smooth, thin ($\approx$ 0.05 inch) layer of frost was formed. The formation of a smooth layer of frost occurred first at the upstream part of the test plate. Once a smooth layer of frost was formed, the gas over the frost appeared to be clear of fog particles.

The time required for the frost on the entire cold plate to become macroscopically smooth decreased with an increase in Reynolds number, but it was almost independent of gas phase humidity and gas temperature. The relationship between time required and the Reynolds number is shown in Table IV-Al. This relationship is very similar to one obtained by Brazinsky (14).

2. Frost Behavior as a Function of Time

The average frost density, frost thickness and the total mass deposition of the frost are continuously increasing functions of time as shown for a typical set of experimental conditions in Figures IV-Al and IV-A2. The time dependence of these parameters were, however, found to be strong functions of the system conditions as described in Sections IV-A3 to IV-A5.

The heat flux through the frost decreased sharply in the initial phase of an experiment, but later levelled out to a quasi-steady state value. The time dependence of heat flux through the frost for a typical set of experimental

conditions is shown in Figure IV-A3. The frost surface temperature increased with time in the initial transient (heat transfer) state of the frosting process, but once a quasi-steady state of heat transfer was reached, it attained almost a constant value.

The average thermal conductivity of the frost increased with time, particularly in the quasi-steady state of heat transfer. The temperature of any differential layer of frost decreased with time, as the additional frost continued to deposit on the cold plate. This can be seen from the data of Table IV-A3.

3.   Effect of Reynolds Number on Average Frost Density, Frost Thickness, Mass Deposition and Heat Transfer through the Frost

In the present study, three gas phase Reynolds numbers (based on hydrolic diameter), namely, 5580, 8,000 and 15,800 were used. At a constant gas temperature of approximately $73^{O}F$ and a constant humidity of dew point at $29.8^{O}F$, the effects of these three levels of Reynolds numbers on average frost density (density of the entire frost layer), frost thickness and on the mass deposition of the frost are described in Figures IV-A1 and IV-A2. It should be noted that each point in the figures represent the measurement of a separate run.

As shown in Figure IV-A1, the increase in Reynolds number from 5,580 to 15,800 increased significantly both the average frost density and the rate of frost densification.

Increases in Reynolds number however, decreased the frost thickness slightly at a given time. The total mass deposition, as shown in Figure IV-A2, increased considerably with the increase in Reynolds number.

The heat flux through the frost at various Reynolds numbers are shown in Figures IV-A3 to IV-A5. The results of these figures indicate that at all Reynolds numbers, the heat flux through the frost decreased sharply initially but levelled out at a later time to (different) quasi-steady state values. The magnitude of quasi-steady state heat flux value increased considerably with an increase in Reynolds number (from 510 Btu/hr ft^2 at Reynolds number = 5,580, to 830 Btu/hr ft^2 at Reynolds number = 15,800). These results are in qualitative agreement with the observation that the frost of a lower thermal resistance was deposited with increase in Reynolds number, as shown in Figure IV-A1.

4. <u>Effect of Humidity on Average Frost Density, Frost Thickness, Mass Deposition and Heat Transfer through the Frost</u>

The effects of varying the gas phase humidity on the average frost density, frost thickness, and mass deposition at two different sets of Reynolds number and gas temperature, two levels of humidities were studied.

Figure IV-A6 shows the effect of variation in humidity from gas dew point at 18°F to dew point at 33.2°F (at Reynolds number of approximately 5,800 and gas temperature

of 48°F) on average frost density and thickness.   For
this humidity range, it was found that at an equivalent
time, an increase in humidity increased the average frost
density slightly but frost thickness considerably. This, of
course, implies that the total mass deposition of the frost
would be significantly increased with humidity. This is
shown in Figure IV-A7. The slight effect of humidity on the
heat flux through the frost is demonstrated in Figures
IV-A10 and IV-A11.

Figures IV-A8, IV-A9, IV-A12 and IV-A4 describe the
results similar to the ones described above for two other
humidities and at Reynolds number of approximately 8,050
and at gas temperature of 75°F. Once again, as shown in
Figures IV-A8 and IV-A9, a slight increase in average frost
density and a considerable infrost thickness and mass
deposition rates were observed with an increase in humidity.
The slight decrease in the quasi-steady state value of heat
flux with increase in humidity for the same experimental
conditions can be seen from the results of Figures IV-A12
and IV-A4.

In summary, even though the effects of humidity on the
time variation in frost thickness, mass deposition and heat
flux found in the present thesis were very similar to ones
obtained by Brazinsky (14), the present research indicate
that the average frost density would be increased slightly
with humidity for the range of gas dew point at 14.3°F to
dew point at 33.2°F.

5. Effect of Gas Temperature on Average Frost Densities,
Frost Thicknesses, Mass Deposition Rates and Heat Fluxes
through the Frost

The effects of gas temperature on the frost properties
were examined for two different sets of Reynolds numbers
and humidities. In both the cases, two gas temperatures
were studied.

As shown in Figure IV-A13, at a Reynolds number of
approximately 5,500 and a gas dew point at 27.2°F, when the
gas temperature was increased from 34°F to 93°F, the average
frost density increased but frost thickness decreased so that
the total mass deposition of the frost at any time was
found to be almost unaffected (see Figure IV-A14). Thus,
a frost of a considerably lower thermal resistance deposited
at a higher gas temperature. It should be noted, however,
that the gas temperature affects the frost properties
significantly only in the quasi-steady state heat flux
region. The density and the thickness of the frost at a very
earlier time of the frosting process (in the transient heat
transfer state) are nearly independent of the gas temperature
as shown in Figure IV-A13.

Figures IV-A15 and IV-A16 show similar results for
another set of gas temperatures. The results of these figures
were obtained at a Reynolds number of approximately 8,200,
a gas dew point of about 30°F and at the gas temperatures of
52°F and 76°F.

As shown in Figures IV-A17 and IV-A18, for Reynolds

number of approximately 5,500 and a gas dew point at 27.2°F,
when the gas temperature was increased from 34°F to 93°F,
the quasi-steady state heat flux increased from 334 Btu/hr ft^2
to 535 Btu/hr ft^2. Similarly, the heat flux through the
frost versus time data for Reynolds number = 8,200, humidity
= dew point at 29.8°F and for the two values of gas
temperatures (52°F and 76°F) are described in Figures IV-A19
and IV-A4 respectively. As shown in the figures, the increase
in gas temperature (at constant Reynolds number and humidity)
from 52°F to 76°F increased the quasi-steady state heat
flux from 460 Btu/hr ft^2 to 560 Btu/hr ft^2.

6. Frost Thermal Conductivity

a. Average Conductivity of the Frost Layer

The average conductivity of the frost layer was
calculated from Equation IV-A1 below, using measured values
of the heat flux, the frost surface temperature thickness
and the temperature of the copper plate. All the thermal
conductivity values were measured in the quasi-steady
state of heat transfer region.

$$q = \frac{k_{avg}}{\delta} (T_s - T_w) \qquad (IV\text{-}A1)$$

Conductivity values calculated from Equation IV-A1
are tabulated in Table IV-A2. In Figure IV-A20, the
average frost conductivity is plotted as a function of
frost density. (The straight line shown in this diagram
was obtained such that the total sum of the square of the
deviation between the experimental values and the values

predicted by line was minimum). Figure IV-A20 also shows
the experimental data of average frost thermal conductivity
as a function of density obtained by Brazinsky(14). It
can be concluded from these results that there is a close
agreement between the average thermal conductivity data
of the present research and those obtained by Brazinsky
(14). The data of both the research works indicate that
over the density range of 0.055 gms./cc. to 0.163 gms/cc.
the average thermal conductivity increases about linearly
with average frost density.

The various points in Figure IV-A20 correspond to
frosts which were formed at different Reynolds numbers,
humidities and gas temperatures. The measured surface
temperatures of these frosts ranged from $-20^{\circ}F$ to $+18^{\circ}F$.
In plotting thermal conductivity as a function of density
only, it was implicitely assumed that a given value of
density implied a given frost structure, and therefore
that the average thermal conductivity of the frost layer
was a unique function of density. This is equivalent
to assuming that the frosts of the same densitym formed
at different Reynolds numbers, humidities and gas
temperatures have the same structure. Actually, some
of the scatter in the data, shown in Figure IV-A20,
may indeed be caused by structural differences of the
frosts of the same density. No definite trend, however,
was observed. (it should be noted that the scatter may
also be partly due to the different surface temperatures).

The measurements of average thermal conductivity by this method are accurate approximately within ± 7%. The detailed error analysis is described in Appendix N.

It should be noted that Equation IV-A1 is rigorously valid only for a true steady state situation. So, the results of Figure IV-A20 can be used to predict thermal conductivity of the frost only in the quasi-steady state heat transfer period.

b. Local or Point Thermal Conductivity

In order to obtain frost thermal conductivity as a function of density over a wide temperature range, temperatures within the frost as well as at the frost interfaces were measured. More specifically, temperatures within the frost were measured at two different vartical positions (in most of the experiments) with 0.003 inch diameter copper-constantan thermocouples. The measuring junctions of these probes were located at known heights from the plate. The stationary probe readings and the measured frost interface temperatures (i.e., frost-gas and frost-plate interfaces) were used to obtain a temperature profile at the end of each experiment. A typical temperature profile is shown in Figure IV-A21. In particular, Figure IV-A21 shows the temperature distribution within the frost at time of 79 minutes from the start of frosting process, (Run number 35) deposited at a Reynolds number of 15, 800, humidity of dew point at approximately 30°F

and gas temperature of 73°F. The data on temperature distribution within the frost for the frosting experiments are listed in Table IV-A3.

The temperature gradient, (dT/dx), was obtained at any particular location by graphical differentiation (i.e., by eye) of the frost temperature profile. These values of the gradient and the measured heat fluxes were used to calculate the local (or point) thermal conductivity from the following Equation IV-A2.

$$q = k_f(\frac{dT}{dx})\qquad\qquad\text{(IV-A2)}$$

Just as Equation IV-A1, above equation can be used only during the quasi-steady state period.

The frost thermal conductivities were generated over a temperature range of -215°F to +10°F and a density range of 0.055 gms./cc. to 0.163 gms./cc. Their values, as shown in Figure IV-A22, lie between 0.01 Btu/hr ft °F to 0.126 Btu/ hr ft °F. The straight lines through the data were calculated by the same method as used for the achievement of the line shown in Figure IV-A20 (by the method of least squares). At any given density, the thermal conductivity showed a marked increase with temperature. For a given temperature, the thermal conductivity increased with density; the rate of this increase being greater at higher temperatures. In calculating point thermal conductivity data from Equation IV-A2, once again, it was implicitly assumed that at any given temperature a particular frost structure was implied

by a given value of frost denisty.

Figure IV-A22 shows the experimental data of Brazinsky (14) for thermal conductivities. It can be seen from the figure that the data of Brazinsky (14) as well as of the present research gave an almost identical correlation for thermal conductivity as a function of density and temperature.

The model of the frost structure as one in which a symmetrical matrix of ice cubes are inrerconnected by ice rods (14) is found to predict thermal conductivity correlation well in agreement with one obtained from experimental data. The dotted lines in Figure IV-A22 show these correlations for various temperatures. It can be seen from the results of this figure that the theoretical predictions agree quite well with the experimental results. The details of the theoretical **model is** described in Section **V-A.**

Table IV-A4 lists the values of point thermal conductivity as a fuction of density ar five different temperatures (-215°F, -145°F, -80°F, 0°F, and +10°F), as described in Figure IV-A22. These values are estimated to be accurate within approximately ±10%. The details of the error analysis is shown in Appendix N.

IV-B Experimental Measurements of the Effects of a Temperature Gradient Across the Frost on its Density

As shown in Section IV-A, it was found experimentally

that there existed a large temperature gradient in the
frost interior. In order to evaluate the effect of this
temperature gradient on the frost density, an experiment
program was undertaken. Since, the experimental study was
essentially divided into two parts based on the magnitude
of the temperature difference across the frost, the results
are also separated on the same basis as described below.

1. Effect of a Large Temperature Difference across the
    Frost on its Density

In this study, a frost layer was exposed to a large
temperature gradient which was very similar to one obtained
in the frosting experiments of Section IV-A (i.e. bottom
end at $-315^{\circ}F$ and top surface at about $15^{\circ}F$).

Several experiments were made for various times,
densities and thicknesses of the frost. The temperature
difference across the frost was almost identical in all
the experiments. The ranges of the independent system
variables considered were as follows:

a. The length of time for an experiment varying from 2.5
hours to 7.0 hours.

b. The initial average frost density varying from 0.148
gms./cc. to 0.314 gms./cc.

c. The initial frost thickness varying from 0.382 inch
to 0.582 inch.

In three tests, the frost layer was divided into two
slices and in the remaining one it was divided into three
slices (see Section III-B). The results of these experiments

are described in Table IV-B1.

The uniformity of the laid frost in each experiment was determined by measuring the densities at various positions on the copper plate. A typical set of results for this kind of measurements are shown in Table IV-B2. From these results it can be concluded that the average frost density values at various positions on the plate were approximately within 5% of each other.

The density values reported in Table IV-B1 are accurate within ± 8.5%. The results of Table IV-B1 indicate that the density values of the frost slices are changed by the temperature gradient only within the accuracy of their measurements. The details of the error analysis of the density measurements is shown in Appendix N.

The experimental results indicate that there was no significant effect of the length of an experiment and of the initial values of the frost density and the thickness on the density of the frost slices. An average of the differences in the intial and the final values of all the frost slices was 0.008 gms./cc. or less than 4% of the average initial frost density values for all the experiments. Thus, it can be concluded from these results that within the accuracy of this kind of measurements, a large temperature difference across the frost layer did not change the density significantly.

2. <u>Effect of a Small Temperature Difference across the Frost on its Density</u>

Two experiments were performed with a small temperature difference across a frost (bottom surface at $-4°F$ and top surface at $+23°F$; see Section IV-B). The lengths of time for the two experiments were six and twelve hours. In each experiment, the frost under investigation was divided into two slices of different thickness. In both the experiments, the total initial thickness was approximately 0.37 inch and the initial average frost density was approximately 0.15 gms./cc. The results of this study are described in details in Table IV-B3.

The results of Table IV-B3 indicate that there is a significant mass transfer (mass transfer = 9.50×10^{-4} gms./ $cm^2 hr$) from the top slice to the bottom slice of the frost at the temperature level considered in this study. The magnitude of mass transfer also increased with time. Thus, it can be concluded from these results that there will be a mass transfer due to temperature gradient at the temperature level of about $15°F$.

The uniformity of the laid frost in this study was identical to one described in Table IV-B2.

3. <u>Measurement of Density Gradient in the Frost by Natural Convection at Liquid Nitrogen Temperature.</u>

As described in Section III-B, one experiment (Run number R-7) was performed to determine the density gradient in the frost deposited by natural convection on a liquid nitrogen cooled plate. The results of this experiment

are shown in Table IV-B4. In this experiment the
deposited frost was divided into three slices by the
method described in Section III-B. The measured density
values of each slice of the frost (of varying thickness)
after 6.5 hours of the experiment was found to be identical
with a deviation of approximately ±4% from the mean value.
The average density value was approximately 0.035 gms./cc.
The surrounding temperature in this experiment was 15°F.

Thus it can be concluded from the results of Table
IV-B4 that there is no significant density gradient in the
frost deposited by natural convection on a surface at
cryogenic temperature.

The measurements of density in all the experiments
described above were, once again accurate within ±8% of
its value. The details of error analysis is shown in
Appendix N.

IV-C <u>Measurement of Density Gradient in the Frost Deposited
by Forced Convection on a Liquid Nitrogen Cooled Plate</u>.

For a typical set of experimental conditions,(Re = ,
15,800; P_g= dew point at 30°F; T_g = 73°F), the density
gradient within the frost was measured by the method
described in Section III-C. The results of these
measurements are described in Figure IV-C1. As shown in
the figure, the density of the bottom 0.0625 inch thick
frost was found to increase almost identically as the
density of the entire frost layer between the time of 26
min to 144 min from the start of the frosting process.

In one experiment, (at time = 106.9 min from the start
of frosting) the density of the bottom 0.1250 inch frost
was measured and was found to be identical to the density
of the entire frost layer.   The thickness of the frost
during this density gradient measurement was found to
increase from 0.091 inch to 0.256 inch.

The variation in temperature distribution with the
frost with time during this period of density gradient
measurement is shown in Figure IV-C2.   As expected, the
temperature of every existing frost layer decreased as
more frost was deposited.

The results of Figure IV-C1 and IV-C2 indicate that
in order for a densification of the bottom 0.0625 inch
thick frost layer from 0.085 gms./cc. to 0.161 gms./cc.,
a significant amount of water had to pass the temperature
level of the frost layer located at 0.0625 inch away from
the cold wall (which varied from -44°F to -173°F)

A possible mechanism by which the required amount of
water can be transported at that temperature level (average
of -108°F) is discussed in Section V-C.

The measurement of the density of each slice of the
frost by this method is accurate within approximately ±12%.
The detailed error analysis for this kind of measurement
is shown in Appendix N.

IV-D Measurement of Heat Transfer Coefficients under the
Non-frosting Conditions

In order to evaluate heat and mass transfer characteristics

of the frosting process, an experimental program was
carried out to measure the heat transfer coefficients
under non-frosting conditions in the system of Figure
III-A1. Dry air was blown over the copper plate which
was covered with a slightly corrigated aluminum foil,
in order to obtain a frost like surface over the copper
plate. The temperature of the aluminum foil was maintained
at approximately -12°F by circulating liquid Freon-12 in
the calorimeter.

The results of this experimental program are shown
in Figure IV-D1. The figure shows the heat transfer
coefficient as a function of Reynolds number for the gas
temperature of approximately 82°F. The experimental
data were obtained with the Reynolds number range from
3,380 to 15,720. The heat transfer coefficient varied
from 3.12 Btu/hr ft^2°F to 11.08 Btu/hr ft^2°F over this
range of Reynolds number.

A solid line in Figure IV-D1 shows the correlation
between heat transfer coefficient and Reynolds number as
obtained from the Sleicher and Tribus's theoretical
analysis at the conditions of the experiments (i.e.
T_g= 82°F, T_w=12°F). One can see from the figure that
the theoretical correlation agree well with the experimental
results. The maximum absolute deviation between
experimental and theoretical values of heat transfer
coefficient is found to be within 5%. The experimental
data are estimated to be accurate within $\pm$4%. The

details of the error analysis of the experimental data
is shown in Appendix N.

The experimental data shown in Figure IV-D1 are also
listed in Table IV-D1.

Table   IV-A1

Effect of Reynolds Number on Length of Time Required to Form a Smooth Frost Layer

Reynolds Number	Time to Form Smooth Frost (minutes)
5,500	~39
8,000	~28
15,800	~10

Table IV-A2

Summary of Experimental Results

Run No.	Time From Start (mins.)	Reynolds Number	Humidity (dew point °F)	Gas Temp. (°F)	Frost (Average) Density (gms/cc)	Thickness of Frost (inch)	Mass Deposition (lbm/ft^2)	Quasi-steady State Heat Flux (Btu/hr ft^2)	Average Thermal Conductivity of Frost ($\frac{Btu}{hr\ ft\ °F}$)	Surface Temp. (°F)
2	64.0	3,800	58.1	75	0.064	0.344	0.1140	368	0.0316	+18
3	36.5	3,740	57.9	76	0.056	0.217	0.0665	-	-	-
4	20.0	3,740	58.0	75	0.054	0.129	0.0364	-	-	-
5	66.7	6,140	16.7	47	0.054	0.119	0.0364	-	-	-
6	98.0	6,100	19.0	47	0.056	0.195	0.0568	368	0.0190	+1
7	141.0	6,090	17.5	48	0.063	0.258	0.0847	368	0.0251	+3
8	73.0	5,490	32.5	47	0.056	0.220	0.0634	348	0.0198	+7
9	68.0	5,500	33.3	48	0.063	0.219	0.0709	348	0.0236	+7
10	43.0	5,590	33.1	48	0.058	0.137	0.0417	-	-	-
11	69.0	5,820	27.5	33	0.064	0.125	0.0417	-	-	-
12	61.0	5,770	26.8	34	-	-	-	-	-	-
13	123.0	5,790	28.0	34	0.065	0.218	0.0747	330	0.0190	+2
14	95.0	5,790	26.1	34	0.062	0.187	0.0606	334	0.0171	-7
15	57.0	5,090	27.1	93	0.059	0.070	0.0215	-	-	-
16	132.5	5,090	25.9	93	0.078	0.187	0.0763	539	0.0279	+15
17	61.0	5,090	25.9	93	0.058	0.086	0.0262	-	-	-
18	97.5	5,130	28.0	93	0.074	0.168	0.0646	539	0.0230	+13
20	61.5	8,110	14.2	72	0.060	0.098	0.0303	-	-	-
21	99.9	8,110	14.6	77	0.077	0.112	0.0449	640	-	-
22	160.0	8,110	14.4	73	0.090	0.157	0.0736	645	0.0349	+1
23	71.4	8,395	30.1	52	0.066	0.162	0.0550	-	-	+1
24	62.6	8,430	29.5	50	0.068	0.160	0.0566	-	-	+3
25	98.2	8,465	30.2	52	0.074	0.258	0.0995	485	0.0230	+5
26	36.2	7,970	30.0	76	0.058	0.125	0.03765	-	-	-
27	122.5	7,995	30.4	75	0.089	0.248	0.1145	560	0.0358	+8
28	60.0	8,050	30.9	77	0.070	0.155	0.0567	-	-	+6
29	76.3	5,570	29.8	74	0.064	0.203	0.0670	510	0.0270	+4
30	104.4	5,600	29.2	72	0.075	0.225	0.0880	510	0.0298	+6
31	45.1	5,570	29.0	72	0.061	0.144	0.0461	-	-	-
32	68.2	5,570	28.6	76	0.068	0.187	0.0658	510	0.0249	+4
33	180.2	8,465	30.7	51	0.095	0.400	0.2003	475	-	-
34	152.5	5,530	33.2	48	0.083	0.375	0.1625	350	0.0338	+7.7
35	79.1	15,800	27.3	73.3	0.126	0.179	0.1170	871	0.0376	+7
36	26.5	15,750	28.0	73.5	0.090	0.091	0.0426	1,031	0.0265	-20
37	58.2	15,680	28.7	70.0	0.124	0.156	0.1011	864	0.0348	+7
38	144.8	15,850	30.2	69.0	0.163	0.256	0.2208	830	0.0534	+10.5
39	106.9	15,800	30.1	70.0	0.136	0.203	0.1440	835	0.0440	+10.0

Table   IV-A3

Temperature as a Function of Position in Frost

Run Number	Position in Frost, i.e., Distance from Copper Plate (inches)	Temperature ($^{\circ}$F)
10	0.086	-80
11	0.046	-131
	0.073	-53
13	0.023	-253
	0.077	-120
14	0.078	-116.6
15	0.023	-225
16	0.062	-166
	0.125	-60
17	0.031	-181.5
18	0.054	-161
	0.085	-97
20	0.062	-119
	0.090	-56
21	0.040	-109
	0.062	-65
22	0.078	-76
23	0.034	-131
24	0.069	-151
	0.125	-52
25	0.085	-157
	0.164	-53
27	0.023	-203
	0.102	-69
28	0.023	-221
	0.093	-37
29	0.040	-236
	0.109	-100
30	0.032	-236
	0.071	-160
33	0.074	-214
34	0.101	-163.5
35	0.057	-117
	0.103	-33
36	0.046	-76
37	0.056	-77
38	0.044	-205
	0.070	-159
39	0.069	-143

Table   IV-A4

Calculated Point Conductivities as a Function of Temperature
and Density

Temperature = -215°F

Run number	ρ_f (gms./cc.)	k_f (Btu/hr ft^2°F/ft)
10	0.058	0.0140
11	0.064	0.0122
13	0.066	0.0105
14	0.062	0.0107
15	0.059	0.0128
16	0.078	0.0185
17	0.058	0.0133
18	0.074	0.0166
20	0.060	0.0150
21	0.077	0.0111
22	0.090	0.0151
23	0.066	0.0134
24	0.068	0.0164
25	0.074	0.0198
27	0.089	0.0155
28	0.070	0.0146
29	0.064	0.0184
30	0.075	0.0197
33	0.095	0.0222
34	0.083	0.0162
35	0.126	0.0190
36	0.090	0.0164
37	0.124	0.0153
38	0.163	0.0321
39	0.136	0.0278

Temperature = -145°F

Run number	ρ_f (gms./cc)	k_f (Btu/hr ft°F)
10	0.058	0.0175
13	0.066	0.0139
14	0.062	0.0155
16	0.078	0.0242
18	0.074	0.0249
20	0.060	0.0228
21	0.077	0.0230
22	0.090	0.0224
23	0.066	0.0168

Table IV-A4 (contd.)

Run number	ρ_f (gms./cc.)	k_f (Btu/hr ft°F)
24	0.068	0.0214
25	0.074	0.0255
27	0.089	0.0263
28	0.070	0.0188
29	0.064	0.0236
30	0.075	0.0283
33	0.095	0.0330
34	0.083	0.0278
35	0.126	0.0302
36	0.090	0.0204
37	0.124	0.0216
38	0.163	0.0451
39	0.136	0.0354

Temperature = -80°F

Run number	ρ_f (gms./cc.)	k_f (Btu/hr ft°F)
10	0.058	0.0251
13	0.066	0.0232
14	0.062	0.0278
16	0.078	0.0299
18	0.074	0.0321
20	0.060	0.0317
21	0.077	0.0267
22	0.090	0.0336
23	0.066	0.0287
24	0.068	0.0294
25	0.074	0.0317
27	0.089	0.0343
28	0.070	0.0258
29	0.0641	0.0303
30	0.075	0.0354
33	0.095	0.0495
34	0.083	0.0366
35	0.126	0.0384
36	0.090	0.0444
37	0.124	0.0459
38	0.163	0.0629
39	0.136	0.0494

Table IV-A4 (contd.)

Temperature = 0°F

Run number	ρ_f (gms./cc.)	k_f (Btu/hr ft°F)
13	0.066	0.0557
14	0.062	0.0507
16	0.078	0.0531
18	0.074	0.0535
21	0.077	0.0594
22	0.090	0.0672
23	0.066	0.0577
25	0.074	0.0660
28	0.070	0.0652
29	0.0641	0.0532
30	0.075	0.0567
33	0.095	0.0720
34	0.083	0.0649
35	0.126	0.0980
37	0.124	0.0865
38	0.163	0.1152
39	0.136	0.0988

Temperature = 10°F

Run number	ρ_f (gms./cc.)	k_f (Btu/hr ft°F)
16	0.078	0.0749
18	0.074	0.0720
38	0.163	0.1257
39	0.136	0.1152

Table IV-B1

Measurements for the Effects of a large Temperature Difference across the Frost on its Density

Run No.	Length of Time for run (hours)	Total Thickness of Frost (inches)	Initial Density of frost (gms./cc.)			Final Density of frost (gms./cc.)			Initial Thickness of Frost (inches)			Frost Thickness of Frost (inches)			Frost Surface Temp °F	cold wall Temp °F
			Top Slice	Middle Slice	Bottom Slice	Top Slice	Middle Slice	Bottom Slice	Top Slice	Middle Slice	Bottom Slice	Top Slice	Middle Slice	Bottom Slice		
R-3	2.5	0.531	0.314	–	0.277	0.327	–	0.267	0.187	–	0.344	0.187	–	0.348	15	-305
R-4	7.0	0.586	0.243	–	0.243	0.237	–	0.268	0.219	–	0.367	0.219	–	0.367	13	-305
R-5	6.0	0.500	0.217	0.238	0.220	0.216	0.234	0.218	0.187	0.187	0.125	0.187	0.187	0.125	15	-305
R-6	3.5	0.382	0.142	–	0.145	0.138	–	0.155	0.195	–	0.187	0.187	–	0.187	13	-305

Table IV-B2

Determination of Uniformity of the Laid Frost in Density Measurements of the

Experiments Described in Section IV-B

Density at Position 1 on the Plate	Density at Position 2 on the Plate	Density at Position 3 on the Plate
0.461 gms./cc.	0.448 gms./cc.	0.469 gms./cc.

Positions 1,2 and 3 are random positions on the Copper Plate.

Table   IV-83

Measurements of effects of a Small Temperature   Difference across the Frost on its Density.

Run No.	Length of Run (hours)	Frost Thickness (Initial)			Initial Mass of Frost		Final Mass of Frost		Initial Density		Final Density		Top Surface Temp. °F.	Bottom Surface Temp. °F.
		Top (inches)	Bottom (inches)	Total (inches)	Top Slice $(\frac{gms}{cm^2}$ of frost Cross section)	Bottom Slice $(\frac{gms}{cm^2}$ of frost Cross section)	Top Slice $(\frac{gms}{cm^2})$	Bottom Slice $(\frac{gms}{cm^2})$	Top Slice $(\frac{gms}{cc})$	Bottom Slice $(\frac{gms}{cc})$	Top Slice $(\frac{gms}{cc})$	Bottom Slice $(\frac{gms}{cc})$		
R-8	6.0	0.1328	0.25	0.3828	0.044	0.0909	0.0377	0.0978	0.1305	0.141	0.111	0.150	~23	~-4
R-9	12.0	0.1641	0.2031	0.3672	0.0664	0.0893	0.0560	0.0986	0.1592	0.173	0.136	0.192	~23	~-4

Table   IV-B4

Density Gradient Measurements in Frost Deposited by Natural Convection on a

Liquid-Nitrogen Cooled Surface

Run Number	Length of Run (hours)	Total Thickness of Frost (inches)	Final Thickness of Frost			Final Density of Frost			Cold Plate Temp. (°F)	Surrounding Temp. (°F)
			Top Slice (inches)	Middle Slice (inches)	Bottom Slice (inches)	Top Slice $(\frac{gms.}{cc.})$	Middle Slice $(\frac{gms.}{cc.})$	Bottom Slice $(\frac{gms.}{cc.})$		
R-7	6.5	0.414	0.226	0.117	0.070	0.035	0.034	0.036	-305	20

Table IV-D1

Experimental Heat Transfer Coefficients in Non-Frosting Conditions

Run Number	Gas Temperature ($^\circ$F)	Plate Temperature ($^\circ$F)	Reynolds Number	Heat Transfer Rate (Btu/hr ft^2)	Heat Transfer Coefficient (Btu/hr ft^2 $^\circ$F)
H-1	82.6	-11.5	12,280	870	9.25
H-2	82.6	-11.5	15,720	1,087	11.08
H-3	82.6	-11.5	13,650	931	9.90
H-4	82.6	-11.3	12,300	886	9.45
H-5	82.6	-11.3	11,080	779	8.30
H-6	82.6	-15.3	8,110	698	7.12
H-7	82.6	-11.5	13,410	900	9.55
H-8	82.6	-11.5	15,280	1,087	11.08
H-9	82.6	-11.85	3,380	296	3.14
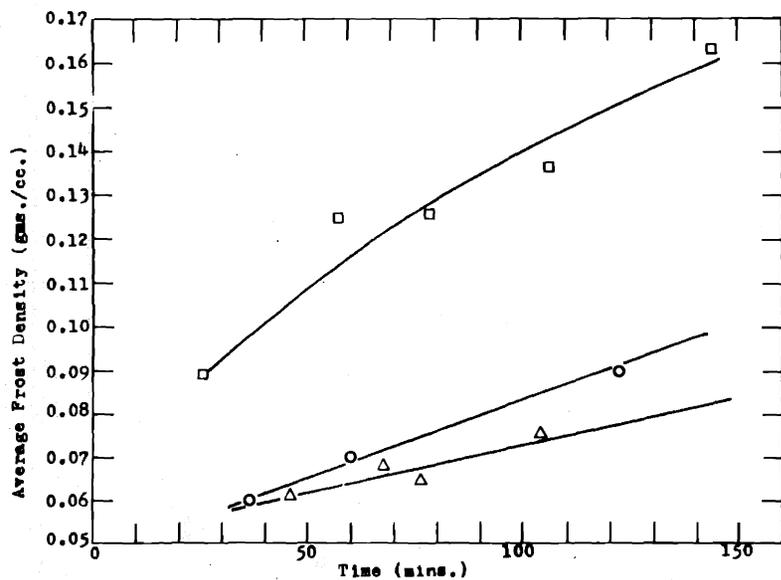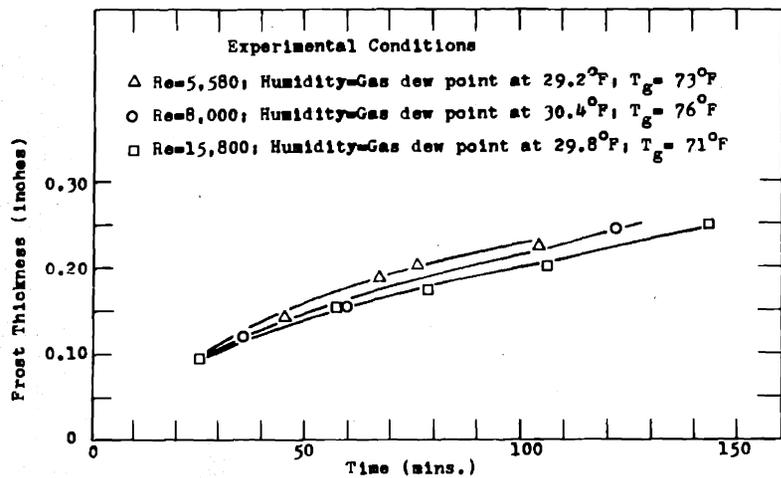
Figure IV-A1   Effect of Reynolds Number on Average Frost Density
                and Frost Thickness
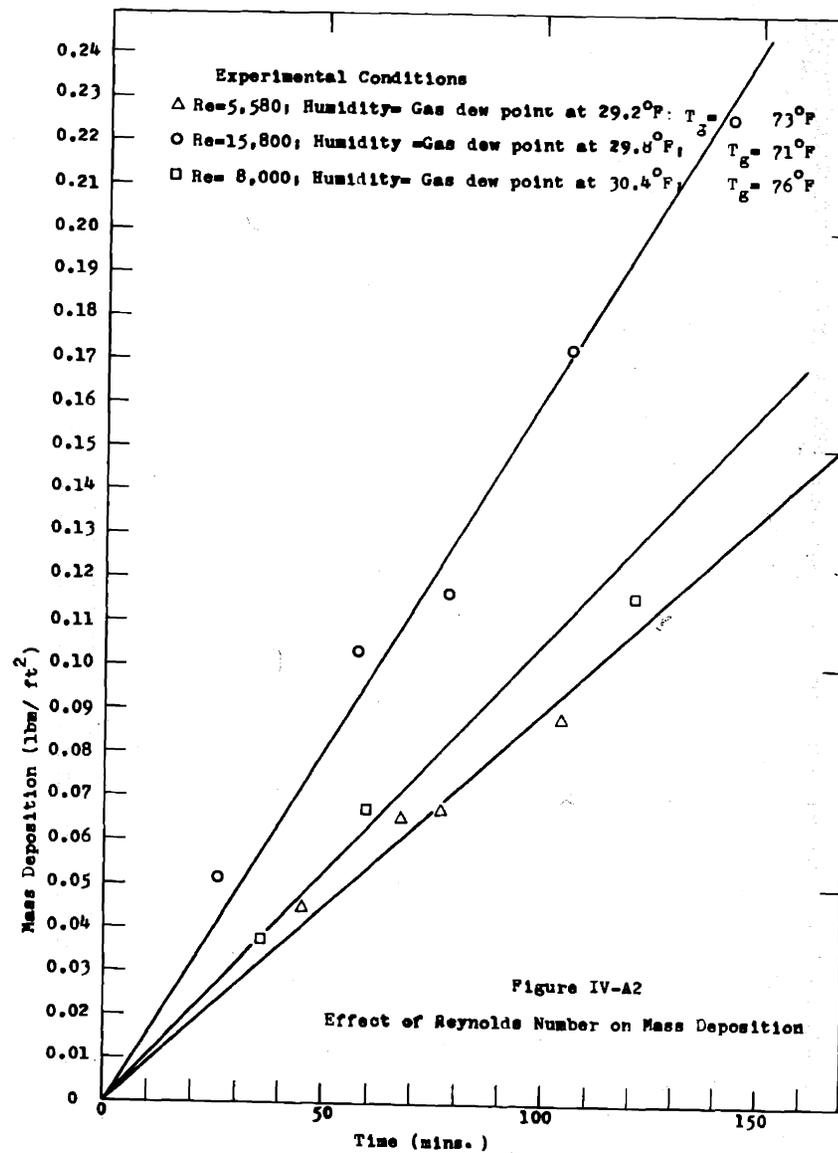
Figure IV-A2

Effect of Reynolds Number on Mass Deposition
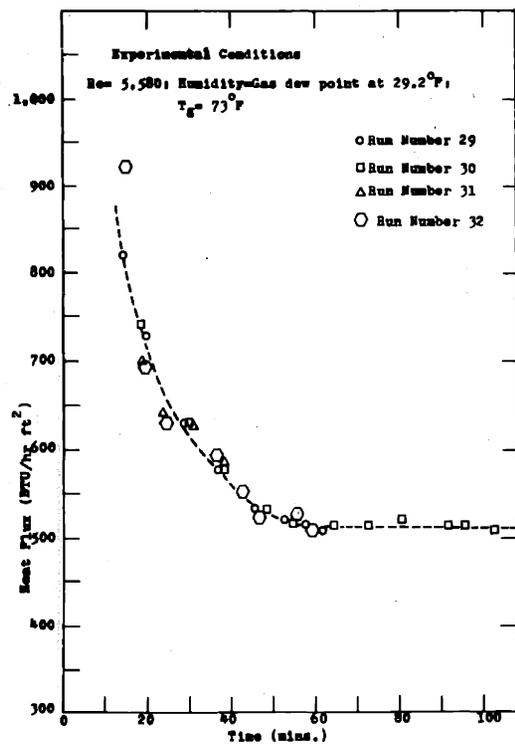
Figure IV-A3   Heat Flux versus Time
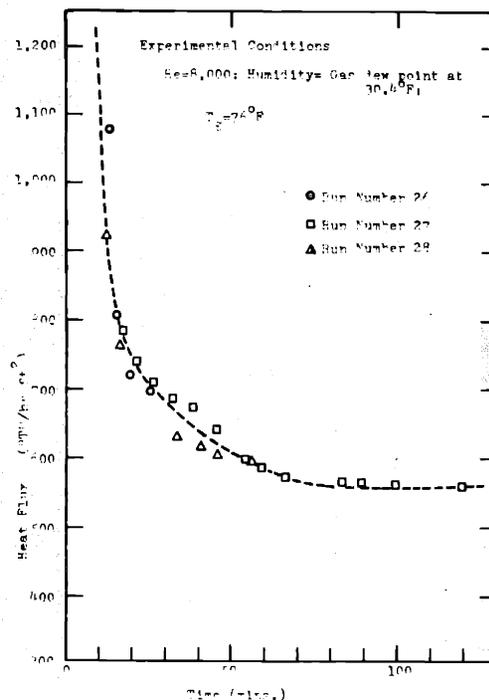
Figure IV-A4   Heat Flux versus Time
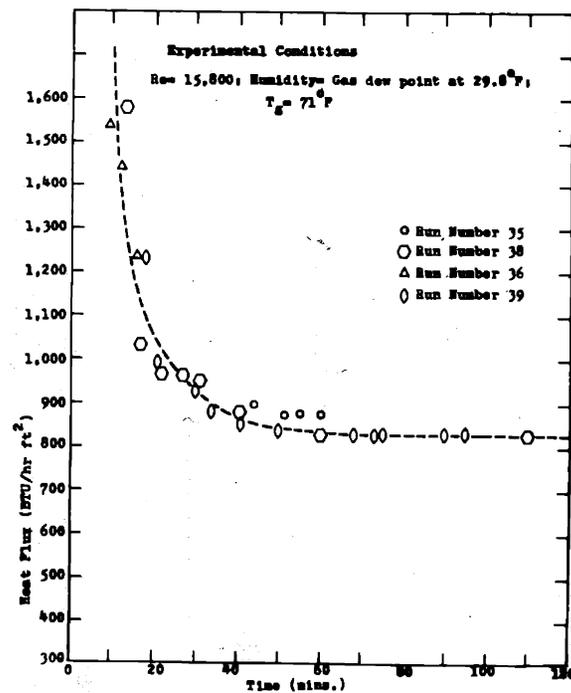
Figure IV-A5   Heat Flux versus Time
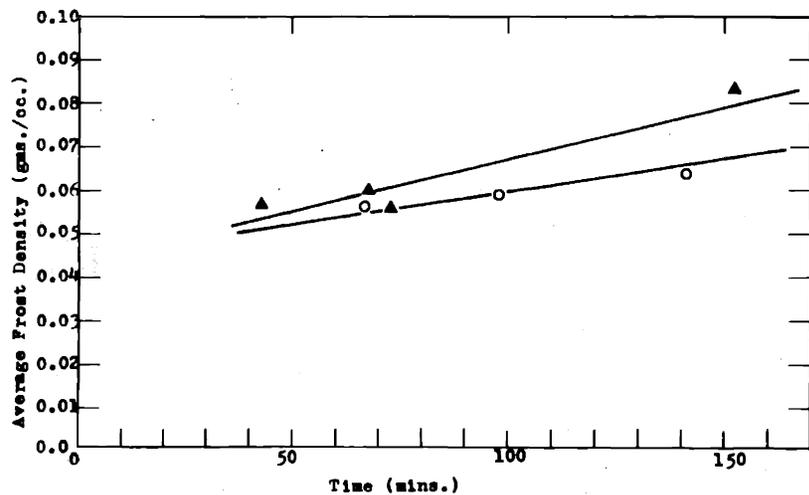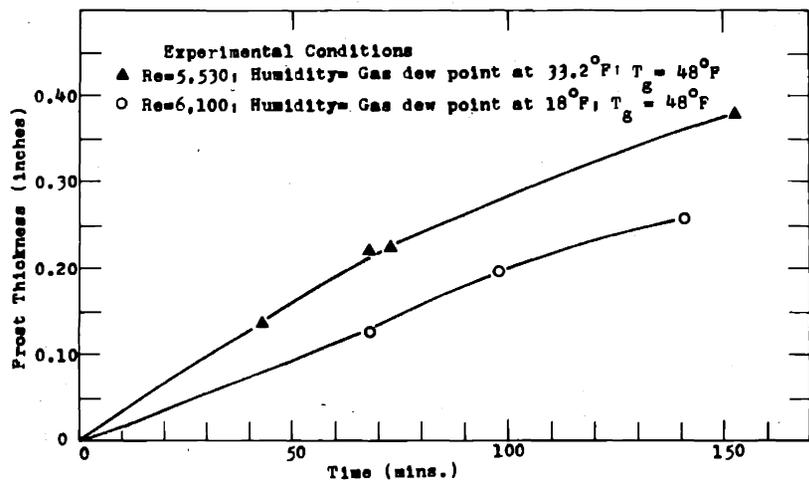
Figure IV-A6 Effect of Humidity on Average Frost Density and
Frost Thickness
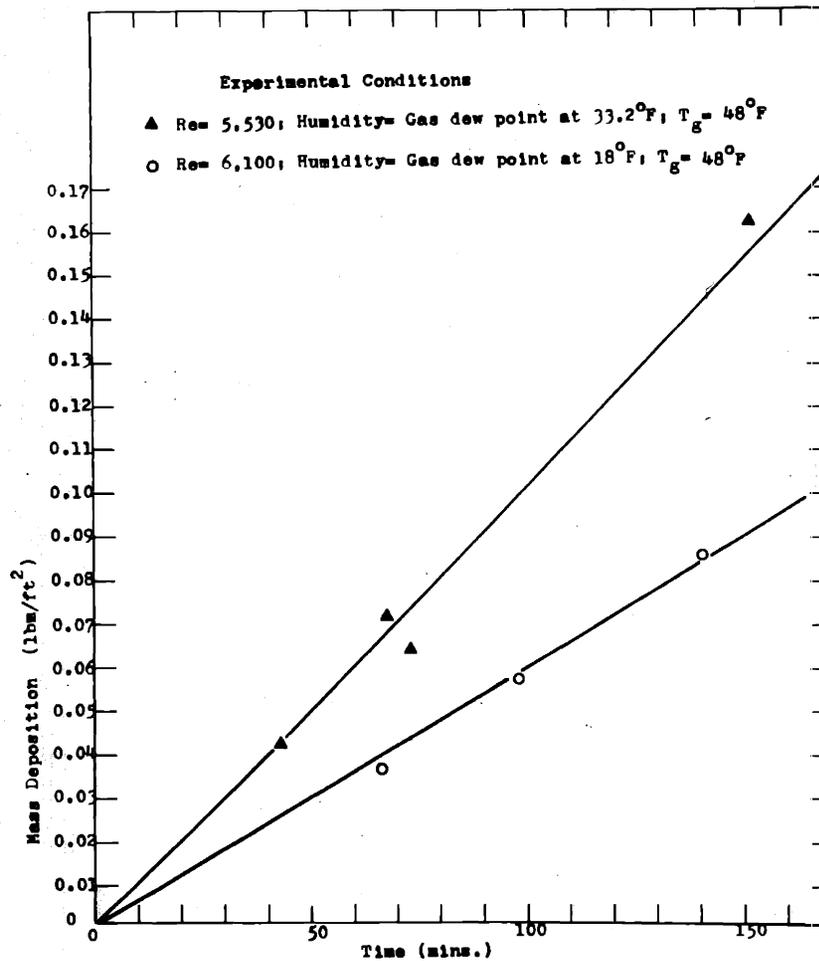
Figure IV-A7 Effect of Humidity on Mass Deposition
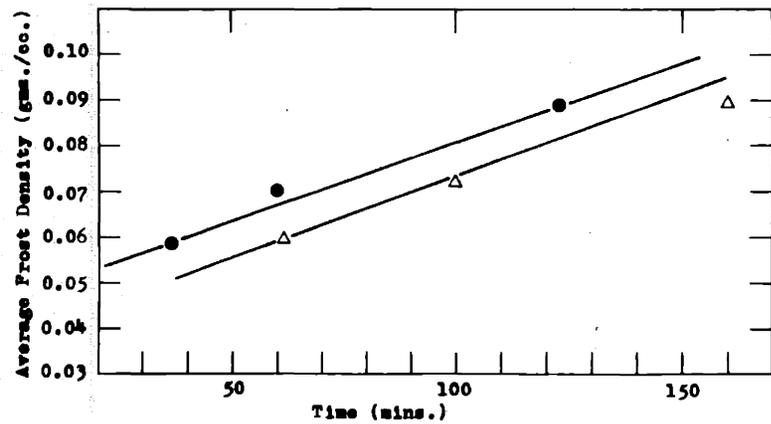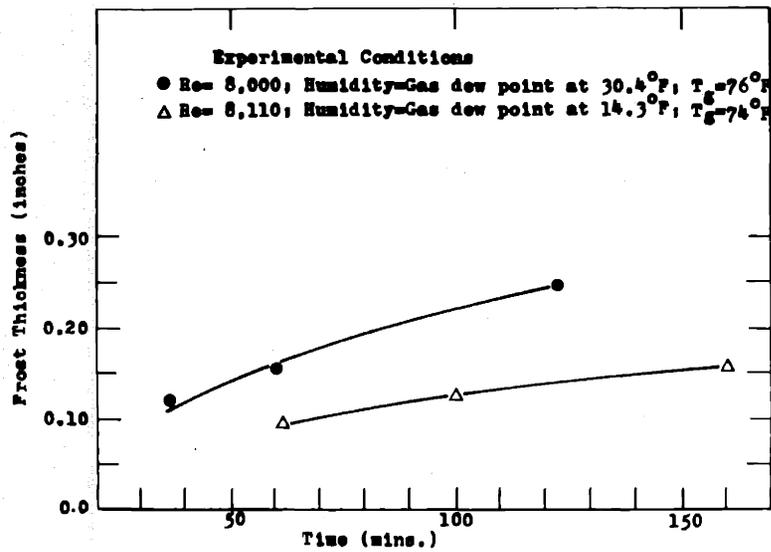
Figure IV-A8 Effect of Humidity on Average Frost Density
and Frost Thickness
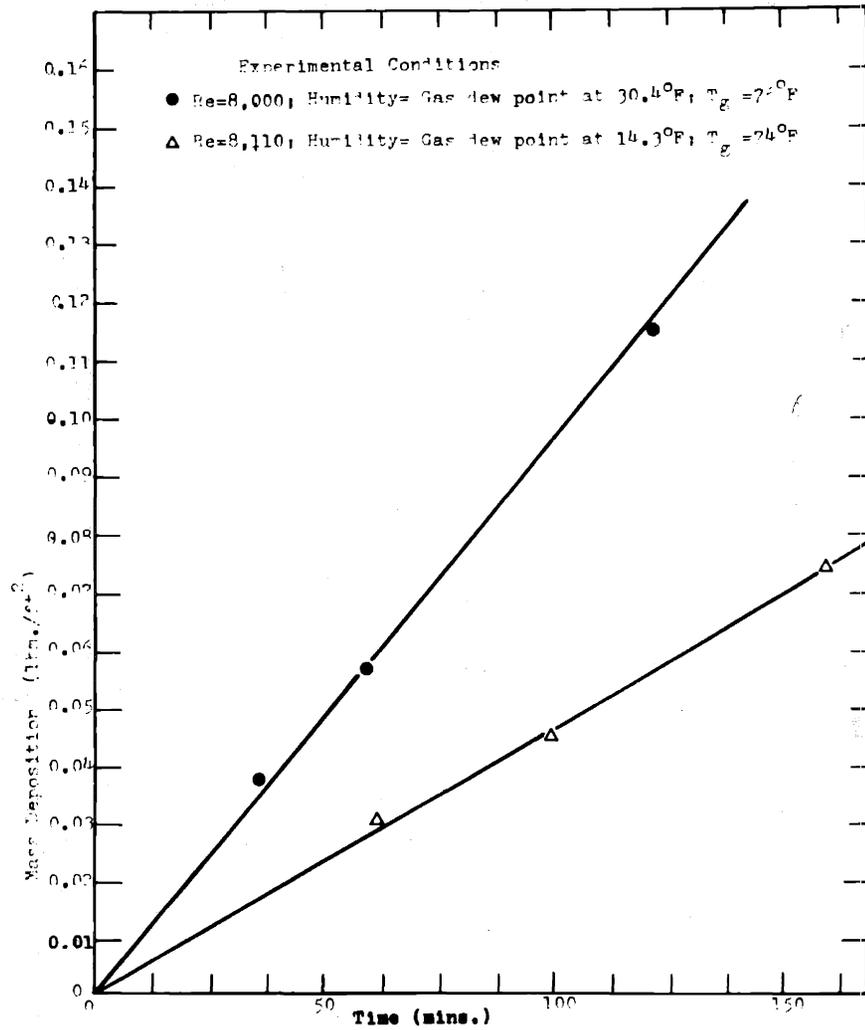
Figure IV-A9 Effect of Humidity on Mass Deposition
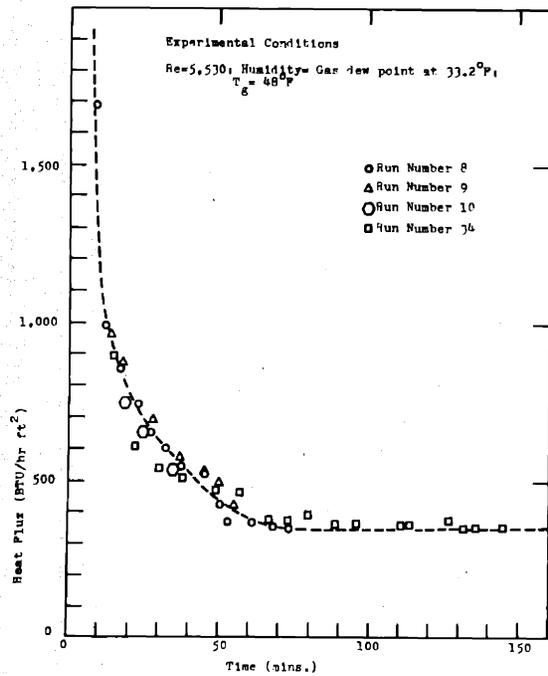
Figure IV-A10   Heat Flux versus Time
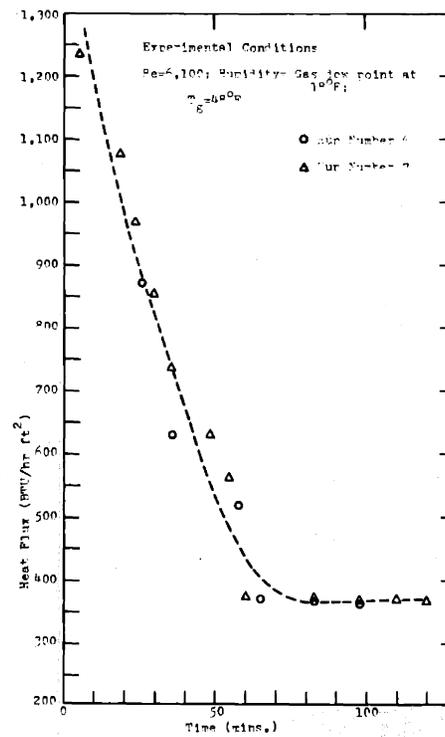
Figure IV-A11   Heat Flux versus Time
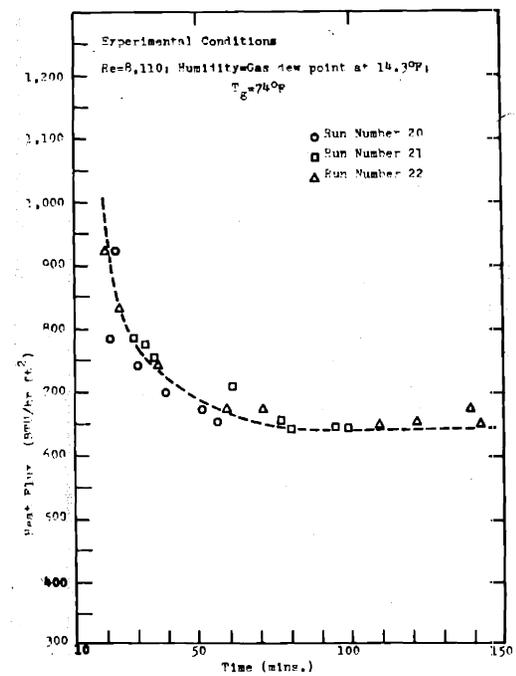
Figure IV-A12   Heat Flux versus Time
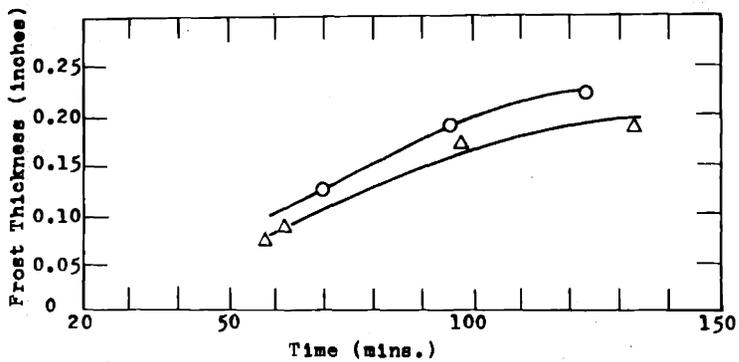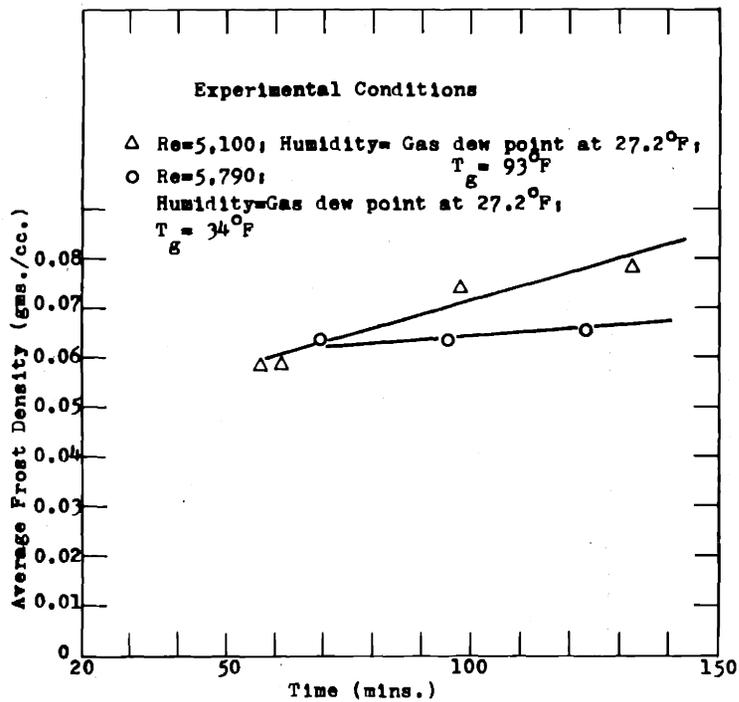
Figure IV-A13   Effect of Gas Temperature on Average
Frost Density and Frost Thickness
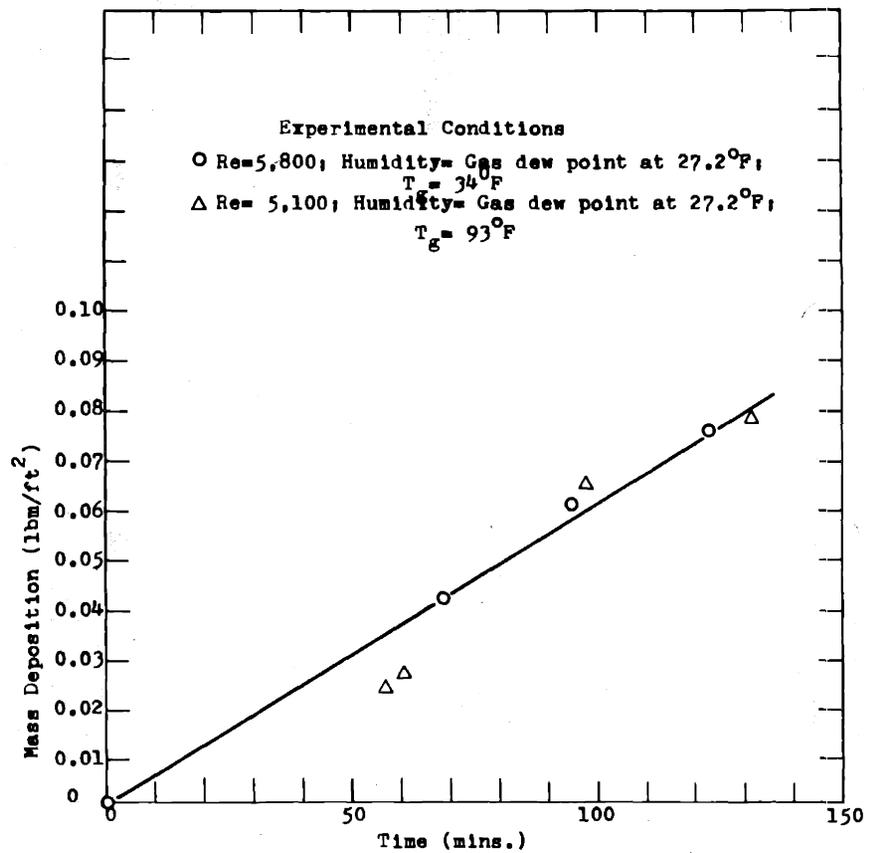
Figure IV-A14   Effect of Gas Temperature on Mass Deposition
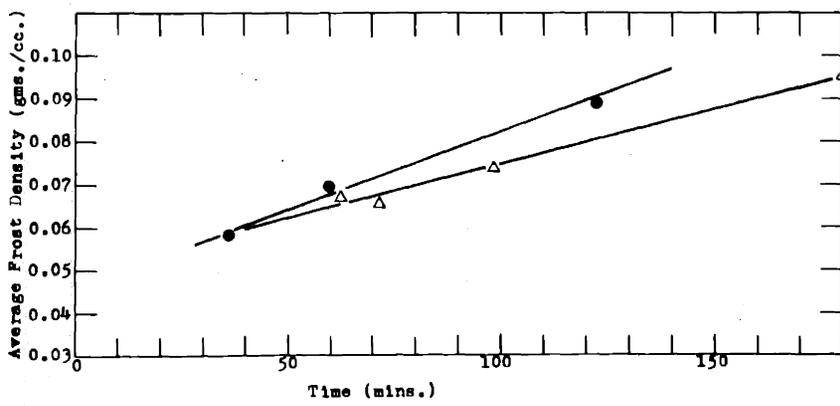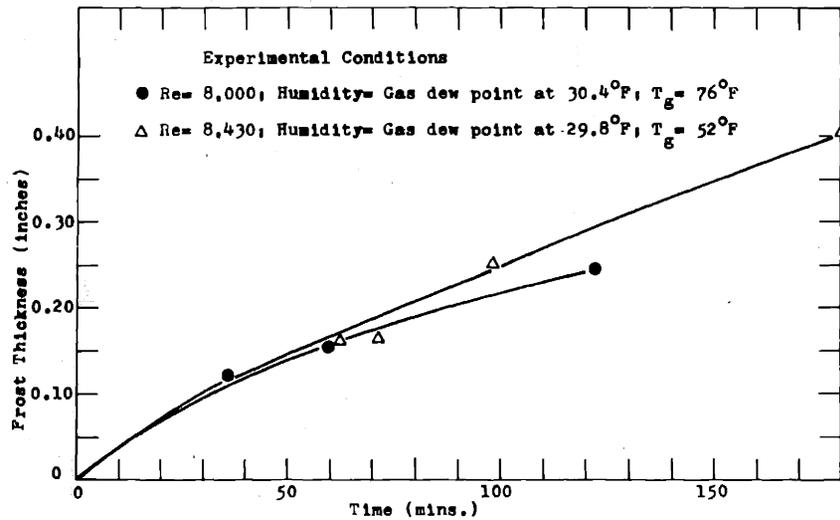
Figure IV-A15   Effect of Gas Temperature on Average Frost Density
and Frost Thickness
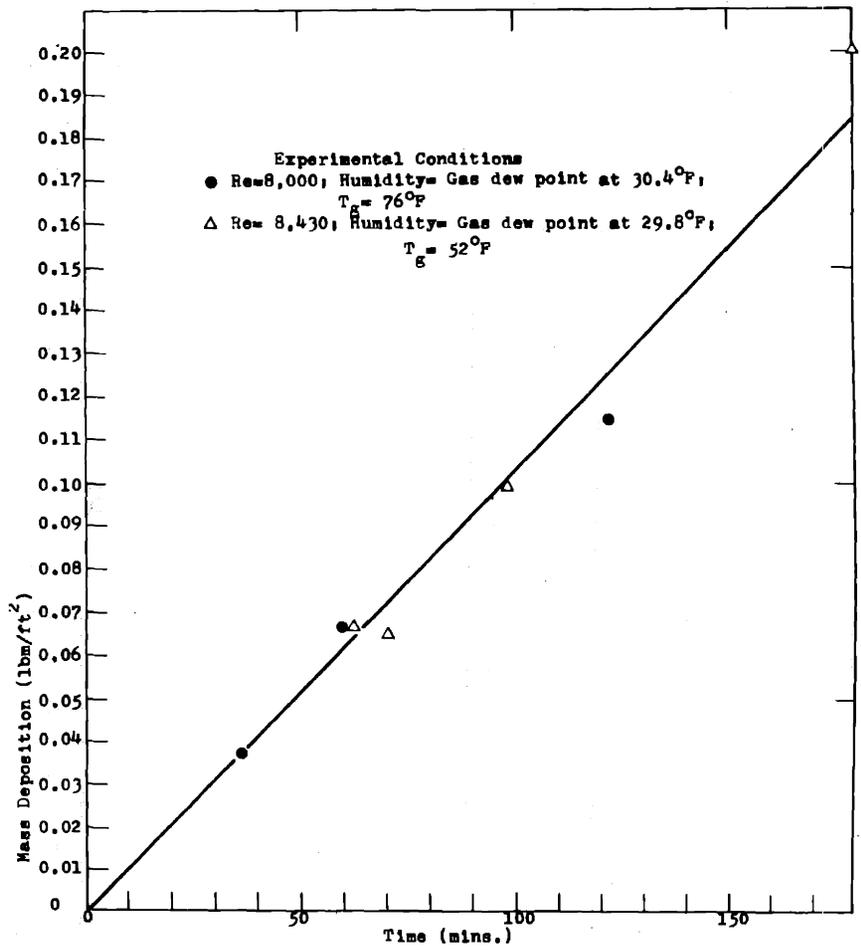
Figure IV-A16   Effect of Gas Temperature on Mass Deposition
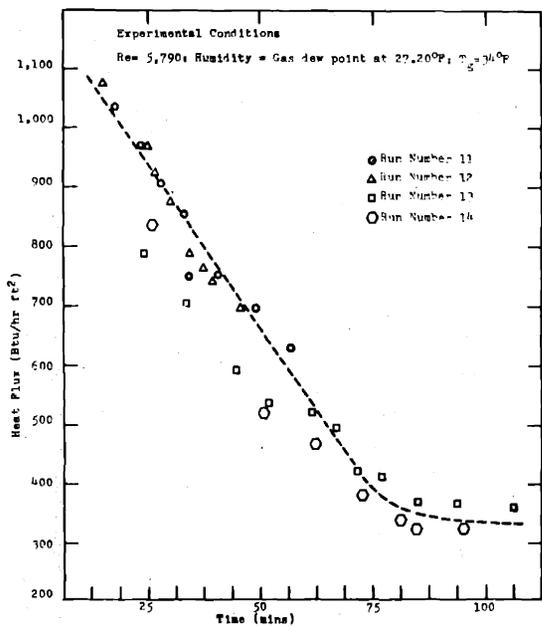
Figure IV-A17   Heat Flux versus Time
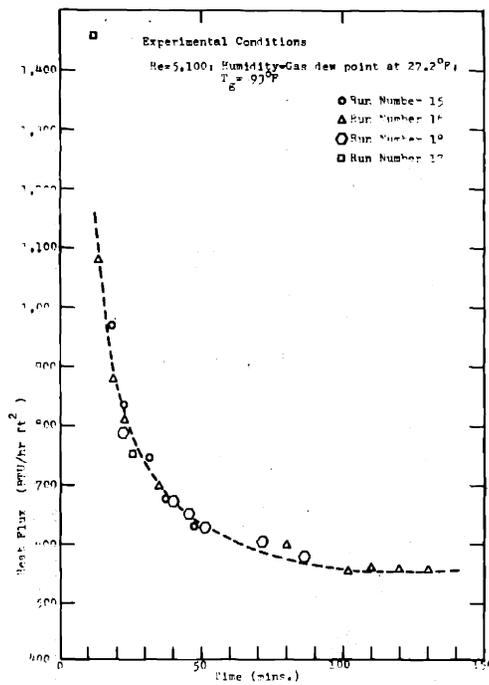
Figure IV-A18   Heat Flux versus Time
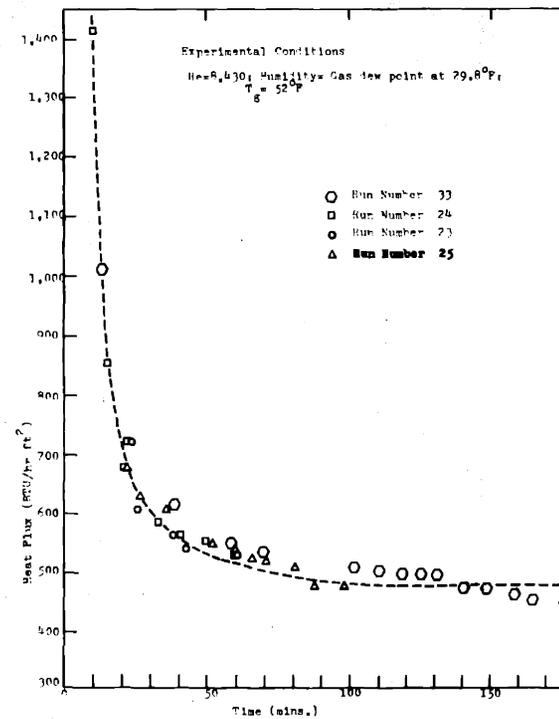
Figure IV-A19   Heat Flux versus Time

Figure IV-A20   Average Thermal Conductivity of the Frost
Layer as a Function of Average Frost
Density
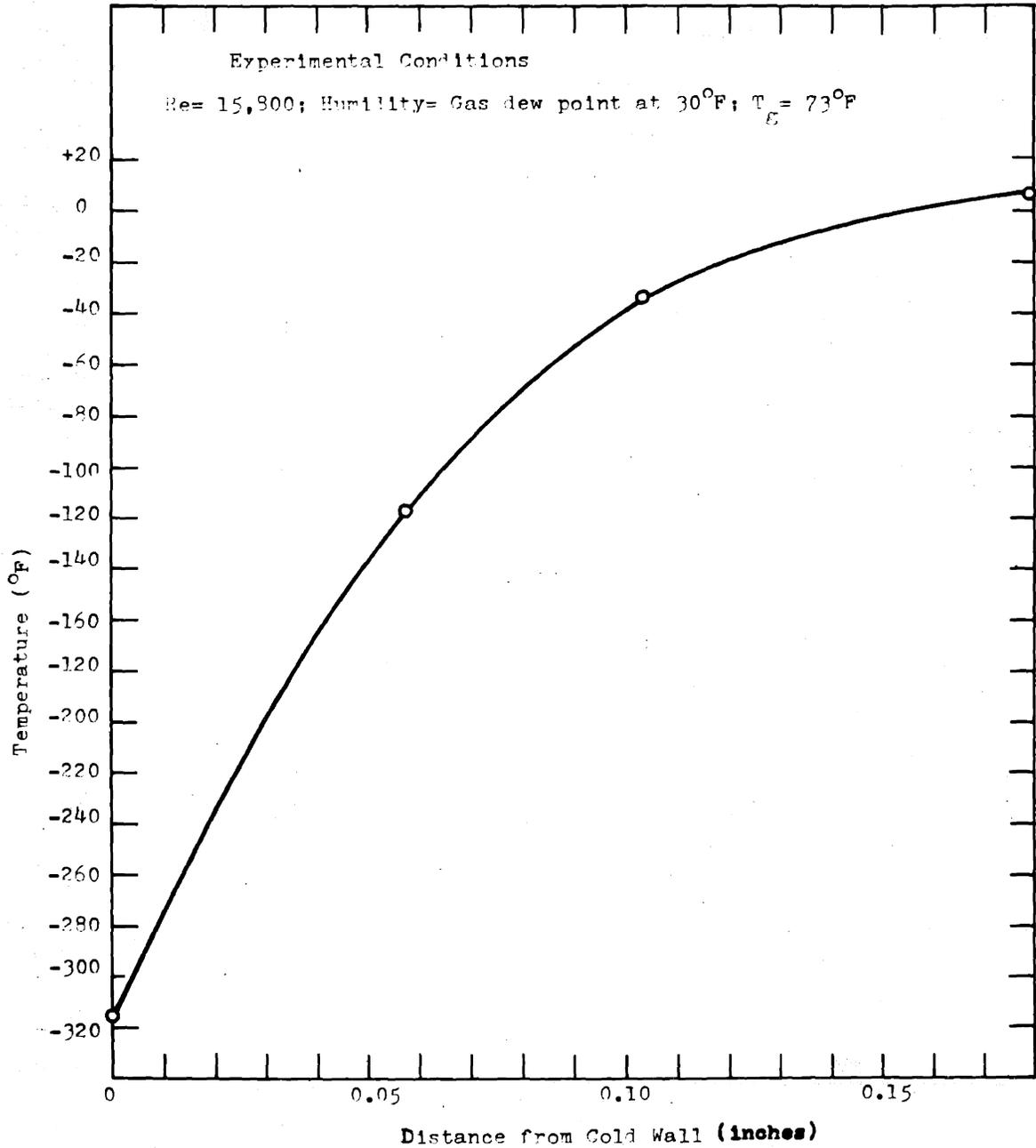
Figure IV-A21   End of Run Temperature Profile within the Frost
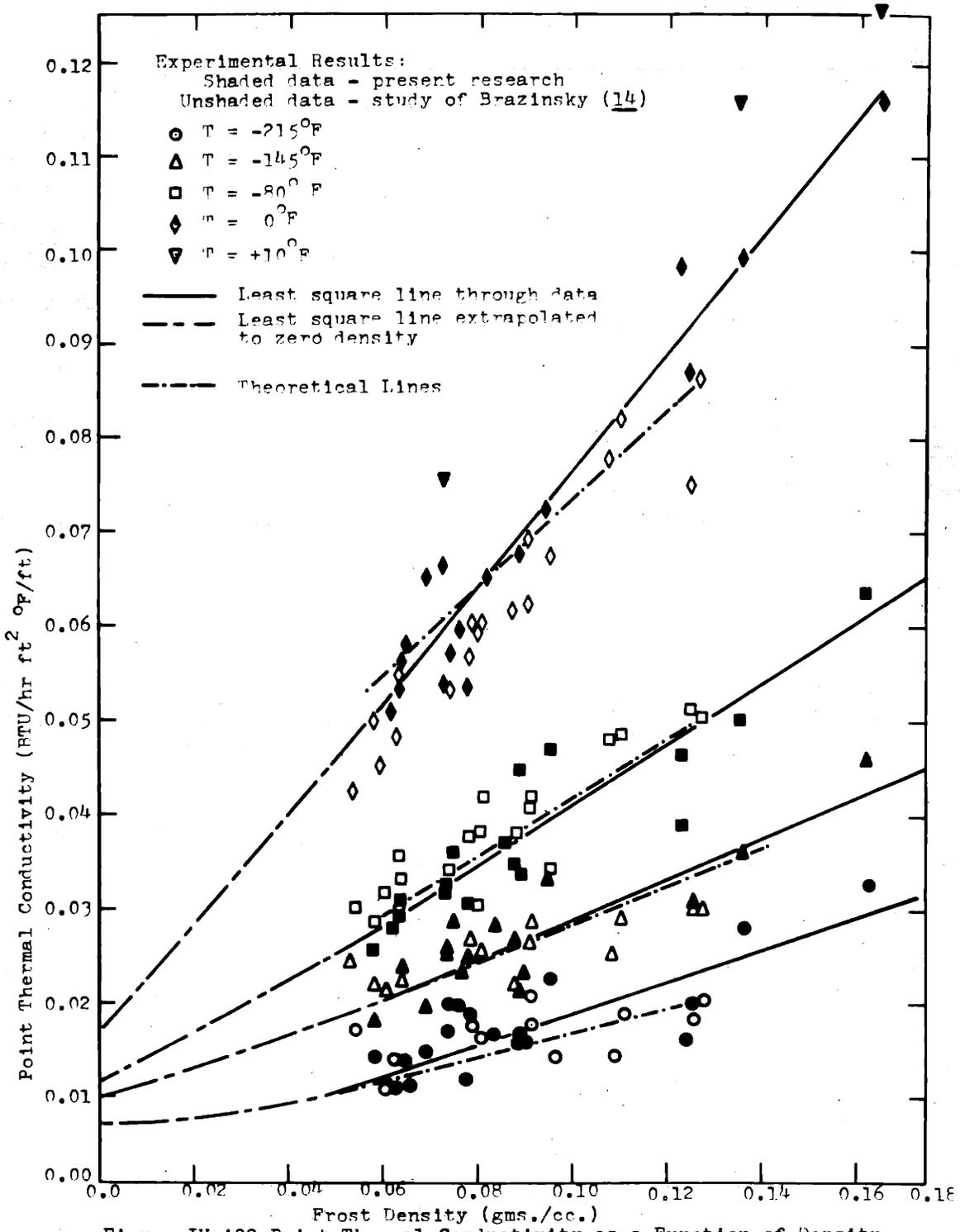
Figure IV-A22 Point Thermal Conductivity as a Function of Density with Temperature as a Parameter
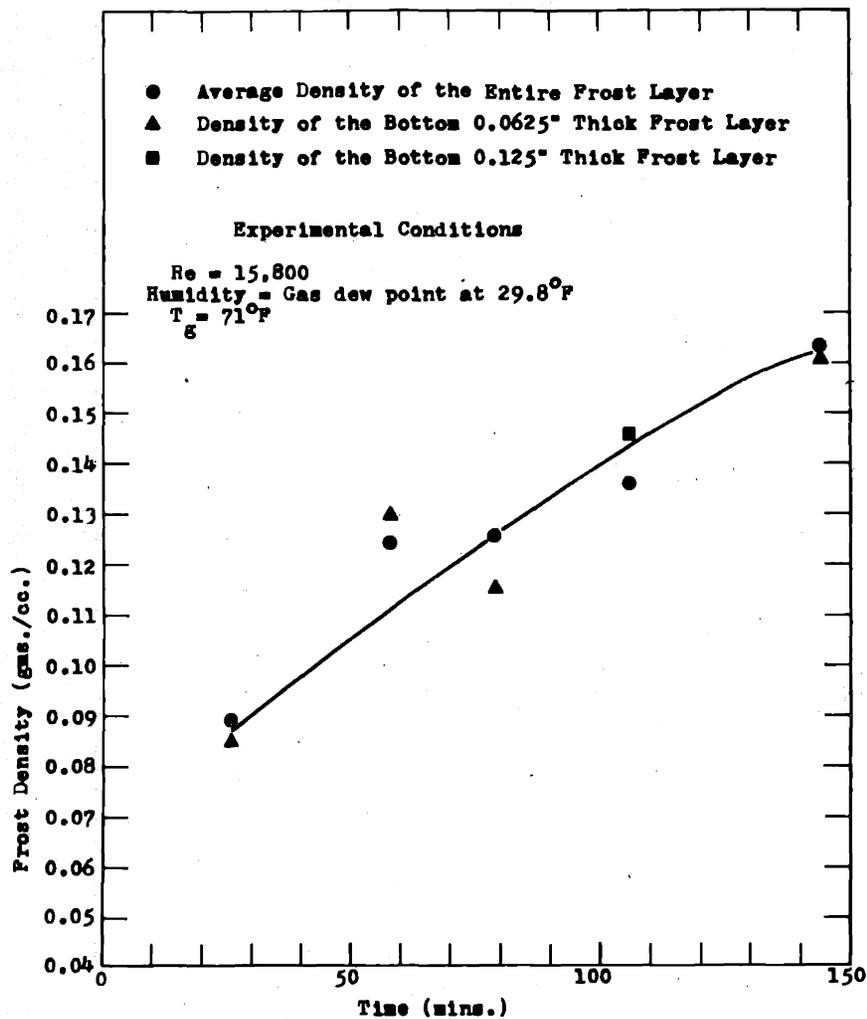
Figure IV-C1   Density Distribution within the Frost as a
Function of Time
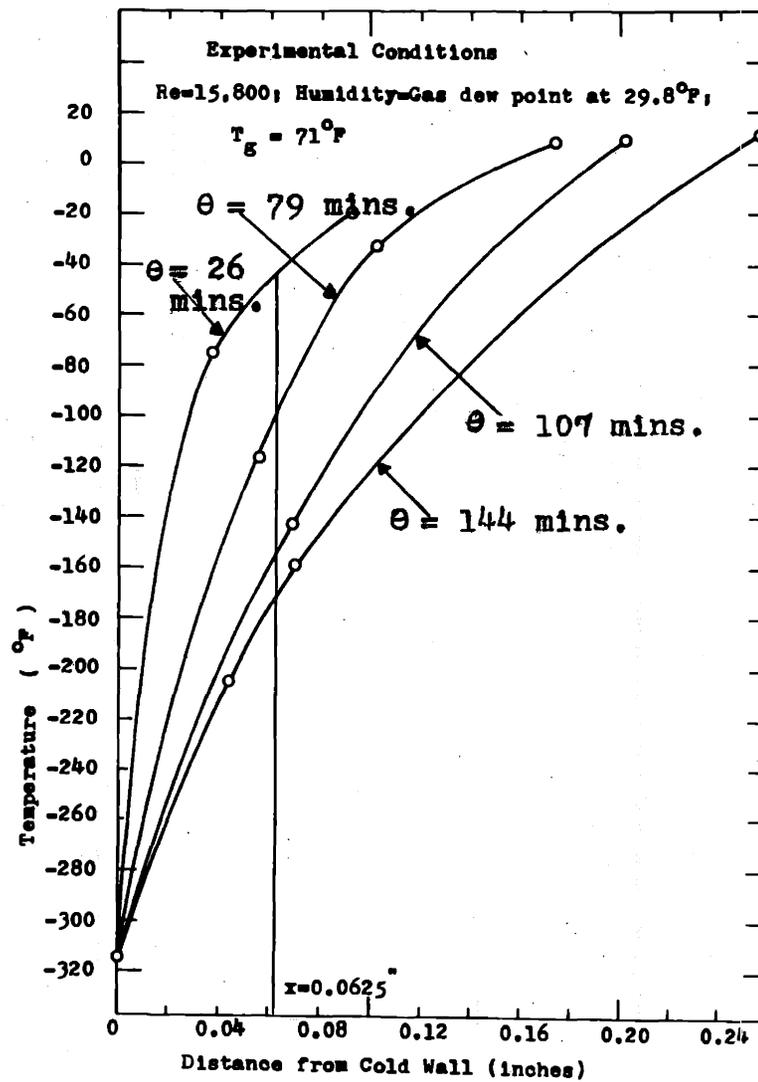
Figure IV-C2   Temperature Distribution within the
Frost as a Function of Time
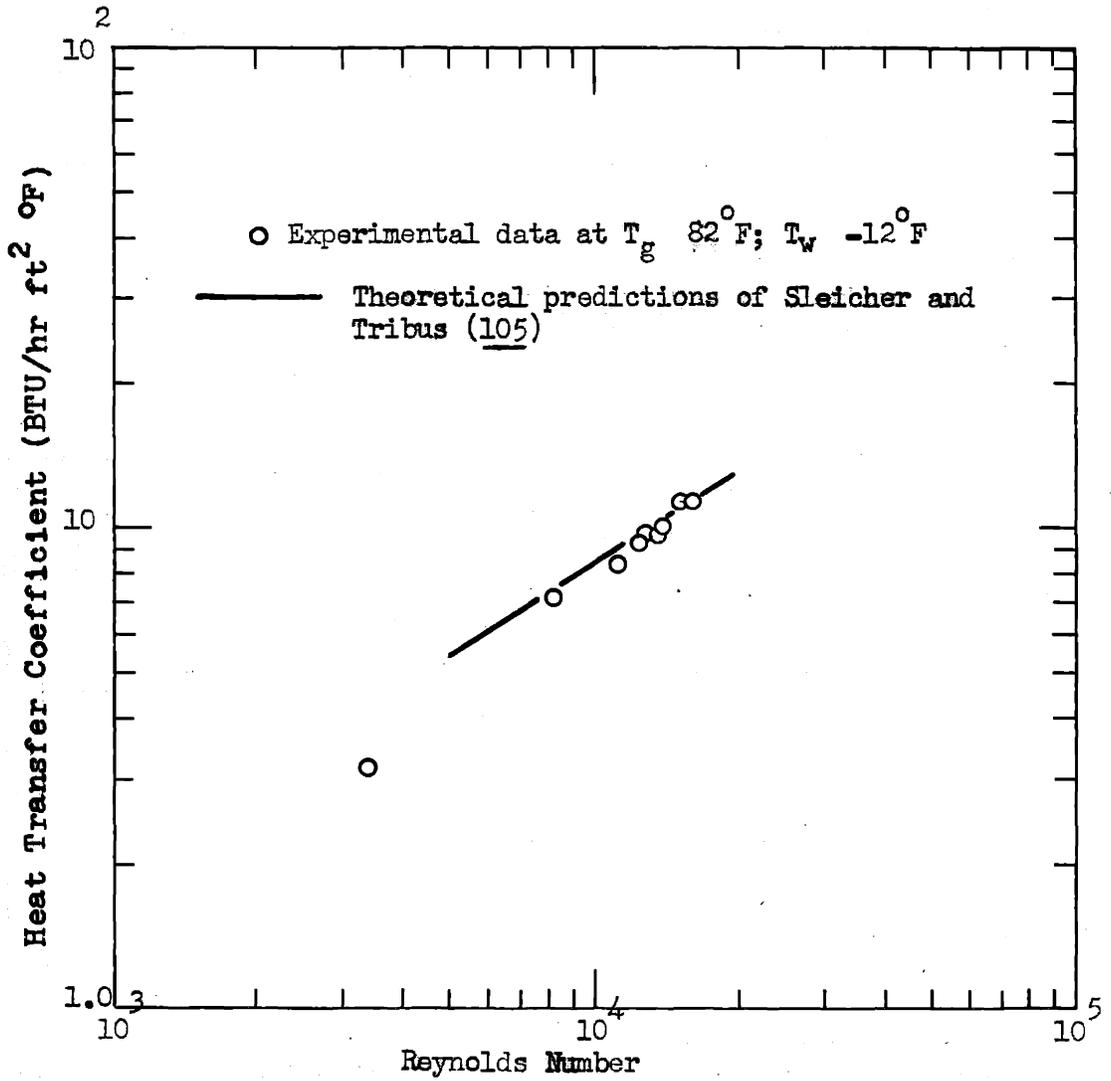
Figure IV-D1   Heat Transfer Coefficient versus Reynolds
Number under Non-Frosting Conditions

S E C T I O N   V

DISCUSSION OF RESULTS

The discussion of results is divided into four main
catagories as follows:

A.   The effect of various independent system parameters on
frost properties.

B.   The results of a temperature gradient across the frost
layer on its density.

C.   The discussion on experimentally measured density
gradient across the frost layer.

D.   The experimentally measured heat transfer coefficient
under the non-frosting conditions.

V-A   Measured Effects of Various Independent System Parameters
on Frost Properties

1.   Initial Phases of Frost Formation

No data were taken during the very initial stages of
frost formation other than the heat flux (except in a few
cases, an approximate value of the density was determined).
However, this period prior to the time when a smooth frost
was attained was observed visually.   At the very start of
a run, the heat flux was quite high and a snowstorm of
small ice particles was observed in the gas phase.   This
snowstorm disappeared entirely when the plate was covered
by an even frost layer.

Fogging is a common occurrence in condensers in those

cases where an appreciable fraction of the gas is cooled
below the saturation temperature.   In the experiments
carried out here, the small cold surface affected the bulk
gas temperature but only slightly and one hypothesizes that
the formation of the snow in the vapor was due to rapid
cooling of the boundary layer.   This hypothesis may be
shown reasonable from the results shown in Figure I-B1.
In this figure, the limits of fog formation in the gas phase
boundary layer in the system similar to one used in the
present study are shown as a function of bulk gas humidity,
temperature and the cold wall temperature.   The results of
this figure indicate that for the cold wall (or the frost
surface) temperatures below -30°F, the fog formation in
the gas phase boundary layer is quite possible for all the
experimentally studied conditions of bulk gas humidity and
temperature.   Thus in the initial phases of an experiment,
the formation if fog in the gas phase boundary layer should
be expected.

Once a smooth thin layer of frost is deposited on the
cold surface, due to highly insulative nature of the frost,
its surface temperature rises significantly.   Hence, the
probability of the formation of fog diminishes significantly.
The criteria of Johnstone and co-workers (57), as shown
in Figure I-B1, indicate that between the experimental
humidity range of dew point at 14.3°F to 33.2°F and bulk
gas temperature range of 34°F to 93°F, the range of the
frost surface temperature for which no fog is formed in the

gas phase boundary layer is $-5^\circ F$ to $+5^\circ F$. The required frost surface temperature for no fog formation in the gas phase boundary layer increases with humidity and the gas temperature. In the present study the values of the frost surface temperature in the quasi-steady state of heat transfer were found to be between $-2^\circ F$ to $+7^\circ F$. Since quasi-steady state of heat transfer is found to be attained a very short time after the formation of a smooth frost layer it could be expected that the frost surface temperature at this time in all the experiments would be very close to the above stated range of $-2^\circ F$ to $+7^\circ F$. Thus, the results of Figure I-B1 indicate that almost no fog should be observed in the experiments of the present thesis after a smooth layer of frost is formed. This is in agreement with the experimental observation.

The fact that the initial portion of a run resulted in the formation of ice particles in the gas phase rather than ice on the cold wall introduces the question - how did the initial frost layer form on the wall? Several ideas have been advanced, e.g. transfer of fog particles by gravity, thermal or electrostatic force etc., but the most reasonable one appears to be that turbulent fluctuating eddy components normal to the cold wall actually drive ice particles against the surface. On the basis of this idea the higher intensity of turbulence will cause the faster rate of mass transfer in the initial phase of a run. This

is in agreement with the experimental observation. The
time for the formation of a smooth frost layer has been
found to depend significantly on the gas Reynolds number
(gas phase turbulence). The brief evaluation of the
various mechanisms which might be causing the transfer of
fog particles in the early phases of a run is shown in
Appendix O.

The time for the formation of a smooth frost layer has
been found to be a very weak function of gas temperature
and humidity. This is because, these independent system
parameters affect <u>only</u> the rate of formation of mass of
fog particles. On the other hand, the time for formation
of a smooth layer should be expected to depend upon the
rate at which these particles are transferred towards the
cold wall.

When ice particles are transferred towards the cold
wall, whether they stick or not is an interesting question.
On very smooth walls, sticking may be difficult; microscopic
projections on the surface act as traps for the first frost
clumps. If the surface is covered with silicon oil, the
frost particles may never be trapped by the cold wall.
Thus, one should expect that the time for the formation
of the first few clumps of frost (and hence for the formation
of a smooth frost layer) depends significantly upon the
surface roughness.

After a few clumps are formed on the surface, each
clump acts as a trap for additional frost particles.

Initially, the heights of the individual clumps increase
as more particles are thrown onto them. Before long,
however, the valleys between the clumps fill in and a
smooth layer of frost is formed. Even though, at present
some research work is being carried out at Lehigh University
(New York) to understand the mechanisms for clump formation
and valley 'filling' process, as yet no conclusive results
have been reported.

For certain experimental conditions, the density of
the clumps were measured. Even though, these experiments
are not reported in this thesis, density values in most
oases were observed to lie between 0.02 to 0.03 gms./cc.
It should be noted that from the knowledge of time for
the formation of a smooth frost layer, an approximate value
of frost density at that time can be obtained from an
extrapolation back in time of the measured average frost
density.

2. Frost Behavior as a Function of Time

As shown in Section IV, both the average frost density
(density of the entire frost layer) and the frost thickness
have been found to be a continuously increasing function of
time. In all the cases mass deposited continuously onto the
cold plate throughout the experiment.

Based solely on the experimental fact that frost
densifies continuously through out an experiment, it can be
concluded that a concentration driving force between the gas

phase and the frost surface was always present. Thus, the frost surface temperature always had to be lower than the gas phase dew point. This was verified experimentally. When the gas phase dew point was varied from 14.3 to 33.2 °F, the measured values of the surface temperature during the quasi-steady state period of heat transfer varied from -2 to +7°F respectively. As discussed in Section II, it is the mechanism of internal diffusion which causes the frost surface temperature to remain constant during quasi-steady state period of heat transfer and which prevents it from ever reaching either 32°F or the gas phase dew point, whichever is lower.

The internal diffusion at the frost surface causes the frost density to increase continuously with time. This internal diffusion also by its very high gain negative feedback relation with the surface temperature causes the frost surface temperature to be constant in the quasi-steady state heat transfer period. The details of this feed-back effect is described in Section I-D and II-A.

The heat flux through the frost have been found to decrease and the frost surface temperature have been found to increase with time in initial phases of the frosting experiment. As more and more frost deposits, the cold plate is insulated and the heat flux decreases. Very shortly, however, frost surface temperature reaches a value at which internal water vapor diffusion becomes quite significant; with the result that frost density increases significantly.

Frost thickness still continues to increase during this period because of the continuous deposition of mass.

A very high sensitivity of internal diffusion to the frost surface temperature causes the thermal resistance, frost surface temperature and the heat flux to attain a constant value. A very small increase in the surface temperature results in a large increase in the internal water vapor diffusion rate. The density (and hence the thermal conductivity of the frost), therefore, increases to a point where the heat flux falls off only very slightly, and the surface temperature rises only very slightly as additional frost is deposited.

During the constant heat transfer period, the frost thermal resistance remains essentially constant as the increasing thickness is balanced by the increasing thermal conductivity. It is highly unlikely that these two effects (i.e. increase in density and thickness) balanced each other merely by chance. It is believed that the heat flux and the frost surface temperature are stabilized by a very high-gain negative feed-back effect. The details of this mechanism are described in Section I-D and II-A.

3. Effect of Reynolds Number on the Average Frost Density, Frost Thickness, Mass Deposition and Heat Transfer through the Frost

The results of Figure IV-Al, indicate that an increase in Reynolds number (at constant humidity and gas temperature) causes the formation of the frost with higher density at

the time when a smooth layer of frost is just formed. This is to be expected, because both the thermal momentum (i.e. momentum imparted on each molecule for the transfer of the thermal energy) as well as the velocity component normal to the cold plate are higher at higher Reynolds number. It is expected that the higher velocity component of the fog particles normal to the cold plate will lead to higher rates of mass transfer. In order to achieve the heat balance on the frosting process, the frost of lower thermal resistance (and hence of higher density) should be produced at the higher thermal forces existing in the gas phase boundary layer.

As seen before (see Sections I-B and II-A), once a smooth layer of frost is formed, diffusional mechanism control the transfer of water vapor from gas to the frost surface. The results shown in Figure IV-A2 indicate that an increase in Reynolds number causes the higher rate of mass transfer. This is in agreement with the theoretical prediction that an increase in Reynolds number will increase the mass transfer coefficient. Quantitatively, it has been reported by Sherwood and Pigford ([104]) that mass transfer coefficients for flow through a rectangular duct vary as approximately 0.8 power to the Reynolds number. Thus,

$$K_g \propto Re^{0.8} \tag{V-A1}$$

Also, the mass flux $= N_s = K_g (p_g - p_s)$ \hfill (V-A2)

hence,

$$K_g = N_s /(p_g - p_s) \tag{V-A3}$$

The mass transfer coefficients calculated from above equations for the three different system conditions, as shown in Figure IV-A2, are listed in Table V-A1.

Table   V-A1

Experimental Mass Transfer Coefficients as a Function of Reynolds Number

Experimental Conditions: Humidity=Gas dew point at 29.9°F,

$$T_g = 73°F$$

Reynolds Number	Mass Transfer Coefficient (ft/hr)
5,580	332
8,000	402
15,800	762

From the data of Table V-A1, comparing the values of K_g at Reynolds number of 5,580 and 15,800, it can be seen that K_g varies as 0.796 power of Reynolds number between this range of Reynolds number. Thus, the experimentally measured dependence of the mass transfer coefficient on the Reynolds number is in excellent agreement with the reported correlation by Sherwood and Pigford (104).

The increase in Reynolds number also increases the heat transfer coefficient between the gas and the frost surface. The experimentally measured correlation between heat transfer coefficient and the Reynolds number is shown

in Figure V-A6. From the figure, it can be seen that the experimentally measured relation between the heat transfer coefficient and the Reynolds number agrees well with one obtained from the theoretical analysis of the system by Sleicher and Tribus (105,106).

The heat balance on the frosting process can be approximately written as

$$q \approx h (T_g - T_s) \approx k_{avg} (T_s - T_w)/\delta \qquad (V-A4)$$

In the frosting process, the surface temperature of the frost varies with time. An increase in Reynolds number would increase the heat flux from the gas to the frost surface because of an increase in the heat transfer coefficient. The increased heat transfer rate would tend to overheat the frost surface. However, as discussed in Section I-C, the higher surface temperature would result in a greater densification rate because of the very high-gain negative feed-back effect of the frost surface temperature on internal diffusion. Thus, the frost deposited at higher Reynolds number would be of greater density and hence increased conductivity. The increased conductivity will maintain the surface temperature nearly constant at various Reynolds numbers. The experimental results of the present studies (see Table IV-A2) borne out these expectations.

As discussed above, the experimental data of Figure IV-A1 indicate that the frost of lower thermal resistance is deposited at higher Reynolds number. At comparable times,

the average frost density increases and the frost thickness
decreases with increase in Reynolds number. The frost
densification is, obviously, expected to be higher at higher
Reynolds number. This expectation is in agreement with the
results of Figure V-AX.

It should be noted that, once a smooth layer of frost
is formed, the behavior of frost with respect to Reynolds
number can not be explained in terms of fluid mechanics,
because at that stage the transfer of fog particles is not
a significant mechanism of frost deposition. A smooth layer
of frost insulates the cold surface sufficiently so that
the frost surface temperature is increased to the point
where the frost deposition occurs only by diffusional
mechanisms. Thus, the intrinsic constants for heat and
mass transfer (h and K_g) control the frost behavior.

The experimentally measured effects of Reynolds number
on the average frost density, frost thickness, mass
deposition and heat transfer through the frost are in
agreement with the reported data of the previous invest-
igators (3,14,25,89,114). Cole (25) obtained the frosts
of higher densities at higher Reynolds number. Richards et
al. (89) also obtained low thermal resistance frosts at
higher Reynolds number. Bothe Richards (89) and Kamei (58)
observed that the thickness of the frost increased with
decrease in Reynolds number. They explained this phenomenon
by saying that a greater shearing action at the higher
velocity streams causes the higher Reynolds number frosts

to have smaller thicknesses. While it is true that the higher density frosts, which are formed at higher Reynolds numbers, have greater shear strengths than lower density frosts, it is implied in Reference 89 that the greater shearing action of the higher velocity gas stream overrides this consideration. Brazinsky (14) obtained the similar qualitative effects of Reynolds number on average frost density, frost thickness, mass deposition and heat transfer through the frost as obtained in the present study. Based on the same preliminary calculations, he concluded, however, that the lower thickness of the frost at higher Reynolds number cannot be explained on the basis of shearing action as described above. However in his system, as frost deposited, it created a hump in the flow path of air. Hence, due to this complex geometry for heat transfer, he could not correlate his experimentally measured heat transfer coefficient with Reynolds number by means of theoretical analysis.

It should be noted that in the present studies the maximum shear strength exerted on the frost (at Reynolds number of 15,800) was approximately 6×10^{-5} psi. (Note that this can be easily calculated from pressure drop estimates over the frosted surface. See page 5-19 of Reference 80). Based on the data presented in References 5 and 20, it was estimated that the frost with a surface temperature of 10°F has a shear strength of approximately 9×10^{-3} psi. Thus, the magnitude of above two shear strengths

indicate that the shearing action on the frost would be negligible in the present experimental conditions.

It can be expected that in earlier phases of a frosting process when the frost deposits in the clumps, some frost is sheared off at higher Reynolds number because in this situation, the surface temperature of the frost is quite low and the corresponding shear strength of the frost would also be small.   The experimental values of frost thickness at time of 26 minutes, as shown in Figure IV-A1, however, indicate that this is really not the case and frosts of almost identical thicknesses are deposited during this stage of the frosting process.   Thus, it is believed that after a smooth layer of frost is formed a frost of lower thickness is deposited at higher Reynolds numbers in response to the thermal force acting upon the surface.

4.   **Effect of Humidity on Average Frost Density, Frost Thickness, Mass Deposition and Heat Transfer through the Frost**

The results of Figures IV-A6 and IV-A8 indicate that for the humidity range of dew points at $14.3^{\circ}F$ to $33.25^{\circ}F$ both the average frost density and frost thickness increase with humidity (at constant Reynolds number and gas temperature) at equivalent time.   Thus, the increase in humidity causes the higher rate of mass transfer as shown in Figures IV-A7 and IV-A9.

The increase in mass flux with humidity is caused by the increase in driving force between the gas and the cold surface of the frost.   The driving force for the mass transfer rate is $p_g - p_s$, where p_g is the partial pressure

of water vapor in the bulk gas phase and p_s is the
equilibrium vapor pressure of ice at the frost surface.
It is observed experimentally that, even though the frost
surface temperature with p_g (see Table IV-A2), the difference
between p_g and p_s continues to increase with p_g.

The mass flux between the gas and the frost surface
can be mathematically obtained from Equation V-A2.

From the results of Figure IV-A7, the validity of the
representation of Equation V-A2 can be examined as follows.

For Reynolds number = 5,800 and gas temperature $48^{\circ}F$,
at dew point of $33.25^{\circ}F$, mass flux = 0.0608 lbm/hr ft^2
and, at dew point of $18.02^{\circ}F$, mass flux = 0.0354 lbm/hr ft^2.

The concentration driving force $(p_g - p_s)$ for the two
experimental conditions are as follows,

at a humidity = gas dew point at $33^{\circ}F$, $p_g - p_s = 1.728 \times 10^{-4}$
lbm/cu ft.   (V-A5)

at a humidity = gas dew point at $18^{\circ}F$, $p_g - p_s = 0.904 \times 10^{-4}$
lbm/cu ft.   (V-A6)

It should be noted that in the above calculations p_s's
are obtained as equilibrium vapor pressures at the measured
frost surface temperatures, whose values are listed in Table
IV-A2.

Thus, the mass transfer coefficients for the two sets
of experimental conditions are

at a dew point of $33.2^{\circ}F$, $K_g = N_s / (p_g - p_s) = 352$ ft/hr
similarly, at a dew point of $18^{\circ}F$, $K_g = 392$ ft/hr.

Thus, the values of K_g at two different humidities
agree with each other within approximately 10%. Considering

the experimental errors involved, particularly in the measurement of T_s (see Appendix A), it can be said that Equation V-A2 is quite good mathematical representation of the mass flux from gas to the frost surface.

As shown in Table IV-A2, an increase in humidity increases slightly the quasi-steady state value of frost surface temperature. On the basis of theoretical models examined in Section II-A, the mass of water vapor diffusing in the frost interior increases with an increase in the frost surface temperature. The increase in humidity, however, also increases the frost thickness (at eqivalent time, Reynolds number and gas temperature). So, the increase in humidity may or may not give the higher average frost density. For the humidity range considered in the present thesis, the results of Figure IV-A6 and IV-A8 show that at equivalent times, the average frost density is slightly larger at a higher humidity.

It should be noted, that in the initial phases of the frosting process when the particle transfer is a significant mechanism for the frost densification, the humidity would have a very little effect of the frost densification because the frost density responses only to the thermal force exerted by the gas phase boundary layer. The extrapolation of the average frost density versus time data of Figure IV-A6 and IV-A8 to a very low time indicate this to be the case.

As seen above, the slight effect of humidity on the

average frost density, as described in Figure IV-A6 and
IV-A8 may not hold true outside the humidity range
considered in the present study.   Actually, Brazinsky ([14])
found that for the humidity range of dew point at 29°F
to dew point at 40°F, the average frost density is
essentially independent of humidity.   Richards et al.([89]),
on the other hand, obtained the frosts consisting of
alternate layers of ice and porous frosts for humidity
higher than that corresponding to a dew point of 69°F.
The surface temperature in this kind of frost exceeded
32°F (the melting point of ice), which caused the melting
at the frost surface.   Such frosts have much higher
densities than frosts formed at the lower gas phase
humidities and equivalent Reynolds number and gas temperature.

As mentioned above, the lower humidities result in
lower frost surface temperatures.   In most cases, the
energy transfer due to water deposition contributes only
a very small portion of the total heat flux from gas to
the frost surface.   Since, the heat transfer coefficient
is not affected by the gas phase humidity, it would be
expected that the quasi-steady state heat flux would
increase as the humidity is lowered (at constant gas
temperature and Reynolds number).   This is indeed found
to be the case as seen in Figures IV-A10, IV-A11, IV-A12
and IV-A4.

Alternatively, the variation of heat transfer rates
with gas phase humidities may be explained by focusing

attention on the frost. ‾ For the humidity range considered
in this study, the frost surface temperature was changed
approximately within 7°F (increases in humidity increase
frost surface temperatures). This increase in the frost
surface temperature increase the ΔT across the frost only
by 2%. However, at an equivalent time, the thickness of
the frost increased as much as 50% and the average frost
density increased as mych as 15% with increase in humidity.
It is expected that due to the significant increase of frost
thickness compared to the increase in the average frost
density, the frost thermal resistance will increase with
increase in humidity. Thus, despite the slightly lower
temperature driving force across the lower humidity frost,
the smaller thermal resistance of the frost formed at lower
humidity resulted in higher heat fluxes.

5. Effect of Gas Temperature on the Average Frost Density,
Frost Thickness and Rates of Mass and Heat Transfer

The variation in gas temperature changes the driving
force for the heat transfer between gas and the frost sur-
face. This would either tend to heat the frost surface or
frost of lower thermal resistance will be deposited to
achieve the heat balance on the frosting process.

The experimental results shown in Figures IV-A13 and
IV-A15 indicate that at equivalent times (and at constant
Reynolds number and humidity) an increase in gas temper-
ature results in frost of higher density and lower thickness.
Thus, the frost responses to the thermal forces acting upon

its surface. The data of Table IV-A2 indicate that the frost surface temperature increases only by few degrees with increase in gas temperature of as much as $50^{\circ}F$.

It is expected that the gas temperature would have a significant effect on the average frost density and the frost thickness only after a smooth layer of frost is formed. In initial phases of the frosting experiment, when the transfer of fog particles is a dominant mechanism for the frost deposition, the gas temperature should have a very little effect on the average frost density, frost thickness and the rate of mass transfer. The experimental data shown in Figures IV-A13 and IV-A15 bear out these expectations. As shown in these figures, both the average frost density and frost thickness at different gas temperatures have almost identical values at the time of approximately 40 minutes from the start of the frosting process.

Since the frost surface temperature remains essentially independent of the gas temperature, it is expected that the mass flux from gas to the cold surface remains essentially unchanged with variation in gas temperature. The gas temperature affects the mass transfer coefficient only very slightly because of its effect on the gas properties. These expectations are borne out by the results shown in Figures IV-A14 and IV-A16. As shown in the figures, the mass flux from gas to the frost surface is essentially independent of variation in gas temperature (at constant humidity and Reynolds number).

Since, the thermal resistance of the frost decreases and ΔT across the frost increases slightly with an increase in gas temperature, the quasi-steady state heat flux would increase with increase in the gas temperature. The results shown in Figures IV-A17, IV-A18, IV-A19 and IV-A4 are in agreement with these expectations.

It should be noted that the concept of the frost responding to the thermal forces acting upon it is very significant in explaining the frosting process. The theoretical models studied in the present thesis which are based on this physical idea are described in Sections I-D and II.

6. Thermal Conductivity of Frost

Frost is a heterogeneous material. It consists of a matrix of interconnected ice particles with interstitial gas. It is believed that the frost thermal conductivity is dependent upon the local frost density, temperature and the frost structure. Since frost density does not necessarily imply a particular structure, frosts at the same temperature and density can have significantly different values of thermal conductivity. For the purpose of the present thesis, however, it was assumed, despite any shortcomings of this assumption, that a given value of frost density implied a particular structure regardless of the conditions under which the frost was formed. This is tantamount to assuming that a property such as thermal conductivity of frost depends solely on temperature and density. Experimental

values of point or local frost thermal conductivity were
therefore plotted as a function of local frost density with
temperature as a parameter (see Figure IV-A22). The scatter
in data may possibly due to small structural differences of
frosts of the same density.

The average thermal conductivities of the frost layer
(Figure IV-A20) were obtained using the measured temperature
differences across the layer (see Equation IV-A1). The
temperature differences across the frost samples, whose
conductivities are shown in Figure IV-A20, are substantially
the same. However, it should be noted that, as previously
indicated, that the measured surface temperatures of the
frost varies from -1^OF to $+18^O$F. The scatter in the data
may be partly due to the different surface temperatures.
However, the more plausible explanation is that structural
differences of frosts having equivalent densities are
primarily responsible for the scatter.

It should be noted that heat also flows through the
frost by mechanisms other than conduction through the solid
-gas network. Thus, the values of thermal conductivity shown
in Figures IV-A20 and IV-A22 include contribution made by
other mechanisms. These mechanisms are:

A.   Radiation between the ice particles in the frost.

B.   Enthalpy transport by the diffusion of water through
the frost. This diffusion may be due either to the concen-
tration gradient, resulting from the temperature gradient,
or to the thermal diffusion of water vapor or of nucleated

ice particles.

A. Effect of Radiation

Radiation from the warmer frost particles to the colder ones constitutes a component of the total or overall frost thermal conductivity, the contribution made by interparticle radiation was calculated using Equation V-A7, which was presented by Damkohler (30) (see Appendix P)

$$k_r = \frac{0.685}{100} \epsilon \, D_P(\frac{T}{100}) \, e_H \qquad \text{(V-A7)}$$

(In experiments involving heat transfer through a packed bed, Polack (82) found that contribution of radiation to the bed conductivity was in fair agreement with the predictions of Damkohler equation).

For the experiments of present thesis, it was cal-culated from the Damkohler equation that the component of thermal conductivity due to radiation was less than 1.3% of the lowest measured value of the point thermal conductiv-ity (see Appendix P). It should be noted that values sub-stituted into Equation V-A7 made the computed values of the contribution to the thermal conductivity by inter-particle radiation a maximum. Since this maximum contribution to the over-all thermal conductivity was small, it was ignored. It should be noted that using reasonable values of T, ϵ, e_H and D_p in Equation V-A7, the contribution of radiation can be reduced to well under 1%.

The above described results regarding the internal radiant heat transfer is in agreement with the conclusion of Van der Held, who demonstrated that for particulate

insulators the radiation heat transfer under atmospheric conditions becomes significant only at temperatures above $212^{O}F$ and is negligible below $32^{O}F$. Brazinsky (<u>14</u>) arrived at the same conclusions for his experimental data from the calculations similar to one described above.

B. <u>Diffusion of Water through the Frost</u>

As discussed in Section II, there are several mechanisms by which water can diffuse in the frost interior. These can be stated as follows.

1. Diffusion of water vapor by the vapor pressure gradient.

2. Thermal diffusion of water vapor.

3. Thermal diffusion of ice nuclei.

1. <u>Diffusion of water vapor by the vapor pressure gradient</u>

The diffusion of water vapor under vapor pressure gradient would add the additional component of thermal conductivity added to the ordinary thermal conductivity of air. This additional component can be designated as k_{excess}. Thus, the total or effective value of gas thermal conductivity is equal to the sum of k_{excess} and k_g, where k_g is the gas thermal conductivity. Thus, in calculating the thermal conductivity of frost from different assumed structural models, the total thermal conductivity of the gas phase $(k_g + k_{excess})$ should be used.

An expression for k_{excess} can be obtained by considering the total heat flux through the pore phase at some point in the frost. Thus,

$$q/A = k_{g,e} \frac{dT}{dx} = k_g \frac{dT}{dx} + \frac{\overline{D_B}}{RT} M_v \Delta H \frac{dP_{vp}}{dx} \qquad (V-A8)$$

A more detailed explanation of Equation V-A8 is presented in Appendix F. From Equation V-A8 and the definition of k_{excess},

$$k_{excess} = k_{g,e} - k_g \qquad (V-A9)$$

Equation V-A10 can be derived as,

$$k_{excess} = \frac{D_B}{RT} \left(\frac{dP_{vp}}{dT} \right) M_v \Delta H \qquad (V-A10)$$

Conbining Equation V-A10 with Clausius-Clapeyron equation (80)

$$\frac{dP}{dT} vp = \frac{M_v \Delta H}{RT^2} P_{vp} \qquad (V-A11)$$

the final expression for k_{excess} can be obtained

$$k_{excess} = (D_B \Delta H^2 P_{vp}) M_v^2 / R^2 T^3 \qquad (V-A12)$$

The computed values of k_{excess} as a function of temperature are shown in Table V-A2. At positions within the frost, where the temperature is lower than -10°F, k_{excess} makes a small contribution to the total gas phase thermal conductivity and hence the point thermal conductivity of the frost. However, k_{excess} becomes significant at higher temperatures. For example, at 20°F, the contribution is about 37% of the total gas phase conductivity. Obviously, k_{excess} increases the over-all conductivity of the frost since it increases the total gas phase conductivity. It can

be easily seen that the exact contribution made by excess

thermal conductivity to the over-all thermal conductivity

of the frost is dependent on the real frost structure. This

contribution cannot be calculated exactly as the true frost

structure generally cannot be mathematically characterized.

Thus, in order to calculate the fractional contribution

made by k_{excess}, a particular structure has to be assumed.

As an illustration, suppose the frost consists of a series

of parallel slabs of ice with heat flow parallel to these

slabs. Then for a 20°F frost having a density of 0.09 gms./

cc. thermal conductivity with k_{excess} is equal to 0.145

Btu/hr ft °F (14), whereas without k_{excess} the conductivity

is 0.138 Btu/hr ft °F. Thus, for this particular model,

k_{excess} adds 5.1% to the point conductivity. However, if

the frost structure is idealized to consist of parallel

array of slabs with heat flow normal to the array, then

the conductivity including k_{excess} is 0.024 Btu/hr ft °F

(14). Without k_{excess} the thermal conductivity is 0.015

Btu/hr ft °F. Thus, in this case k_{excess} increases point

conductivity by 60%.

As described above, since the contribution of k_{excess}

is significant only for the temperature above -10°F, it

is expected that the average thermal conductivity of the

frost will not be significantly affected by k_{excess}. This

can be seen more clearly from the results shown in Figure

V-A1. In this figure, the thermal conductivity of the frost

(based on the Woodside model of the frost structure, which

is a model, as shown in Appendix F, consisting of a cubic
array of ice sphere) is plotted as a function of temperature
for the density of 0.09 gms./cc. The curve ABC shows the
conductivity correlatiin which takes into account the excess
thermal conductivity of the frost. The curve ABC', on the
other hand, does not take into account the excess thermal
conductivity of the frost. The average thermal conductivity
of the frost can be obtained from these correlations using
Equation V-A13

$$k'_{avg,f} = \frac{\int_{T_w}^{T_s} k_f \, dT}{(T_s - T_w)} \qquad (V\text{-}A13)$$

Thus, the average conductivity calculated from curve
ABC was found to be equal to 0.0214 Btu/hr ft °F, whereas
average thermal conductivity calculated from curve ABC' was
found to be 0.0209 Btu/hr ft °F. The value of the average
conductivity of a frost layer having a surface temperature
of 20°F, was thus affected by 4.42% due to excess thermal
conductivity.

B.   Thermal Diffusion of Water Vapor

The existence of a large temperature gradient (see
Section IV) in the frost interior indicate that there could
be a significant enthalpy transport due to thermal diffusion
of water vapor. This, however, is not the case. As shown in
Section II-D, it has been found that the water vapor flux
caused by thermal diffusion is negligible compared with the
flux due to concentration gradient (vapor pressure gradient)
at all levels within the frost. The enthalpy transport due

to thermal diffusion of water vapor is therefore ignored
in the present thesis.

C. Thermal Diffusion of Ice Nuclei

As discussed in Section II, it is believed that thermal
diffusion of ice nuclei plays significant role in the
densification of the frost, particularly in the colder
region of the frost. This transport of ice nuclei will also
cause the enthalpy transport. Mathematically, this kind of
enthalpy transport can be written as,

$$q_h = n \, V_t \, c_p \, \Delta T = k'_{excess} \frac{dT}{dx} \qquad (V-A14)$$

From above equation it can be seen that k'_{excess} varies
with the position in the frost interior. For a typical set
of experimental conditions (Re=15,800, Humidity= Gas dew
point at $30^\circ F$, $T_g = 70^\circ F$) it was estimated that at $\rho_f = 0.133$
gms./cc. and T= $-133^\circ F$, (see Section V-C)

$$\frac{dT}{dx} = 2.52 \times 10^{4 \, \circ}F/ft \quad , \quad n \, V_t = 0.0125 \, lbm/hr \, ft^2$$

and assuming $\Delta T = 100^\circ F$ and $c_p = 1.008 \, Btu/lbm \, ^\circ F$ (80)

the value of $k'_{excess} = (0.0125 \times 4.032 \times 25 \times 10^{-4})/252$
$$= 4.8 \times 10^{-7} \, Btu/hr \, ft \, ^\circ F$$

From Figure IV-A22, k_f at $\rho_f = 0.133$ gms./cc. and
T = $-133^\circ F$ has the value of 0.037 Btu/hr ft $^\circ F$.

Thus, for the chosen experimental conditions k'_{excess}
due to thermal diffusion of ice nuclei is negligible compare
to the total thermal conductivity.

Since, the experimental conditions chosen in the above

calculations were such that the densification of the frost
and hence the mass flux in the frost interior were the
maximum for the present study, it was concluded that the
enthalpy contribution due to mass transfer was negligible
for the present purpose.

7.   Experimental Error in Thermal Conductivity Measurements

Due to experimental errors involved in the measurements
of various quantities, it is believed that the average
thermal conductivity values reported in this thesis are
accurate within approximately ± 7%. The details of the error
analysis is shown in Appendix N.

The calculation of point thermal conductivity from
Equation IV-A2 could be inaccurate due to errors in the
measurements of slope of a T(x) curve or in heat flux
measurements.

The slope of the temperature versus x profile at
various points were measured by graphical differentiation
with the help of a mirror. For a typical T(x) curve, value
of the slope obtained by this method was compared with one
obtained by analytical differentiation. As shown in Appendix
N, the values obtained by these two different methods agreed
quite well. It was estimated that the error in temperature
gradient measurement was approximately within ± 4%. The
error in heat flux measurement was within approximately ±2%.
Thus, the point thermal conductivity values were estimated
to be accurate within ± 10%. The details of the error
analysis is shown in Appendix N.

8. Variation of Conductivity with Density

A. Average Frost Layer Conductivity

The average frost layer conductivity is plotted as a function of density is shown in Figure IV-A20. Since it has been shown that radiation and excess thermal conductivities do not affect the average thermal conductivity of the frost layer significantly, it can be concluded that the major contributor to the average frost thermal conductivity is conduction through the solid gas matrix.

The thermal conductivity increases with increasing frost density because at the higher densities larger areas of low thermal resistance paths are present. The larger contact areas are a consequence of the increased solid fraction. In addition, higher density frosts may have structures which are significantly different than lower density frosts. These different structural characteristics may also be partly responsible for the increased conductivities at the higher densities.

B. Point Thermal Conductivity

Point thermal conductivity at different density value and with temperature as a parameter are plotted in Figure IV-A22. As was true for average frost layer conductivities, higher densities result in larger values of point conductivities because of the larger areas of low thermal resistance paths. These large areas are a consequence of the increased percentages of solid present at the higher frost densities. In addition, possible structural differences implied by the higher densities may be partly responsible for the increased

conductivities.

9. <u>Variation of Thermal Conductivity with Temperature</u>

As shown in Figure IV-A22, at equivalent densities, higher frost temperatures lead to increased thermal conductivity values for three reasons. First, the contribution of k_{excess} to the over-all thermal conductivity increases with temperature. Secondly, it is believed that the contact areas between the various ice particles increase with increasing temperature. At the higher temperatures the processes of constructive and destructive metamorphism (<u>34</u>, <u>62</u>) are more active, and it seems likely that additional water vapor is transferred to the contact areas between the particles. Thirdly, the conductivity of the gas phase increases with increasing temperature and, at the high frost porosities encountered in this thesis, the gas conductivity is very important in determining the over-all conductivity of the frost. Thus, despite the fact that ice thermal conductivity decreases with increasing temperature, the intrinsic conductivity of the ice-gas matrix increases with temperatures.

10. <u>Comparison of Experimental Data of Thermal Conductivity with those Predicted from a Frost Structure Model</u>

Frost is a heterogeneous structure consisting of an array of irregular particles. In order to obtain a mathematical relation between frost thermal conductivity, density and temperature, it is important to model the frost structure. It is obvious, considering the irregularities involved

in the frost structure, that a unique mathematical representation of frost structures is almost impossible. Usually the frost structure is visualized by a simple model which would not only fairly well represent the true structure but which can be mathematically defined such that a correlation between thermal conductivity, density and temperature can be obtained.

The previous investigators (3,14,25,47) of this area have analyzed various idealized models of the frost structure. The detailed descriptions of these models are given in References 14 and 47.

As shown in Figure IV-A22, the thermal conductivity data of the present thesis are in quite good agreement with those obtained by Brazinsky (14). A model which was found to be successful in correlating the experimental data of Brazinsky (14) for thermal conductivity is, therefore, also used in the present study.

A. Model of the Frost Structure: Cubes of Ice Connected by Ice Rods

The assumed model is a symmetrical matrix of ice cubes interconnected by ice rods. The rods are square prisms (see Figure V-A2). As is the case for other structural models, this structure only very approximately models the true physical situation. However, a desirable characteristics of this model is that the dimensions of the rods may be taken as a measure of the actual contact between the ice particles.

An equation for calculating frost thermal conductivity

is derived by considering a typical unit cell of hetero-
geneous structure (see Figure V-A3). x is the linear dimen-
sion of the ice cube, and z is the width of the square ice
rod. Actually x and z are dimensionless as they represent,
the ratio of the ice cube length to unity and the ratio of
rod width to unity, respectively. It should be noted that
the actual size of the unit cell does not affect the
computed value of the <u>frost</u> <u>thermal</u> <u>conductivity</u>.

From Figure V-A3 it can be seen that $(1-\epsilon)$, the solid
fraction, is given by

$$1 - \epsilon = \frac{\text{volume of solid in a unit cell}}{\text{volume of a unit cell}} \qquad (\text{V-A15})$$

$$= \text{volume fraction of solid ice in frost}$$

Thus,

$$1 - \epsilon = x^3 + 6 \left((1-x/2) z^2 \right) \qquad (\text{V-A16})$$

or,

$$1 - \epsilon = x^3 + 3 z^2 (1-x) \qquad (\text{V-A17})$$

$(1-\epsilon)$ is related to the densities of ice, gas and
frost by

$$1 - \epsilon = \frac{\rho_f - \rho_g}{\rho_{ice} - \rho_g} \qquad (\text{V-A18})$$

B. <u>Equation for Frost Thermal Conductivity</u>

The three dimensional and planar views of the frost
structure are shown in Figures V-A2 and V-A3 respectively.
A representative unit cell of the homogeneous structure is
shown in Figure V-A4. Only the case of infinite sidewise
thermal conductivity will be considered. Thus the equivalent

thermal resistance of the unit cell is obtained by consid-
ering the resistances of zones 1,2,3,4 and 5 to be in series.

The length of the ice cube is x. The rods are square
prisms with cross sectional area equal to z^2. It should be
noted that the resistances of zones 1 and 5 are identical
and so are the resistances of zones 2 and 4. The combined
thermal resistance of zones 1 and 5 is

$$R_{1-5} = \frac{1 - x}{k_{g,e}(1-z^2) + k_1 z^2} \qquad \text{(V-A19)}$$

The combined thermal resistance of zones 2 and 4 is

$$R_{2-4} = \frac{(x - z)}{k_{g,e}(1 - x^2) + k_1 x^2} \qquad \text{(V-A20)}$$

For zone 3 the thermal resistance is

$$R_3 = \frac{z}{2k_1 z (1-x) + k_1 x^2 + k_{g,e}(1-x^2-2z(1-x))} \qquad \text{(V-A21)}$$

The combined thermal resistance is obtained by adding
Equations V-A19, V-A20 and V-A21 as these resistances are
in series.

$$\text{Total resistance of unit cell} = \frac{\overbrace{(\text{thickness})}^{=1}}{k_f \underbrace{(\text{area})}_{=1}} \qquad \text{(V-A22)}$$

Thus,

$$\frac{1}{k_f} = \frac{(1-x)}{k_{g,e}(1-z^2)+k_1 z^2} + \frac{z}{2k_1 z(1-x)+k_1 x^2+k_{g,e}(1-x^2-2z(1-x))}$$

$$+ \quad \frac{(x-z)}{k_{g,e}(1-x^2)+k_1 x^2} \qquad \text{(V-A23)}$$

Equation V-A23 can be used to calculate frost thermal conductivities with the knowledge of adjustable constants, namely the ratio of cube length to the width of the ice rod. This is because there are two equations (V-A17 and V-A23) and three unknowns (k_f, x and z). The x/z ratio is a function of temperature. In the present thesis a correlation (14) between x/z and temperature described in Figure V-A5 is used to obtain the point thermal conductivity values shown in Figure IV-A22. In general, however, a particular value of adjustable constant can be obtained by matching the thermal conductivity calculated from Equation V-A23 with a value on experimental curve. The specific procedure is described in Reference 14.

The results shown in Figure IV-A22 indicate that at all temperatures there is a fair agreement between theoretical values and the experimental data. This agreement tends to indicate that over the density range involved, the contacts between the ice particles in the frost are reasonably well represented by the dimensions of the interconnecting ice rods. In addition, it should be noted that the ratio (x/z) increases with increasing temperature, thus indicating that contact areas between particles are greater in the higher temperature sections of the frost than in the lower temperature sections. This conclusion seems reasonable

since higher temperature results in increased rates of the metamorphic processes (34, 62). These increased rates cause additional mass to be deposited in the particle contact areas hence results in a greater degree of bonding. The various types of metamorphic processes are discussed in Reference 14.

11. Applicability of an Analogy for Simultaneous Heat and Mass Transfer for the Frosting Process

As discussed in Section II-A, the formation of frost on a liquid nitrogen cooled surface is governed by the simultaneous heat and mass transfer from gas to the cold surface, once a smooth layer of frost is deposited. It is expected, therefore, that an analogy for simultaneous heat and mass transfer can be applied to the frosting process.

For the purpose of evaluating the applicability of such an analogy, the experimentally measured coefficients of heat and mass transfer are compared with ones obtained from the theoretical correlations. The experimental heat transfer coefficients are calculated from the following heat balance Equation V-A24 on the frosting process.

$$q = h \ (T_g - T_s) \ + \ N_s \ \Delta H \qquad\qquad (V-A24)$$

With the knowledge of experimentally measured quantities q, T_g, T_s and literature value of ΔH (54), above equation can be used to calculate heat transfer coefficients for various system conditions.

The theoretical heat transfer coefficients are calculated using the theoretical analysis of Sleicher and

Tribus (105, 106). A comparison between the experimental and theoretical correlation between heat transfer coefficient and Reynolds number at various gas temperatures is shown in Figure V-A6. The details of the theoretical heat transfer analysis are shown in Appendix L.

From the results of Figure V-A6, it can be seen that for all the experimental conditions studied in the present research there is a good agreement between the values of theoretical and experimental heat transfer coefficients. The maximum percentage deviation between the experimental and the theoretical values (% deviation = absolute value of $((h_{exp}-h_{theo})/h_{exp})$ x 100) is approximately within 17% and the average of the deviations for all the experimental conditions is approximately within 10%. The experimental heat transfer coefficients are estimated to be accurate within approximately ± 12.7%. The details of the error analysis is shown in Appendix N.

As discussed previously, the experimental mass transfer coefficients can be calculated from the mass balance Equation V-A2 for the frosting process. The theoretical mass transfer coefficients are calculated using the theoretical heat transfer coefficients and Lewis analogy (39, 72) for the simultaneous heat and mass transfer. For small vapor concentration, the Lewis analogy can be written as,

$$h/K_g = \rho_g \, c_p \, Le^{2/3} \qquad\qquad (V-A25)$$

The details of Lewis analogy are shown in Appendix L.

A comparison between experimental and theoretical mass transfer coefficients for the various experimental conditions is shown in Figure V-A7. From the figure it can be seen that the maximum percentage deviation between the experimental and theoretical values of mass transfer coefficient (% deviation = absolute value of $((K_{gexp} - K_{gtheo})/K_{gexp}) \times 100)$ is approximately within 17% and the average of deviations for all the experimental conditions is approximately within 11%. As shown in Appendix N, the experimental mass transfer coefficients are accurate within approximately $\pm 7\%$. Thus, it can be said that the theoretical and the experimental values of mass transfer coefficients agree well for all the experimental conditions studied in the present thesis.

Possible Reasons for Discrepancy between Experimental and Theoretical Values of Heat and Mass Transfer Coefficients

There are several possible reasons for slight discrepancy between the experimental and theoretical heat and mass transfer coefficients. The errors lie both in experimental measurements as well as in theoretical predictions.

There are two main possible errors involve in experimental measurements. First, there could be an error involved in the measurement of frost surface temperature. This is because a significant difficulty involved in locating the exact position of the frost surface (see Section III). The error in this measurement causes the inaccuracy in the calculations of heat and mass transfer coeff-

icients.

Secondly, there is a possibility of an error in the determination of the exact value of D_H (hydrolic diameter of the duct). As frost deposits on the cold surface during a frosting experiment, the effective clearance of the duct for the flow decreases. In present research, the duct clearance is kept almost constant during an experiment by lowering the cold plate as frost deposits upon it such that the frost surface and bottom of the duct are always flushed. This is done, however, by visual examination through lucite side windows and the accuracy with which the frost surface and bottom of the duct can be flushed together by this method is approximately within 0.03 to 0.04 inch.

The clearance of the duct in the present frosting system is 0.4 inch. The reduction of this clearance by 0.04 inch causes 10% reduction in clearance and hence at the same Nusselt number the heat transfer coefficient increases by the same amount. Thus, the reduction in clearance of the duct gives higher value of experimental heat transfer coefficient than the expected one. The same statement can be made for the mass transfer coefficient.

Levy (65) states that heat transfer characteristics of turbulent flow in a rectangular duct varies significantly with the nature of the boundary conditions at the two walls of the duct. This is particularly true for low Prandtl number (< 1.0) when thermal boundary layer thickness can exceed velocity boundary layer thickness. Since Prandtl

number of air is 0.73 and the nature of the boundary
conditions in the theoretical and experimental heat and mass
transfer analysis are different, one should expect the
slight difference in the values of theoretical and
experimental heat and mass transfer coefficients.

Finally, the roughness of the frost surface causes
the experimental heat and mass transfer coefficients to be
higher than ones calculated from the theoretical analysis.
This is because the theoretical analysis assumes the duct
wall to be completely smooth (i.e. no loss due to friction).

Considering all the possible sources of errors
described above it can be said that there is good agreement
between experimental and theoretical heat and mass transfer
coefficients.

The applicability of the Lewis analogy for the frosting
process has been studied by the various previous invest-
igators (6, 14, 52, 89, 92, 114). In low temperature natural
convection studies (6, 52, 92), it has been found that the
Lewis analogy was not successful in predicting the
experimental mass transfer rates. Since Lewis analogy is
applicable to the case when heat and mass transfer rates
are controlled by diffusional mechanisms in the gas phase
thermal boundary layer, this discrepancy has been generally
attributed to the formation of ice particles in the boundary
layer.

In the forced convection low temperature studies the
experimental results of Richards et al. (89) and of

Brazinsky (14) for heat and mass transfer rates did not
agree well with ones predicted from Lewis relation. In
early phases of the experiments Brazinsky's mass transfer
data (from mass versus time curve) were only 50% of those
predicted from Lewis relation. These results can be explain-
ed on the basis of formation of ice particles in the gas
phase boundary layer. Both Richards (89) and Brazinsky (14)
could not correlate their data with Lewis relation even in
the later phases of the frosting experiments. It is believed
that the reason for discrepancy was a complicated geometry
of the frosting system which failed them to carry out
accurate theoretical heat and mass transfer analysis.

In the high temperature, forced convection studies,
on the other hand, Chung and Algren (24) evaluated theoret-
ical mass transfer rates using a correlation for mass
transfer coefficient applicable to flow past single
cylinder. These investigators found that the mass transfer
rates predicted from Lewis analogy (39, 72) showed good
agreement with their experimental values of frost accumul-
ation rates. This would be expected as the studies were
conducted at relatively high temperature thus ensuring
that deposition occurred solely by the molecular and
turbulent diffusion of water vapor from the gas phase to
the frost surface. It is believed that the better agreement
between the experimental and the theoretical mass transfer
rates in the present study as well as in the study of Chung
and Algren (24) are due to the better defined systems used

in the studies of Richards et al.(89) and Brazinsky (14).

In summary, the results shown in Figures V-A6 and V-A7 indicate that if no fogging occurs in the gas phase, then the Lewis analogy can be used to study the simultaneous heat and mass transfer phenomena during the frosting process.

V-B   Effect of a Temperature Gradient on the Frost Density

Frost is a heterogeneous material consisting of mainly a solid and a gas phase. Its density varies from 0.02 gms./cc. (for a snow formed at cryogenic temperatures) to almost that of solid ice (0.917 gms./cc.) for the high temperature frosts deposited from humid air flowing at extremely high velocity.

The frost formed on a liquid nitrogen cooled surface is very fluffy and hence has a very low density. Due to the fluffy structure, this frost has a very low thermal conductivity. Thus, a thin layer of this kind of frost creates a considerable insulation on the cold surface.

As seen in Section IV-A, there exists a large temperature gradient in the frost interior. It has also been found that the density of the frost increases with time. Thus, this experimental program was undertaken to evaluate a relation between above two experimentally observed occurrences.

A uniform layer of the frost in all the experiments was obtained by sprinkling the snow on the cold plate. The

data of Table IV-B2 indicate that a uniform frost density
over the entire plate within an accuracy of 4% of its value
can be obtained by this method. It should be noted that an
achievement of a uniform layer of frost is important because
a representative sample for the frost density can then be
obtained from any position on the plate.

The data of Table IV-B1 indicate that in general, there
was no significant mass transfer between two adjacent slices
of the frost when the entire frost layer was exposed to a
large temperature difference in the manner described in
Section III-B. This was found to be the case for various
values of frost densities. It was, however, qualitatively
observed in all the experiments that the surface of the
frost at the end of an experiment was quite hard. Thus, it
is possible that even though there was no significant mass
transfer between two adjacent slices of the frost, there
was a significant mass flux between the adjacent layers of
the top slice in each experiment and the density of a very
thin layer at the frost surface was increased significantly
by a temperature gradient.

In order to examine more critically the effect of a
temperature gradient on the top slices of the frost layers
in the above discussed experiments, a few more experiments
were performed in which a frost layer was exposed to a small
temperature difference at the high temperature level (the
average temperature of the frost layer being approximately
15°F). The results of these experiments are shown in Table

As shown in the table, when a frost layer of density
approximately 0.15 gms./cc. and thickness of 0.317 inch was
exposed to a temperature difference of about 27°F, there was
a noticeable amount of mass transfer from the top to the
bottom slice of the frost. This mass transfer also increased
with time. Thus, qualitatively it can be said that the mass
transfer of water vapor due to a temperature gradient does
take place at the temperature level of approximately 15°F.
The quantitative explanation of the results of Table IV-B3
can be given as follows.

If it is assumed that at every layer in the frost
interior, there was an equilibrium between the ice crystals
and the interstitial bulk gas at the prevailing temperature,
then the temperature gradient causes a vapor pressure
gradient at every layer. The amount of water vapor that can
be transferred from the top to the bottom slice under this
situation can be approximately calculated as follows (see
Figure V-B1).

$$N = \frac{D_B}{RT} \frac{(1 - \rho_f/\rho_{ice})}{\tau} \frac{dP_{vp}}{dx}\bigg|_{x=\delta/2} \approx \frac{D_B}{RT} \frac{(1 - \rho_f/\rho_{ice})}{\tau} \frac{\Delta P_{vp}}{\delta}$$

$$(V-B1)$$

It should be noted that above calculation for the mass
transfer rate is very approximate because vapor pressure
does not vary linearly with distance along the depth (x).
However, it is believed that the vapor pressure gradient
at x= $\delta/2$, would be reasonably close to $\Delta P_{vp}/\delta$ (see Figure

V-B1).

For,

$$\tau = 1.10 \quad (\underline{94})$$

$$1 - \rho_f / \rho_{ice} = 1 - 0.15/0.917 = 0.8365$$

$$\Delta P_{vp}/\delta = (3.013-0.776) \times 12/0.37 = 7.25 \ \frac{mm. \ of \ Hg.}{ft.}$$

$$T = 470^{\circ}R \ (average)$$

$$D_B = 0.1965 \ cm^2/sec \quad (\underline{94})$$

$$R = 555.0 \ (mm.of \ Hg. \ cu. \ ft.)/(^{\circ}R \ lb \ mole)$$

from Equation V-B1

$$N = \frac{0.1965 \times 0.8365 \times 7.25 \times 3,600 \times 18 \times 454}{1.10 \times 555.0 \times 470 \times (30.47)^4}$$

$$= \underline{1.51 \times 10^{-3}} \ gms./cm^2 \ hr.$$

The data of Table IV-B3 indicate that experimental mass flux from top to bottom slice was $9.50 \times 10^{-4} \frac{gms.}{cm^2 \ hr}$.
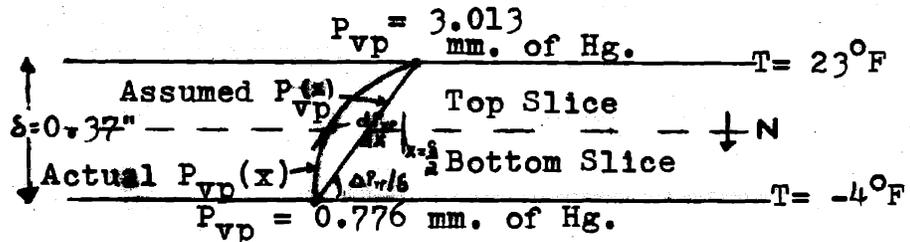
Figure V-B1   Schematic of Physical Process Visualized by Equation V-B1.

From the above described calculation, it can be seen that the experimentally measured mass flux agrees well with one calculated by Equation V-B1. Thus, if the magnitudes of the vapor pressures are high, a temperature gradient does cause the significant transfer of mass due to vapor pressure

driving force.

The results of both large and small temperature differences across the frost indicate that in the static system conditions, as shown in Figures IV-B1 and IV-B2, the sandwiched frost layer probably acquires the equilibrium conditions in its interior. This means that under such system conditions, at every layer of the frost interior, ice crystals and the interstitial gas are in equilibrium at the prevailing temperature.

Under the equilibrium conditions, the mass transfer of water vapor at every point in the frost interior will occur by the prevailing vapor pressure gradient. Since the vapor pressure of ice is appreciable only for temperatures above $-10^\circ F$, the mass transfer by the physical mechanism described above will take place only for a temperature level above $-10^\circ F$. The experimental data with a large and a small temperature difference across the frost indicate this to be the case.

V-B1   Density Distribution within the Frost Deposited by Natural Convection

It is believed that, even though the theoretical models of the present thesis are verified only for the occurrence of the frosting process by forced convection, they can still be applied to the frosting process by natural convection. So, in order to examine the density gradient in the frost deposited by natural convection experiment number R-7 (see Table IV-B4) was carried out.

The results of this experiment indicate that there was no significant density gradient in the frost deposited by natural convection on a liquid nitrogen cooled surface. Since, the density measurements in this experiment were carried out at time of 6.5 hours from the start of the frosting process, one can expect the similar kind of density distribution in the frost interior at any earlier time. Thus, just like density of the frost deposited by forced convection, the natural convection frost is also of uniform density (with depth) at all time. The possible explanation for the uniformity of the density is described in Section II-E.

V-C   Discussion on Results of Measurements on Density Gradient within the Frost

The results of Figure IV-C1 indicate that for a typical set of experimental conditions (Re=15,800, Humidity= Gas dew point at $30^{\circ}F$, $T_g=71^{\circ}F$) the density of the bottom 0.0625 inch thick layer of cryogenic frost increases essentially at the same rate as the average density of the entire frost over the period of 26 to 144 minutes from the start of the frosting process. The thickness of the frost for the same experimental conditions increased from 0.093 to 0.256 inch over the same period of time. The density gradient measurements were carried out at various positions on the heat transfer section of the copper plate. The results similar to ones shown in Figure IV-C1 were obtained.

The maximum possible error in the density values of

Figure IV-C1 is within ±12%. The major errors were caused
in slicing and in thickness measurements. The details of
the error analysis is shown in Appendix N.

Figure IV-C2 shows the variation in temperature
distribution within the frost with time for the same
experimental conditions as used for the results of Figure
IV-C1. The results of this figure show that the temperature
of the frost layer, 0.0625 inch away from the cold wall
varied from -44°F to -173°F over the period of 26 to 144
minutes. Thus, the average temperature of that layer during
the frost densification process was -108°F.

The densification of the bottom 0.0625 inch thick
frost from 0.085 gms./cc. to 0.161 gms./cc. over a period
of 118 minutes required the transport of 0.0125 lbm/hr ft^2
of water in that region, i.e., this amount of water has
to pass the frost layer at x=0.0625 inch from the cold wall.
In the discussion that follows, a feasible mechanism for
this transport of water will be developed.

If, it is assumed that there exists an equilibrium
between bulk gas and ice crystals at every point in the
frost interior then the prevailing temperature gradient will
establish a vapor pressure gradient at every point. Under
these circumstances, molecular diffusion of water vapor by
vapor pressure gradient will transport the water at every
point in the frost interior. Mathematically, the water flux
by this mechanism can be written as,

$$N = \frac{D_B}{RT} \frac{(1- \rho_f/\rho_{ice})}{\tau} \frac{\partial P_{vp}}{\partial x} \qquad \text{(V-C1)}$$

If Equation V-C1 represents truly the mechanism of water transport in the frost interior, then it should satisfy the experimental results for mass flux at x=0.0625 inch. From the results of Figure IV-C2 and with the help of Equation V-C1, the water vapor flux at x=0.0625 inch can be calculated as follows:

At x = 0.0625 inch, and at time = 85 mins. (Arithmatic mean time),

$$T = 342°R = 190°K$$

$$\frac{\partial P_{vp}}{\partial x} = 6.25 \frac{lb_f}{cu\ ft.} \qquad (\text{ from Figure IV-C2})$$

$$D_B = 2.6795 \times 10^{-6} T^{2.0087} = 0.0965\ cm./sec.\ (\text{from Figure II-B10})$$

$$= 0.133\ gms./cc.$$

$$N = \frac{0.0965 \times 118 \times 18 \times (1-0.133/0.917) \times 6.25}{342 \times 1.544 \times 10^3 \times 1.10}$$

$$= \underline{0.00189} \quad lbm/hr\ ft^2$$

Comparing the above value of mass flux with the experimental one, it can be seen that the experimental mass flux is considerably higher than one calculated from Equation V-C1. Thus, Equation V-C1 can not represent the true process for water transport in the frost interior.

If water vapor transport occurs by non-equilibrium

partial pressure gradient, then as shown in Section II-C,
partial pressure at x=0.0625 inch can be calculated from
the following Equation V-C2

$$P_{x=0.0625"} = \int_{x=0}^{x=0.0625"} x \frac{RT}{D_B} \frac{\tau}{(1 - \rho_f/\rho_{ice})} dx \qquad \text{(V-C2)}$$

Substituting τ=1.10 (94), D_B=3.3 x 10^{-6} $T^{2.0087}$
(see Figure II-B10), where, D_B is in ft^2/hr and T is in $^\circ$R
and using the data of Figures IV-C1 and IV-C2 at time of
85 minutes, $P_{x=0.0625"}$ can be calculated to be 1.485 mm.
of Hg.   Hence, this calculated partial pressure indicates
that at x=0.0625", supersaturation ratio $= \frac{p}{P_{vp}} = \frac{1.485}{5.2 \times 10^{-4}} =$
2.86 x10^3.

It should be noted that in the above calculation $p_{x=0}$
was assumed to be zero.   This assumption makes the above
calculated value of $p_{x=0.0625"}$ the most conservative one.

The strong possibility for nucleation indicate that
water transport at every layer could not occur by the
diffusional mechanism under the non-equilibrium partial
pressure gradient.   This indication can be verified by
calculating the partial pressure at the frost surface from
Equation V-C2 by setting upper limits on the integrals
as x = δ.   For the present experimental conditions (see
Figures IV-C1 and IV-C2), this value is found to be 16.865
mm. of Hg. which is higher than even the bulk gas humidity
(4.14 mm. of Hg.).   Thus, this result shows that Equation
II-C1, does not represent the true mechanism of the frost

densification process.

It should be obvious to note that if the boundary
condition for Equation II-C4 is set at the frost surface,
then the partial pressure at x = 0.0625 inch can be
calculated from the following Equation V-C3.

$$P\Big|_{x=\delta} - P\Big|_{x=0.0625''} = \int_{x=0.0625''}^{x=\delta} x\, \frac{d\rho_f}{d\theta}\, \frac{\gamma\, RT}{(1-\rho_f/\rho_{ice})D_B}\, dx \qquad (V\text{-}C3)$$

Assuming $P\Big|_{x=\delta} = P_{vp}\Big|_{x=\delta} = 1.632$ mm. of. Hg.
(Note that this assumption is quite realistic as indicated
by simple model) and calculating the right hand side of
the above Equation V-C3 from the data of Figures IV-C1
and IV-C2, $P_{x=0.0625''}$ can be found to be -13.648 mm. of
Hg.   This absurd value for partial pressure, once again,
indicates that Equation II-C1 does not represent the
true mehcanism of the frost densification process.   The
water transport past every layer in the frost interior
should occur by a mechanism other than only molecular
diffusion of water vapor as assumed in Equation II-C1.

So far, the critical evaluation of the experimental
results of Figures IV-C1 and IV-C2 have indicated that in
the colder region of the frost, most of the water should
exist in the form of ice nuclei.   These nuclei could be
formed by any of the three mechanisms of nucleation des-
cribed in Appendix H. The existence of a large temperature

driving force as shown in Figure IV-C2, suggests that the
required water flux at x=0.0625 inch can be obtained by
thermal diffusion of ice nuclei. This hypothesis can be
varified as follows.

The phenomenon of thermal diffusion of solid or liquid
particles in air is discussed in detail in Appendix K. A
literature survey has indicated that a theoretical correla-
tion of Brock (15) is the best known, as yet, for the
calculation of the force acting on a solid particle in a
thermal unequilibrium state. This correlation along with
Stoke-Cunningham equation (96) can be used to calculate a
diffusive velocity of a particle under a thermal force.

Assuming that ice nuclei are 50 °A in diameter (See
Figure H-1) and calculating thermal diffusive velocity
to be 82 ft/hr from Equation II-E32, the nuclei concentra-
tion needed for the required water flux will be

$$n' = \frac{0.0125 \times 454}{82.0 \times 2.81 \times 10^4 \times 6 \times 10^{-20}} = 4 \times 10^{13} \frac{molecules}{cc.}$$

If it is assumed that the above calculated nuclei are
formed in 10^{-5} sec (note that there is no basic ground for
this assumed time except that it may give a maximum value
of nucleation rate), then required nucleation rate at x=
0.0625 inch will be 4×10^{18} nuclei/cm^3 sec.

Even in the worst case of nucleation, when homogeneous
nucleation is a predominant mechanism, the partial pressure
required to form above calculated nuclei concentration rate
can be obtained from the theoretical relationship of Becker

and Doring (8) as shown in Figure H-4.

From Figure H-4, at $T=190^{\circ}K$ and for nucleation rate of 4×10^{18} nuclei/cm^3 sec , $p/P_{vp} = 282$

Since, at $T=190^{\circ}K$ $P_{vp} = 2.45 \times 10^{-4}$ mm. of Hg., partial pressure at $x =0.0625$ inch, necessary to form a sufficient number of nuclei for the required water flux, is .069 mm. Hg.

The magnitude of this partial pressure and its comparison with the partial pressure calculated from Equation V-C2 indicate that the required water flux by the mechanism of thermal diffusion of ice nuclei appears quite feasible.

Thus, the above described discussion shows that the quantitative explanation of the results of Figures IV-C1 and IV-C2 demands a feasible explanation for the transport of water in the colder region of the frost. The most conceivable physical process that could explain this transport is the thermal diffusion of ice or water nuclei. The detailed theoretical discussion for this experimentally observed phenomenon of uniform densification of the frost is described in Section II-B to II-E.

In order to examine the phenomenon of uniform densific-ation more critically, an experiment was performed in which the transfer of water in the colder region was examined qualitatively. The set-up for this experiment was as follows.

A stainless-steel screen was sandwiched between two

glass wool plugs of total thickness of approximately 0.05 inches. The glass wool screens were so designed that their porosities were almost the same as that of cryogenic frost. The total thickness of this glass wool-screen assembly was approximately 0.0625 inch. The assembly was fastened on to the copper plate and the surface of the top glass wool was flushed with the bottom of the duct.

A regular frosting experiment was then performed with this kind of experimental set-up. The experiment lasted for about an hour. The frost deposition on the top glass wool from flowing humid air was observed during this time.

After the experiment, the top glass wool screen and the deposited frost were removed gently. Both the stainless steel screen and the glass wool screen near the cold wall were examined visually for the presence of frost particles. It was found that both screen and lower glass wool were filled with scattered collections of tiny frost particles (size < 0.05 cm.).

Comparing this experiment with the usual frosting experiment, it can be seen that is this experiment the bottom 0.0625 inch thick glass wool-stainless steel screen assembly was used as the replacement for the frost layer. Thus, if the results of Figure IV-C1 are actual facts then there should be water flux into the glass wool screens in the present experiment. As described above, the results of the experiment indicate qualitatively

that there is indeed transfer of water flux in the colder

region of the glass wool screens. Thus, this additional

experimental fact supports the previous conclusion that

there is a transport of water in the colder region of the

frost.

As discussed previously, the thermal diffusion of ice

nuclei appears to be, at present, the most feasible

explanation for the water flux in the colder region of the

frost.

V-D <u>Discussion of Results of Heat Transfer Coefficients</u>
<u>in Non-frosting Conditions</u>

The data of Figure IV-D1 indicate that heat transfer

coefficients at various Reynolds numbers under non-frosting

conditions agree quite well with ones predicted by Sleicher

and Tribus's theoretical analysis (<u>105</u>). The cold wall

temperature in these experiments were maintained at the

same temperature level as that of frost surface temperature

obtained (in the quasi-steady state of heat flux) during

the frosting experiments. Thus, it is expected that the

heat transfer characteristics of the non-frosting and the

frosting experiments are almost identical.

While comparing the experimental data with the

theoretical analysis of Sleicher and Tribus (<u>105</u>), it

should be noted that the measurements of heat transfer

coefficients were carried out for gas flow over a rough

surface (i.e. surface of corrigated aluminum foil). The

Sleicher and Tribus's theoretical analysis, on the other hand, assumed that there was no loss of energy due to frictional force between the flowing gas and the rough cold surface. One would expect, however, that for low viscous fluid like air the dissipation of energy due to friction is negligible. The following calculations evaluate the importance of frictional force in the present experimental conditions.

The Calculation of Energy Dissipation due to Frictional Force in the non-frosting Experiments:

The energy loss due to frictional force between the flowing gas and the rough surface can be calculated from Equation V-D1 shown below (page 5-19 of Reference 80)

$$F = \frac{32 \ f \ L \ q'^2}{2 \ g_c \ D^5_H} \qquad (V-D1)$$

At Reynolds number=10,000, f=0.01 (for the surface roughness like corrigated aluminum from Figure 5-25 in Reference 80).

L = 0.23 ft. (radius of the copper plate)

$q'^2 = (42/60)^2 = 0.49 \ ft^2/sec^2$

$D^5_H = (0.8/12)^2 \ ft^2$

Substituting all the values in Equation V-D1, one obtains

$$F = \frac{32 \times 0.01 \times 0.23 \times 0.49 \times (1.2)^5 \times 10^5}{9.87 \times 32.17 \times .327}$$

= 35.2 ft lb force/lb of gas flowing

Thus, the rate of frictional loss of energy

$$=(35.2)x(42x0.0734)x(32.2x3.995x10^{-5}x\ 60)$$

$$= \underline{8.37}\ Btu/hr$$

The heat flux from gas to cold wall as measured
experimentally for Reynolds number of 10,000 is 784 Btu/hr
ft^2.   If it is assumed that a constant heat transfer over
the entire plate, then the total heat transfer rate over
the entire rough surface

$$Q = 784x(\pi/4)x(5.54/12)^2 = 131.5\ Btu/hr$$

percentage contribution of the frictional energy to the
heat energy transport is $(8.37x100)/131.5 = 6.36\%$

It should be noted that in actual case, the heat
transfer rate over the entire plate would be considerably
higher than the one calculated above because the heat
transfer coefficient in the thermal entrance region would
be much higher than one used above.   Thus, in reality,
the percentage contribution of frictional energy to the
heat energy would be considerably lower than one computed
above.   The application of Equation V-D1 for the present
calculation is only approximately correct because it is
derived only for isothermal conditions of the system.

The above described calculations indicate that
frictional energy loss is insignificant and can be safely
neglected in the evaluation of the heat transfer coefficient
measurements under the non-frosting conditions.   Thus, a
good agreement between the experimental and the theor-
etical values of heat transfer coefficient as shown in

Figure IV-D1, should be expected.

It is assumed that Sleicher and Tribus's theoretical correlations between the heat transfer coefficients and Reynolds number at other gas temperatures will be equally close to the truth as it is for the gas temperature studied in the present experimental studies.

Table V-A2

Excess Thermal Conductivity as a
Function of Temperature

Temperature ($^{\circ}$F)	K_{excess} $\dfrac{Btu}{(hr\ ft^2\ ^{\circ}F/ft)}$
-215	negligible
-145	negligible
-80	negligible
0	0.0030
+20	0.0078
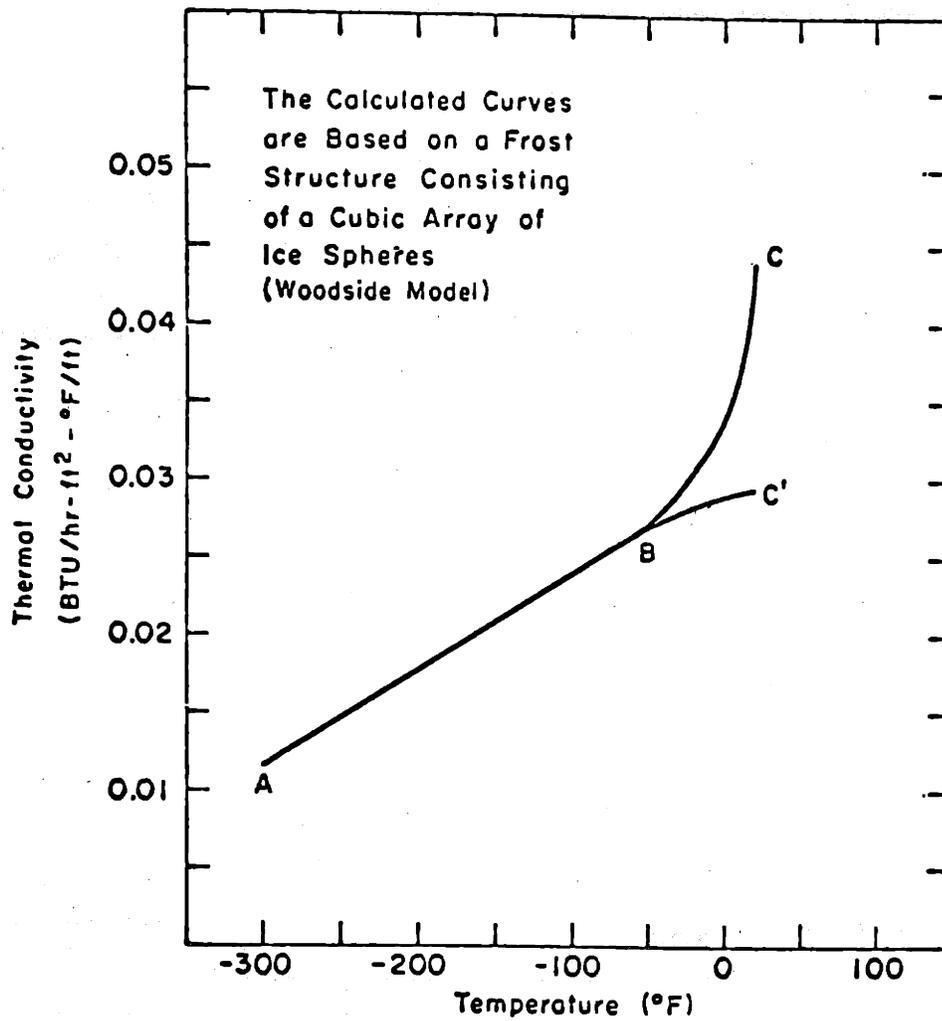
Figure V-A1   Point Thermal Conductivity as a Function of
Temperature for a Frost Density of 0.09 gm/cc
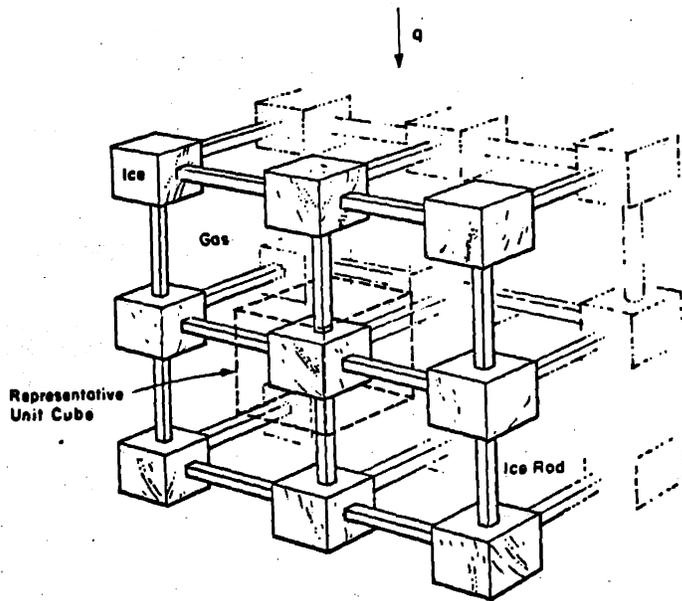
Note: Though it is not Shown in this Diagram,
Rods Extend from all Six Faces of
Each Cube

Figure V−A2   Assumed Frost Structure ; Cube and
Rod Model
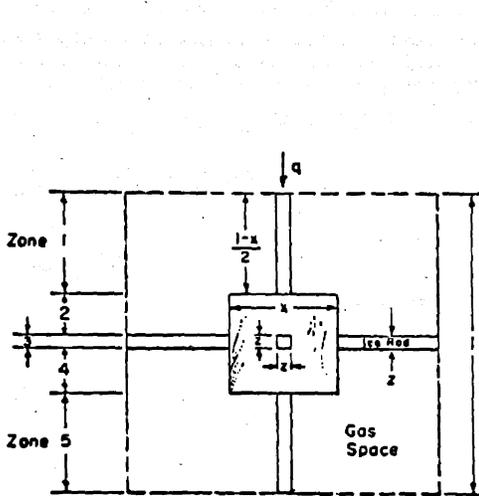
FigureV−A3 Planar View of a Representative Unit Cell
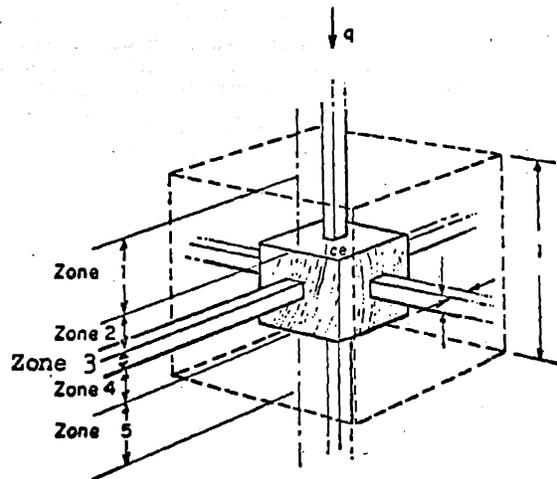
Figure V−A4   Representative Unit Cell for
Cube and Rod Model
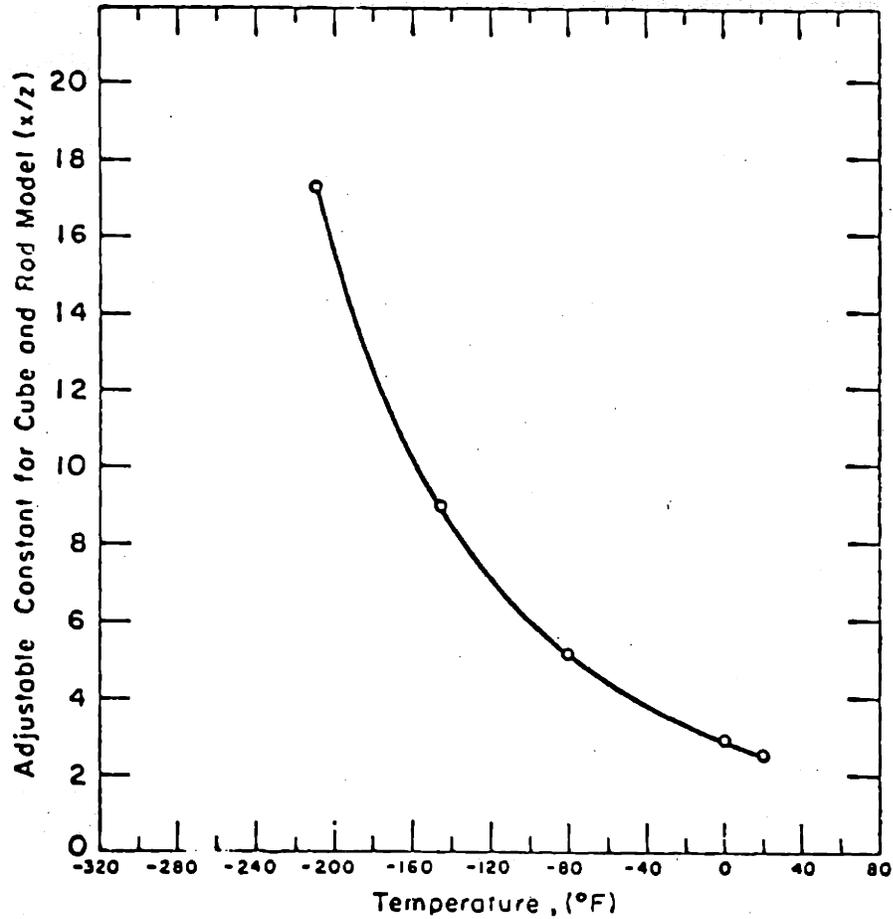
Figure V-A5 x/z as a Function of Temperature
for Cube and Rod Model

Figure V-A6 (left)

Heat Transfer Coefficient (BTU/hr ft² °F)

Reynolds Number

① T_g=93°F, T_s= 15°F
② T_g= 75°F, T_s= 8°F
③ T_g= 50°F, T_s= 5°F
④ T_g= 34°F, T_s= 2°F
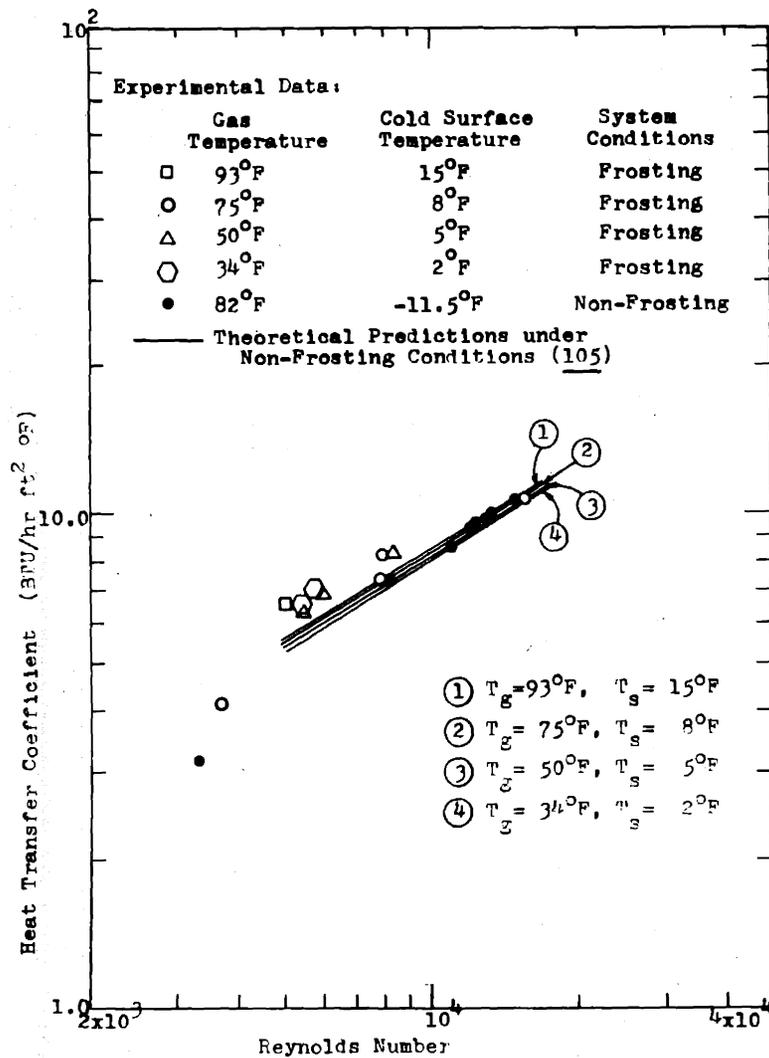
Figure V-A6   Heat Transfer Coefficient versus Reynolds Number (at Various Gas Temperatures) under Frosting and Non-Frosting Conditions

Figure V-A7 (right)

Mass Transfer Coefficient (ft/hr)

Reynolds Number

① T_g= 93°F, T_s=15°F
② T_g= 75°F, T_s= 8°F
③ T_g= 50°F, T_s= 5°F
④ T_g= 34°F, T_s= 2°F
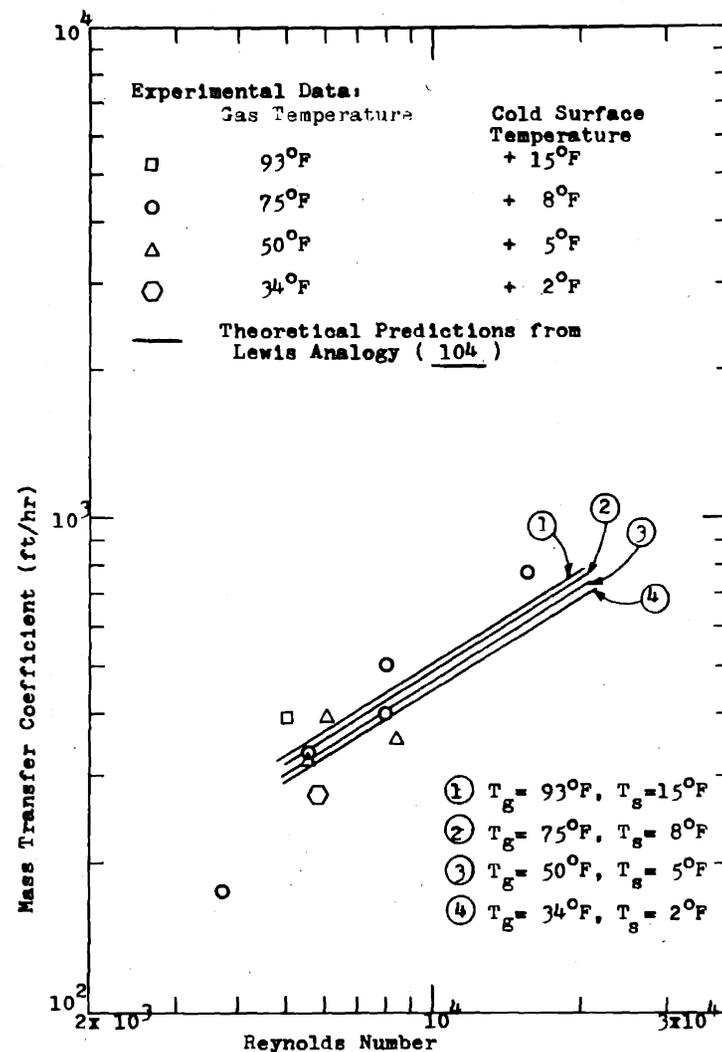
Figure V-A7   Mass Transfer Coefficient versus Reynolds Number (at Various Gas Temperatures) under Frosting Conditions

S E C T I O N   VI

CONCLUSIONS

1. After a smooth layer of frost is formed on a liquid nitrogen cooled surface, heat and mass transfer during the frosting process are governed by diffusional mechanisms in the gas phase boundary layer (i.e. no fogging occurs).

2. For all the system conditions,

   A. Both frost density and thickness increase continuously with time.

   B. The heat flux through the frost decreases at first, but levels off and attains a constant quasi-steady state value.

   C. The frost surface temperature increases rapidly at first, but attains a constant value at a later time.

3. In the quasi-steady state of heat flux, both surface temperature and the thermal resistance of the frost remain constant due to a high gain negative feed-back effect of internal diffusion of water vapor to the frost surface temperature.

4. The frost thermal conductivity increases with frost density and temperature.

5. Increase in Reynolds number (at constant humidity and gas temperature),

   A. Increases the frost density at equivalent time.

   B. Decreases the frost thickness at equivalent time.

   C. Increases the quasi-steady state heat flux.

D. Slightly increases the frost surface temperature in the quasi-steady state of heat flux.

6. Increase in gas temperature (at constant humidity and Reynolds number),

A. Increases the frost density at equivalent time.

B. Decreases the frost thickness at equivalent time.

C. Increases the quasi-steady state of heat flux.

D. Slightly increases the frost surface temperature in the quasi-steady state of heat flux.

7. Increase in humidity (at constant gas temperature and Reynolds number)

A. Slightly increases the frost density at equivalent time for the humidity range of gas dew point at 14.3^OF to gas dew point at 33.2^OF.

B. Increases the frost thickness at equivalent time.

C. Slightly decreases the quasi-steady state heat flux.

D. Increases the frost surface temperature in the quasi-steady state of heat flux.

8. With the help of accurate knowledge of heat and mass transfer coefficients, the computer program of Appendix D will successfully predict the time variation of average frost density, frost thickness, mass deposition and heat flux through the frost. The predictions can be made for all the practical range of system conditions, once a smooth layer of frost is deposited from a flowing gas on the liquid nitrogen cooled surface.

9. If an accurate correlation between the frost thermal conductivity, temperature and the frost density is known for the range of interest of density and temperature, then a computer program similar to one described in Appendix D can be used to predict the frost behavior under an arbitrary set of system conditions. Thus, 'simple model' can be used for design of cryogenically cooled equipment under frosting conditions.

10. A temperature difference imposed across the frost in the static conditions (no transfer of heat and mass from o outside) causes the mass transfer solely due to temperature gradient only at high temperature levels (where the vapor pressures of ice are of significant magnitude) within the frost.

11. Sleicher and Tribus's theoretical analysis can be well used for the heat transfer calculations for the frosting process in the systems similar to one used in the present thesis.

12. The densification of the frost by the transport of water vapor under the driving force of vapor pressure gradient (caused by a temperature gradient) prevailing at every layer in the frost interior will cause a significant build-up of density gradient in the frost interior.

13. The density of the frost deposited on a liquid nitrogen cooled plate stays always uniform with depth.

14. Even though the water transport past the frost-gas interface can be successfully predicted with the assumption of an equilibrium between ice and gas at the frost surface,

the complete picture of the frosting process can only be
successfully modelled with the assumption that water
transport at every layer in the frost interior occurs under
non-equilibrium conditions. The uniform densification of the
frost appears to be explained by 'Non-Equilibrium Model'.

S E C T I O N — VII

RECOMMENDATIONS

1.   In order to expand the range of application of the successful theoretical model ('simple model') of the present thesis, the experimental studies of carbon dioxide frosting process should be carried out in the system similar to one used in the present study.

2.   As seen in Section II, the quantitative theoretical explanation for the uniform (with depth) densification of the frost demands the following investigations:

A.   The experimental study of phenomenon of secondary nucleation from vapor phase at low temperatures.

B.   The experimental study of homogeneous nucleation from vapor phase at temperatures below $200^{\circ}K$.

C.   The experimental study of thermal diffusion of aerosols in air at low temperatures (at all temperatures below $32^{\circ}F$).

D.   The experimental study of crystal growth from vapor phase at the temperatures below $-30^{\circ}C$.

E.   The theoretical study of dendritic crystal growth from vapor phase.

APPENDIX   A̲

Instrumentation for the Apparatus of Figure III-A1

1. Temperature Measurements

Temperature measurements were made with both chromel-constantan and copper-constantan thermocouples. The various temperature measurements carried out in the system of Figure III-A1 are described below.

A. Gas Temperatures

Gas temperatures were measured at the inlet and the outlet of the duct and right above the copper plate. The gas temperature above the copper plate was measured with a movable thermocouple probe---- the same probe used to measure the temperature of the frost surface. The gas temperatures at the duct inlet and outlet were measured with 72 inches long No. 24 gauge chromel-constantan thermocouples fixed in the gas phase. (Thermocouples were made by Nonmac Corporation, 140, Crescent Road, Needham, Massachusetts; according to their catalogue No. 40-E specification). The long and thin thermocouple wires were used to reduce the error in the measurement due to heat conduction along the wires to the measuring junction.

B. Temperature Measurements on Copper Plate

The thermocouples located on the copper plate were made of No. 24 gauge copper-constantan wire. Two thermocouples were silver soldered to the underside of the inner and the outer section of the plate as shown in Figure A-1. One thermocouple was used to check the reading of the other.

C. Calorimeter Temperature

The temperature of the gas space in the outer chamber
was measured with No. 24 gauge, copper-constantan
thermocouple. During normal operation of the calorimeter,
this temperature was usually within few degrees of the
liquid temperature (The liquid nitrogen in the guard chamber
was essentially at the normal boiling point). The location
of this thermocouple in the calorimeter is shown in Figure A-1.

D. Temperature Measurements in the Frost Interior

Temperatures in the frost interior were measured with
No. 30 gauge (wire diameter = 0.005 inch) thermocouples
located at the fixed heights over the cold plate. The exact
distances between the copper plate and the centre of thermo-
couple beads were determined at the beginning and the end of
each experiment. The wires were kept taut and parallel to
the plate as shown in Figure A-2. The gas flowed in a direction
parallel to the length of the wire. The distance between the
two closest thermocouples and between the lowest thermocouple
and the plate was about 0.05 inch to 0.06 inch in most of the
experiments. The maximum thickness of the thermocouple bead
was about 0.02 inches. Since there is a large temperature
gradient existing in the frost interior, there could be
significant error in the temperature versus distance profile
due to inaccuracy involved in the determination of the exact
location for the thermocouple joint.

E. Movable Probe for Measurement of Frost Surface Temperature

A movable thermocouple probe was used to measure the

surface temperature of the frost. This probe, which could move up and down in a vertical plane, was a loop type thermocouple as shown in Figure III-A2.

The maximum thickness of the measuring junction was about 0.02 inches. With the help of this thermocouple, the frost surface temperature was measured by the method described in Section III-A. The thermocouple was made of No. 30 gauge copper-constantan wires.

F. Errors in the Surface Temperature Measurement

A possible source of error in the measurement of the frost surface temperature was conduction to the junction along the thermocouple wires. This error was made negligible by taking two precautions: first, thin thermocouple wire was used; secondly, when a surface temperature measurement was being made, a copper and a constantan wire, each two inches long, extended from the junction and contacted the frost surface. This ensured long isothermal paths on either side of the junction and hence conduction to the bead was minimized.

Another possible source of error was radiant heat transfer from the warm duct to the bead in contact with the surface. The magnitude of this error could not be estimated accurately as the contact thermal resistance between the thermocouple junction and the frost itself was unknown. The error was reduced by taking two precautions. First, when making a surface temperature measurement, the thermocouple junction was allowed to remain contact with the frost surface for a

relatively long length of time (about one minute). Thus,
presumably, a substantial portion of bead was covered by
the growing frost for a long time to minimize radiation
effect. Secondly, radiant heat transfer from the warm inside
of the duct to the colder thermocouple junction was minimized
by lining the inside of the Lucite section right above the
copper plate with aluminum foil.

The magnitude of the error caused by gas flow over the
thermocouple bead in contact with the frost surface also
cannot be estimated accurately, since the thermal contact
resistance between bead and frost is unknown. Again, this
error was reduced by allowing a significant portion of the
thermocouple bead to become covered with the frost when a
surface temperature measurement was being made. Errors
caused by both radiation and gas flow over the thermocouple
bead would result in thermocouple readings which are too
high.

As mentioned earlier, the movable thermocouple probe
also measured the temperature of the gas stream over the
copper plate. The gas flow past the probe did not cause a
significant error in the gas stream temperature measurement.

2. Pressure Measurements

Pressure measurements for the orifice meter were carried
out with water-filled manometers. In the initial runs,
pressures at the inlet and the outlet of the duct were
measured with low pressure gauges. These pressure values are
not reported in this thesis. It should be noted, though,

that the pressure in the gas stream over the copper plate
was essentially atmospheric for all the flow rates studied
in this thesis.   Pressures in the inner and outer
cylinders of the calorimeter were also measured with
water-filled manometers.

3.   Flow Measurement

As mentioned earlier the flow rate was measured with
an orifice meter.   Three different orifice meters with the
hole diameters of 0.346",0.535" and 0.80" were used.   The
meter was constructed according to the ASME code described
in Reference 4.   The centres of the upstream and the
downstream tap holes were located exactly at distances of
one tube diameter from the upstream and the downstream
faces of the orifice plate respectively.   The tap lines
were $\frac{1}{4}$ inch copper tubes soldered into the $\frac{1}{4}$ inch tap holes.

For maximun accuracy the orifice hole was positioned
so that it was concentric with the tube openings.   To
further ensure accurate flow rate determination the
lengths of straight pipe upstream and downstream of the
orifice plate were made longer than the recommended minimum
requirements (80).

Despite all the precautions taken in constructing
the orifice meter, it was still decided to calibrate
(see Appendix B for details of the calibration procedure).

4.   Measurement of Humidity

The humidity of the flowing gas was measured at a

short distance upstream of the duct by analyzing a sample
drawn from the flowing stream. To be more specific, the
humidity was measured by determining the quantity of water
vapor contained in a measured volume of gas sample. A schematic
of the humidity measuring equipment is shown in Figure A-3.
The gas sample was flown through a tube containing molecular
sieve 10X and then through a wet test meter. The flow rate
of the gas sample was insignificant compared with the flow rate
of the flowing gas in the system.

The volume of gas bled off for analysis was measured
with a wet test meter. The weight of water vapor contained in
this gas sample was determined by weighing the tube containing
molecular sieve before and after the sample was passed
through it. This method of measuring gas stream humidity was
found to be quite reliable as the tube was designed long
enough so that substantially all the moisture in the gas
sample was adsorbed by molecular sieve. Complete drying of
the air was also verified by changing the flow rate of the
gas. The reliability of the method was checked by measuring
the humidity of a gas stream which had been saturated with
water vapor at a known temperature. "Checks" were performed
at several humidities. In all the cases the humidity measured
by the method described above was within 3% of the true
humidity.

During a frosting run, the humidity of the flowing gas
was measured several times. Frequencies of the measurement
depended upon the length of the experiment. The measured

humidity variation during a run was generally within $\pm$ 2%
of the values given in column 4 of Table IV-A2. The humidity
variation was usually random with time; i.e., it did not show
a consistent trend during the course of a run.

It should be noted that the observed humidity variation
and the error in the humidity measurement were approximately
equal. Thus, it is probable that the observed random humidity
variation was due to errors in the measurement of the
humidity rather than to variation in the performance of the
drier and the humidifier system.

5. <u>Pipings for the System</u>

The majority of the pipings for the system consisted of
polyvinyl chloride tubing and the rest was made of metal and
rubber tubing. The majority of tubings were one inch in
diameter. Smaller diameter tubings, however, were employed
for some of the parallel and by-pass gas flow lines. The
section of the system after the heat exchanger was insulated
with fibreglass aircraft insulation in order to control the
gas temperature.

Copper Plate

Thermocouples

Thermo-
couples

Outer
Brass
Chamber

Inner
Stainless-
steel
Chamber
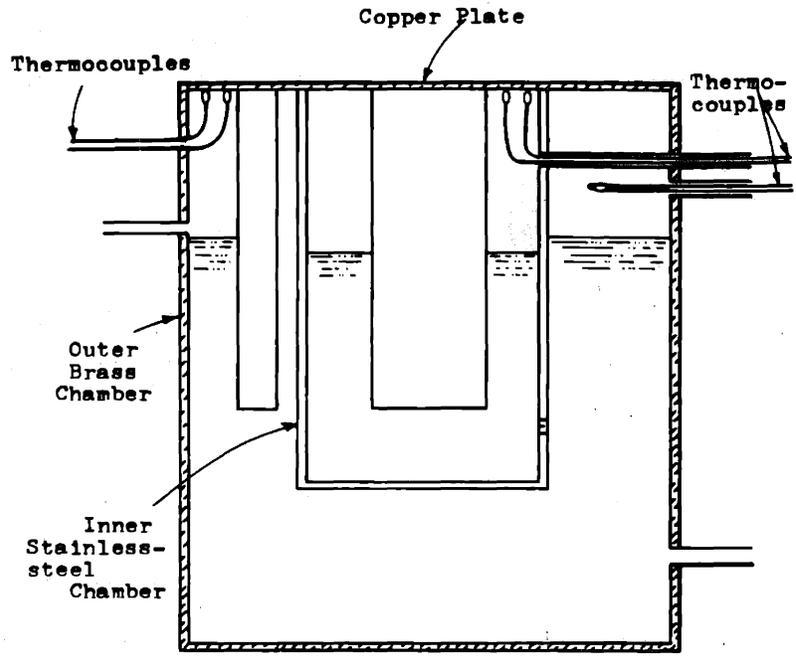
Figure A-1   Schematic Diagram Showing the
Temperature Measurement Locations
in the Calorimeter Assembly

Movable Thermocouple
to Measure Frost
Surface Temperature

Fixed Thermo-
couples to
Measure the Temperature

Thermocouple Bead

Air Flow

Distribution within the
Frost

5.54m

Thermocouples Measuring
the Temperature of the
Copper Plate
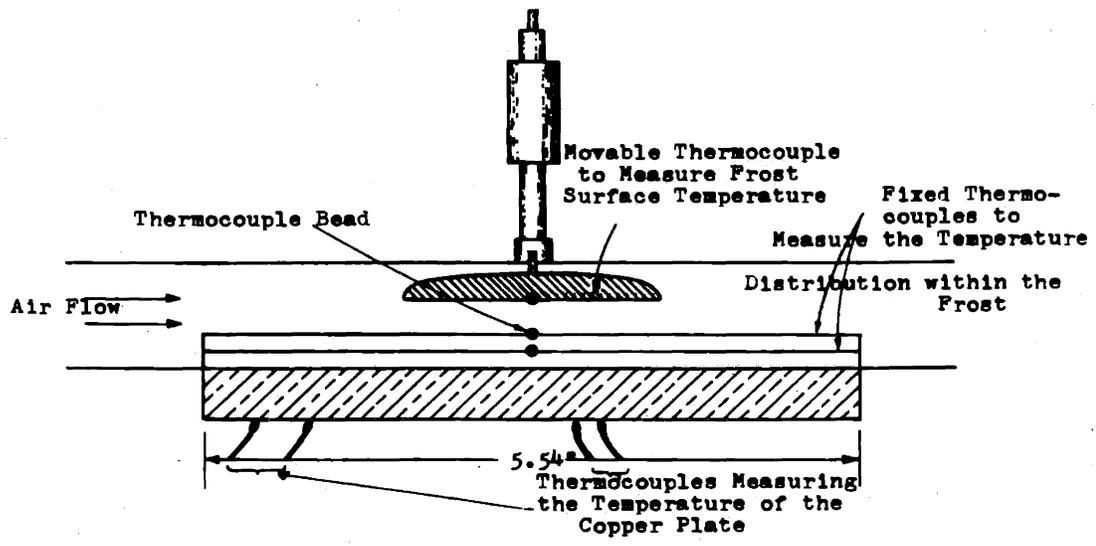
Figure A-2   Schematic Diagram Showing the Fixed and Movable
Thermocouples over the Copper Plate
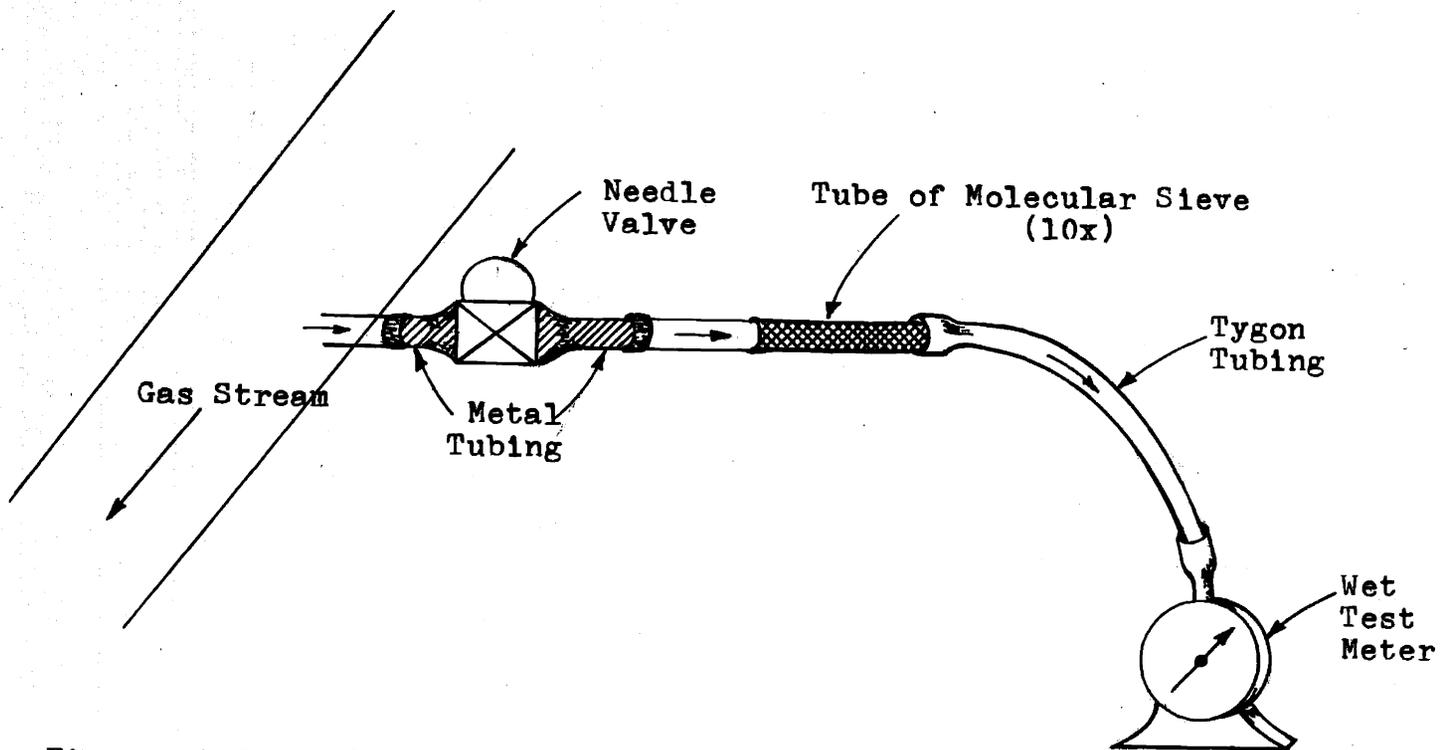
Figure A-3   Schematic Diagram for Gas Sampling
                       for Humidity Analysis

APPENDIX   B

Calibration of Orifice Meters

The two orifice meters (0.346 inches and 0.535 iches
in inside diameters) were calibrated over the entire range
of pressure measurements. Where-as 0.80 inches diameter
orifice meter was calibrated only for its lower 25% range
of the pressure measurements. These calibrations covered
the entire range of their application.

The calibrating device was a large gasometer. Constant
flow rates were produced by the displacement of gas from
an inverted vessel which fell with a constant velocity
through a tank containing oil. Gas flows up to about 60
std. ft^3 / minute were produced. The schematic of the set-up
for the calibration is shown in Figure B-1.

Agreement to within 2% was obtained between the actual
flow rates determined by measuring the displacement of
gasometer and the calculated rates. "Calculated" rates were
obtained using standard sharp edged orifice meter equation (4).
The error values at the various flow rates did not exhibit
any trend with flow rate.
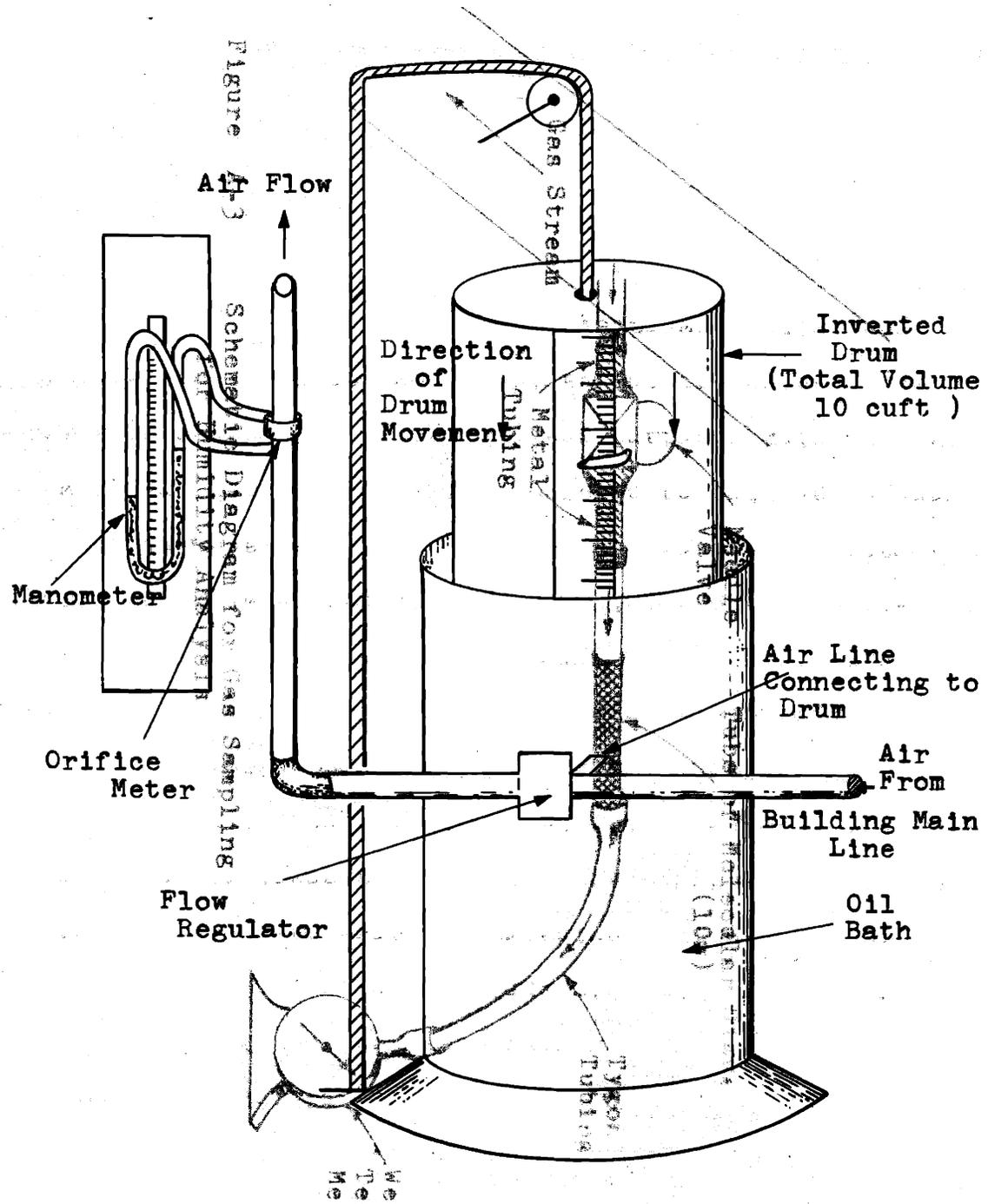
Figure B-1   Schematic Diagram of Set-up for the
Calibration of Orifice Meter

APPENDIX   C

Calibration of Calorimeter

The details of the calorimeter construction and
operation have been presented in Section III-A.   When
heat flux is measured by the method described in Section
III-A, errors can arise from various sources.   For example,
one possible source of error is the entrainment of liquid
droplets in the calorimeter boil-off and the subsequent
vaporization of these droplets in the inner cylinder outlet
line (see Figure III-A2).   In addition, another source
of error is the superheating of the boil-off nitrogen vapor
in the inner stainless steel calorimeter vessel.   Thus
in order to have confidence in the heat flux measurements
the calorimeter had to be calibrated.

The source of heat for the calibration was an electrical
heater, which was well insulated.   The electrical energy
output of the heater could be varied by changing the voltage.
This electrical heater was sandwiched between two different
slabs of cork.   The top slab was approximately 3 inches
thick. The thickness of the lower slab varied from 2 to 3
inches. Some experiments were also made without the lower
slab (i.e., by direct contact of heater with copper plate).
The sides of the heater were insulated by 6 inches thick
fibre glass insulation. The complete heater assembly was
placed on the copper plate. The details of the experimental
"set-up" are shown in Figure C-1.

With the calibration set-up described above, substantially
all the electrical energy produced by the heater was passed

into the copper plate through the lower slab of cork. The following measurements were carried out during a calibration experiment.

1. The current and the voltage across the heater were measured to calculate energy output from the heater. (Direct current was employed for all the calibration experiments).

2. Temperature differences across both lower and upper cork slabs were measured by the thermocouples. The thermal conductivities of the cork slabs were obtained from the literature (48, 54, 118)

3. The boil-off of liquid nitrogen was measured by a calibrated rotameter.

The comparison between the heat fluxes calculated from the liquid nitrogen boil-off measurement, electrical heat input to the heater and the calculated heat flux through the bottom cork slab for three different calibration experiments is shown in Table C-1. The close agreement among all of them indicate that the measurement of the liquid nitrogen boil-off is a reliable method for obtaining the true heat flux into the calorimeter. In the worst case, the heat flux values disagreed by 3.90%.

No calibration curve for the calorimeter was established as the agreement between known heat fluxes and the values determined from the boil-off measurements was quite good. The reported heat flux values for the various frosting runs were, therefore, determined solely from the liquid nitrogen boil-off measurement. The brief descriptions

of the electrical heater and the available literature
information on the cork thermal conductivities are given
below.

A.   Electrical Heater

The heating element was Nichron replacement electrical
heating wire (maximum output 600 watts). It was wound in
a number of horizontal loops. These loops were all
located in the same plane and were sandwiched between two
1/8 inch stainless steel plates. The stainless steel
plates were cemented to each other and the space between
the two plates was filled with glass wool to minimize heat
loss.

The measured electrical resistance of the heater was
19.437 ohms. This value was essentially independent of
wire temperature or applied voltage over the range of the
conditions used in the calibration runs.

B.   Cork Thermal Conductivities

In order to calculate the heat fluxes through the cork
slabs, it was important to know the accurate values of the
cork thermal conductivities. Cork conductivity data were
obtained from different sources (48,54,118). These
references furnished the data over a wide range of
temperature and cork density. These data indicated that
conductivity is a strong function of density. The densities
of the various pieces of cork employed in the calibration
experiments were therefore measured and these values were
used to obtain the appropiate conductivities.

C.   Sample Calculation for Calibration Experiment

Case 1 in Table C-1

1.   Calculation of Electrical Heat Output

R = Resistance of electric heater = 19.437

V = Voltage = 10 volts

Electrical heat input = $\dfrac{V^2}{R}$ = $\dfrac{100}{19.437}$ = 5.14 watts

$$= 4.87 \times 10^{-3} \text{ Btu/sec.}$$

Area of heater = $\dfrac{6"x6"}{144}$ = 0.25 ft^2

heat input/area = $4.87 \times 3.6 \times 10^3 \times \dfrac{144}{36} \times 10^{-3}$

$$= 70.2 \text{ Btu/hr ft}^2$$

2.   Calculation of Heat Flux Through Upper Cork Slab.

The cork slab density = 0.1144 gms/cc

ΔT across the cork stab = 80–72 = 8°F

K_{avg} , at 76°F and density of 0.1144 gms/cc = 0.28 Btu/hr ft^2
°F/inch
(54)

Thickness of cork slab = 3.08 inch

heat flux through
the upper cork   = $\dfrac{k_{avg}}{\delta}$ ΔT   = $\dfrac{0.28 \times 8}{3.08}$
slab

$$= 0.736 \text{ Btu/hr ft}^2$$

3. Calculation of Heat Flux Through Lower Cork Slab

The cork slab density = 0.1144 gms./cc.

ΔT across the cork slab = 315 + 70 = 385°F

Thickness of cork slab = 1.05 inches

k_{avg} at density of 0.1144 gms./cc. and temperature
of -123°F = 0.193 Btu/hr ft^2°F/inch   (54)

heat flux through the lower
cork slab

$$= \frac{k_{avg}}{\delta} \Delta T$$

$$= 0.193 \times \frac{385}{1.05}$$

$$= \underline{70.7} \text{ Btu/hr ft}^2$$

4. Calculation of Heat Flux Through Calorimeter

Liquid nitrogen boil-off as measured by calibrated

rotameter $= 0.0053 \text{ ft}^3/\text{minute}$

heat flux $= \dfrac{0.0053 \times 2405 \times 0.07245}{0.0277 \times 28}$

$$= \underline{71.1} \text{ Btu/hr ft}^2$$

Table C-1

Calibration of Calorimeter

Run	Electrical Heat Output (Btu/hr ft^2)	Heat Flow Through Lower Cork (Btu/hr ft^2)	Heat Flow Through Upper Cork (Btu/hr ft^2)	Heat Measured By LN$_2$-Boil off (Btu/hr ft^2)	% Error (Heat by LN$_2$ Boil off + Heat Flow Through upper Cork-Electrical Heat)/Electrical Heat x100
1	70.2	70.7	0.736	71.1	+2.33%
2	280.8	-	2.19	279.0	+0.1385%
3	631.8	-	3.19	604.0	-3.90%
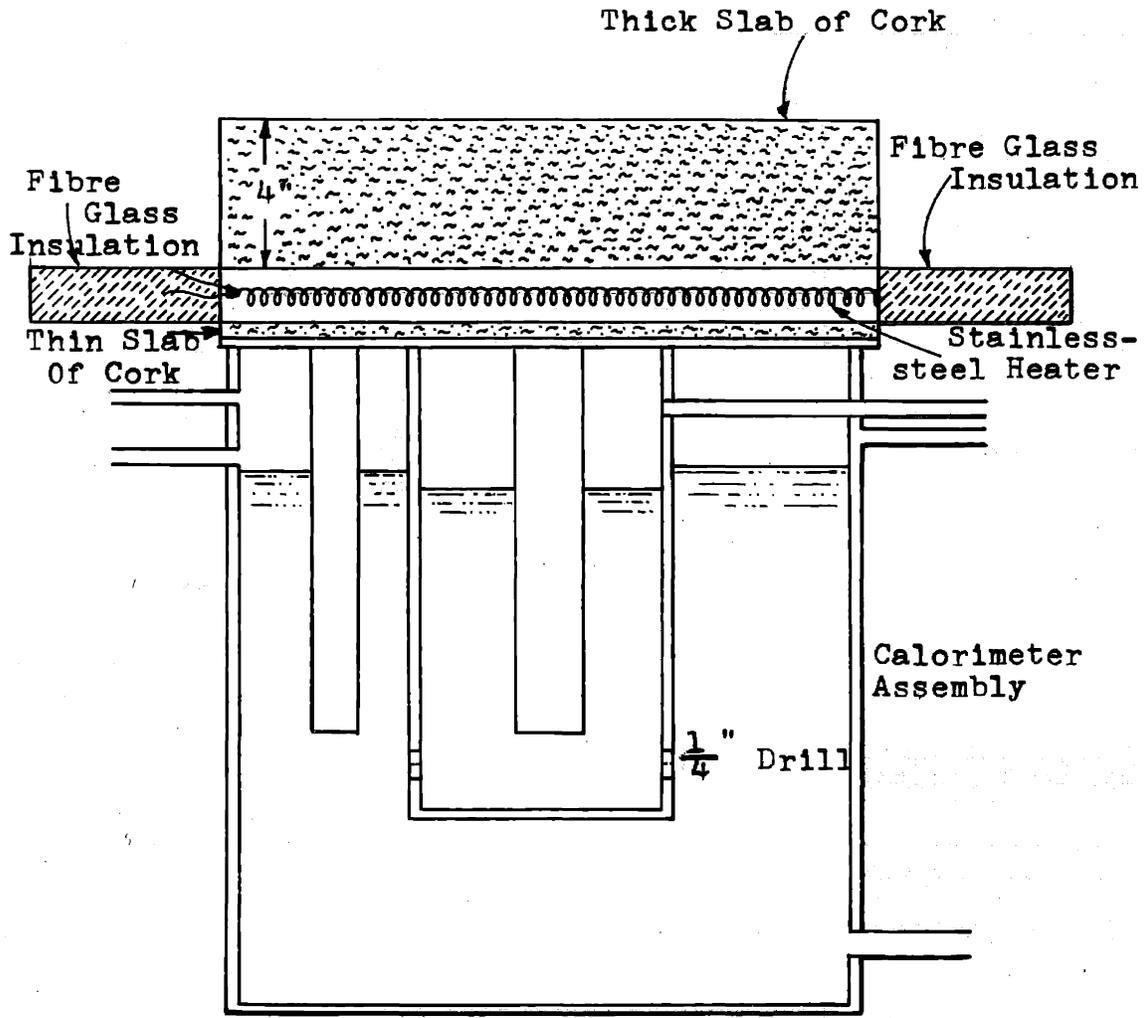
Figure C-1   Arrangement for Calibration of
Calorimeter

APPENDIX D

Computer Program For the "Simple Model" of the Frosting

Process

The three basic equations of the "simple model" which are solved on the computer can be summarized as follows.

Heat Balance

$$q = h (T_g - T_s) + K_g (p_g - p_s) \Delta H = k_{f,s} \left(\frac{dT}{dx}\right)_s = k_{f,x} \left(\frac{dT}{dx}\right)_x$$

$$= \left(\int_{T_w}^{T_s} k_f \, dT \right) / \delta \qquad (D-1)$$

Mass Balance

$$K_g (p_g - p_s) = \rho_f \frac{d\delta}{d\theta} + \delta \frac{d\rho_f}{d\theta} \qquad (D-2)$$

and Internal Diffusion Equation,

$$\frac{d\rho_f}{d\theta} = - \beta (T_s) \left(\frac{(1 - \rho_f/\rho_{ice})}{\tau \, \delta} \right) \left(\frac{dT}{dx} \right)_s \qquad (D-3)$$

where, $\beta (T_s) = D_B M_v \Delta H \, P_{vp} / R^2 T_s^3$

For simplicity in programming, $\beta (T_s) = f(T_s)$ and $k_f = f(T, \rho_f)$ were obtained in the form of empirical equations. The correlation among the frost thermal conductivity, density and temperature was obtained from the experimental data of Brazinsky (14). The following Equations D-4 and D-5 show these correlations.

For $\rho_f > 0.025$ gms./cc. and $T < 460°R$

$$k_f = 3.875 \times 10^{-6} \, T^{1.441} + 4.08 \times 10^{-9} x \, (\rho_f - 0.025) x \, T^{3.055} \quad (D-4)$$

For $\rho_f > 0.025$ gms./cc. and $T > 460°R$

$$k_f = 8.49 \times 10^{-17} x T^{5.44} + 6.86 \times 10^{-14} x \, (\rho_f - 0.025) x T^{4.84} \quad (D-5)$$

where, T is in $°R$, ρ_f is in gms/cc. and k_f is in Btu/hr ft $°F$

The following correlation for $\beta (T_s) = f(T_s)$ was obtained:

$$\beta(T_s) = 3.42 \exp(-4460.0/(T_s - 140.0)) \tag{D-6}$$

where, T_s is in $^\circ R$ and units of $\beta(T_s)$ are lbm/ft^3 hr

It should be noted that since there is no thermal conductivity correlation for the frost density below 0.025 gms./cc. included in the computer program, theoretical calculations for $\rho_f < 0.025$ gms./cc. can not be carried out with this program. However, the following correlation for the thermal conductivity of water frost can be used when $\rho_f < 0.025$ gms./cc.

For $\rho_f < 0.025$ gms./cc. , $T < 460^\circ R$

$$k_f = 6.58 \times 10^{-6} \times T^{1.272} + 8.17 \times 10^{-6} \times \rho_f \times T^{1.74} \tag{D-7}$$

where once again, T, ρ_f and k_f are in the same units as those used in Equations D-4 and D-5.

Method of Solution

At starting time, knowledge of δ and ρ_f is required. Starting with these initial values of δ and ρ_f, transcendental Equation D-1 was solved for T_s at starting time using Newton-Raphson method. Equations D-2 and D-3 were then used to calculate δ and ρ_f at new time. The following finite difference analogues of Equations D-2 and D-3 were used for this purpose in the listed sequence. The finite difference equations were solved by a simple Euler's method.

$$\frac{\rho_{f,N} - \rho_{f,0}}{\Delta\theta} = \frac{\left[(1 - \rho_{f,0}/0.917) \times \beta(T_{s,0}) \left(\frac{k_{avg}(\rho_{f,0}, T_{s,0})}{k_{fs}(\rho_{f,0}, T_{s,0})}\right)(T_{s,0} - T_w)\right]}{(62.4)(\tau)(\delta_0^2)} \tag{D-8}$$

and

$$\frac{\delta_N - \delta_0}{\Delta\theta} = \frac{\left[k_g(P_g - P_{s,0}(T_{s,0})) - \delta_0((\rho_{f,N} - \rho_{f,0})/\Delta\theta)\right]}{\left[(\rho_{f,N} + \rho_{f,0})/2.0\right]} \tag{D-9}$$

where, τ , tortuosity was assumed to be 1.10 (94)

The time variations of the average frost density, frost thickness and surface temperature were obtained by iterating the above described calculations.

Convergence Test for the Computer Results

In order to verify the convergence of the computer solution for the frost density, thickness and surface temperature, the final results were obtained for various time increments. These results are shown in Table D-1.

The computer results shown in Figures II-A1 to II-A12 and in Figures D-1 to D-3 were obtained with time increment of 1 minute. From the results shown in Table D-1, therefore, one can conclude that all the computer results of the "simple model" presented in this thesis are convergent.

Additional Computer Results of the "simple model"

Figures D-1 to D-3 show the predictions of the "simple model" regarding the effects of gas temperature on the frost density and thickness versus time profiles for the typical sets of experimental conditions. The results shown in Figures D-1 and D-2 indicate that at constant Reynolds number and humidity, the frost densifies at a faster rate and the thickness of the frost increases at a slower rate as gas temperature is increased. Thus, the thermal resistance of the deposited frost is higher at a higher gas temperature. Figure D-3 shows the effect of a step change in gas temperature on the average frost density and frost thickness. As expected, the model predicts that a step decrease in gas temperature

at constant Reynolds number and humidity would decrease

the rate of frost densification and increase the rate of

change of frost thickness. Thus, the conclusions regarding

the effects of gas temperature on the frost density and

thickness versus time profiles one can draw from the Figures

D-1 to D-3 are the same as those stated in Section II-A.

A listing of the computer program written in Fortran

4 language is included in this appendix.

Application of the "simple model" to the Carbon Dioxide

Frosting Process

In order to apply the "simple model" to the carbon

dioxide frosting process, another similar computer program

was written. The functional correlation $k_f = f(\rho_f, T)$ for this

program was obtained from Riemann's model for the frost

structure (see Appendix F), and hence the program can be

used only for the carbon dioxide frost density greater than

0.85 gms./cc. Since this $k_f = f(\rho_f, T)$ correlation needs

experimental verification, the computer program has not

been used to obtain theoretical predictions. However, once

an experimentally verified thermal conductivity correlation

is obtained, a similar computer solution can be used to

apply the "simple model" to carbon dioxide frosting process.

A listing of this program written in Fortran 2 language

is included in this appendix.

Table D-1

Convergence Tests for the Computer Solution of

Mathematical Equations of the "Simple Model"

A. Experimental Conditions

Re= 5,600; Humidity= dew point at 29.2°F; T_g=70°F

θ (mins.)	$\Delta\theta$ (min.)	ρ_f ($\frac{gms.}{cc.}$)	δ (inches)	T_s(°F)
76	1/8	0.0582136	0.190055	13.7810
76	1/4	0.0582125	0.190052	13.7815
76	1/2	0.0582127	0.190046	13.7791
76	1	0.0582152	0.190033	13.7769
77	1/4	0.0589166	0.190192	13.5691
77	1/2	0.0589170	0.190182	13.5657
77	1	0.0589220	0.190156	13.5598

B. Experimental Conditions

Re=14,500; Humidity= dew point at 40°F; T_g= 75°F

θ (mins.)	$\Delta\theta$ (mins.)	ρ_f ($\frac{gms.}{cc.}$)	δ (inches)	T_s(°F)
15	1	0.0700815	0.0877733	-1.30444
15	5	0.0688806	0.0903255	0.709229
25	1	0.0855971	0.1141870	5.834230
25	5	0.0857849	0.1158120	6.441650
35	1	0.0976174	0.1348040	9.562260
35	5	0.0982676	0.1362070	9.826660
45	1	0.1074510	0.1523850	12.07890
45	5	0.1083240	0.1537150	12.21140

Table D-1 (contd.)

θ (mins.)	$\Delta\theta$ (mins.)	ρ_f ($\frac{gms.}{cc.}$)	δ (inches)	T_s ($^\circ$F)
55	1	0.115824	0.167948	13.9622
55	5	0.116818	0.169263	14.0337
65	1	0.123149	0.182035	15.4556
65	5	0.124212	0.183357	15.4961
75	1	0.129679	0.194975	16.6855
75	5	0.130782	0.196313	16.7097
85	1	0.135586	0.206989	17.7258
85	5	0.136712	0.208346	17.7407
95	1	0.140988	0.218232	18.6235
95	5	0.142125	0.219611	18.6333
105	1	0.145973	0.228821	19.4099
105	5	0.147114	0.230220	19.4170

Experimental Conditions

①= Re=14,500; Humidity=Gas dew point at 40°F;
    T_g = 70°F

②= Re=9,300; Humidity=Gas dew point at 29.2°F;
    T_g = 70°F

③= Re=5,600; Humidity=Gas dew point at 29.2°F;
    T_g= 70°F

④= Re=14,500; Humidity=Gas dew point at 40°F;
    T_g = 30°F

⑤= Re=9,300; Humidity=Gas dew point at 29.2°F;
    T_g = 30°F

⑥= Re=5,600; Humidity=Gas dew point at 29.2°F;
    T_g= 30°F
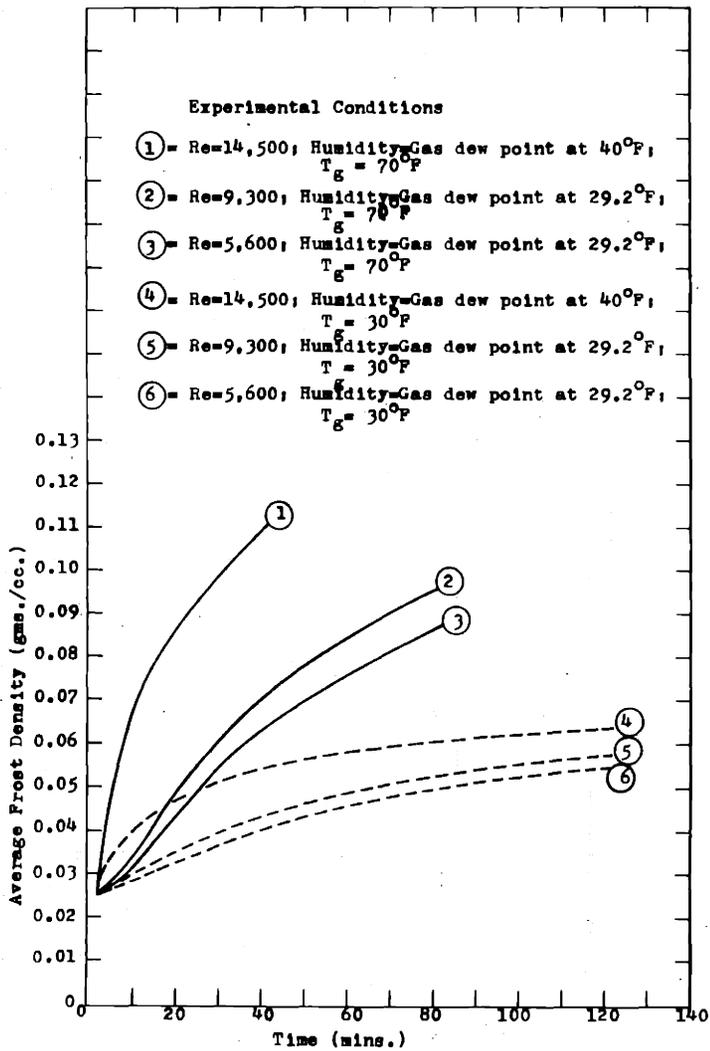
Figure D-1   'Simple Model' Predictions Regarding Effect
of Gas Temperature on Average Frost
Density

Experimental Conditions

①=Re=14,500; Humidity= Gas dew point at 40°F;
    T_g = 30°F

②= Re=9,300; Humidity= Gas dew point at 29.2°F;
    T_g = 30°F

③= Re=5,600; Humidity= Gas dew point at 29.2°F;
    T_g= 30°F

④= Re=14,500; Humidity= Gas dew point at 40°F;
    T_g = 70°F

⑤= Re=9,300; Humidity= Gas dew point at 29.2°F;
    T_g = 70°F

⑥= Re=5,600; Humidity= Gas dew point at 29.2°F;
    T_g= 70°F
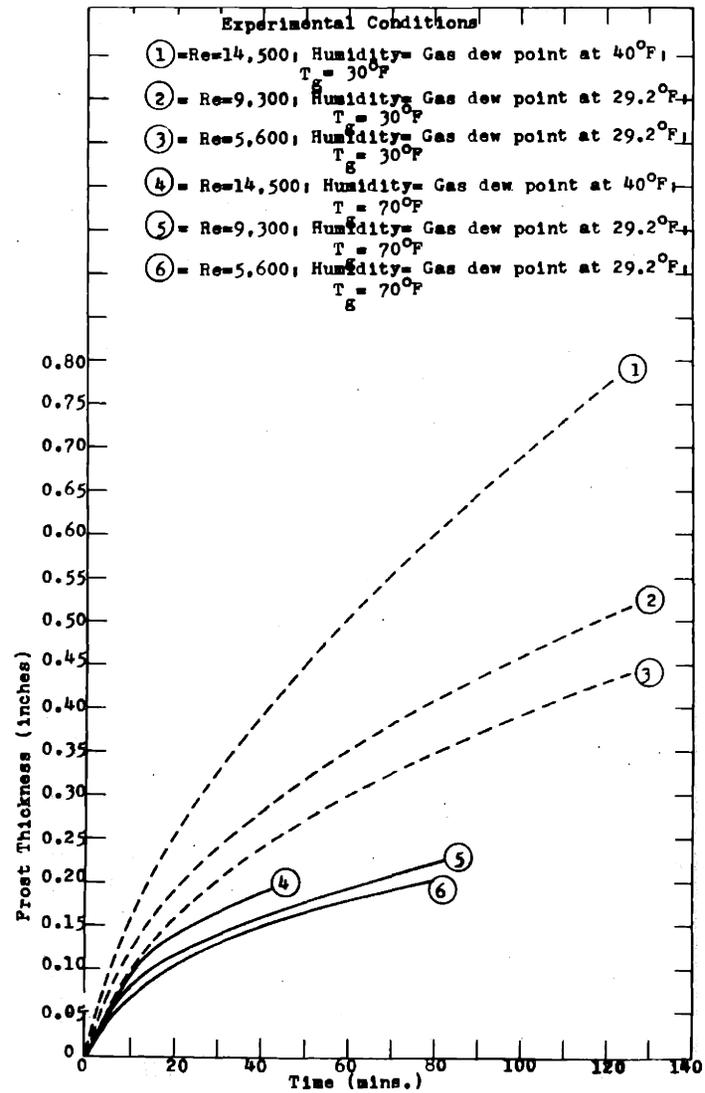
Figure D-2   'Simple Model' Predictions Regarding Effect
of Gas Temperature on Frost Thickness
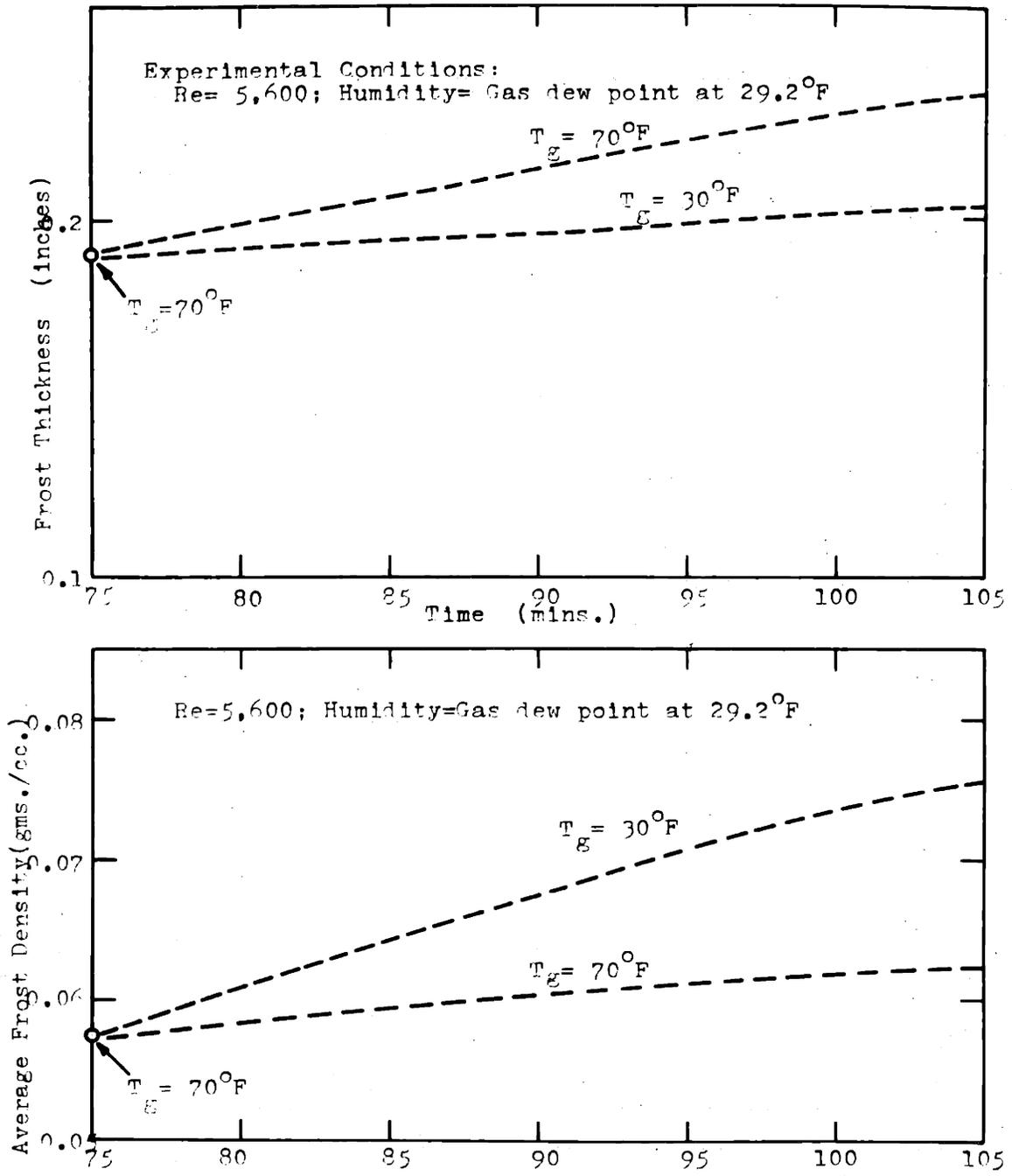
Figure D-3 Predictions of Simple Model for the Effects of
Gas Temperature on Average Frost Density and
Frost Thickness

Computer Program for 'Simple Model'

(Water Frosting Process)

```
      DIMENSION FLUX(400),FLUXP(400)
50    READ (5,100) H,RHOFI,TG,P,FLUX1,F1
100   FORMAT (6F10.5)
      READ (5,101) TW,DELX,DELI,TZI,N
101   FORMAT (4F10.5,I3)
      RHOFO=RHOFI
      DELO=DELI
       TS=460.00
      IJ=0
      TZ=TZI
       DO 10 I=1,N
      IF(I-1) 487,483,487
483   FLUX(I)=FLUX1
487   IF(TZ-460.0) 482,482,28
28       DO 493 J=1,25
      TZ=TZ/1.80
      P1=8.2312*0.4343*ALOG(TZ)
      PVP=EXP(((-2445.5646/TZ)&P1-(0.01677006*TZ)&(1.20514*(10.**(-5.0)
     1)*TZ*TZ)-6.757169)/(0.4343))
       TZ=TZ*1.80
      IF(I-1) 511,510,511
511   FLUX(I)=F*(P-PVP)
510   PP=(((2445.5646*1.80)/(TZ*TZ))&(0.4343*8.2312)/TZ-(0.01677006/
     11.80)&(2.41028*(10.**(-5.0)*TZ))/(3.240))/(0.4343)
      PVPP=PVP*PP
      IF(I-1) 33,34,33
34    F=F1
33    FLUXP(I)=-(F*PVPP)
      CI=                  (H*DELO*TG)&(1.319*(10.**(-17.0))
     1*(TS**(6.44)))&(1.175*(RHOFO-0.025)*(10.**(-14.0))*(TS**(5.84)))
     2&(1.587*(10.**(-6.0))*(TW**(2.441)))&(1.005*(10.**(-9.0))*
     3(RHOFO-0.025)*(TW**(4.055)))
       FTZ=(1.319*(10.**(-17.0))*(TZ**(6.44)))&(1.175*(RHOFO-0.025)*
     1(10.0**(-14.0))*(TZ**(5.84)))&(H*DELO*TZ)-CI-((FLUX(I)*DELO)*
     1(422.5*(TZ**(0.1712))))&((1.587*(10.**(-6.0))*(TS**(2.441)))
     2&(1.005*(10.**(-9.0))*(RHOFO-0.025)*(TS**(4.055))))
       FPTZ=(6.440*1.319*(10.**(-17.0))*(TZ**(5.44)))&(5.840*(RHOFO-0.025
     1)*(1.175*(10.0**(-14.0)))*(TZ**(4.84)))&(H*DELO) -(FLUX(I)*DELO*
     2422.50*0.1712*(TZ**(-0.8288))) -(DELO)*(422.50*(TZ**(0.1712)))
     3*FLUXP(I))
       TZ=TZ-(FTZ/FPTZ)
      CAVG1=((1.319*(10.**(-17.0))*((TZ**(6.44))-(TS**(6.44))))&(
     11.175*(10.**(-14.0))*(RHOFO-0.025)*((TZ**(5.84))-(TS**(5.84)))))
      CAVG2=((1.587*(10.**(-6.0))*((TS**(2.441))-(TW**(2.441))))&(1.005
     1*(10.**(-9.0))*(RHOFO-0.025)*((TS**(4.055))-(TW**(4.055)))))
       CAVG=(CAVG1&CAVG2)/(TZ-TW)
       FUT=(CAVG*(TZ-TW))/DELO
       FUPT=(H*(TG-TZ))&(FLUX(I)*(422.5)*(TZ**(0.1712)))
       EP=(FUT/FUPT)-1.0


          IF(ABS(EP)-(10.**(-4.0))) 491,28,28
  493 CONTINUE
      GO TO 491
  482    DO 490 K=1,25
      TZ=TZ/1.80
      P1=8.2312*0.4343*ALOG(TZ)
      PVP=EXP(((-2445.5646/TZ)&P1-(0.01677006*TZ)&(1.20514*(10.**(-5.0)
     1)*TZ*TZ)-6.757169)/(0.4343))
      TZ=TZ*1.80
      IF(I-1) 16,502,16
  16     FLUX(I)=F*(P-PVP)
```

```
502    PP=((((2445.5646*1.80)/(TZ*TZ))&(0.4343*8.2312)/TZ-(0.01677006/
      11.80)&(2.41028*(10.**(-5.0)*TZ))/(3.240))/(0.4343)
       PVPP=PVP*PP
       IF(I-1) 19,17,19
17     F=F1
19     FLUXP(I)=-(F*PVPP)
       CJ=                        (H*DELO*TG)&(1.587*(10.**(-6.0))*
      1(TW**(2.441)))&(1.005*(10.**(-9.0))*(RHOFO-0.025)*(TW**(4.055)))
       FTZ=(1.587*(10.**(-6.0))*(TZ**(2.441)))&(1.005*(10.**(-9.0))
      1*(RHOFO-0.025)*(TZ**(4.055)))&(H*DELO*TZ)-CJ-(FLUX(I)*DELO*422.5*
      2(TZ**(0.1712)))
       FPTZ=(3.875*(10.**(-6.0))*(TZ**(1.441)))&(4.08*(10.**(-9.0))
      1*(RHOFO-0.025)*(TZ**(3.055)))&(H*DELO)-(FLUX(I)*DELO*422.5
      1*0.1712*(TZ**(-0.8288)))-(DELO*(422.5*(TZ**(0.1712))))*FLUXP(I))
       TZ=TZ-(FTZ/FPTZ)
       CAVG=(((1.587*(10.**(-6.0))*((TZ**(2.441))-(TW**(2.441))))&(1.005
      1*(10.**(-9.0))*(RHOFO-0.025)*((TZ**(4.055))-(TW**(4.055)))))/
      2(TZ-TW)
       FUT=(CAVG*(TZ-TW))/DELO
       FUPT=(H*(TG-TZ))&(FLUX(I)*(422.5*(TZ**(0.1712)))
       FP=(FUT/FUPT)-1.0
       IF(ABS(FP)-(10.**(-4.0))) 481,482,482
490    CONTINUE
       GO TO 481
491    WRITE(6,108) FP,J
108    FORMAT (E16.6,I2)
       CAS=(8.490*(10.**(-17.0))*(T/**(5.44)))&(6.860*(10.**(-14.0))
      1*(TZ**(4.84))*(RHOFO-0.025))
       CAVG1=((1.319*(10.**(-17.0))*((TZ**(5.44))-(TS**(4.44))))&(
      11.175*(10.**(-14.0))*(RHOFO-0.025)*((TZ**(5.84))-(TS**(5.84)))))
       CAVG2=((1.587*(10.**(-6.0))*((TS**(2.441))-(TW**(2.441))))&(1.005
      1*(10.**(-9.0))*(RHOFO-0.025)*((TS**(4.055))-(TW**(4.055)))))
       CAVG=(CAVG1&CAVG2)/(T7-TW)
       DELC=(CAVG/CAS)*(T7-TW)
        GO TO 492
481    IF(TZ-460.0) 11,11,487
11     WRITE(6,107) FP,K
107    FORMAT (E16.6,I2)
       CAS =(3.875*(10.**(-6.0))*(TZ**(1.441)))&(4.08*(10.**(-9.0))*


      1(RHOFO-0.025)*(TZ**(3.055)))
       CAVG=(((1.587*(10.**(-6.0))*((TZ**(2.441))-(TW**(2.441))))&(1.005
      1*(10.**(-9.0))*(RHOFO-0.025)*((TZ**(4.055))-(TW**(4.055)))))/
      2(T7-TW)
       DELC=(CAVG/CAS)*(TZ-TW)
492    BETA=3.42*EXP(-4460.0/(T7-140.0))
       DELH=422.5*(TZ**(0.1712))
        DEL2=DELO*DELO
        FP=FLUX(I)
       HEAT=(H*(TG-TZ))&(FLUX(I)*(422.5)*(TZ**(0.1712)))
       AST=RHOFO*DELO*62.40
       DELO=DELO*12.00
       TZ=TZ-459.67
       WRITE (6,102) RHOFO,DELO,TZ,FP,HEAT,AST
102    FORMAT (6E16.6)
       DELO=DELO/12.00
       RHOFT=((1.0-(RHOFO/0.917))*(BETA)*DELC)/(62.40*1.10*DEL2)
       TZ=T7&459.67
       IF(I-1) 531,521,521
521    F=F1
531     RHOFN=RHOFO&DELX*RHOFT
       RHOFT=RHOFT*62.40
       RHO=((RHOFO&RHOFN)/2.0)*62.40
       DELN=DELO&(DELX*(FLUX(I)-(DELO*RHOFT)))/(RHO)
       RHOFO=RHOFN
10     DELO=DELN
       WRITE (6,104) H,F
104    FORMAT (2E16.6)
       GO TO 50
       END
```

Computer Program for 'Simple Model'

(Carbon Dioxide Frosting Process)

```
      DIMENSION FLUX(400),FLUXP(400)
      L=1
      GO TO (5,2),L
5     READ (2,100) H,RHOFI,TG,P,F1,RG
100   FORMAT (6F10.5)
      READ (2,101) TW,DELY,DELI,TZI,N
101   FORMAT (4F10.5,I3)
      RHOFO=RHOFI
      DELO=DELI
      TZ=TZI
          DO 10 I=1,N
       DO 493 J=1,25
      TZ=TZ/1.80
      IF (TZ-138.0) 41,41,42
41     PVP=EXP(((-1275.620/TZ)+(0.006833*TZ)+8.3071)/(0.4343))
      TZ=TZ*1.80
       PP=(((1275.620*1.80)/(TZ*TZ)+(0.006833/1.80))/(0.4343)
      GO TO 815
42    PVP=EXP(((-1367.3448/TZ)+9.9082)/(0.4343))
      TZ=TZ*1.80
      PP=(((1367.3448*1.80)/(TZ*TZ))/(0.4343))
815   PVPP=PVP*PP
      FLUX(I)=F1*(P-PVP)
      FLUXP(I)=-(F1*PVPP)
      IF (RHOFO-1.0) 11,11,12
11    CI=(H*DELO*TG)+(3.558*(TZ**(-0.584)))*(RHOFO**(23.920*(TZ**(
     1-0.239))))*TW
       FIZ=(3.558*(TZ**(-0.584))*(RHOFO**(23.920*(TZ**(-0.239))))*TZ)
     1+(H*DELO*TZ)-CI-((FLUX(I)*DELO)*(583.50*(TZ**(-0.1469))))
      FPTZ=((3.558*(TZ**(-0.584))*(RHOFO**(23.920*(TZ**(-0.239)))))*
     1(23.920*(-0.239)*(TZ**(-1.239)))*
     1ALOG(RHOFO))-(3.558*(0.584)*(TZ**(-1.584))*(RHOFO**(23.920*(
     1TZ**(-0.239))))))*(TZ-TW)+(3.558*(TZ**(-0.584))*(RHOFO**(23.920
     1*(TZ**(-0.239))))+(H*DELO)-(FLUX(I)*DELO*583.50*(-0.1469)*
     1(TZ**(-1.1469)))-(DELO*(583.50*(TZ**(-0.1469))))*FLUXP(I))
       GO TO 13
12    CJ=(H*DELO*TG)+(3.558*(TZ**(-0.584)))*(RHOFO**(2.220*(TZ**
     1(-0.03445))))*TW)
       FTZ=(3.558*(TZ**(-0.584))*(RHOFO**(2.22*(TZ**(-0.03445)))))*TZ)
     1+(H*DELO*TZ)-CJ-((FLUX(I)*DELO)*(583.50*(TZ**(-0.1469))))
      FPTZ=((3.558*(TZ**(-0.584))*(RHOFO**(2.220*(TZ**(-0.03445)))))
     1*(2.220*(-0.03445)*(TZ**(-1.03445)))
     1*ALOG(RHOFO))+(3.558*(-0.584)*(TZ**(-1.584))*(RHOFO**(2.220
     1*(TZ**(-0.03445))))))*(TZ-TW)+(3.558*(TZ**(-0.584))*(RHOFO**(2.220
     1*(TZ**(-0.03445)))))+(H*DELO)-(FLUX(I)*DELO*583.50*(-0.1469)*
     1(TZ**(-1.1469)))-(DELO*(583.50*(TZ**(-0.1469))))*FLUXP(I))
   13     TZ=TZ-(FTZ/FPTZ)
      TZ=TZ/1.80
      IF (TZ-138.0) 81,81,82
81    PVP=EXP(((-1275.620/TZ)+(0.006833*TZ)+8.3071)/(0.4343))
      GO TO 816
82    PVP=EXP(((-1367.3448/TZ)+9.9082)/(0.4343))
816   TZ=TZ*1.80
      FLUX(I)=F1*(P-PVP)
       IF(RHOFO-1.0) 61,61,62
61    CAVG=(3.558*(TZ**(-0.584))*(RHOFO**(23.92*(TZ**(-0.239)))))
      FOT=(CAVG*(TZ-TW))/DELO
```

```
       FUPT=(H*(TG-TZ))+(FLUX(I)*(583.50)*(TZ**(-0.1469)))
       EP=(FUT/FUPT)-1.0
       GO TO 14
  62   CAVG=(3.558*(TZ**(-0.584))*(RHOFO**(2.220*(TZ**(-0.0345))))))
       FUT=(CAVG*(TZ-TW))/DELO
       FUPT=(H*(TG-TZ))+(FLUX(I)*(583.50)*(TZ**(-0.1469)))


       EP=(FUT/FUPT)-1.0
  14   IF (ABS(EP)-(10.**(-4.0))) 481,481,493
  493     CONTINUE
  481   WRITE (3,192) EP,J
  192   FORMAT (E15.6,I3)
         IF(RHOFO-1.0) 54,64,65
  64   IF (TZ-265.0) 66,66,67
  66   CAS=(41.50*(TZ**(-1.081))*(RHOFO**(93.50*(TZ**(-0.5075)))))
       GO TO 818
  67   CAS=(0.100*(RHOFO**(8.060*(TZ**(-3.380))*(10.**(8.0)))))
       GO TO 818
  65   IF (TZ-265.0) 68,68,69
  68   CAS=(41.50*(TZ**(-1.081))*(RHOFO**(2.36+(TZ**(-0.0882)))))
       GO TO 818
  69   CAS=(0.100*(RHOFO**(1.173*(TZ**(-1.5730))*(10.**(4.0)))))
  818  DELC=(CAVG*(TZ-TW))/CAS
        TZ=TZ/1.80
       DIF=(2.380*(10.**(-6.0))*(TZ**2.00877))
       TZ=TZ*1.80
       DEL2=DELO*DELO
       RHOFT=((1.0-(RHOFO/1.60))*DELC*DIF*PVPP)/(1.10*62.40*DEL2*RG*TZ)
       DELO=DELO*12.00
       TZ=TZ-459.67
       WRITE (3,108) RHOFO,DELO,TZ
  108    FORMAT (3E16.6)
       TZ=TZ+459.67
       DELO=DELO/12.00
       RHOFN=RHOFO+DELX*RHOFT
        RHOFT=RHOFT*62.40
       RHO=((RHOFO+RHOFN)/2.0)*62.40
       DELN=DELO+(DELX*(FLUX(I)-(DELO*RHOFT)))/(RHO)
        RHOFO=RHOFN
  10   DELO=DELN
       GO TO 5
  2     CALL EXIT
        END
```

APPENDIX E

Computer Solution of the Mathematical Equations of the 'Sophisticated Model'

The basic equations of the 'sophisticated model' in the dimensionless form can be summarized as follows.

Heat Balance

$$q = \frac{k_f}{\delta} \frac{\partial T}{\partial z} \tag{E-1}$$

Mass Balance

$$\left(\frac{\partial \rho_f}{\partial \theta}\right)_z - z \frac{\dot{\delta}}{\delta}\left(\frac{\partial \rho_f}{\partial z}\right)_\theta = \frac{1}{\delta}\frac{\partial}{\partial z}\left[\frac{(1-\rho_f/\rho_{ice})D_B}{RT\tau(1-P_{vp}/P)}\left(\frac{M\cdot\Delta H\cdot P_{vp}}{RT^2}\right)\frac{1}{\delta}\left(\frac{\partial T}{\partial z}\right)\right] \tag{E-2}$$

Boundary Conditions

1. At Cold Wall

A. Heat Boundary Condition

$$T\Big|_{z=0} = T_w \quad \text{at all time} \tag{E-3}$$

B. Mass Boundary Condition

$$J_s\Big|_{z=0} = \frac{D_B(1.-\rho_f/\rho_{ice})}{RT\tau(1-P_{vp}/P)}\left(\frac{M\,\Delta H\,P_{vp}}{RT^2}\right)\frac{1}{\delta}\frac{\partial T}{\partial z}\Big|_{z=0} = 0 \tag{E-4}$$

2. At Frost Surface

A. Heat Boundary Condition

$$q\Big|_{z=1} = h(T_g - T_{z=1}) + K_g(p_g - p_{z=1})\Delta H = \frac{k_f}{\delta}\frac{\partial T}{\partial z}\Big|_{z=1} \tag{E-5}$$

B. Mass Boundary Condition

$$J_s\Big|_{z=1} = K_g(p_g - p\big|_{z=1}) = \rho_{f,s}\frac{d\delta}{d\theta} + \frac{D_B(1-\rho_f/\rho_{ice})}{RT\tau(1-P_{vp}/P)}\left(\frac{M\,\Delta H\,P_{vp}}{RT^2}\right)\frac{1}{\delta}\frac{\partial T}{\partial z}\Big|_{z=1} \tag{E-6}$$

Finite difference analogues of Equations E-2, E-4 and E-6 used in the computer solution can be written as,

$$D_B = 2.67953 \times 10^{-6} \times T^{2.00877} \qquad (E-7)$$

where,

D_B is in $cm^2/sec.$ and T is in $^{\circ}K.$

The brief description of the numerical method used in this program to obtain $T(z)$, ρ_f (z,θ) and $\delta(\theta)$ profiles is shown below.

At starting time, ρ_f (z,θ) and $\delta(\theta)$ values were assumed. In all the cases studied in the present thesis, initial values of ρ_f (z,θ) were assumed to be constant across the frost layer. Equations E-1, E-3 and E-5 were then used to solve the temperature distribution in the frost interior at the starting time. The fourth order Runga-Kutta method was used for this purpose. A thorough description of the fourth order Runga-Kutta method is given by Mickley et al. (74).

Knowing $T(z)$, $\rho_f(z,\theta)$ and $\delta(\theta)$ at the starting time, Equations E-2, E-4 and E-6 were then used to obtain $\rho_f(z,\theta)$ and $\delta(\theta)$ at new time. The schematic of a six point finite difference scheme used to solve these equations is shown in Figure E-0. As shown in the figure, in the finite difference scheme, two levels in time and three levels in distance (z-direction) were used. The weighing coefficients were given equal values (a=b=c=d=1/2).
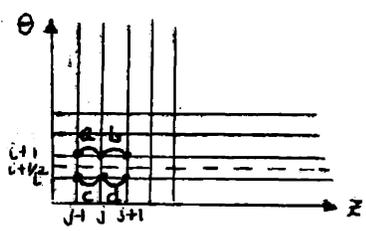
Figure E-0: Schematic of Six Points Finite Difference Method

$$\frac{\rho_f\big|_{i+1,j} - \rho_f\big|_{i,j}}{\Delta\theta} = Z \frac{\dot{\delta}_{i+\frac{1}{2},j}}{\delta_{i+\frac{1}{2},j}} \left[\frac{\rho_f\big|_{i+\frac{1}{2},j+1} - \rho_f\big|_{i+\frac{1}{2},j}}{\Delta z}\right] + \frac{1}{\delta_{i+\frac{1}{2},j}} \frac{1}{\Delta z}$$

$$\left[\left(\frac{\left(\frac{(1-\rho_f/\rho_{ice})\mathcal{D}_B}{\tau RT(1-P_{vf}/P)}\right)\left(\frac{M\cdot\Delta H\cdot P_{vp}}{RT^2}\right)\frac{q}{\delta R_f}}{2\Delta z}\right)_{i+\frac{1}{2},j+1} - \left(\frac{\left(\frac{(1-\rho_f/\rho_{ice})\mathcal{D}_B}{\tau RT(1-P_{vf}/P)}\right)\left(\frac{M\cdot\Delta H\cdot P_{vp}}{RT^2}\right)\frac{q}{\delta R_f}}{2\cdot\Delta z}\right)_{i+\frac{1}{2},j-1}\right] \quad (E-7)$$

The boundary condition at the cold wall will be,

COLD WALL
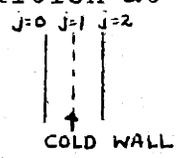
$$\frac{\rho_f\big|_{i+1,j} - \rho_f\big|_{i,1}}{\Delta\theta} = 0 + \frac{1}{\delta_{i+\frac{1}{2},j}} \times \frac{1}{\Delta z}\left[\frac{\left(\frac{(1-\rho_f/\rho_{ice})\mathcal{D}_B}{\tau RT(1-P_{vf}/P)}\right)\left(\frac{M\cdot\Delta H\cdot P_{vp}}{RT^2}\right)\frac{q}{\delta R_f}\Big|_{i+\frac{1}{2},j} - 0}{2\Delta z}\right] \quad (E-8)$$

and the boundary condition at the frost surface will be,

MASS FLUX $= K_g\left(P_g - P\big|_{i+\frac{1}{2},j}\right)$
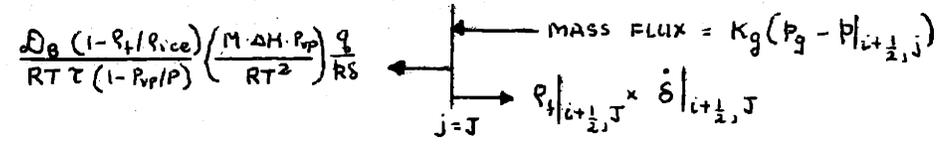
$$K_g\left(P_g - P_{i+\frac{1}{2},J}\right) = \rho_f\big|_{i+\frac{1}{2},J}\cdot\dot{\delta}\big|_{i+\frac{1}{2},J} + \left[\frac{\mathcal{D}_B(1-\rho_f/\rho_{ice})}{RT\tau(1-P_{vf}/P)}\left(\frac{M\cdot\Delta H\cdot P_{vp}}{RT^2}\right)\frac{q}{R_f\delta}\right]_{i+\frac{1}{2},J} \quad (E-9)$$

Method of Solution

Above described equations were solved by finite diffrence techniques on computer. A listing of the computer program written for this purpose is shown at the end of this appendix. This program is written in Fortran 4 language.

For simplicity in programming, the empirical correlation among the frost thermal conductivity, density and temperature, described in the Appendix D was used in this program. Similarly, an empirical correlation between molecular diffusivity and the temperature was used in the program. This correlation is shown in Equation E-7 and described in Figure II-B10.

Thus, the method of solution of mathematical equations essentially involve the iterative procedure for the solution of the Equations E-1,E-3 and E-5 by Runga-Kutta method and the solution of the finite difference Equations E-7 to E-9.

Stability and Convergence Tests for the Finite Difference Solution:

The stability and convergence of the computer results were examined by varying Δz and $\Delta \theta$ values respectively. Figures E-1 to E-4 show the effects of variation in Δz and $\Delta \theta$ values on the frost density at various points in the frost interior. The results of the figures indicate that the finite difference method used in the computer solution gave stable and convergent results.

Additional Results of the ' Sophisticated Model'

Figure E-5 shows the additional results for the time variation of the density distribution within the frost and the frost thickness for a set of system conditions (Re=5,600, humidity= dew point at $29.2^{\circ}F$ and $T_g = 70^{\circ}F$). These system conditions were studied experimentally by Brazinsky (14). The initial values for the theoretical calculations were taken as uniform frost density (with depth) of 0.0575 gms./ cc. and the frost thickness of 0.189 inches. Brazinsky(14) showed experimentally that these values of frost density and thickness are obtained in the quasi-steady state of heat transfer. The results of Figure E-5 convey the same meaning as those obtained from the results of Figures II-B1 and II-B3.

Modification of the ' Sophisticated Model'

As an additional thought to the mathematical formulation

of the frosting process, a slight modification of the

'sophisticated model' was examined. The mathematical

equations of this modified 'sophisticated model' were based on

The postulation that the driving force for the frost

densification is $\frac{\partial}{\partial x}\left[\frac{D_B(1-\rho_f/\rho_{ice})}{\tau(1-P_{vp}/P)}\frac{\partial}{\partial x}(\frac{P_{vp}}{RT})\right]$ instead of

$$\frac{\partial}{\partial x}\left[\frac{D_B(1-\rho_f/\rho_{ice})}{RT\tau(1-P_{vp}/P)}\frac{\partial P_{vp}}{\partial x}\right]$$ as taken in the 'sophisticated

model'. All other features of the modified 'sophisticated

model' were identical to those of 'sophisticated model'.

The computer solution of the mathematical equations of

the modified 'sophisticated model' by the same numerical

technique as described before was found to be stable and

convergent.

Figure E-6 shows the comparison between the predictions

of the 'sophisticated' and the 'modified sophisticated'

models for the time variation of the density distribution

in the frost interior and the frost thickness. It can

be seen that both the models predict almost identical

results for a set of experimental system conditions. The

modified 'sophisticated' model, however, predict a slightly

lower densification rate and a slightly higher rate of

change of thickness than those predicted by the 'sophisticated'

model.

The results of Figure E-6 also indicates that the

simple model will also predict a little lower rate of the

frost densification and a little higher rate of change

of frost thickness, if the driving force for the

densification rate is taken as $\frac{\partial}{\partial x}\left(\frac{P_{vp}}{RT}\right)$ instead of $\frac{1}{RT}\frac{\partial P_{vp}}{\partial x}$

at the frost surface. This can be seen mathematically

by realizing that the driving force for the former case

is $\left(\frac{1}{RT}\frac{\partial P_{vp}}{\partial x} - \frac{P_{vp}}{RT^2}\frac{\partial T}{\partial x}\right)$, which is smaller than the driving

force for the latter case by the quantity $\frac{P_{vp}}{RT^2}\frac{\partial T}{\partial x}$.

Since this difference is quite small at the frost surface,

the modification of the simple model was not examined.

It should be noted, however, that the results of Figures

II-A1 to II-A12 indicate that the above-mentioned

modification of the simple model will give the results

in better agreement with the experimental facts.
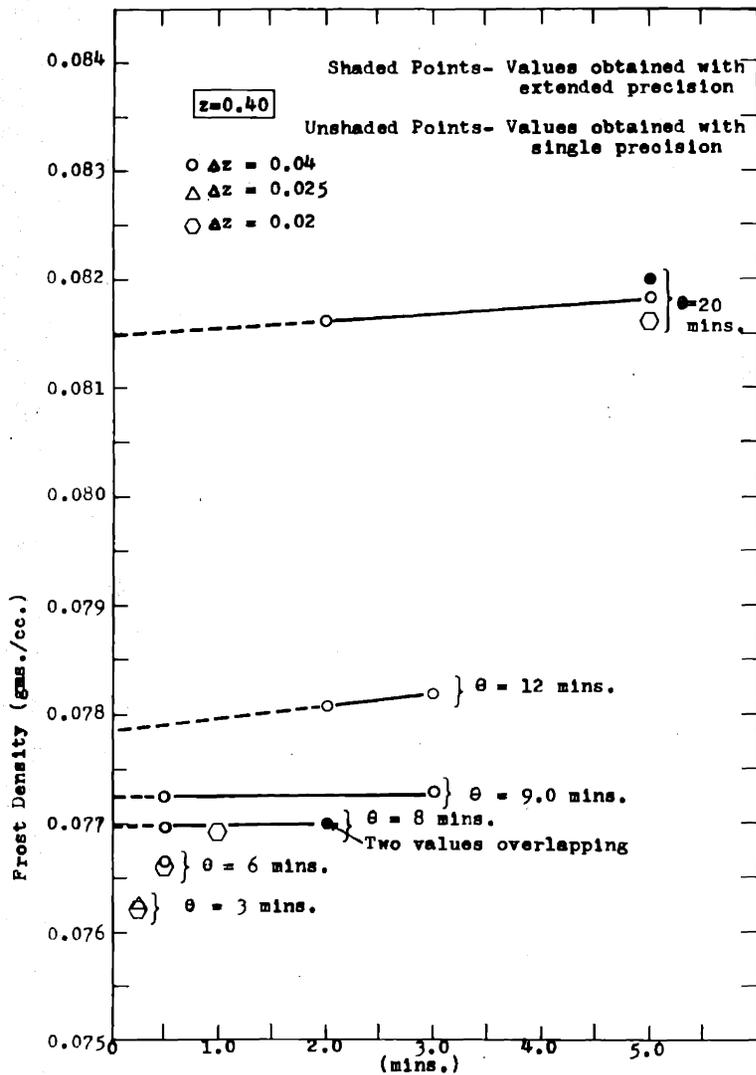
Figure E-1   Stability and Convergence Test for Finite
Difference Technique Used for Solution of
Equations of 'Sophisticated Model'
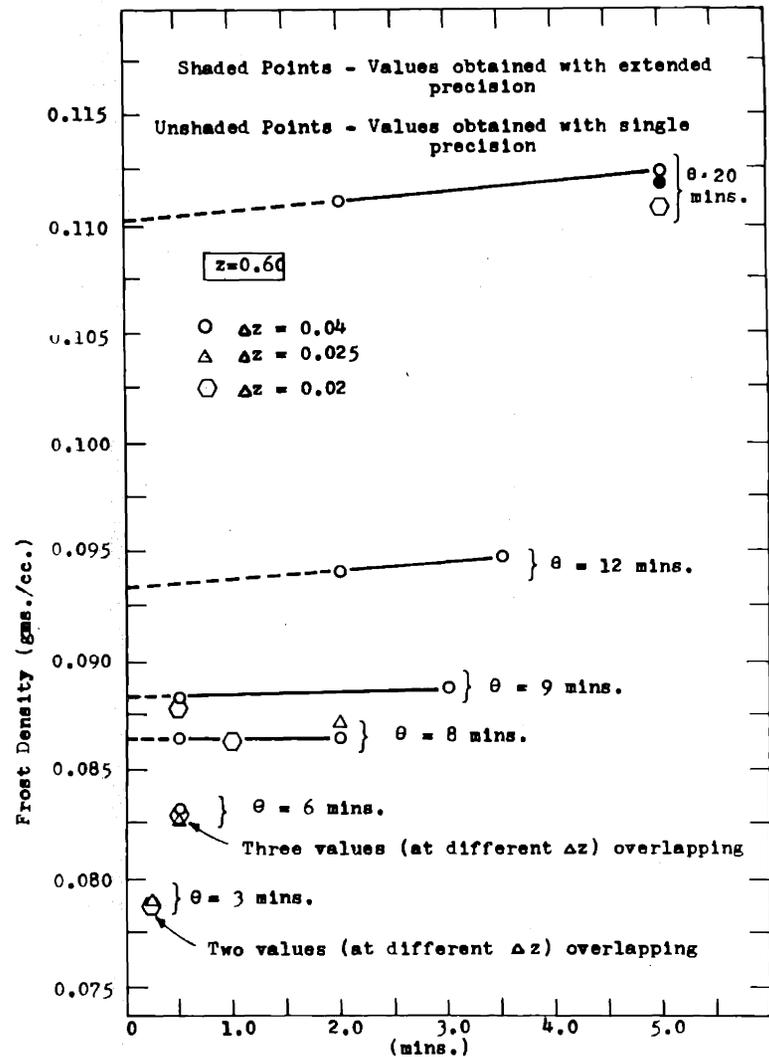
Figure E-2   Stability and Convergence Tests for Finite
Difference Technique used for Solution of
Equations of 'Sophisticated Model'
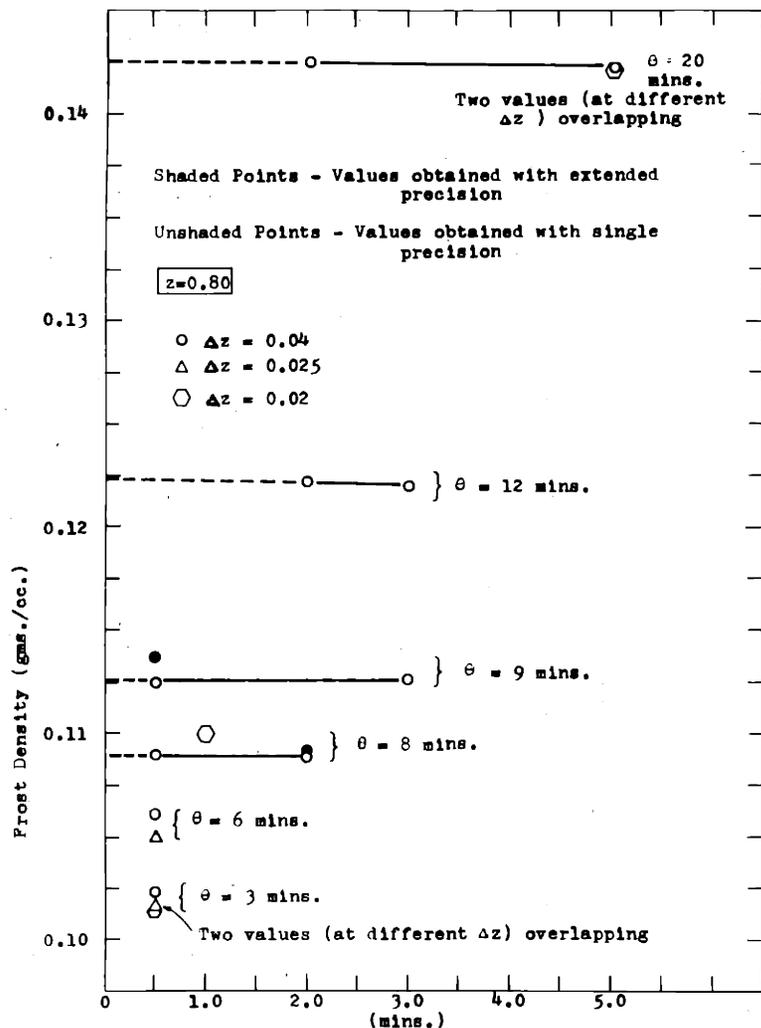
Figure E-3 Stability and Convergence Tests for Finite
Difference Technique Used for Solution of
Equations of 'Sophisticated Model'
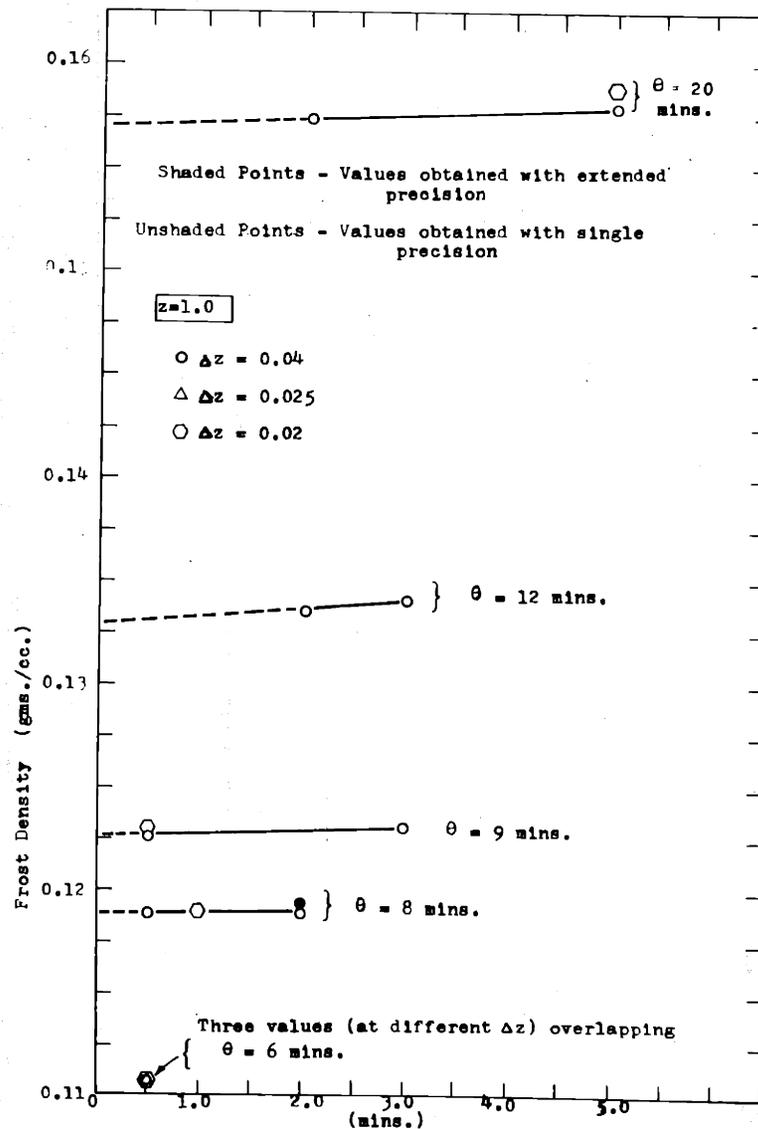
Figure E-4 Stability and Convergence Tests for Finite
Difference Solution of 'Sophisticated Model'
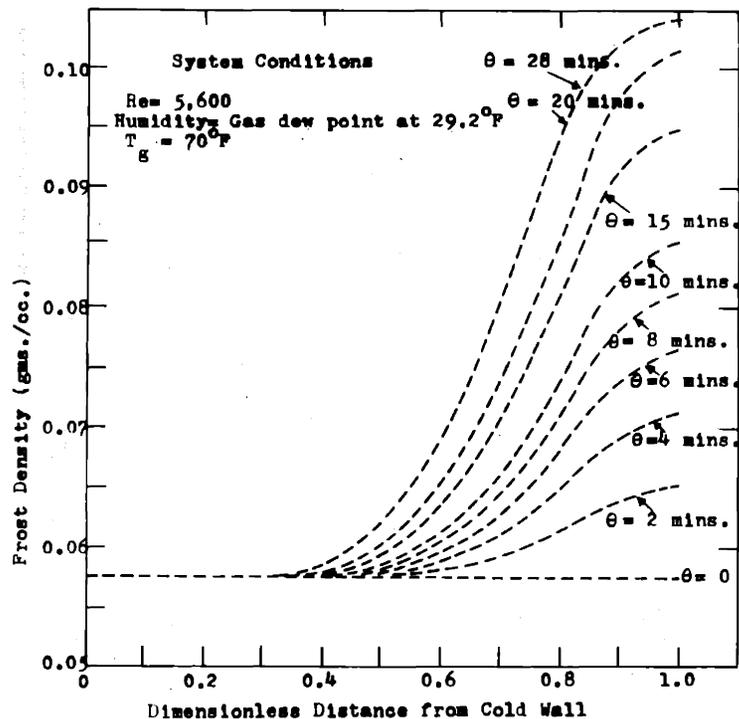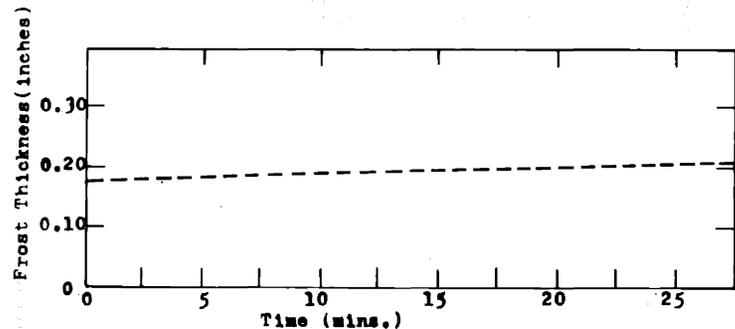
Figure E-5   Predictions of 'Sophisticated Model' for
              the Time Variation in Density Distribution
              within the Frost and the Frost Thickness
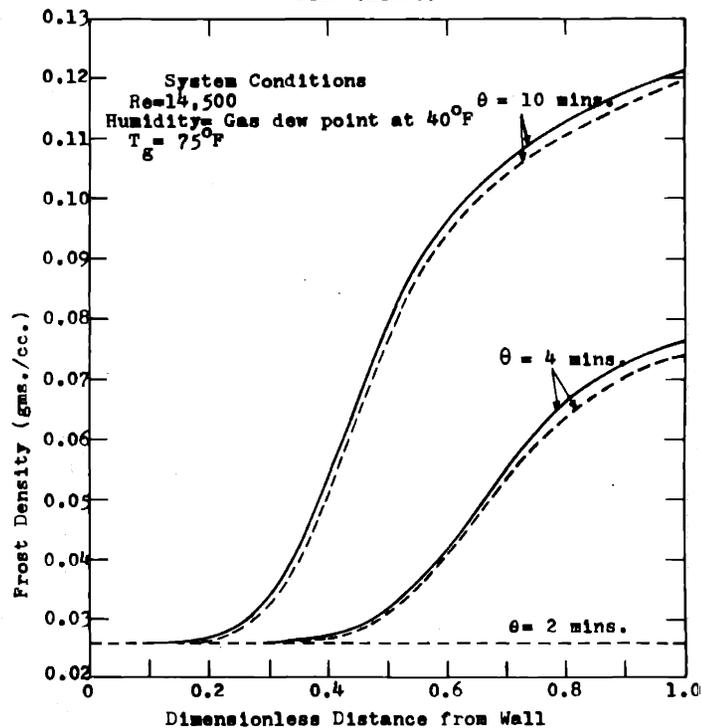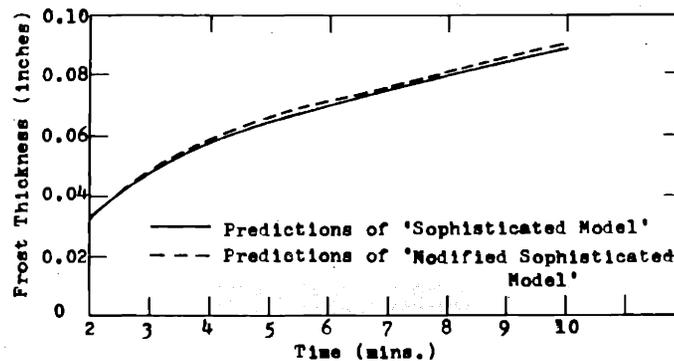
Figure E-6   Comparison between Predictions of
              'Sophisticated Model' and 'Modified
              Sophisticated Model'

Computer Program for 'Sophisticated Model'

```
          DIMENSION FLUX(50),RHOF(60),T(60),RHOFN(60),FU (   ),
     1FUM1(60),RHOFI(60),RHOFO(60),FUT(100),TP(100)
          L=1
          GO TO (50,2),L
 50       READ (2,100) H,TG,P,FLUX1,RG,PP,M
100       FORMAT (6F10.5,I )
          READ (2,101) T ,DELX,DELZ,DELI,TZI,THETA,
101       FORMAT (6F10.5,I3)
          READ (2,102) (RHOFI(I),I=1,M)
102       FORMAT (7F10.5)
          READ(2,105) (TP(I),I=1,N)
105       FORMAT(7F10.5)
          DO 112 I=1,M
112       RHOF(I)=RHOFI(I)
          RHOFZ=RHOF(1)
          RHOFS=RHOF(M)
          FLUX(1)=FLUX1
          DELO=DELI
          TZ=TZI
          DO 31 I=1,N
          IF(I-1) 53,54,53
 53       THETA=THETA+DELX
 54       MM=0
          IF(I-1) 36,128,36
128       IQ=M-1
          T(1)=TW
          TZ=TP(I)
          IF(I-1) 42,43,42
 42       TZ=TZ/1.80
          P1=8.2312*0.4343*ALOG(TZ)
          PVP=EXP(((-2445.5646/TZ)+P1-(0.01677006*TZ)+(1.20514*(10.**(-5.0))
     1*TZ*TZ)-6.757169)/(0.4343))
          TZ=TZ*1.80
          FLUX(I)=F*(P-PVP)
 43       HEAT=H*(TG-TZ)+(FLUX(I)*(422.5)*(TZ**(0.1712)))
          DO 10 K=1,IQ
          IF(T(K)-460.0) 181,181,182
182       G1=(DELO*HEAT)/((8.490*(10.**(-17.0))*(T(K)**(5.44)))+(6.860*(10.
     1**(-14.0))*(T(K)**(4.84))*(RHOF(K)-0.025)))
          T1=T(K)+(DELZ*G1)/2.0
 52       G2=(DELO*HEAT)/((8.490*(10.**(-17.0))*(T1**(5.44)))+(6.860*(10.
     1**(-14.0))*(T1**(4.84))*(RHOF(K)-0.025)))
          T2=T(K)+(DELZ*G2)/2.0
 56       G3=(DELO*HEAT)/((8.490*(10.**(-17.0))*(T2**(5.44)))+(6.860*(10.
     1**(-14.0))*(T2**(4.84))*(RHOF(K)-0.025)))
          T3=T(K)+(DELZ*G3)
 58       G4=(DELO*HEAT)/((8.490*(10.**(-17.0))*(T3**(5.44)))+(6.860*(10.
     1**(-14.0))*(T3**(4.84))*(RHOF(K)-0.025)))
          GO TO 18
181       G1=(DELO*HEAT)/((3.875*(10.**(-6.0))*(T(K)**(1.441)))+(4.080*(
     110.**(-9.0))*(T(K)**(3.055))*(RHOF(K)-0.025)))
          T1=T(K)+(DELZ*G1)/2.0
          IF(T1-460.0) 51,51,52
 51       G2=(DELO*HEAT)/((3.875*(10.**(-6.0))*(T1**(1.441)))+(4.080*(10.
     1**(-9.0))*(T1**(3.055))*(RHOF(K)-0.025)))
          T2=T(K)+(DELZ*G2)/2.0
          IF(T2-460.0) 55,55,56
 55       G3=(DELO*HEAT)/((3.875*(10.**(-6.0))*(T2**(1.441)))+(4.080*(10.
     1**(-9.0))*(T2**(3.055))*(RHOF(K)-0.025)))
          T3=T(K)+(DELZ*G3)
          IF(T3-460.0) 57,57,58
 57       G4=(DELO*HEAT)/((3.875*(10.**(-6.0))*(T3**(1.441)))+(4.080*(10.
```

```
      I**(-9.0))*(T2**(3.055))*(RHOF(K)-0.025)))
18    T(K+1)=T(K)+DELZ*(G1+2.0*G2+2.0*G3+G4)/6.0
10    CONTINUE
      IF(MM-2) 62,126,62
62    IF(I-1) 36,32,36
32    TZ=TZ/1.80
      P1=8.2312*0.4343*ALOG(TZ)
      PVP=EXP(((-2445.5646/TZ)+P1-(0.01677006*TZ)+(1.20514*(10.**(-5.0))
     I*TZ*TZ)-6.757169)/(0.4343))
      TZ=TZ*1.80
      F=FLUX1/(P-PVP)
      GO TO 126
36    IF(TZ-460.0) 39,39,38
39    DELC=(DELO*HEAT)/((3.875*(10.**(-6.0))*(TZ**(1.441)))+(4.080*
     I(10.**(-9.0))*(TZ**(3.055))*(RHOFS-0.025)))
      GO TO 84
38    DELC=(DELO*HEAT)/((8.490*(10.**(-17.0))*(TZ**(5.44)))+(6.860*(
     110.**(-14.0))*(TZ**(4.84))*(RHOFS-0.025)))
84    TZ=TZ/1.80
      DIF1=(2.760*(10.**(-6.0))*(TZ**2.009))
      P2=8.2312*0.4343*ALOG(TZ)
      PVP1=EXP(((-2445.5646/TZ)+P2-(0.01677006*TZ)+(1.20514*(10.**(-5.0)
     1)*TZ*TZ)-6.757169)/(0.4343))
      TZ=TZ*1.80
      IF(MM-1) 119,119,120
119   FLUX(I)=F*(P-PVP1)
120   YW=1.0-(PVP1/PP)
      PP1=(((2445.5646*1.80)/(TZ*TZ))+(0.4343*8.2312)/TZ-(0.01677006/
     11.80)+(2.41028*(10.**(-5.0))*TZ)/3.240))/(0.4343)
      PVPP1=PVP1*PP1
      DIP=((FLUX(I)-((DIFI*(1.0-RHOFS/0.917)*PVPP1*DELC)/(1.10*YW*RG*TZ
     1*DELO)))/(RHOFS*62.40))
      IF(MM-1) 93,98,93
93    DIP1=DIP
      DELN=DELO+DELX*DIP
98    MM=MM+1
      IF(MM-1) 99,99,75
75    DELN=DELS+DELX*(DIP1+DIP)/2.0
99    DO 11 J=1,IQ
      T(J+1)=T(J+1)/1.80
      DIF2=(2.760*(10.**(-6.0))*(T(J+1)**2.009))
      P3=8.2312*0.4343*ALOG(T(J+1))
      PVP2=EXP(((-2445.5646/T(J+1))+P3-(0.01677006*T(J+1))+(1.20514*(
     110.**(-5.0))*T(J+1)*T(J+1))-6.757169)/(0.4343))

      YW1=1.0-(PVP2/PP)
      T(J+1)=T(J+1)*1.80
      PP2=(((2445.5646*1.80)/(T(J+1)*T(J+1)))+(0.4343*8.2312)/T(J+1)
     1-(0.01677006/1.80)+(2.41028*(10.**(-5.0))*T(J+1))/3.240)/(0.4343)
      PVPP2=PVP2*PP2
      T(J)=T(J)/1.80
      DIF3=(2.760*(10.**(-6.0))*(T(J)**2.009))
      P4=8.2312*0.4343*ALOG(T(J))
      PVP3=EXP(((-2445.5646/T(J))+P4-(0.01677006*T(J))+(1.20514*(10.**
     1(-5.0))*T(J)*T(J))-6.757169)/(0.4343))
      YW2=1.0-(PVP3/PP)
      T(J)=T(J)*1.80
      PP3=(((2445.5646*1.80)/(T(J)*T(J)))+(0.4343*8.2312)/T(J)-(0.01677
```

```
              1006/1.80)+((2.41028*(10.**(-5.0))*T(J))/3.240))/(0.4343))
                 PVPP3=PVP3*PP3
              IF(T(J+1)-460.0) 292,292,293
      293     FUT(J+1)=(DIF2*(1.0-(RHOF(J+1)/0.917))*PVPP2*((HEAT*DELO)/((
             18.490*(10.**(-17.0))*(T(J+1)**(5.44)))+(6.860*(10.**(-14.0))*
             1(T(J+1)**(4.840))*(RHOF(J+1)-0.025)))))/(1.10*YW1*RG*T(J+1)*DELO)
                 GO TO 295
      292     FUT(J+1)=(DIF2*(1.0-(RHOF(J+1)/0.917))*PVPP2*((HEAT*DELO)/((3
             1.875*(10.**(-6.0))*(T(J+1)**(1.441)))+(4.080*(10.**(-9.0))*(
             1T(J+1)**(3.055))*(RHOF(J+1)-0.025)))))/(1.10*YW1*RG*T(J+1)*DELO)
      295     IF(T(J)-460.0) 297,297,299
      299     FUT(J)=(DIF3*(1.0-(RHOF(J)/0.917))*PVPP3*((HEAT*DELO)/((8.490
             1*(10.**(-17.0))*(T(J)**(5.44)))+(6.860*(10.**(-14.0))*(T(J)**(4.84
             10))*(RHOF(J)-0.025)))))/(1.10*YW2*RG*T(J)*DELO)
                 GO TO 301
      297     FUT(J)=(DIF3*(1.0-(RHOF(J)/0.917))*PVPP3*((HEAT*DELO)/((3.875
             1*(10.**(-6.0))*(T(J)**(1.441)))+(4.080*(10.**(-9.0))*(T(J)
             1**(3.055))*(RHOF(J)-0.025)))))/(1.10*YW2*RG*T(J)*DELO)
      301     FUM(J)=((RHOF(J+1)-RHOF(J))*(J*DELZ*DIP)*62.40)/(DELO*DELZ)+
             1(FUT(J+1)-FUT(J))/(DELO*DELZ)
       11     CONTINUE
                 IF(MM-1) 92,89,92
       89        DO 111 J=1,IQ
      111     FUM1(J)=FUM(J)
                 DO 121 J=1,IQ
      121     RHOFO(J+1)=RHOF(J+1)
                 DO 88 J=1,IQ
                 RHOFN(J+1)=RHOF(J+1)*62.40+DELX*FUM(J)
       88     RHOFN(J+1)=RHOFN(J+1)/62.40
                 DO 85  J=1,IQ
       85     RHOF(J+1)=RHOFN(J+1)
                 DELO=DELN
                 RHOFS=RHOF(M)
                 GO TO 128
       92        DO 118 J=1,IQ
                 RHOF(J+1)=RHOFO(J+1)*62.40+DELX*(FUM1(J)+FUM(J))/2.0
      118     RHOF(J+1)=RHOF(J+1)/62.40
                 DELO=DELN
                 RHOFS=RHOF(M)
                 IF(MM-2) 126,128,126

      126     DELO=DELO*12.0
                 THETA=THETA*60.0
                 WRITE(3,103) THETA,DELO
      103     FORMAT(2E14.6)
                 WRITE(3,104) (RHOF(J),J=1,M)
      104     FORMAT (11E13.6)
                 DO 113 J=1,M
      113     T(J)=T(J)-459.67
                 WRITE (3,108) (T(J),J=1,M)
      108     FORMAT (11E13.5)
                 DO 114 J=1,M
      114     T(J)=T(J)+459.67
                 RHOFS=RHOF(M)
                 DELO=DELO/12.0
                 THETA=THETA/60.0
                 DELS=DELO
       31     CONTINUE
                 GO TO 50
        2     CALL EXIT
                 END
```

Appendix F

Empirical Correlation between Carbon Dioxide Frost Thermal Conductivity, Density and Temperature from the Frost Structure Models.

As demonstrated in Section II of the thesis an application of any theoretical model to the frosting process requires an accurate knowledge of thermal conductivity of frost. The thermal conductivity of the frost is usually assumed to be the function of frost density, temperature and frost structure. For the purpose of theoretical development of models for water frost formation process this correlation was obtained from an empirical curve fitting of the experimental data of Brazinsky **(14)** and of the present work. In order to use the successful models of the present thesis to explain the frosting process of other materials (e.g. carbon dioxide), a similar thermal conductivity correlation is needed.

At present there are no experimental data available on properties of carbon dioxide frost. Hence, in the absence of experimental data, thermal conductivity correlation for carbon dioxide frost can only be obtained by modelling of the frost structure.

The heterogeneous frost structure can be usually classified into three catagories; (1) dispersions, (2) packed beds and (3) continuous pairs.

Dispersions are defined as a discontinuous phase

dispersed in a continuous phase.   Continuous pairs
refers to materials where both phases are significantly
continuous.   Packed beds are limiting cases between
dispersions and continuous pairs, e.g. dispersions with
point contacts.

Usually low density structure is expected to be
of dispersion model and high density structure is expected
to be like the continuous pairs.   The dispersion frost
structure have been often successfully characterized by
Woodside model (121).   The continuous pairs structure,
on the other hand, have been well characterized by
Riemann's model (47).   Hence in this appendix, the carbon
dioxide frost thermal conductivity at various density and
temperature are obtained with the help of these two
frost structure models.   For low density frost ($\rho_f < 0.85$),
Woodside model is used for the thermal conductivity
correlation and Riemann's model is assumed to represent
high density ($\rho_f > 0.85$) frost structure.

The thermal conductivity values reported in this
appendix include the excess thermal conductivity component
of carbon dioxide.   In order to study the theoretical
models for the carbon dioxide frosting process, empirical
equations of this appendix could be used for thermal
conductivity calculations.   The results, however, should
be checked with the help of experimental data in order to
verify the validity of each model.

Empirical Correlation for low Density Frost

The low density carbon dioxide frost ($\rho_f < 0.85$gms/cc) structure is modelled by Woodside model (121). This model assumes that the heterogeneous structure of frost consists of a simple cubic array of ice spheres and that conductivity is infinite in a sidewise direction (see Figure F-1 for a three dimensional view of the structure). This is tantamount to assuming that the isotherms are parallel planes. The final expression $k/k_{g,e}$ was derived by considering the resistance of Zone I and II (see Figure F-2) to be in series. The resistance of Zone I was a parallel combination of the resistances of the solid and gas in that zone. The derivation of an expression for calculating the thermal conductivity of this array is presented in Reference 90. The final results are

$$\frac{k_f}{k_{g,e}} = \left\{ 1 - \left(\frac{6(1-\epsilon)}{\pi} \right)^{1/3} \left[1 - \frac{(a^2-1)}{2a} \ln \frac{(a+1)}{(a-1)} \right] \right\}^{-1} \qquad \text{(F-1)}$$

where

$$a = 1 + \frac{4}{\psi \pi \left[\frac{6(1-\epsilon)}{\pi} \right]^{2/3}} \qquad \text{(F-2)}$$

$$\psi = \frac{k_i - k_{g,e}}{k_{g,e}} \quad \text{and} \quad (1-\epsilon) = \frac{(\rho_f - \rho_g)}{(\rho_s - \rho_g)} \qquad \text{(F-3)}$$

Here $k_{g,e}$ is the total conductivity of the gas phase which includes k_g, the intrinsic gas conductivity and k_{excess}, the additional component of conductivity due to internal mass transport.

An expression for k_{excess} can be obtained by considering the total heat flux through the pore phase at some point

in the frost.

$$\frac{q}{A} = K_{g,e} \frac{dT}{dx} = k_g \frac{dT}{dx} + \frac{D_B}{RT} M_v \frac{dP_{vp}}{dx} \Delta H \qquad (F-4)$$

where the second term in the right hand side of Equation F-4 is enthalpy transport due to mass transport.

From Equation F-4 and the definition of k_{excess}

$$k_{excess} = k_{g,e} - k_g \qquad (F-5)$$

Equation F-6 can be derived as

$$k_{excess} = \frac{D_B}{RT} \left(\frac{dP_{vp}}{dT}\right) \Delta H \, M_v \qquad (F-6)$$

Combining Equation F-6 with Claussius-Clapyson Equation ($\underline{80}$)

$$\frac{dP_{vp}}{dT} = \frac{M_v \Delta H P_{vp}}{RT^2} \qquad (F-7)$$

The final expression for k_{excess} is obtained as

$$k_{excess} = \frac{D_{1-2} \Delta H^2 P_{vp} (M_v)^2}{R^2 T^3} \qquad (F-8)$$

Computer Results

The computer results of solution of Equations F-1 to F-3 are shown in Table F-1. The following empirical correlations for various properties of carbon dioxide and air were used in the computer program

$$\Delta H = 583.0 \times T^{-0.1469} \qquad (F-9)$$

where T is in ^{o}R and ΔH is in Btu/lb

$$K_s = 325/T^{1.22} \qquad (F-10)$$

where T is in ^{o}R K_s is in Btu/hr ft^2 ^{o}R/ft   ($\underline{3}$)

$$k_g = 57.86\times10^{-6}\left(\frac{T}{273.16}\right)^{0.773} - 0.57\times10^{-4} \, t \; 0.4\times10^{-7} \, t^2 \quad (\underline{54})$$

$$(F-11)$$

where $t = {}^{o}C$

$T = {}^{o}K$ and $K_g = \dfrac{Cal}{cm \; sec \; deg \; c}$

Also, $\rho_g = \dfrac{38.3}{T}$

where T is in $°R$ and ρ_g is in $\dfrac{lb_m}{cu\ ft}$ (F-12)

For $T < 270°R$

$\rho_s = 1.7304 - 4.01 \times 10^{-4} T$ (54) (F-13)

and for $T > 270°R$

$\rho_s = 1.8318 - 7.76 \times 10^{-4} T$ (54) (F-14)

where $T = °R$

$\rho_s = gms./cc.$

$D_{CO_2\text{-Air}} = 1.765 \times 10^{-6} T^{2.009}$ (F-15)

$D_{CO_2\text{-}N_2} = 2.38 \times 10^{-6} T^{2.0087}$ (F-16)

Details of the above Equations are shown in Figure II-B10 and Reference 94

where $T = °k$

$D_{1-2} = cm^2/sec.$

$k_g = 0.0089 \left(\dfrac{T}{360}\right)^{.95}$ (3) (F-17)

where $T = °R$

$k_g = Btu/hr\ ft°R$ (F-18)

for $138°k < T < 216.3°k$

$\log_{10} P_{vp} (mm.\ Hg.) = -\dfrac{1367.3448}{T} + 9.9082$ (54) (F-19)

for $90°k < T < 138°k$

$\log_{10} P_{vp} = -\dfrac{1275.62}{T} + 0.006833T + 8.3071$ (54) (F-20)

Empirical Correlation for High Density Frost.

The high density carbon dioxide frost structure is

represented by a truncated sphere model by Riemann (47).
This model is tested extensively by Gorring and Churchill
(47). In this model the solid phase is assumed to be
composed of spheres of diameter 2R with common intersecting
circles of diameter 2r (see Figure F-3). The derivation
of the mathematical equation are summarized in Reference 47.
The final results are as follows.

$$\frac{k_{f1}}{k_{g,e}} = \left(\frac{R}{r} + \frac{1}{\pi} \ell n \left(\frac{2R}{r} \right) \right)^{-1} \qquad \text{(F-21)}$$

k_{f1} is the contribution to the frost conductivity due to
the solid sphere.

The ratio (R/r) is related to density parameter
$S = (\rho_f - \rho_g) / (\rho_s - \rho_g)$ by a material balance

$$S = \frac{\pi}{6\left[1-(\frac{r}{R})^2\right]^{3/2}} \left\{ 1 - \frac{3}{2}\left[(\frac{r}{R})^2 + 1 - \left[1-(\frac{r}{R})^2\right]^{\frac{1}{2}}\right] \left[1-(1-(\frac{r}{R})^2)^{\frac{1}{2}}\right] \right\} \qquad \text{(F-22)}$$

or ϵ = void fraction = $\dfrac{1}{6\left[1-(\frac{r}{R})^2\right]^{2/3}} \times \left[1-(\frac{r}{R})^2(2-\sqrt{1-(\frac{r}{R})^2}) \right]$ (F-23)

Equation F-17 is not applicable to dispersion models
i.e. r)R. Solving Equations F-21 and F-22 simultaneously
$k_{f1}/k_{g,e}$ as a function of S can be obtained.

Equation F-21 allows only for the contribution due to
the solid phase. Some heat flow will be due to the
interstitial gas (air) and this contribution k_{f2} is
estimated approximately as (47)

$$\frac{k_{f2}}{k_{g,e}} = 2(1-S)/(2+S) \qquad \text{(F-24)}$$

where $k_{g,e} = k_g + k_{excess}$ $\qquad$ (F-25)

k_g = dry gas conductivity

k_{excess} = excess thermal conductivity due to
evaporative transport as defined previously.

The total frost conductivity is defined as

$$k_f = k_{f1} + k_{f2} \qquad (F\text{-}26)$$

This model is applicable for high density frost where $S > 0.524$ but less than about 0.9.

The results of the computer solution of the above described equations are shown in Table F-2.

Table F-1

Thermal Conductivity as a Function of Density and Temperature from Woodside Model (121)

$T_w = -315\,°F$

ρ_f (gms./cc)	T_s (°R)	k_f (Btu/hr ft °R)	$k_{avg}\,(T_s-T_w)$ (Btu hr ft)
0.500000E-01	0.150000E 03	0.813384E-02	0.428062E-01
0.100000E 00	0.150000E 03	0.971429E-02	0.511383E-01
0.150000E 00	0.150000E 03	0.112009E-01	0.589746E-01
0.200000E 00	0.150000E 03	0.127335E-01	0.670541E-01
0.249999E 00	0.150000E 03	0.143625E-01	0.757527E-01
0.299999E 00	0.150000E 03	0.162082E-01	0.855855E-01
0.349999E 00	0.150000E 03	0.182747E-01	0.962937E-01
0.399999E 00	0.150000E 03	0.206617E-01	0.108899E 00
0.449999E 00	0.150000E 03	0.234751E-01	0.123766E 00
0.499999E 00	0.150000E 03	0.268648E-01	0.141691E 00
0.549999E 00	0.150000E 03	0.310518E-01	0.163650E 00
0.599999E 00	0.150000E 03	0.363800E-01	0.192081E 00
0.649999E 00	0.150000E 03	0.434187E-01	0.229424E 00
0.500000E-01	0.160000E 03	0.850903E-02	0.126032E 00
0.100000E 00	0.160000E 03	0.101530E-01	0.150488E 00
0.150000E 00	0.160000E 03	0.116989E-01	0.173490E 00
0.200000E 00	0.160000E 03	0.132907E-01	0.197193E 00
0.249999E 00	0.160000E 03	0.150017E-01	0.222697E 00
0.299999E 00	0.160000E 03	0.168931E-01	0.250919E 00
0.349999E 00	0.160000E 03	0.190303E-01	0.282851E 00
0.399999E 00	0.160000E 03	0.214942E-01	0.319717E 00
0.449999E 00	0.160000E 03	0.243918E-01	0.363148E 00
0.499999E 00	0.160000E 03	0.278735E-01	0.415439E 00
0.549999E 00	0.160000E 03	0.321600E-01	0.479978E 00
0.599999E 00	0.160000E 03	0.375926E-01	0.562031E 00
0.649999E 00	0.160000E 03	0.447306E-01	0.670282E 00
0.699999E 00	0.160000E 03	0.545605E-01	0.820188E 00
0.749999E 00	0.160000E 03	0.690055E-01	0.104221E 01
0.799999E 00	0.160000E 03	0.923747E-01	0.140598E 01
0.849999E 00	0.160000E 03	0.136765E 00	0.211295E 01
0.500000E-01	0.170000E 03	0.807211E-02	0.212948E 00
0.100000E 00	0.170000E 03	0.105761E-01	0.254146E 00
0.150000E 00	0.170000E 03	0.121779E-01	0.292889E 00
0.200000E 00	0.170000E 03	0.138255E-01	0.332793E 00
0.249999E 00	0.170000E 03	0.155942E-01	0.375698E 00
0.299999E 00	0.170000E 03	0.175462E-01	0.423141E 00
0.349999E 00	0.170000E 03	0.197403E-01	0.476774E 00
0.399999E 00	0.170000E 03	0.222819E-01	0.538633E 00
0.449999E 00	0.170000E 03	0.252546E-01	0.611423E 00
0.499999E 00	0.170000E 03	0.288166E-01	0.698942E 00
0.549999E 00	0.170000E 03	0.331875E-01	0.806779E 00
0.599999E 00	0.170000E 03	0.387035E-01	0.943595E 00
0.649999E 00	0.170000E 03	0.459120E-01	0.112355E 01
0.699999E 00	0.170000E 03	0.557673E-01	0.137196E 01
0.749999E 00	0.170000E 03	0.700994E-01	0.173792E 01
0.799999E 00	0.170000E 03	0.929186E-01	0.233269E 01
0.849999E 00	0.170000E 03	0.135048E 00	0.347224E 01
0.500000E-01	0.180000E 03	0.922406E-02	0.303437E 00
0.100000E 00	0.180000E 03	0.109868E-01	0.361963E 00
0.150000E 00	0.180000E 03	0.126392E-01	0.416989E 00
0.200000E 00	0.180000E 03	0.143391E-01	0.473633E 00
0.249999E 00	0.180000E 03	0.161614E-01	0.534496E 00
0.299999E 00	0.180000E 03	0.181695E-01	0.601744E 00
0.349999E 00	0.180000E 03	0.204368E-01	0.677699E 00
0.399999E 00	0.180000E 03	0.230273E-01	0.765213E 00
0.449999E 00	0.180000E 03	0.260666E-01	0.868070E 00
0.499999E 00	0.180000E 03	0.296982E-01	0.991565E 00
0.549999E 00	0.180000E 03	0.341389E-01	0.114347E 01
0.599999E 00	0.180000E 03	0.397198E-01	0.133578E 01
0.649999E 00	0.180000E 03	0.469730E-01	0.158811E 01
0.699999E 00	0.180000E 03	0.568174E-01	0.193501E 01
0.749999E 00	0.180000E 03	0.709886E-01	0.244351E 01
0.799999E 00	0.180000E 03	0.951943E-01	0.326645E 01
0.849999E 00	0.180000E 03	0.133096E 00	0.481314E 01
0.500000E-01	0.190000E 03	0.956667E-02	0.397397E 00
0.100000E 00	0.190000E 03	0.113811E-01	0.473801E 00
0.150000E 00	0.190000E 03	0.130852E-01	0.545623E 00
0.200000E 00	0.190000E 03	0.148341E-01	0.615513E 00
0.249999E 00	0.190000E 03	0.167065E-01	0.698852E 00
0.299999E 00	0.190000E 03	0.187664E-01	0.786443E 00
0.349999E 00	0.190000E 03	0.210820E-01	0.885287E 00
0.399999E 00	0.190000E 03	0.237351E-01	0.999054E 00
0.449999E 00	0.190000E 03	0.268334E-01	0.113260E 01
0.499999E 00	0.190000E 03	0.305246E-01	0.129272E 01
0.549999E 00	0.190000E 03	0.350229E-01	0.148933E 01
0.599999E 00	0.190000E 03	0.406516E-01	0.173770E 01
0.649999E 00	0.190000E 03	0.479272E-01	0.206270E 01
0.699999E 00	0.190000E 03	0.577297E-01	0.250785E 01
0.749999E 00	0.190000E 03	0.716957E-01	0.315706E 01
0.799999E 00	0.190000E 03	0.932523E-01	0.419584E 01
0.849999E 00	0.190000E 03	0.130992E 00	0.613362E 01
0.500000E-01	0.200000E 03	0.990447E-02	0.494755E 00
0.100000E 00	0.200000E 03	0.117702E-01	0.589560E 00
0.150000E 00	0.200000E 03	0.135218E-01	0.678662E 00
0.200000E 00	0.200000E 03	0.153174E-01	0.770275E 00
0.249999E 00	0.200000E 03	0.172369E-01	0.868576E 00
0.299999E 00	0.200000E 03	0.193454E-01	0.977012E 00
0.349999E 00	0.200000E 03	0.217110E-01	0.109926E 01
0.399999E 00	0.200000E 03	0.244159E-01	0.123982E 01
0.449999E 00	0.200000E 03	0.275667E-01	0.140462E 01
0.499999E 00	0.200000E 03	0.313096E-01	0.160191E 01
0.549999E 00	0.200000E 03	0.358564E-01	0.184375E 01
0.599999E 00	0.200000E 03	0.415175E-01	0.214359E 01
0.649999E 00	0.200000E 03	0.487967E-01	0.254657E 01
0.699999E 00	0.200000E 03	0.585327E-01	0.308924E 01
0.749999E 00	0.200000E 03	0.722645E-01	0.387695E 01
0.799999E 00	0.200000E 03	0.931433E-01	0.512793E 01
0.849999E 00	0.200000E 03	0.128802E 00	0.743270E 01

Table F-1 (contd.)

0.500000E-01	0.310000E 03	0.114219E 00	0.349972E 01
0.100000E 00	0.310000E 03	0.119162E 00	0.394077E 01
0.150000E 00	0.310000E 03	0.123966E 00	0.435603E 01
0.200000E 00	0.310000E 03	0.128718E 00	0.477466E 01
0.249999E 00	0.310000E 03	0.133466E 00	0.521142E 01
0.299999E 00	0.310000E 03	0.138244E 00	0.567749E 01
0.349999E 00	0.310000E 03	0.143076E 00	0.618389E 01
0.399999E 00	0.310000E 03	0.147982E 00	0.674310E 01
0.449999E 00	0.310000E 03	0.152981E 00	0.737059E 01
0.499999E 00	0.310000E 03	0.158088E 00	0.808673E 01
0.549999E 00	0.310000E 03	0.163318E 00	0.891980E 01
0.599999E 00	0.310000E 03	0.168866E 00	0.991096E 01
0.649999E 00	0.310000E 03	0.174206E 00	0.111235E 02
0.699999E 00	0.310000E 03	0.179892E 00	0.126614E 02
0.749999E 00	0.310000E 03	0.185760E 00	0.147110E 02
0.799999E 00	0.310000E 03	0.191826E 00	0.176495E 02
0.500000E-01	0.320000E 03	0.181990E 00	0.495508E 01
0.100000E 00	0.320000E 03	0.185142E 00	0.543790E 01
0.150000E 00	0.320000E 03	0.188258E 00	0.589408E 01
0.200000E 00	0.320000E 03	0.191357E 00	0.635329E 01
0.249999E 00	0.320000E 03	0.194452E 00	0.683054E 01
0.299999E 00	0.320000E 03	0.197550E 00	0.753727E 01
0.349999E 00	0.320000E 03	0.200660E 00	0.788462E 01
0.399999E 00	0.320000E 03	0.203785E 00	0.848520E 01
0.449999E 00	0.320000E 03	0.206930E 00	0.913456E 01
0.499999E 00	0.320000E 03	0.210999E 00	0.991319E 01
0.549999E 00	0.320000E 03	0.213295E 00	0.107894E 02
0.599999E 00	0.320000E 03	0.216521E 00	0.118245E 02
0.649999E 00	0.320000E 03	0.219780E 00	0.130819E 02
0.699999E 00	0.320000E 03	0.223074E 00	0.146655E 02
0.749999E 00	0.320000E 03	0.226406E 00	0.167618E 02
0.799999E 00	0.320000E 03	0.229779E 00	0.197481E 02
0.500000E-01	0.330000E 03	0.288253E 00	0.726541E 01
0.100000E 00	0.330000E 03	0.288669E 00	0.776431E 01
0.150000E 00	0.330000E 03	0.289089E 00	0.823647E 01
0.200000E 00	0.330000E 03	0.289512E 00	0.871161E 01
0.249999E 00	0.330000E 03	0.289929E 00	0.920478E 01
0.299999E 00	0.330000E 03	0.290369E 00	0.972743E 01
0.349999E 00	0.330000E 03	0.290803E 00	0.102907E 02
0.399999E 00	0.330000E 03	0.291239E 00	0.109073E 02
0.449999E 00	0.330000E 03	0.291678E 00	0.115927E 02
0.499999E 00	0.330000E 03	0.292121E 00	0.123675E 02
0.549999E 00	0.330000E 03	0.292566E 00	0.132600E 02
0.599999E 00	0.330000E 03	0.293014E 00	0.143114E 02
0.649999E 00	0.330000E 03	0.293465E 00	0.155852E 02
0.699999E 00	0.330000E 03	0.293919E 00	0.171854E 02
0.749999E 00	0.330000E 03	0.294376E 00	0.192984E 02
0.799999E 00	0.330000E 03	0.294835E 00	0.223014E 02
0.500000E-01	0.340000E 03	0.459421E 00	0.109458E 02
0.100000E 00	0.340000E 03	0.466592E 00	0.114791E 02
0.150000E 00	0.340000E 03	0.474471E 00	0.119879E 02
0.200000E 00	0.340000E 03	0.483096E 00	0.125022E 02
0.249999E 00	0.340000E 03	0.492534E 00	0.130372E 02
0.299999E 00	0.340000E 03	0.502869E 00	0.136043E 02
0.349999E 00	0.340000E 03	0.514204E 00	0.142151E 02
0.399999E 00	0.340000E 03	0.526668E 00	0.148825E 02
0.449999E 00	0.340000E 03	0.540415E 00	0.156222E 02
0.499999E 00	0.340000E 03	0.555633E 00	0.164552E 02
0.549999E 00	0.340000E 03	0.572351E 00	0.174103E 02
0.599999E 00	0.340000E 03	0.591454E 00	0.185293E 02
0.649999E 00	0.340000E 03	0.612696E 00	0.198761E 02
0.699999E 00	0.340000E 03	0.636726E 00	0.215556E 02
0.749999E 00	0.340000E 03	0.664117E 00	0.237552E 02
0.799999E 00	0.340000E 03	0.695615E 00	0.268532E 02
0.500000E-01	0.350000E 03	0.712269E 00	0.167269E 02
0.100000E 00	0.350000E 03	0.731541E 00	0.173854E 02
0.150000E 00	0.350000E 03	0.753539E 00	0.180373E 02
0.200000E 00	0.350000E 03	0.779293E 00	0.187147E 02
0.249999E 00	0.350000E 03	0.809622E 00	0.194361E 02
0.299999E 00	0.350000E 03	0.845676E 00	0.202178E 02
0.349999E 00	0.350000E 03	0.889086E 00	0.210774E 02
0.399999E 00	0.350000E 03	0.942227E 00	0.220364E 02
0.449999E 00	0.350000E 03	0.100868E 01	0.231229E 02
0.499999E 00	0.350000E 03	0.109414E 01	0.243753E 02
0.549999E 00	0.350000E 03	0.120820E 01	0.258498E 02
0.599999E 00	0.350000E 03	0.136855E 01	0.276326E 02
0.649999E 00	0.350000E 03	0.161191E 01	0.298681E 02
0.699999E 00	0.350000E 03	0.203027E 01	0.328293E 02
0.749999E 00	0.350000E 03	0.294492E 01	0.371684E 02
0.799999E 00	0.350000E 03	0.703943E 01	0.461575E 02
0.500000E-01	0.360000E 03	0.107813E 01	0.255735E 02
0.100000E 00	0.360000E 03	0.111490E 01	0.265035E 02
0.150000E 00	0.360000E 03	0.115989E 01	0.274818E 02
0.200000E 00	0.360000E 03	0.121532E 01	0.285529E 02
0.249999E 00	0.360000E 03	0.128466E 01	0.297547E 02
0.299999E 00	0.360000E 03	0.137342E 01	0.311326E 02
0.500000E-01	0.370000E 03	0.159322E 01	0.387876E 02
0.100000E 00	0.370000E 03	0.165617E 01	0.402087E 02
0.150000E 00	0.370000E 03	0.173562E 01	0.417984E 02
0.200000E 00	0.370000E 03	0.183724E 01	0.436392E 02
0.249999E 00	0.370000E 03	0.197050E 01	0.458303E 02
0.299999E 00	0.370000E 03	0.215200E 01	0.485203E 02
0.349999E 00	0.370000E 03	0.241344E 01	0.519591E 02

Table F-1 (contd.)

0.500000E-01	0.210000E 03	0.102500E-01	0.595510E 00
0.100000E 00	0.210000E 03	0.121669E-01	0.709228E 00
0.150000E 00	0.210000E 03	0.139656E-01	0.816081E 00
0.200000E 00	0.210000E 03	0.156074E-01	0.925880E 00
0.249999E 00	0.210000E 03	0.177354E-01	0.104360E 01
0.299999E 00	0.210000E 03	0.199292E-01	0.117336E 01
0.349999E 00	0.210000E 03	0.223434E-01	0.131951E 01
0.399999E 00	0.210000E 03	0.250976E-01	0.147737E 01
0.449999E 00	0.210000E 03	0.282977E-01	0.166592E 01
0.499999E 00	0.210000E 03	0.320879E-01	0.191888E 01
0.549999E 00	0.210000E 03	0.366736E-01	0.220637E 01
0.599999E 00	0.210000E 03	0.423614E-01	0.256797E 01
0.649999E 00	0.210000E 03	0.496316E-01	0.303651E 01
0.699999E 00	0.210000E 03	0.592844E-01	0.367832E 01
0.749999E 00	0.210000E 03	0.727607E-01	0.460210E 01
0.799999E 00	0.210000E 03	0.929472E-01	0.605841E 01
0.849999E 00	0.210000E 03	0.126605E 00	0.870971E 01
0.500000E-01	0.220000E 03	0.106567E-01	0.699888E 00
0.100000E 00	0.220000E 03	0.126099E-01	0.833047E 00
0.150000E 00	0.220000E 03	0.144605E-01	0.958138E 00
0.200000E 00	0.220000E 03	0.163530E-01	0.108660E 01
0.249999E 00	0.220000E 03	0.183699E-01	0.122423E 01
0.299999E 00	0.220000E 03	0.205776E-01	0.137580E 01
0.349999E 00	0.220000E 03	0.230446E-01	0.154635E 01
0.399999E 00	0.220000E 03	0.258524E-01	0.174201E 01
0.449999E 00	0.220000E 03	0.291058E-01	0.197082E 01
0.499999E 00	0.220000E 03	0.329464E-01	0.224393E 01
0.500000E-01	0.230000E 03	0.111466E-01	0.808645E 00
0.100000E 00	0.230000E 03	0.131940E-01	0.961884E 00
0.150000E 00	0.230000E 03	0.151133E-01	0.110580E 01
0.200000E 00	0.230000E 03	0.170728E-01	0.125350E 01
0.249999E 00	0.230000E 03	0.191573E-01	0.141162E 01
0.299999E 00	0.230000E 03	0.214339E-01	0.158559E 01
0.349999E 00	0.230000E 03	0.239717E-01	0.178114E 01
0.399999E 00	0.230000E 03	0.268519E-01	0.200521E 01
0.449999E 00	0.230000E 03	0.301782E-01	0.226889E 01
0.499999E 00	0.230000E 03	0.340900E-01	0.257873E 01
0.549999E 00	0.230000E 03	0.387832E-01	0.295887E 01
0.599999E 00	0.230000E 03	0.445443E-01	0.343482E 01
0.649999E 00	0.230000E 03	0.518133E-01	0.405062E 01
0.699999E 00	0.230000E 03	0.613032E-01	0.488176E 01
0.749999E 00	0.230000E 03	0.742541E-01	0.606977E 01
0.799999E 00	0.230000E 03	0.930312E-01	0.791583E 01
0.849999E 00	0.230000E 03	0.122779E 00	0.112013E 02
0.500000E-01	0.250000E 03	0.134341E-01	0.105012E 01
0.100000E 00	0.250000E 03	0.158134E-01	0.124702E 01
0.150000E 00	0.250000E 03	0.180388E-01	0.143183E 01
0.200000E 00	0.250000E 03	0.202988E-01	0.162117E 01
0.249999E 00	0.250000E 03	0.226870E-01	0.182346E 01
0.299999E 00	0.250000E 03	0.252757E-01	0.204551E 01
0.349999E 00	0.250000E 03	0.281366E-01	0.229445E 01
0.399999E 00	0.250000E 03	0.313521E-01	0.257887E 01
0.449999E 00	0.250000E 03	0.350242E-01	0.290990E 01
0.499999E 00	0.250000E 03	0.392867E-01	0.330282E 01
0.549999E 00	0.250000E 03	0.443221E-01	0.377957E 01
0.599999E 00	0.250000E 03	0.503895E-01	0.437316E 01
0.649999E 00	0.250000E 03	0.578705E-01	0.513589E 01
0.699999E 00	0.250000E 03	0.673566E-01	0.615642E 01
0.749999E 00	0.250000E 03	0.798138E-01	0.759854E 01
0.799999E 00	0.250000E 03	0.969415E-01	0.980452E 01
0.849999E 00	0.250000E 03	0.122030E 00	0.136409E 02
0.500000E-01	0.270000E 03	0.212646E-01	0.138155E 01
0.100000E 00	0.270000E 03	0.246137E-01	0.163424E 01
0.150000E 00	0.270000E 03	0.277371E-01	0.187115E 01
0.200000E 00	0.270000E 03	0.308708E-01	0.211310E 01
0.249999E 00	0.270000E 03	0.341296E-01	0.237057E 01
0.299999E 00	0.270000E 03	0.375568E-01	0.265192E 01
0.349999E 00	0.270000E 03	0.413486E-01	0.296578E 01
0.399999E 00	0.270000E 03	0.454660E-01	0.332238E 01
0.449999E 00	0.270000E 03	0.500426E-01	0.373483E 01
0.499999E 00	0.270000E 03	0.551931E-01	0.422096E 01
0.549999E 00	0.270000E 03	0.610634E-01	0.480605E 01
0.599999E 00	0.270000E 03	0.678446E-01	0.552772E 01
0.649999E 00	0.270000E 03	0.757965E-01	0.644484E 01
0.699999E 00	0.270000E 03	0.852795E-01	0.765579E 01
0.749999E 00	0.270000E 03	0.968143E-01	0.933951E 01
0.799999E 00	0.270000E 03	0.111118E 00	0.115631E 02
0.849999E 00	0.270000E 03	0.129612E 00	0.161379E 02
0.500000E-01	0.290000E 03	0.458435E-01	0.200924E 01
0.100000E 00	0.290000E 03	0.508235E-01	0.234919E 01
0.150000E 00	0.290000E 03	0.565139E-01	0.266000E 01
0.200000E 00	0.290000E 03	0.601513E-01	0.297940E 01
0.249999E 00	0.290000E 03	0.648566E-01	0.331852E 01
0.299999E 00	0.290000E 03	0.697085E-01	0.368120E 01
0.349999E 00	0.290000E 03	0.747723E-01	0.406358E 01
0.399999E 00	0.290000E 03	0.801670E-01	0.453536E 01
0.449999E 00	0.290000E 03	0.857723E-01	0.505123E 01
0.499999E 00	0.290000E 03	0.913516E-01	0.565084E 01
0.549999E 00	0.290000E 03	0.983553E-01	0.636167E 01
0.599999E 00	0.290000E 03	0.105626E 00	0.722847E 01
0.649999E 00	0.290000E 03	0.113313E 00	0.856041E 01
0.699999E 00	0.290000E 03	0.121594E 00	0.968364E 01
0.749999E 00	0.290000E 03	0.130946E 00	0.115888E 02
0.799999E 00	0.290000E 03	0.141257E 00	0.143418E 02

Table F-2
Thermal Conductivity as a Function of Density and Temperature function of Riemann's Model (47)

$T_w = -315°F$

ρ_f (gms./cc.)	T_s (°R)	K_f (BTU/hr ft °R)	$K_{avg}(T_s-T_w)$ (BTU/hr ft)
0.899999E 00	0.160000E 03	0.831098E-01	0.133194E 01
0.949999E 00	0.160000E 03	0.122739E 00	0.196873E 01
0.999999E 00	0.160000E 03	0.172576E 00	0.279910E 01
0.104999E 01	0.160000E 03	0.188986E 00	0.306579E 01
0.109999E 01	0.160000E 03	0.206119E 00	0.334422E 01
0.114999E 01	0.160000E 03	0.223972E 00	0.363433E 01
0.119999E 01	0.160000E 03	0.242540E 00	0.393606E 01
0.124999E 01	0.160000E 03	0.261821E 00	0.424936E 01
0.899999E 00	0.170000E 03	0.788450E-01	0.214123E 01
0.949999E 00	0.170000E 03	0.116313E 00	0.316326E 01
0.999999E 00	0.170000E 03	0.161233E 00	0.446688E 01
0.104999E 01	0.170000E 03	0.176524E 00	0.489195E 01
0.109999E 01	0.170000E 03	0.192489E 00	0.533574E 01
0.114999E 01	0.170000E 03	0.209126E 00	0.579816E 01
0.119999E 01	0.170000E 03	0.226432E 00	0.627912E 01
0.124999E 01	0.170000E 03	0.244402E 00	0.677853E 01
0.899999E 00	0.180000E 03	0.751164E-01	0.291063E 01
0.949999E 00	0.180000E 03	0.110690E 00	0.429767E 01
0.999999E 00	0.180000E 03	0.151281E 00	0.602840E 01
0.104999E 01	0.180000E 03	0.165588E 00	0.660135E 01
0.109999E 01	0.180000E 03	0.180529E 00	0.719956E 01
0.114999E 01	0.180000E 03	0.196098E 00	0.782291E 01
0.119999E 01	0.180000E 03	0.212294E 00	0.847126E 01
0.124999E 01	0.180000E 03	0.229113E 00	0.914449E 01
0.899999E 00	0.190000E 03	0.718354E-01	0.364504E 01
0.949999E 00	0.190000E 03	0.105737E 00	0.537929E 01
0.999999E 00	0.190000E 03	0.142487E 00	0.749636E 01
0.104999E 01	0.190000E 03	0.155924E 00	0.820795E 01
0.109999E 01	0.190000E 03	0.169957E 00	0.895094E 01
0.114999E 01	0.190000E 03	0.184582E 00	0.972516E 01
0.119999E 01	0.190000E 03	0.199796E 00	0.105304E 02
0.124999E 01	0.190000E 03	0.215596E 00	0.113666E 02
0.899999E 00	0.200000E 03	0.689328E-01	0.434859E 01
0.949999E 00	0.200000E 03	0.101349E 00	0.641429E 01
0.999999E 00	0.200000E 03	0.134666E 00	0.888138E 01
0.104999E 01	0.200000E 03	0.147328E 00	0.972339E 01
0.109999E 01	0.200000E 03	0.160553E 00	0.106025E 02
0.114999E 01	0.200000E 03	0.174336E 00	0.115187E 02
0.119999E 01	0.200000E 03	0.188676E 00	0.124717E 02
0.124999E 01	0.200000E 03	0.203569E 00	0.134613E 02
0.899999E 00	0.210000E 03	0.663559E-01	0.502478E 01
0.949999E 00	0.210000E 03	0.974472E-01	0.740790E 01
0.999999E 00	0.210000E 03	0.127674E 00	0.101924E 02
0.104999E 01	0.210000E 03	0.139642E 00	0.111575E 02
0.109999E 01	0.210000E 03	0.152141E 00	0.121653E 02
0.114999E 01	0.210000E 03	0.165171E 00	0.132154E 02
0.119999E 01	0.210000E 03	0.178727E 00	0.143078E 02
0.124999E 01	0.210000E 03	0.192807E 00	0.154422E 02
0.899999E 00	0.230000E 03	0.620538E-01	0.630704E 01
0.949999E 00	0.230000E 03	0.908808E-01	0.928858E 01
0.999999E 00	0.230000E 03	0.115763E 00	0.126225E 02
0.104999E 01	0.230000E 03	0.126532E 00	0.138146E 02
0.109999E 01	0.230000E 03	0.137784E 00	0.150595E 02
0.114999E 01	0.230000E 03	0.149514E 00	0.163568E 02
0.119999E 01	0.230000E 03	0.161721E 00	0.177064E 02
0.124999E 01	0.230000E 03	0.174403E 00	0.191080E 02

Table F-2 (contd.)

0.899999E 00	0.250000E 03	0.589898E-01	0.751501E 01
0.949999E 00	0.250000E 03	0.859337E-01	0.110537E 02
0.999999E 00	0.250000E 03	0.106312E 00	0.148391E 02
0.104999E 01	0.250000E 03	0.116060E 00	0.162362E 02
0.109999E 01	0.250000E 03	0.126249E 00	0.176953E 02
0.114999E 01	0.250000E 03	0.136876E 00	0.192160E 02
0.119999E 01	0.250000E 03	0.147939E 00	0.207980E 02
0.124999E 01	0.250000E 03	0.159435E 00	0.224411E 02
0.899999E 00	0.270000E 03	0.582671E-01	0.868170E 01
0.949999E 00	0.270000E 03	0.835085E-01	0.127422E 02
0.999999E 00	0.270000E 03	0.999110E-01	0.168949E 02
0.104999E 01	0.270000E 03	0.108664E 00	0.184771E 02
0.109999E 01	0.270000E 03	0.117827E 00	0.201298E 02
0.114999E 01	0.270000E 03	0.127397E 00	0.218526E 02
0.119999E 01	0.270000E 03	0.137372E 00	0.236451E 02
0.124999E 01	0.270000E 03	0.147750E 00	0.255070E 02
0.849999E 00	0.290000E 03	0.487437E-01	0.173423E 02
0.899999E 00	0.290000E 03	0.653403E-01	0.990179E 01
0.949999E 00	0.290000E 03	0.894987E-01	0.144571E 02
0.999999E 00	0.290000E 03	0.100198E 00	0.188816E 02
0.104999E 01	0.290000E 03	0.107709E 00	0.206275E 02
0.109999E 01	0.290000E 03	0.115617E 00	0.224519E 02
0.114999E 01	0.290000E 03	0.123920E 00	0.243543E 02
0.119999E 01	0.290000E 03	0.132614E 00	0.263345E 02
0.124999E 01	0.290000E 03	0.141699E 00	0.283919E 02
0.849999E 00	0.310000E 03	0.737007E-01	0.185131E 02
0.899999E 00	0.310000E 03	0.881148E-01	0.113974E 02
0.949999E 00	0.310000E 03	0.109472E 00	0.164165E 02
0.999999E 00	0.310000E 03	0.114162E 00	0.209919E 02
0.104999E 01	0.310000E 03	0.119275E 00	0.228671E 02
0.109999E 01	0.310000E 03	0.124806E 00	0.248296E 02
0.114999E 01	0.310000E 03	0.130752E 00	0.268766E 02
0.119999E 01	0.310000E 03	0.137108E 00	0.290101E 02
0.124999E 01	0.310000E 03	0.143871E 00	0.312287E 02
0.849999E 00	0.320000E 03	0.988622E-01	0.193567E 02
0.899999E 00	0.320000E 03	0.111191E 00	0.123850E 02
0.949999E 00	0.320000E 03	0.128493E 00	0.175979E 02
0.999999E 00	0.320000E 03	0.131017E 00	0.222104E 02
0.104999E 01	0.320000E 03	0.133999E 00	0.241267E 02
0.109999E 01	0.320000E 03	0.137435E 00	0.261340E 02
0.114999E 01	0.320000E 03	0.141318E 00	0.282316E 02
0.119999E 01	0.320000E 03	0.145643E 00	0.304191E 02
0.124999E 01	0.320000E 03	0.150405E 00	0.326960E 02
0.849999E 00	0.330000E 03	0.137967E 00	0.205877E 02
0.899999E 00	0.330000E 03	0.147078E 00	0.136638E 02
0.949999E 00	0.330000E 03	0.159280E 00	0.190258E 02
0.999999E 00	0.330000E 03	0.158552E 00	0.236478E 02
0.104999E 01	0.330000E 03	0.158346E 00	0.255790E 02
0.109999E 01	0.330000E 03	0.158655E 00	0.276061E 02
0.114999E 01	0.330000E 03	0.159469E 00	0.297282E 02
0.119999E 01	0.330000E 03	0.160782E 00	0.319469E 02
0.124999E 01	0.330000E 03	0.162585E 00	0.342556E 02
0.849999E 00	0.340000E 03	0.196901E 00	0.220776E 02
0.899999E 00	0.340000E 03	0.201148E 00	0.153871E 02
0.949999E 00	0.340000E 03	0.206694E 00	0.208395E 02
0.999999E 00	0.340000E 03	0.201142E 00	0.254315E 02
0.104999E 01	0.340000E 03	0.196214E 00	0.273387E 02
0.109999E 01	0.340000E 03	0.191900E 00	0.293472E 02
0.114999E 01	0.340000E 03	0.188186E 00	0.314563E 02
0.119999E 01	0.340000E 03	0.185062E 00	0.336653E 02
0.124999E 01	0.340000E 03	0.182516E 00	0.359736E 02
0.849999E 00	0.350000E 03	0.283291E 00	0.245409E 02
0.899999E 00	0.350000E 03	0.280353E 00	0.177703E 02
0.949999E 00	0.350000E 03	0.277022E 00	0.232355E 02
0.999999E 00	0.350000E 03	0.264430E 00	0.277394E 02
0.104999E 01	0.350000E 03	0.252621E 00	0.295650E 02
0.109999E 01	0.350000E 03	0.241576E 00	0.314987E 02
0.114999E 01	0.350000E 03	0.231277E 00	0.335397E 02
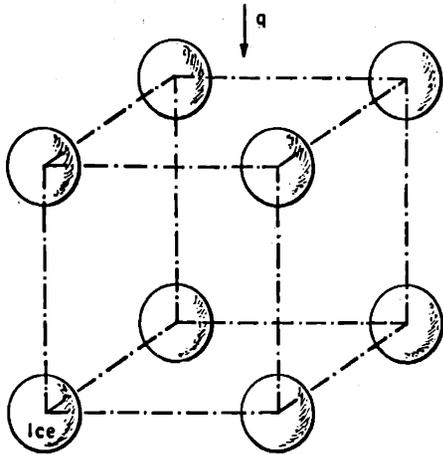
Figure F-1   Three Dimensional View of Structure Consisting
of a Simple Cubic Array of Non-Touching Ice Spheres
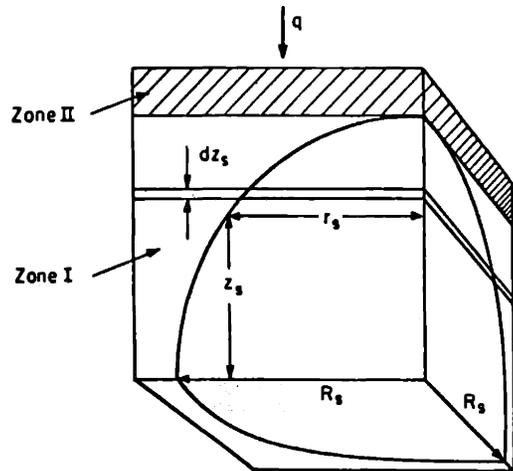
Figure F-2   Unit Cube of Heterogeneous Structure Consisting of
a Simple Cubic Array of Non-Touching Ice Spheres .
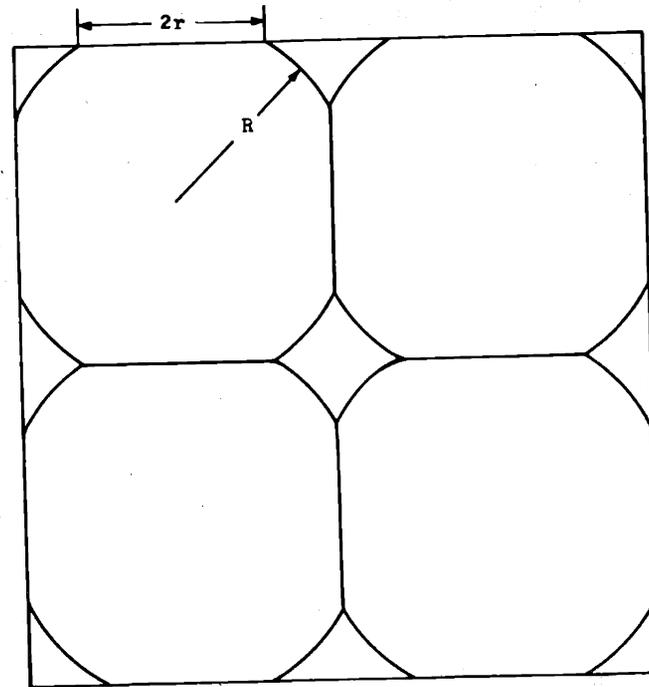
Figure F-3   Model for Riemann Equation

Appendix G

Empirical Correlations for Starting Values of Frost Density and Thickness

As discussed in Section II-A, the success of the predictions of the simple model depends on judicious choice of starting or initial values of frost density and thickness. One of the judicious choices for the starting values can be obtained from an empirical correlation between the experimentally measured average frost density, thickness and the independent system parameters at a certain time. In this appendix such a correlation is obtained from the experimental data of the present thesis at the time of forty minutes from the start of the frosting process.

The three important parameters which affect the starting values of frost density and thickness are believed to be humidity, gas temperature and heat (hence mass) transfer coefficient. Hence empirical correlations between starting values of frost density and frost thickness and these three parameters are obtained.

Since simple model applies only after a smooth layer of frost is formed (see Section II-A), it is difficult to pick a starting time which could be used for the wide range of experimental conditions. This is because the time for a smooth layer of frost is found to be dependent upon independent system parameters. For these reasons, in order to apply the empirical correlation the complete

range of experimental conditions studied in the present
thesis, it was obtained at forty minutes from the start
of frosting runs.

Method of Attack

The expirical correlations were obtained by assuming
polynomial relationships between frost density and frost
thickness and three independent system variables. Thus
it was assumed that

$$\rho_f = a \, h^{\alpha} \, T_g^{\beta} \, p_g^{\gamma} \tag{G-1}$$

and

$$\delta = b \, h^{\gamma} \, T_g^{\psi} \, p_g^{\xi} \tag{G-2}$$

where ρ_f = Frost density (gms/cc)

  h = Heat transfer coefficient (Btu/hr ft^2°F)

  T_g = Gas temperature (°R)

  p_g = Dew point of gas (°F)

  δ = Frost thickness (inches)

The constants in Equation G-1 and G-2 were obtained
from the experimental data as follows:

The polynomials α, β and γ were obtained from the
log-log plots of frost density versus heat transfer
coefficient (at constant T_g and p_g), versus gas temperature
(at constant h and p_g) and versus dew point of gas (at
constant h and T_g) respectively. The polynomials of
Equation G-2 γ, ψ and ξ were obtained similarly. Once all
the polynomials were calculated, the constants a and b
were obtained from the experimental data point of frost
density and thickness at known heat transfer coefficient,
gas temperature and humidity. The experimental results

used for the correlation are described in Tables G-1 to G-4. The following correlations were obtained by this method.

$$\rho_f = 1.930 \times 10^{-3} \, h^{0.933} \, T_g^{0.2062} \, p_g^{0.1511} \qquad (G-3)$$

and,

$$\delta = 6.21 \times 10^5 \, h^{-0.1231} \, T_g^{-2.878} \, p_g^{0.779} \qquad (G-4)$$

As shown in Tables G-1 to G-4, the ranges of independent variables used to obtain above mentioned were h varying from 5.60 Btu/hr ft^2°F to 10.8 Btu/hr ft^2°F, T_g varying from 494°R to 553°R and p_g varying from dew point of 14.3°F to dew point of 33.25°F.

It is the author's belief that the empirical correlations G-3 and G-4 should be applicable in predicting frost density and thickness values at forty minutes from the beginning of the frosting process for the system conditions outside the ranges considered above, if the criterion of smooth layer of frost is satisfied. It should also be noted that these correlations are independent of system's geometries as long as it is well defined such that heat and mass transfer coefficients can be obtained accurately.

A comparison between the experimental values and the values predicted from Equation G-3 and G-4 for various system conditions are shown in Table G-5.

Table G-1

Experimental data for Calculation of α and γ

$T_g = 533°R$; $p_g =$ dew point of 30°F

$h(\frac{Btu}{hr\ ft^2°F})$	$\rho_f(\frac{gms.}{cc.})$	δ(inches)
5.80	0.0582	0.135
7.20	0.0620	0.131
10.80	0.1030	0.125

Table G-2

Experimental data for Calculation of β and ψ

$h = 5.60\ \frac{Btu}{hr\ ft^2°F}$ $p_g =$ dew point at 27.16°F

$T_g(°R)$	$\rho_f(\frac{gms.}{cc.})$	δ(inches)
553°R	0.0620	0.058
494°R	0.0606	0.080

Table G-3

Experimental data for Calculation of γ and ξ

$h = 5.87\ \frac{Btu}{hr\ ft^2°F}$ $T_g = 508°R$

p_g(dew pt°F)	$\rho_f(\frac{gms.}{cc.})$	δ(inches)
33.25	0.0555	0.130
18.02	0.0523	0.0825

Table G-3 (Contd.)

$$h = 7.25 \frac{Btu}{hr\ ft^2\ ^\circ F} \quad T_g = 535\ ^\circ R$$

p_g(dew pt $^\circ$F)	$\rho_f \left(\frac{gms.}{cc.}\right)$	δ(inches)
30.4°F	0.0620	0.1310
14.3°F	0.0535	0.0750

Table G-4

Experimental data for Calculation of **a** and **b**

$h\left(\frac{Btu}{hr\ ft^2\ ^\circ F}\right)$	T_g($^\circ$R)	p_g(dew pt $^\circ$F)	$\rho_f\left(\frac{gms.}{cc.}\right)$	δ(inches)
10.80	530°R	29.84°F	0.1030	0.125

Table G-5

Experimental Data versus Values predicted from

Equations (G-3) and (G-4) for various

System Conditions

Re	T_g	Humidity (dew point) $^\circ$F	$\rho_{f\ exp}\left(\frac{gms.}{cc.}\right)$	$\rho_f\left(\frac{gms.}{cc.}\right)$ from Eq(G-3)	δ_{exp} (inch)	δ(inch) from Eq(G-4)
5,100	93°F	27.16	0.0620	0.0612	0.058	0.060
8,000	73°F	30.0	0.0620	0.0625	0.131	0.129
6,100	48°F	18.02	0.0523	0.0575	0.0825	0.0820

Appendix   H

Literature Survey on Homogeneous Nucleation from Vapor Phase

As seen in Section II, the transport of water in the colder region of the frost is possible only by the thermal diffusion of water or ice nuclei. Since homogeneous nucleation is expected to occur in the frost interior, the available literature on this phenomenon is reviewed in this appendix.

Numerous literature is available on the subject of homogeneous nucleation from vapor phase. The critical reviews of all the existing theories and the experimental facts about this process are given by Amelin (2) and Byers(21). Sander and Damkohler (93) and Hinckley et al. (3) have also given some discussion on the mathematical aspects of this process.

For the present purpose, the knowledge of nucleation rate and the critical size of a nuclei under a set of environmental conditions are of considerable significance. The critical nucleus size can be calculated from Kelvin's equation (60) shown below.

$$\ln\left(\frac{p}{P_{vp}}\right) = \frac{2\,\sigma\,M}{R\,T\,\rho\,r} \qquad \text{(H-1)}$$

All the nomenclatures of Equation H-1 are described in Appendix R.

Schaefer (100) calculated critical size of a nuclei from his experimental data and found that it was in good agreement with one computed from Equation H-1. These results are shown in Figure H-1.

The three significant theoretical relationships for
the calculation of the homogeneous nucleation rate are those
of Volmer's(112), Becker and Doring's (8) and Frankel's
(9,40,42). All these relationships were obtained from Gibbs
stability criteria for formation of a stable aggregate of
nuclei (embryo). The mathematical formulations of all the
three theoretical models were based on the same assumptions.
The final expressions, however, were arrived at with increasing
degree of sophistication in the mathematical derivation, in
the order of the investigation listed above.

The experimental results on nucleation rates (12,43)
have been found to be in better agreement with Becker and
Doring equation (8) and Frankel equation (42) than with
Volmer equation (112). A comparison between the predictions
of nucleation rate as a function of supersaturation ratio
and temperature obtained from Volmer and Becker-Doring
equations is shown in Figure H-4.

Since Becker-Doring equation has been proven to be
good with the help of experimental results (12,43), it is
used for the preliminary calculations described in Section
II-E. This equation is shown below.

$$\dot{N}_r = 10^{26} \frac{\alpha}{\rho} \left(\frac{p}{T}\right)^2 (M\sigma)^{1/2} e^{-A(1-3g^{-2/3}+2g^{-1})} \tag{H-2}$$

where,

$$g = \frac{35.2}{\ln^3 S} \left(\frac{M}{\rho}\right)^2 \left(\frac{\sigma}{T}\right)^3$$

and

$$A = \frac{17.6}{\ln^2 S} \left(\frac{M}{\rho}\right)^2 \left(\frac{\sigma}{T}\right)^3$$

All the nomenclatures of above equation are described
in Appendix R.

The experimental measurements of the homogeneous
nucleation rate have been found to be an extremely difficult
task. The major problems involved in the measurement are
the inaccuracy involved in the counting of the nuclei and
the difficulties in complete removal of dust or other foreign
particles from air. Most of the experimental studies are
carried out in Wilson's chamber (44,85,99,119) and in
sonic nozzles (73).

Wilson (119) and Powell(85) carried out some original
experimental investigations of the process of homogeneous
nucleation. Their results, however, were qualitative in
nature. Their experimental technique was elaborated and used
for achievement of quantitative data by the later investigators.
Volmer and Flood (111) checked Equation H-2 by determining
experimentally the value of p/P_{vp} at which the rate of
nucleation, $\dot{N}_t$, attained a value of 1 nuclei/cm^3 sec, and
obtained very good agreement between the theory and the
observation. The lowest system temperature they considered
was 261°K, and the nucleation rate at that temperature was
observed to be increased rapidly at supersaturation ratio
greater than 5. Schaefer (100) and Maybank and Mason (71)
later on carried out the measurements of homogeneous
nucleation rate at the system temperatures slightly lower
than that studied by Volmer and Flood (111). Both of them
arrived at the same conclusion that in clean air, crystals

formed by spontaneous condensation followed by homogeneous crystallization, appeared only when the supersaturation exceed 400% and the terminal temperature fell below $-40^{\circ}C$. There was discrepancy, however, in crystal concentration formed by both the investigators under these conditions. Maybank and Mason (71) reported nuclei concentration of $4.0 \times 10^{6}/cm^{3}$ as opposed to $10^{11}/cm^{3}$ found by Schaefer (100). They claimed that Schaefer's results were errneous because of maltechnique involved in their experimental measurements. The final results of these investigators are shown in Figures H-2 and H-3.

Sander and Damkohler (93), Rau (87) and Pound et al. (84) have also obtained quantitative measurements of nucleation rate at the system temperature as low as $-73^{\circ}C$. Pound et al. (84) suggested that because homogeneous nucleation of liquid water droplet at $-40^{\circ}C$ had been well established, the particles appearing between this temperature and $-65^{\circ}C$ were frozen spheres which had not developed crystalline faces. Sander and Damkohler (93) correlated their data for nucleation rate of 1 nuclei/cm^{3} sec in a following way.

above $-62^{\circ}C$ $\quad \ln \dfrac{p}{P_{vp}} = \dfrac{780}{T} - 1.521$ (with ions) (H-3)

above $-62^{\circ}C$ $\quad \ln \dfrac{p}{P_{vp}} = \dfrac{765}{T} - 1.537$ (without ions)(H-4)

below $-62^{\circ}C$ $\quad \ln \dfrac{p}{P_{vp}} = \dfrac{1.373}{T} - 3.748$ (with or without ions) (H-5)

Above empirical correlations are found to be in well agreement with Becker-Doring Equation H-2 for predicting supersaturation ratios (p/P_{vp}) and temperatures for nucleation rate of 1 nuclei/cm^3 sec.

At present, there are no quantitative experimental data available for nucleation rate at the temperatures below -73°C. Some observations, however, have been made regarding the nature of ice crystals formed at temperatures below -73°C. Mason (67) observed the mother of pearl clouds at temperature of about -80°C in the stratosphere. Blackman and Lisgarten (10) have described the structure of ice formed at temperatures below -73°C. Cwilong (29) has given a good qualitative description of the nature of ice cloud formed in the Wilson chamber at the temperatures as low as -120°C. He also concluded that at that low temperature, the nature of cloud formed would make the quantitative measurement of nucleation rate extremely difficult.
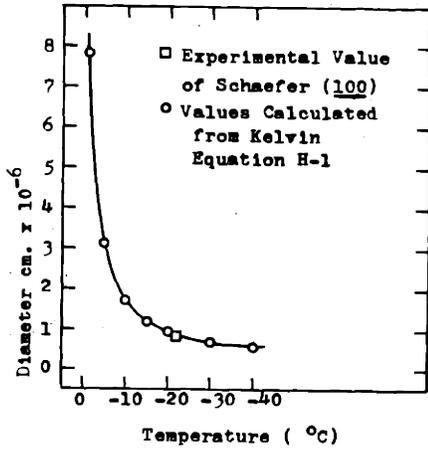
Figure H-1   The Relationship of Critical Size of
              Ice Nuclei to Temperature
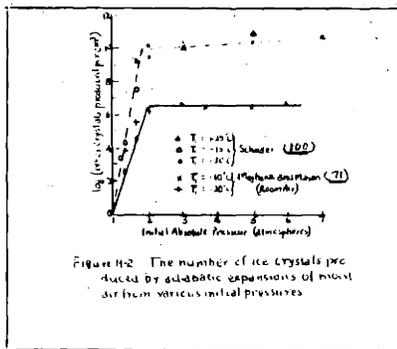
Figure H-2   The number of ice crystals pro-
              duced by adiabatic expansions of moist
              air from various initial pressures
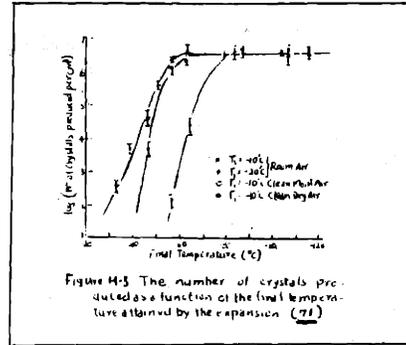
Figure H-3   The number of crystals pro-
             duced as a function of the final tempera-
             ture attained by the expansion (71)
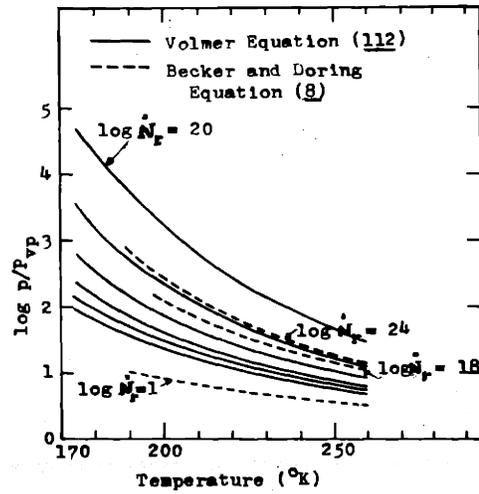
Figure H-4   Homogeneous Nucleation Rate as a
             Function of Supersaturation Ratio
             and Temperature

APPENDIX $\dot{J}$

Literature Survey on Non-Equilibrium Growth of an Ice
Crystal from Vapor Phase

Since frost densification is essentially a result of
growth of ice crystal network, in this appendix, a very
brief description of the available literature on the non-
equilibrium growth of an ice crystal is presented.

In the usual case, diffusion, degree of supersaturation,
kinetics of bonding and presence of impurities are the
factors which modify the crystal form and habit. Hence, in
order to obtain a theoretical model for the crystal growth
process, it is important to determine the factors which
control the growth under a given set of environmental
conditions.

The probability for presence of impurities in the ice
crystals of frost is highly remote. The ice crystal growth
from a stagnant vapor phase is expected to be controlled
by the rate of diffusion and heat conduction since molecular
diffusional processes in this environmental condition are
usually small in magnitudes. The calculations shown in
Section II-E describe one of the ways for determining the
controlling factors for crystal growth. The results of these
calculations indicate that most likely, the growth of ice
crystals from vapor phase in the present case would be
controlled by molecular diffusional mechanisms.

The first theoretical equation for the diffusion
controlled growth of a single crystal, which is at rest

relative to air and that the diffusion field around the crystal has achieved a steady state, was given by Jeffrey (56) as follows,

$$\frac{dm}{d\theta} = 4 \pi C D_B (\rho - \rho_s) \qquad (J-1)$$

Equation J-1 was later used by Houghton (53) to calculate the growth rate of crystal by a trial and error method based on a table of values of ρ_s against crystal surface temperature.

Mason (68) carried out first systematic mathematical approach to derive an analytical expression for $\frac{dm}{d\theta}$ in terms of parameters which, for a water saturated environment, are determined only by the temperature and by the geometry of the crystal. This significant contribution to the present subject can be briefly summarized as follows:

If it is assumed that the vapor pressure p_s in the viscinity of the crystal surface is the equilibrium vapor pressure with respect to ice at the surface temperature T_s of the crystal, i.e. $p_s = p_e(T_s)$, Equation J-1 can be written as,

$$\frac{p - p_e(T_s)}{p_e(T)} \simeq \frac{RT}{4 \pi D_B C p_e(T) M} \frac{dm}{d\theta} \qquad (J-2)$$

where, $p_e(T)$ is the saturation vapor pressure over a plane ice surface at the ambient temperature T, p is the ambient vapor pressure and M the molecular weight of ice.

While the crystal is growing, the surface temperature T_s

will be higher than that of the surrounding air. If it is
assumed that latent heat of sublimation ΔH is dispersed
solely by conduction through air, we have

$$\Delta H \frac{dm}{d\theta} = 4\pi C k_g (T_s - T) \qquad (J-3)$$

where, k_g is the thermal conductivity of air.
Now,

$$\frac{1}{p_e} \frac{dp_e}{dT} = \frac{\Delta H \, M}{R \, T^2} \qquad (\text{Clausius-Clapeyron}) \quad (J-4)$$

and integrating this equation from the crystal surface to
a boundary in the environment remote from the crystal gives

$$\ln \frac{p_e(T_s)}{p_e(T)} = \frac{\Delta HM}{R} \frac{(T_s - T)}{TT_s} \simeq \frac{\Delta HM(T_s - T)}{RT^2} \qquad (J-5)$$

From Equation J-3

$$\frac{p_e(T_s) - p_e(T)}{p_e(T)} = \exp\left(\frac{\Delta H^2 M}{4\pi C k_g RT^2} \frac{dm}{d\theta}\right) - 1 \qquad (J-6)$$

Adding Equations J-2 and J-6

$$\frac{p}{p_e(T)} = \exp\left(\frac{\Delta H^2 M}{4\pi C k_g RT^2} \frac{dm}{d\theta}\right) + \frac{RT}{4\pi C D_B p_e(T)M} \frac{dm}{d\theta} \qquad (J-7)$$

When the exponent in Equation J-7 is small compared
with unity, one may write

$$\frac{dm}{d\theta} = 4\pi C \sigma / \left(\frac{\Delta H^2 M}{k_g RT^2} + \frac{RT}{D_B M p_e(T)}\right) = 4\pi C \sigma / f(T) \quad (J-8)$$

where, $\sigma = (P/p_e(T)) - 1$ is the supersaturation of the
environment relative to ice and the term in the brackets

is a function of temperature only at constant air pressure.

Electrostatic capacity of crystal C, was calculated by Houghton (53), for several geometries. He treated a then hexagonal prism as a prolate spheroid of revolution of large accentricity and obtained (53) the following area terms.

For sphere $C = r$ $\qquad$ (J-9)

For circular disc $C = 2r/\pi$ $\qquad$ (J-10)

and for prolate spheroid $C = \dfrac{2ae}{\ln (1+e)/(1-e)}$ (J-11)

Where, accentricity $e = (1 - \dfrac{b^2}{a^2})^{\frac{1}{2}}$ and a and b are major and minor semi-axes respectively.

The Equation J-8 can be used to calculate growth rate of crystal as long as crystal retains its geometrical shape. In reality, however, it has been found that after the early stages of growth, the crystals generally loose their simple geometrical shapes and develop into dendritic structures. Equation J-8 could not be applied for the dendritic crystal growth.

The growth rate Equation J-7 has been found to agree with experimental results of Mason (68) and Houghton (53) only in the early stages of growth. In both the studies, the crystal developed into dendritic structure after a short duration. The criterion for this transition from polyhedral to dendritic growth has been derived by Mason (68).

The experimental studies of Mason (68) and Houghton (53) were carried out in the temperature range between

0°C to -30°C.   Mason (67) also reported experimental as
well as theoretical studies on growth rate of a spherical
droplet.   Schaefer (98) and Bradley (13) have also reported
some data on growth rate of a single ice crystal.   At
present, however, no experimental data available for growth
of an ice crystal from vapor phase below -30°C.

As yet, no systematic theoretical or experimental
studies of dendritic crystal growth have been carried out.
This phenomenon was, however, correctly interpreted by
Kossel (19,63) as to be due to the fact that the corners
of a growing crystal have a greater surface energy (because
of higher area to volume ratio) than the edges which, in
turn, have a greater energy than the faces of the crystal.
The greater area to volume ratio provides more heat conduction
to the surrounding vapor, and makes the dissipation of the
heat of crystallization take place at a smaller difference
in temperature between the crystal surface and the vapor
phase, giving the corners and edges a higher effective
supersaturation than the faces of the crystal.   The higher
effective supersaturation brings on an increase in the
growth rate at these locations, thus perpetrating and
intensifying the effect.   The mathematical study of this
perpetrating and intensifying effect is an extremely
difficult task.

APPENDIX   K

Literature Survey on Thermal Diffusion of Solid Particles
in Stagnant Gas

A radiometric or thermal force is defined as a force on a body suspended in gas which is not in thermal equilibrium. The movement or diffusion of this suspended body by thermal force is called the process of thermal diffusion.

The strong possibility for an existence of fog or ice nuclei (see Section II-C) along with the existence of a large temperature gradient (see Section IV) in the frost interior suggests the occurrence of process of thermal diffusion of aerosols in gas within the frost.   For the same thermal force, the mass transport of a material by this process, as reported by Mason (69), could be as high as 10^6 times that due to thermal diffusion of the same material in the gaseous phase.

In trying to seek an explanation for the phenomenon of uniform densification of frost, one must find a mechanism by which frost at extremely low temperature densifies with time.   Since at that low temperature one would expect that appreciable water vapor could not exist before nucleation takes place, the crystal growth from the vapor phase may not be a sufficiently rapid process. Under this situation, in the colder region of the frost, densification could occur only if water vapor is transported there in an other phase.   Since both nucleation and thermal diffusion of fog or ice nuclei in

gas are highly conceivable processes occurring in the
frost interior, it is possible that thermal diffusion
of nucleated fog or ice particles could transport water
vapor in the colder region of the frost.   It is for these
reasons, that thermal diffusion of aerosols in gas may be
a very significant phenomenon in interpreting and clarifying
results.   The available literature on both theories as
well as some pertinent experimental facts are outlined below.

Poppoff (83) showed that the thermal force is not
appreciable for particle greater than 10 microns in diameter.
In fact, the efficiency with which particles can be
separated from a gas by thermal diffusion have been found
to decrease rapidly when particle radius exceeds 2 microns
(46).   Hence this literature on thermal diffusion can
be meaningfully applied only to particles with a diameter
of less than 4 microns.   Since the size of ice nuclei
is always smaller than this, the literature information
would be meaningfully applied to the present purpose.

Theoretical treatments to the subject have been carried
out by several investigators.   Since the guide lines for
the development of the theoretical equations depended upon
the flow regimes (i.e. on the value of ratio λ/r_p; where
λ is mean free bath and r_p is particle radius) the
discussion of the process will be separated on that basis.

Although Tyndall(110), Rayleigh(88), Aitken (1) and
Lodge and Clark (66) first conceived and performed some
early pioneering experiments for the understanding of

movement of aerosols under the effect of thermal force.

The first significant theoretical treatment to the thermal

diffusion phenomenon in the free molecular regime ($\frac{\lambda}{r_p} \gg 1.0$)

was given by Cawood (22).

Considering a cylinder of gas, of length about twice
the mean free path of the gas, whose axis is perpendicular
to a hot surface and radius of the magnitude of the mean
free path of the gas, being situated in a temperature
gradient, dT/dx, Cawood concluded that a particle inside
this cylinder would experience bombardment due to the
motion of gas molecules parallel to the axis of the
cylinder but would experience no net lateral bombardment.

The net energy flow through the cylinder is given by

$$E=1/6(N_2 V_{g2}) \, (\pi r_p^2) \, (\tfrac{1}{2}mV_{g2}^2) -1/6 \, (N_1 V_{g1}) \, (\pi r_p^2) \, (\tfrac{1}{2}mV_{g1}^2)$$

$$\text{(K-1)}$$

Where subscripts 1 and 2 refer to temperature
conditions T_1 and T_2, $T_2 > T_1$. The flux of molecules
in one direction is equal to that in the opposite
direction so that $N_1 V_{g1} = N_2 V_{g2}$. Replacing $\tfrac{1}{2} mV_{g1}^2$ with
$3/2 \left(\dfrac{RT_1}{N_o}\right)$ Equation K-1 simplifies to

$$E = -\tfrac{1}{2}(N_1 R/N_o) \, (\pi r_p^2 V_{g2}) \, (\lambda \, dT \, dx) \qquad \text{(K-2)}$$

The net force acting on a particle can now be found
by dividing the net energy flow per unit time by the average
velocity of the gas molecules whereby

$$F_t = E/V_g = -\tfrac{1}{2} \, (N_1 R/N_o) \, (\pi r_p^2) \, (\lambda \, dT/dx) \qquad \text{(K-3)}$$

It is assumed here that $V_g = \dfrac{V_{g1}+V_{g2}}{2}$ is very nearly

V_{g1}.   Replacing NR/N_0 by p/T Equation (K-3) then becomes

$$F_t = -\tfrac{1}{2} (\pi \gamma_p^2) (p\lambda/T) \, dT/dx \tag{K-4}$$

which is Cawood's equation in the final form.

The values of thermal forces given by Cawood's equation were within an order of magnitude of those found by experiments.

The elementary treatment of Cawood (22) was later improved by Derjaguin, Bakanov (35) and by Waldmenn(113). The improved theory starts from the basic statement that the velocity distribution of incoming gas molecules, as they approach a suspended particle, is not appreciably changed by the presence of the particle. The Chapman-Enskog velocity distribution function for a gas with an imposed temperature gradient is used to describe the incoming gas molecules. The rebounding molecules are considered to have a velocity distribution made up in part by a fraction of molecules specularly reflected and in part by those molecules which leave the particle surface after having reached equilibrium with it. The expression for thermal force in this case is given by:

$$F_t = \frac{-32 r_p^2 K}{15 V_g} \qquad \frac{dT}{dx} \tag{K-5}$$

This equation can be shown to have the same form as Cawood's equation but to contain a different numerical coefficient by making the following substitutions for the monoatomic gases.

$$K = \frac{15}{4} \frac{k\eta}{m_g} \; , \quad \eta = 6Nm_g v_g \lambda \quad k=R/N_o \text{ and } pT= Rn/V \qquad (K\text{-}6)$$

Thus, assuming ideal gas behavior, equation K-6 becomes

$$F_t = \frac{-32 r_p^2 K}{15 v_g} \frac{dT}{dx} = -4 r_p^2 \; (p\lambda/T) \frac{dT}{dx} \qquad (K\text{-}7)$$

The thermopheretic velocity in this regime is given by,

$$V_t = \frac{15\pi}{14\psi} \left(\frac{v_g \lambda}{T}\right) \frac{dT}{dx} \qquad (K\text{-}8)$$

where is dependent upon the nature of the gas particle interaction. The velocity, V_t, does not depend on the size of the particle at all, and only to a small degree on their nature through ψ .

For slip region ($\lambda/r_p \ll 1.0$), when the size of a particle becomes large compared to the mean free path, the molecule particle interaction changes; the molecule no longer sees the particle as another molecule, but sees the particle as a solid surface. Hence a different approach must be taken to define the thermal force. Epstein (95) was the first to solve this problem analytically. He considered both the kinetic and hydrodynamic aspects of gas flow around a spherical particle and took into account the fact that the behavior of the particle in the gas would depend on the ratio of heat transported through the interior of the particle to the heat received on the surface from molecular impacts. Therefore, the thermal conductivities of the gas and the immersed material should come into the derivation of the thermal stress. Three basic assumptions were made:

1. $\lambda/r_p \ll 1.0$

2. A uniform temperature distribution exists in the gas

at a great distance from the particle.

3. Convective heat transfer to the particle is negligible compared to heat transfer by conduction.

He then broke down the problem into two phases of hydrodynamics and conduction which were treated independently initially and later combined through the concept of the thermal creep. Epstein's procedure may be summarized as follows:

Heat conduction probles was solved to obtain the temperature gradient over the surface of the sphere. Using the thermal creep velocity, defined by Maxwell (70), as a boundary condition, the Navier-Stokes equations were solved. By intergrating over the entire surface, the total force on the particle was obtained. The thermal force was then calculated as a component of the total force parallel to the direction of the temperature gradient. Epstein's final equation for the thermal force is given by

$$F_t = (-9\pi)\ (r_p)\ (\eta^2/\rho T)\ \left(\frac{k_g}{2k_g + k_p}\right)\frac{dT}{dx} \qquad (K-9)$$

Numerous experimental investigations have been carried out which can test Epstein's equation. The data of Rosenblatt and Lamer (91) showed satisfactory agreement with the theory considering the assumptions used in its development. Additional support for the theory was given by the work of Saxon and Rans (95). However, results obtained by Schadt and Cadle (96,97) cast some doubt on the Epstein theory particularly for aerosole particles

of high thermal conductivity. Equation K-9 shows, when k_p becomes large the thermal force tends to zero. Yet Schadt and Cadle found no such tendency in their experimental observations while using particles where thermal conductivity ranged from 1.45×10^{-2} Btu/hr ft°F to 39.4 Btu/hr ft°R. In fact, the thermal force on iron and sodium chloride particles was from twenty to thirty times greater than those predicted by Equation K-9.

Brock (15,16), has been able to account for these differences by resolving the steady state Navier-Stokes equation subject to two corrections of the Epstein theory. 1. Boundary conditions more suitable for the step flow regime were used and 2. the continuous energy equation has been solved taking into account convective terms. Brock's equation which is applicable into the slip flow regime ($\lambda/r_p \ll 1.0$) for thermal diffusive force of particles in air has the form

$$F_t = (-9\pi)(r_p)\left(\frac{\eta^2}{\varrho T}\right)\left(\frac{1}{1+6\lambda/r_p}\right)\left(\frac{\frac{k_g}{k_p}+\frac{15}{4}\lambda/r_p}{\left(\frac{1+2k_g}{k_p}+\frac{15}{2}\frac{\lambda}{r_p}\right)}\right)\frac{dT}{dx} \quad \text{(K-10)}$$

Where λ is calculated from Equation D-24 as follows,

$$\eta = 0.499\,\varrho\,\bar{v}\lambda \qquad\qquad \text{(K-11)}$$

All the nomenclatures in Equations K-10 and K-11 are described in Appendix R.

On the basis of coefficients obtained by these equations, the thermal force as calculated by Equation K-10 has been shown in good agreement with the thermal force found for liquid aerosols by Jacobsen and Brock (55).

A completely different approach to defining
thermophoresis of large particles has been taken by
Derjagiun and Bakanov (35). Their calculations give a
thermal slip coefficient which is 35 times smaller then
that obtained by Maxwell (70), the latter being the basis
of boundary conditions used by Epstein and Brock.
Derjagiun and Bakanov use the Chapman-Enskog method of
solving the kinetic equation which make possible the
calculation of the isothermal heat transfer in a gas stream
when the space derivatives of the velocity gradient are
not equal to zero. This approach introduces a new turn
into the boundary condition for the component of the heat
flux normal to the surface. Their result for the
thermophoretic force is,

$$F_t = (-) \ \frac{3\pi\eta^2 r_p}{\rho T} \ \frac{(8k_g + k_p)}{(2k_g + k_p)} \ \frac{dT}{dx} \qquad \text{(K-12)}$$

More recently Derjaguin and Yalamov (37) have taken the
temperature jump into account with the result

$$F_t = (-) \ \frac{3\pi\eta^2 r_p}{\rho T} \ \frac{(8k_g + k_p + 2C_t \lambda/r_p k_p)}{(2k_g + k_p + 2C_t \lambda/r_p k_p)} \ \frac{dT}{dx} \qquad \text{(K-13)}$$

This equation, valid only for large particles, gives
results to within 20% of experimental (36). But the
theory infers that the thermal velocity is size independant
which does not agree with the data of Rosenblatt and Lamer
(91) or the results of this work.

Due to the complexity of the problem, no work has
been done to define the thermal force when the size of the

particle becomes comparable to the mean free path ($\frac{\lambda}{r_p} = 1.0$, the transition region) until recently. Brock (17) is the first to give a description of the mechanism in this regime. In principle, the approach is similar to that of the free molecular regime, that is, the calculation is based on momentum transfer between the gas molecule and the suspended particle. The important difference has to do with velocity distribution of the incoming and outgoing gas molecules. The qualitative description of Brock's first attempt is given in Reference 17.

APPENDIX   L

Heat and Mass Transfer Analysis of the Forced Flow in a

Smooth Pipe

As seen in Section II, a quantitative theoretical analysis of the frosting process requires an accurate knowledge of heat and mass transfer characteristics of the system. This appendix briefly describes the applicability of various theoretical analysis for the evaluation of the heat and mass transfer characteristics of the frosting system of the present research. The theoretical studies are carried out both in laminar and turbulent flow regimes.

A.   Heat Transfer Characteristics of the Forced Flow in a

Smooth Pipe

In the frosting system of the present research, a long calming section was used to obtain a fully developed velocity profile in gas before it passed over the heat transfer section of the duct. Also, the measurements of heat flux through the frost were carried out in the thermal entrance region (where thermal boundary layer is being developed). Hence, for the present purpose, heat transfer characteristics of a fully developed flow through a duct (or pipe) in thermal entrance region are of significance. The boundary condition of constant wall temperature is assumed to be valid one for theoretical predictions. Since the flow is usually divided into the turbulent, laminar and transition regimes, the following discussion of forced convection heat transfer is also separated on that basis.

1. Turbulent Heat Transfer

The turbulent heat transfer analysis for a fully developed flow through a smooth pipe (see Figure L-1) can be theoretically studied with the help of the basic energy Equation L-1 and boundary conditions Equations L-2 to L-4 as described below.

$$u \frac{\partial T}{\partial x} = \frac{1}{r} \frac{\partial}{\partial r} \left[r \left(\frac{\nu}{Pr} + \epsilon_H \right) \frac{\partial T}{\partial r} \right] \qquad (L-1)$$
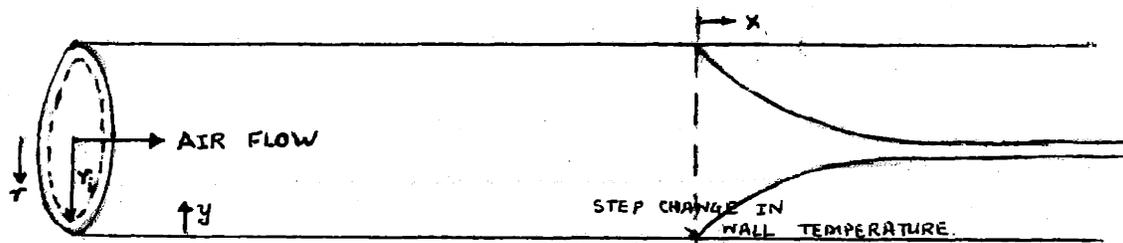
Figure L-1   Schematic of Heat Transfer Process for a

Fully Developed Forced Flow through a Smooth

Pipe

Boundary Conditions

$$T(x,r) = T_o \quad ; \qquad x < 0 \qquad\qquad (L-2)$$

$$T(x,r_o) = T_w \quad ; \qquad x > 0 \qquad\qquad (L-3)$$

$$T(0,r_o) = T_o \quad ; \qquad r \neq r_o \qquad\qquad (L-4)$$

All the nomenclatures of Equations L-1 to L-4 are described in Appendix R.

The system satisfying the Equation L-1 is subjected to the following restrictions.

1. Fluid properties are constant.

2. Mean velocity in axial direction is independent of angular position.

3. Mean radial velocity is zero.

4. Mean temperature at any radius does not vary with time

or angular position.

5.   Frictional dissipation of energy is negligible.

6.   Axial diffusion is negligible with respect to bulk transport in the x-direction.

Several attempts have been made to obtain a mathematical solution of Equation L-1 with varying degree of sophistication. First, Latzko ($\underline{64}$) obtained an approximate solution of Equation L-1 for Pr = 1.0. His final result for heat transfer coefficient is as follows:

$$h(x) = h_\infty \left(1 + 0.1\, e^{\frac{-2.7x}{Re^{.25} D_H}} + 0.90\, e^{\frac{-29.27x}{Re^{.25} D_H}} - 0.023\, e^{\frac{-31.96x}{Re^{.25} D_H}} \right) \quad \text{(L-5)}$$

where,

$$h_\infty = \frac{0.0384\, G\, c_p}{Re^{0.25}} \quad \text{(L-6)}$$

All the nomenclatures of Equations L-5 and L-6 are described in Appendix R.

Deissler ($\underline{31},\underline{32},\underline{33}$) and Sleicher and Tribus ($\underline{105},\underline{106}$), later on, carried out sophisticated mathematical analysis of Equation L-1. The main difference in their solutions lies in the estimation of ϵ_H.

Deissler ($\underline{31},\underline{32}$) used experimentally determined velocity and concentration distribution to obtain the following correlations for ϵ_M. He, then, assumed $\epsilon_H = \epsilon_M$.

Near cold wall,

for $y^+ < 26$

$$\epsilon_M = n^2 uy \left(1 - e^{-(n^2 uy/(\mu/\rho))}\right) \tag{L-7}$$

where, $y^+ = y \left(g_c \tau_o / \rho \right)^{1/2} / \nu$

for $y^+ > 26$

$$\epsilon_M = k^2 \frac{(du/dy)^3}{(d^2u/dy^2)^2} \tag{L-8}$$

The values of the constants $n=0.124$ and $k =0.36$ in above equations were obtained from the mass transfer experiments in turbulent flow through pipe.

Sleicher and Tribus (105,106) measured not only the velocity distribution but also the temperature distribution in pipe to calculate ϵ_H. They found that the ratio of ϵ_H and ϵ_M was 1.4 instead of unity as assumed by Deissler (31,32). The results of Sleicher and Tribus (105,106) for agree well with ones obtained by Corcoran et al. (27). Their final result for heat transfer coefficient in thermal entrance region can be given by the following mathematical equation (105,106).

$$Nu(x) = \frac{h(x) D_H}{k} = \frac{\sum_{n=0}^{\infty} A_n \exp(-\lambda_n^2 X_*)}{2 \sum_{n=0}^{\infty} (A_n/\lambda_n^2) \exp(-\lambda_n^2 X_*)} \tag{L-9}$$

where,

$$X_* = 2 x /Re \, Pr \, D_H$$

The constants A_n and λ_n are dependent on the Reynolds and Prandtl numbers. Their values are reported in Reference 105. The heat transfer coefficients calculated from Equation L-9 have been found to agree with the experimental data of Boelter (11).

In order to evaluate the applicability of each of
the above described method for the present purpose, the heat
transfer coefficient at the centre of the test section under
a set of system conditions are calculated using Equations
L-5 and L-9 and Figures 6 and 8 of Reference 32. These values
are then compared with the experimental one. The final results
of these calculations are summarized below.

For <u>system conditions</u>:

Reynolds number = 6,100

Humidity = dew point at 14.3°F

Gas Temperature = 48°F

x = 2.77 inches

D_H = 0.8 inch

Method	h (Btu/hr ft^2 °F)
Latzko	4.24
Deissler	5.61
Sleicher-Tribus	5.95
Experimental(frosting)	6.92

From the above described results it can be concluded
that, as expected, Latzko method (64) predicts too low heat
transfer coefficient compare to the experimental value.
Both Sleicher-Tribus method (105) and Deissler method (32)
predict almost identical values of heat transfer coefficient.
These values are also in good agreement with the experimental
one. Since Sleicher-Tribus (105) uses the experimentally
measured values of ϵ_H in solution of Equation L-1, their

theoretical analysis is believed to be more realistic than that of Deissler (31,32). Hence, it is used for the purpose of a comparison between theoretical and experimental values of the heat transfer coefficients in the frosting experiments.

It should be noted that in the present research, the heat transfer coefficients were also measured under non-frosting conditions (see Section IV-D). These results were found to be in very good agreement with the predictions of Sleicher-Tribus Equation L-9.

2. Laminar Heat Transfer

Although, no frosting experiments were carried out to obtain the properties of frost deposited from the gas in laminar flow regime, It is believed that the theoretical models for the frosting process are valid in this flow regime. Thus, the application of the theoretical models in the laminar flow regime also demands the accurate knowledge of heat transfer coefficient.

Heat transfer characteristics of a laminar flow through a pipe or a duct are well studied by Graetz (61). Graetz solution for the heat transfer coefficient, however, can not be used when Reynolds number is less than about 130 (101) because axial conduction then becomes significantly important. Graetz solution, of course, does not take into account the effect of axial (or back) conduction on the heat transfer coefficient. Schneider (101) has solved the problem of heat transfer in laminar flow (with flat velocity profile) when back conduction is important. The problem of heat

transfer in laminar flow, both with or without back

conduction and for both flat and parabolic velocity profiles

is solved by the author and co-workers (103). The effects

of back conduction and of velocity profile on the laminar

heat transfer characteristics in a rectangular duct are

described in Figures L-2 and L-3 respectively for two

different Reynolds numbers of air. As shown in Figure

L-2 the back conduction at very low Reynolds number causes

the heat transfer coefficient to attain a finite value at

the entrance of the heat transfer regime. It should be

noted that in the absence of back conduction heat transfer

coefficient is infinity at the entrance of the heat

transfer regime. The thermal boundary layer thickness (at

any downstream distance) is higher hence heat transfer

coefficient is lower in case of laminar flow with parabolic

velocity profile than ones in case of flat velocity profile

laminar flow as shown in Figure L-3.

3. Heat Transfer in Transition Flow

The theoretical analysis of heat transfer in transition

flow regime is quite difficult. Usually, the correlation for

heat transfer coefficient in transition flow regime is

obtained by interpolating between the correlations for

laminar and turbulent flow regimes.

B. Mass Transfer Analysis of the Forced Flow in a Rectangular

Duct

The process of frosting occurs with simultaneious

transfer of heat and mass. Hence, the mass transfer

characteristics of the frosting process can be studied
with the help of heat transfer analysis of the process
and using an analogy between heat and mass transfer.

Two simple analogies between heat and mass transfer
are those of Lewis (39) and of Chilton and Colburn (104).
The experimental data of Coles (26) and Chung (24) for the
studies of heat and mass transfer analogies have been
found to agree well with Lewis relation (39,72). Hence,
for the present purpose of evaluating the mass transfer
characteristics of the frosting process, Lewis relation is
used.

<u>Lewis Relation for Simultaneous Heat and Mass Transfer</u>

The Lewis relation for simultaneous heat and mass
transfer can be used in all the flow regimes (turbulent,
transition and laminar). For small vapor concentration
it can be writted as (39)

$$j_D = j_H \qquad\qquad (L-10)$$

$$\frac{h}{K_g} = \rho c_P \, (Sc/Pr)^{2/3} \qquad (L-11)$$

or,
$$\frac{h}{K_g} = \rho c_P \, Le^{\,2/3} \qquad (L-12)$$

Thus, the mass transfer coefficient in the frosting
process can be calculated from Equation L-12 with the
knowledge of h (heat transfer coefficient) and gas
properties.
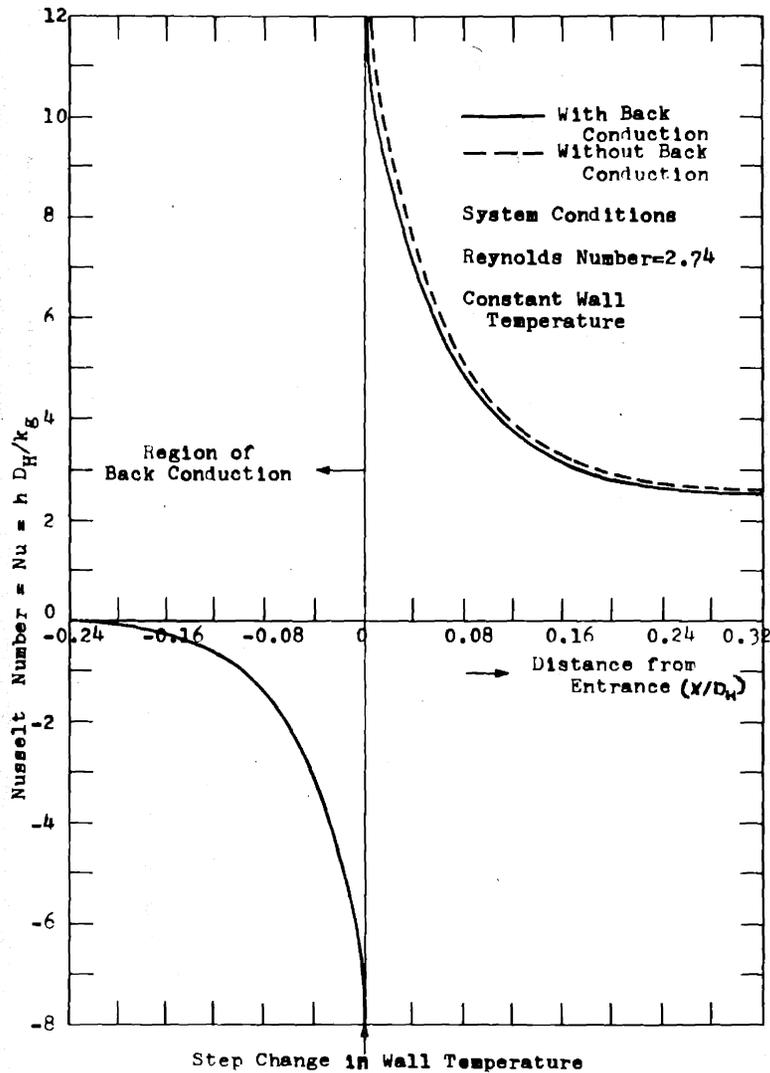
Figure L-2 Effect of Back Conduction on Heat Transfer
            Coefficient for Plug Flow of Air in a
            Rectangular Duct (103)
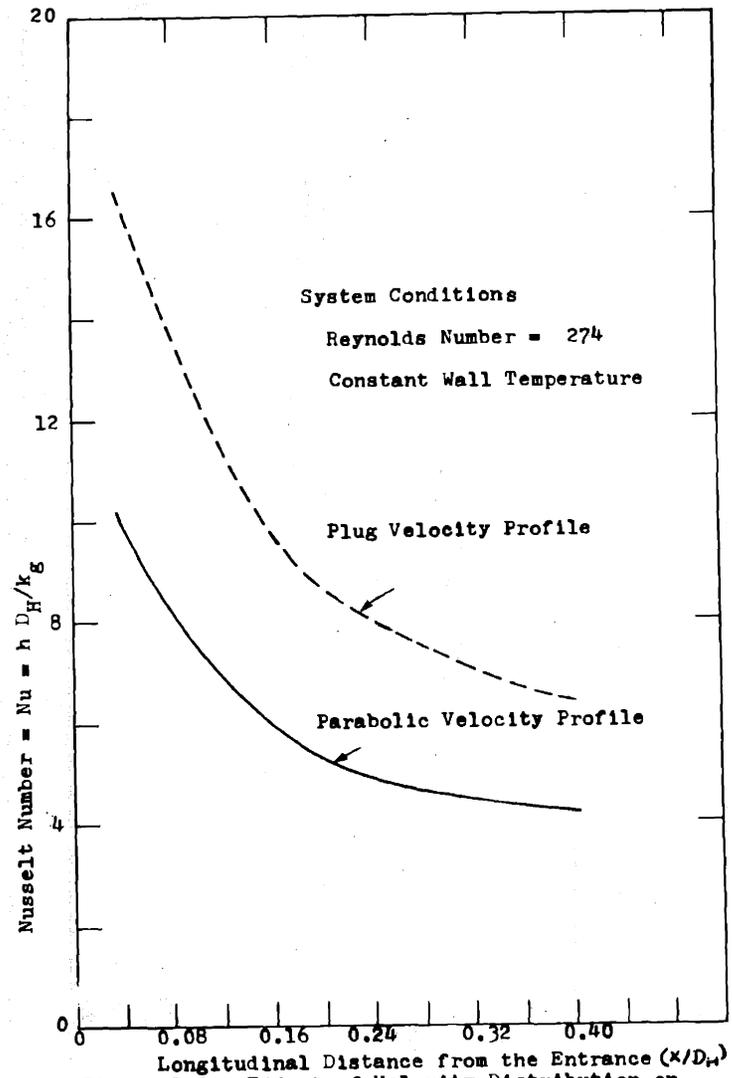
Figure L-3 Effect of Velocity Distribution on
            Convection Heat Transfer coefficient for
            Laminar Flow of Air in a Duct (103)

APPENDIX N

Sample Calculations and Error Analysis

1.   Average Frost Density

All the frost density values reported in this thesis are actually indirectly measured quantities, since they were calculated from the measured weight of the collected frost samples and the correspondingly measured sample thicknesses.   A sample calculation for the frost density is described below.

For Run number 30, at time of 104.36 minutes from the start.

Mass of the frost collected by 0.866 cm^2 cross section (inside), cylindrical, hollow glass vial = .0372 gms.

Thickness of the frost = 0.225 inch (as measured by depth micrometer)

Density of the frost = $\dfrac{.0372}{0.866 \times 2.54 \times .225}$

=   0.0751 gms./cc.

The error in the density measurement is related to the errors involved in weighing the frost sample and in measuring the frost thickness.   The error in the density measurement, $\Delta \rho_f$, can be estimated from Equation N-1 (74) shown below.

$$\Delta \rho_f = \frac{\partial \rho_f}{\partial m_{f,v}} \Delta m_{f,v} + \frac{\partial \rho_f}{\partial A_v} \Delta A_v + \frac{\partial \rho_f}{\partial \delta} \Delta \delta \qquad (N\text{-}1)$$

since $\rho_f = m_{f,v}/A_v$, Equation N-1 reduces to

$$\Delta \rho_f = \frac{1}{A_v \delta} \Delta m_{f,v} - \frac{m_{f,v}}{\delta} \frac{1}{A_v^2} \Delta A_v - \frac{m_{f,v}}{A_v \delta^2} \Delta \delta \qquad (N\text{-}3)$$

It was estimated that in general the weight of the
collected frost sample could be determined to the nearest
0.002 gms. This limitation on the accuracy was due to loss
of material during the collection process. In the
measurements of density gradient in the frost interior (the
results described in Section 1V-C), the weight of the
frost slice could be determined to the nearest 0.003 gms.
because of additional error involved during the slicing.
It was also estimated that the frost thickness could be
measured accurately to the nearest 0.005 inch (or 0.0127 cm).
The primary cause of error in this measurement is the
difficulty involved in determining the actual location of
the frost surface.

The diameter of the vial used to collect the frost
sample could be estimated to the nearest 0.002 inches
(0.00508 cm). From Equation N-4 shown below

$$\Delta A_v \quad = \quad \frac{D_v \pi}{2} \quad \Delta D_v \qquad\qquad (N-4)$$

it was calculated that this uncertainty in the diameter
implied and error of 0.00836 cm^2 in the vial cross sectional
area. Thus, from the preceding discussion, the values
of ΔA_v, $\Delta m_{f,v}$ and $\Delta \delta$ chosen for this calculation were

$$\Delta A_v \quad = \quad 0.00836 \text{ cm.}^2$$

$$\Delta m_{f,v} = \quad 0.002 \text{ gms.}$$

and $\quad \Delta \delta \quad = \quad 0.0127 \text{ cm.}$

It should be noted that these error values are applicable
to all the frosting experiments.

Substituting in Equation N-3 the values of ΔA_v, $\Delta m_{f,v}$ and $\Delta\delta$ listed above, and the values of A_v, $m_{f,v}$ and δ shown earlier, $\Delta\rho_f$ was found to be 0.00644. Since ρ_f for Run 30 is equal to 0.0751 gms./cc., the <u>maximum</u> percentage error in density measurement is $\dfrac{0.00644}{0.0751}$ x 100 % or $\pm$ 8.57%

In the density gradient measurement, where $\Delta m_{f,v}$ =0.003 gms., the maximum percentage error for a typical experiment can be calculated as follows.

For Run number 37, the mass of the bottom 0.0625 inch thick frost = 0.01468 $(=m_{f,v})$, A_v= 0.714 cm^2

Thus, $\rho_f = \dfrac{0.01468}{2.54 \times 0.0625 \times 0.714}$ = 0.1295 gms./cc.

Since, once again,

ΔA_v = 0.00836 cm^2

$\Delta m_{f,v}$ = 0.001 gms.(since 0.003 gms for three slices)

and $\Delta\delta$ = 0.0042 cm.

Thus, the maximum percentage error in this kind of measurement is calculated as follow,

$\Delta\rho_f$ = .01582

maximum % error = $\dfrac{.01582}{.1295}$ x100 % or $\pm$12.22%

It should be noted that the calculation of error by Equation N-3 does not allow for compensating errors. The true magnitude of the errors (maximum) are most certainly lower than the ones calculated above.

2. <u>Thermal Conductivities</u>

A. <u>Average Frost Layer Conductivity</u>

The average frost layer thermal conductivity was calculated from Equation N-5 shown below.

$$q = \frac{k_{avg}}{\delta} \left(T_s - T_w \right) \qquad (N-5)$$

From the experimental measurements of q, T_s, T_w and k_{avg} for a typical set of experimental conditions can be calculated as follows.

For Run number 16,

q = 539 Btu/hr ft^2 (quasi-steady state value)

T_s= 15°F (value in the quasi-steady state of heat flux)

T_w= -315°F

δ = 0.1875 inch

hence,

$$k_{avg} = \frac{539 \times 0.1875 \times 1}{330 \times 12} \qquad = 0.02784 \text{ Btu/hr ft°F}$$

The method if determining the error in the conductivity measurement is essentially the same as that used for determining $\Delta \rho_f$.

The error in the conductivity measurement is given by

$$\Delta k_{avg} = \frac{\partial k_{avg}}{\partial \delta} \Delta \delta + \frac{\partial k_{avg}}{\partial Q} \Delta Q + \frac{\partial k_{avg}}{\partial A} \Delta A$$
$$+ \frac{\partial k_{avg}}{\partial T_s} \Delta T_s + \frac{\partial k_{avg}}{\partial T_w} \Delta T_w \qquad (N-6)$$

where, Q/A = q

The combination of Equations N-5 and N-6 yields Equation N-7 shown below.

$$\Delta k_{avg} = \frac{Q \Delta \delta}{A(T_s - T_w)} + \frac{\delta}{A(T_s - T_w)} \Delta Q + \frac{\delta Q}{A^2(T_s - T_w)} \Delta A$$
$$+ (\Delta T_s + \Delta T_w) \frac{\delta Q}{A(T_s - T_w)^2} \qquad (N-7)$$

The signs of all terms have been taken as positive as was done in estimating Δq_f.

Due to thermocouple error, the plate temperature could only be measured to about the nearest $2^\circ F$. The measurement of surface temperature, on the other hand, may involve an error as large as $5^\circ F$. The reasons for an error of such magnitude have been previously discussed in section II-A and in Appendix A.

Based on the calorimeter calibration results, it was estimated that the maximum error in the heat flux measurement was 0.4 Btu/hr. In addition, the uncertainty with which the area of the heat transfer test section is known is about 0.0001228 ft^2. This value of ΔA was obtained from Equation N-8 using a value of ΔD equal to 0.000416 ft (i.e., 0.005 inches).

$$\Delta A = \frac{D\pi}{2} \Delta D \qquad\qquad (N-8)$$

The diameter of the inner copper plate was actually known more accurately than to the nearest five thousandths of an inch. However, the heat transfer test section area also included one-half the area of the epoxy ring, as it was assumed that the heat transferred into the inner half of the epoxy ring boiled off liquid nitrogen in the inner stainless steel chamber, whereas the heat transferred into the outer half of the epoxy ring boiled off liquid nitrogen in the outer chamber. It is the difficulty involved in determining half the thickness of the epoxy

ring which leads to an error estimate as large as 0.005 inches. The diameter of the actual copper inner plate could be determined to the nearest 0.002 inches.

As mentioned earlier, the error in the frost thickness measurement is five-thousandths of an inch or 0.000416 ft. Based on the above discussion, the errors involved in the various measured quantities were taken as follows:

$$\Delta Q = 0.4 \text{ Btu/hr}$$

$$\Delta T_w = 2 \text{°F}$$

$$\Delta T_s = 5 \text{°F}$$

$$\Delta \delta = 0.000416 \text{ ft}$$

and, $$\Delta A = 0.0001228 \text{ ft}^2$$

Using the data of Run number 16 for the calculation one can write

$$Q = 14.92 \text{ Btu/hr}$$

$$A = 0.0277 \text{ ft}^2$$

$$\delta = 0.01561 \text{ ft}$$

$$T_s = 15 \text{°F}$$

$$T_w = -315 \text{°F}$$

Substituting these values into Equation N-7, Δk_{avg} was calculated to be 0.002019. The measured k_{avg} for Run 16 is 0.02784 and, therefore, the estimated error is

$$\frac{0.002019 \times 100}{0.02784} \% = \pm 7.24\%$$

Once again it should be noted that since Equation N-7 does not allow for compensating errors, the true magnitude of the maximum error is most likely to be lower than one

calculated above.

3. Heat and Mass Transfer Coefficients in the Frosting Experiments

A. Heat Transfer Coefficient

The heat transfer coefficients in the frosting experiments for various system conditions were calculated from Equation N-9 shown below.

$$h = \frac{q - N_S \Delta H}{(T_g - T_s)} \qquad (N-9)$$

For a typical set of experimental conditions, the heat transfer coefficient can be calculated as follows.

For Run number 38, q = 832 Btu/hr ft^2

N_S = 0.1125 $\frac{lbm}{hr\ ft^2}$ (from mass deposition versus time curve)

ΔH = 1,210 Btu/lbm (54)

T_g = 73°F

T_s = 8°F

hence, from Equation N-9

$$h = \frac{832 - 0.1125 \times 1210}{65} = 10.71\ Btu/hr\ ft^2°F$$

The errors involved in the calculation of heat transfer coefficient by the above method can be obtained as follows.

From Equation N-9

$$N = \frac{Q/A - n/A_V\ (\Delta H)}{(T_g - T_s)} \qquad (N-10)$$

where, $Q/A = q$ and $n/A_V = N_S$

The error (maximum) in heat transfer coefficient is given by

$$\Delta h = \frac{\partial h}{\partial Q} \Delta Q + \frac{\partial h}{\partial n} \Delta n + \frac{\partial h}{\partial (\Delta H)} \Delta (\Delta H) + \frac{\partial h}{\partial T_g} \Delta T_g$$

$$+ \frac{\partial h}{\partial T_s} \Delta T_s + \frac{\partial h}{\partial A_v} \Delta A_v + \frac{\partial h}{\partial A} \Delta A \qquad (N-11)$$

Combining Equations N-10 and N-11, following relation for Δh can be obtained,

$$\Delta h = \frac{\Delta Q}{A(T_g - T_s)} + \frac{\Delta H}{A_v(T_g - T_s)} \Delta n + \frac{n/A_v \Delta(\Delta H)}{(T_g - T_s)}$$

$$+ \frac{(Q/A - n/A_v(\Delta H))}{(T_g - T_s)^2} (\Delta T_g + \Delta T_s) + \frac{Q}{A^2(T_g - T_s)} \Delta A$$

$$+ \frac{n \Delta A_v}{A_v^2 (T_g - T_s)} \qquad (N-12)$$

The errors involved in the various measured quantities were taken as follows.

ΔQ = 0.4 Btu/hr

ΔA = 0.0001228 ft^2

Δn = 4.41x10^{-6} lbm/ft

ΔA_v = 9.0x10^{-6} ft^2

$\Delta(\Delta H)$ = 2.5 Btu/lb

ΔT_g = 1°F

and ΔT_s = 5°F

Again Run 38 is used to illustrate the following calculation of h. For this run

$\dot{Q}$ = 23.2 Btu/hr

A = .0277 ft^2

n = 1.049x10^{-4} lbm/hr

ΔH = 1210 Btu/lb

A_v = 9.32x10^{-4} ft^2

$$T_g = 73^\circ F$$

$$T_s = 8^\circ F$$

Substituting all the above values into Equation N-12, Δh was calculated to be 1.36. The value of h for this run is 10.71 Btu/hr ft^2 $^\circ$F (as calculated before). Hence, the estimated error is $\dfrac{1.36}{10.71}$ x 100 $= \pm 12.69\%$.

The true error in the measurement of heat transfer coefficient will be most likely less than one calculated above because of presence of compensating errors.

B. Mass Transfer Coefficient

The mass transfer coefficients for various system conditions studied in the present thesis were calculated from Equation N-13 shown below.

$$K_g = \frac{N_s}{(p_g - p_s)} \qquad (N-13)$$

For a typical set of experimental conditions, mass transfer coefficient can be calculated as follows.

For Run number 38, $N_s = 0.1125$ lbm/hr ft^2 (from Figure

IV-A2)

$$p_g = 2.542 \times 10^{-4} \text{ lbm/ft}^3$$

$$T_s = 8^\circ F, \text{ hence } p_s = 1.03 \times 10^{-4} \text{ lbm/ft}^3$$

Thus, from Equation N-13

$$K_g = \frac{0.1125 \times 10^4}{1.512} = 744 \text{ ft/hr.}$$

The method for determining the error in the mass

transfer coefficient measurement is essentially the same as that used for Δk_{avg}.

The mass transfer coefficient is given by

$$K_g = \frac{n}{A_v(p_g - p_s)} \qquad (N-14)$$

Hence, the error in the mass transfer coefficient measurement is given by

$$\Delta K_g = \frac{\partial K_g}{\partial n} \Delta n + \frac{\partial K_g}{\partial A_v} \Delta A_v + \frac{\partial K_g}{\partial p_g} \Delta p_g + \frac{\partial K_g}{\partial p_s} \Delta p_s \qquad (N-15)$$

The combination of Equation N-14 and N-15 yields Equation N-16 shown below

$$K_g = \frac{\Delta n}{A_v(p_g - p_s)} + \frac{\Delta A_v n}{A_v^2(p_g - p_s)} + (\Delta p_g + \Delta p_s) \left(\frac{n}{A_v(p_g - p_s)^2}\right) \qquad (N-16)$$

The signs of all the terms have been taken as positive ir order to obtain the maximum value of ΔK_g.

The errors involved in the measured quantities were taken as follows.

$\Delta n = 0.002$ gms./hr or 4.41×10^{-6} lbm/hr

$\Delta A_v = 9.0 \times 10^{-6}$ ft^2

$\Delta p_g = .1007 \times 10^{-4}$ lbm/ft^3

$\Delta p_s = .264 \times 10^{-4}$ lbm/ft^3 (since $T_s = 5^\circ F$, as discussed before)

Again, Run number 38 will be used to illustrate the calculation of ΔK_g. For this run

$n = N_s A_v = 1.049 \times 10^{-4}$ lbm/hr

$A_v = 9.32 \times 10^{-4}$ ft^2

$$p_g = 2.542 \times 10^{-4} \text{ lbm/ft}^3$$

$$p_s = 1.03 \times 10^{-4} \text{ lbm/ft}^3$$

Substituting all these values in Equation N-16, ΔK_g was calculated to be 49.81. The measurement of K_g for this run is 744 (as calculated before), and therefore, the estimated maximum error is $\frac{49.81 \times 100}{744}$ % or $\pm$ 6.7%.

The true error will be most likely less than one calculated above because of the presence of the compensating errors.

4. **Heat Transfer Coefficient in Non-frosting Experiment**

The heat transfer coefficient in the non-frosting experiment can be calculated from Equation N-17 shown below.

$$h = q/(T_g - T_s) = Q/A \ (T_g - T_s) \qquad (\text{N-17})$$

where all the nomencatures are the same as the ones described before.

For a typical set of experimental conditions, heat transfer coefficient in the non-frosting conditions can be calculated as follows.

For Run number H-2, q = 1,087 Btu/hr ft^2

$$T_g = 82.6^\circ F$$

$$T_s = -11.5^\circ F$$

hence, from Equation N-17

$$h = \frac{1,087}{(94.10)} \qquad = 11.08 \text{ Btu/hr ft}^2{}^\circ F$$

The errors involved in the calculation of heat transfer coefficient can be obtained as follows.

From Equation N-17

$$h = Q/A \ (T_g - T_s) \qquad (\text{N-18})$$

The maximum error in heat transfer coefficient is given by

$$\Delta h = \frac{\partial h}{\partial Q} \Delta Q + \frac{\partial h}{\partial A} \Delta A + \frac{\partial h}{\partial T_g} \Delta T_g + \frac{\partial h}{\partial T_s} \Delta T_s \qquad (N-19)$$

Combining Equation N-18 and N-19, Equation N-20 can be obtained as follows.

$$\Delta h = \frac{\Delta Q}{A(T_g - T_s)} + \frac{Q \, \Delta A}{A^2(T_g - T_s)} + (\Delta T_g + \Delta T_s) \times \frac{Q}{A(T_g - T_s)^2} \qquad (N-20)$$

The errors involved in the various measured quantities were taken as follows

$\Delta Q = 0.30$ Btu/hr.

$\Delta A = 0.0001228$ ft^2

$\Delta T_g = 1^{\circ}F$

and $\Delta T_s = 1^{\circ}F$

Again, Run number H-2 is used to illustrate the following calculation of Δh. For this run

$Q = 30.15$ Btu/hr.

$A = 0.0277$ ft^2

$T_g = 82.6^{\circ}F$

$T_s = -11.5^{\circ}F$

Thus, substituting all these values into Equation N-20 Δh was calculated to be 0.4124. The measured h for this Run is 11.08. Hence, the maximum % error in the calculation of heat transfer coefficient would be $\frac{0.4124}{11.08} \times 100 = \pm 3.72\%$

Once again, it should be noted that compensating errors will most likely cause the true error to be less than the one calculated above.

5. Point Thermal Conductivities

The point thermal conductivity values shown in Table IV-A5 and in Figure IV-A22 were obtained from the heat flux measurements and the graphical differentiation (with the help of a mirror) of the measured temperature distribution within the frost. A sample calculation for the point thermal conductivity is described below.

For Run number 35, at time of 79 minutes from the start of frosting the heat flux was found to be 871 Btu/hr ft^2 and average frost density was found to be 0.1258 gms./cc. From Figure IV-A21, the following values of dT/dx at various temperatures were obtained.

Temperature (^{O}F)	(dT/dx) (^{O}F/ft)
-215	4.57×10^4
-145	2.883×10^4
-80	2.267×10^4
0	0.889×10^4

Since, $k_f = q/(\frac{dT}{dx})$, the following values of point thermal conductivities at various temperatures can be obtained.

Temperature (^{O}F)	k_f (Btu/hr ft ^{O}F)
-215	0.01905
-145	0.03020
-80	0.03840
0	0.09800

Error Analysis

The error in point thermal conductivity measurements can be evaluated in the manner analogous to one described previously. Thus,

$$\Delta k_f = \frac{\Delta Q}{A(\frac{dT}{dx})} + \frac{Q \, \Delta A}{A^2(\frac{dT}{dx})} + \frac{Q \, \Delta(\frac{dT}{dx})}{A \, (\frac{dT}{dx})^2} \qquad (N-21)$$

For a typical set of experimental conditions (Run number 35), Δk_f can be evaluated as follows,

for, $T = 0^{\circ}F$

$Q = 24.13$ Btu/hr

$A = 0.0277$ ft^2

$(dT/dx) = 0.889 \times 10^4$ $^{\circ}$R/ft

$\Delta Q = 0.40$ Btu/hr

$\Delta A = 0.000128$ ft^2

$\Delta(dT/dx) = 7.0 \times 10^2$ $^{\circ}$F/ft

Thus, substituting all these values in Equation N-21, one obtains,

$$\Delta k_f = 9.70 \times 10^{-3} \text{ Btu/hr ft}^2 \, ^{\circ}F/ft$$

or, the maximum % error = 0.978/0.0980 = $\pm$9.95%

The actual error is likely to be lower than one calculated above due to presence of compensating errors.

6. Temperature Gradient Measurements

In order to calculate point thermal conductivity accurately, the precise determinations of temperature gradients are required. In the present thesis, the temperature gradients were measured with the help of a mirror. However, an accuracy of this differentiation procedure was tested

for a typical run by formulating a cubic equation which
passed through the measured temperatures in the frost
interior and at the interface of gas and frost. Temperature
gradients were obtained by analytically differentiating
this equation.

Run number 35 was chosen as a typical run. The measured
temperature profile in the frost interior for this run is
shown in Figure IV-A21. Temperature gradients calculated
by analytical and graphical differentiations at temperatures
of $-215^{\circ}F$, $-145^{\circ}F$, $-80^{\circ}F$ and $0^{\circ}F$ are compared in Table N-1.
The agreement was found to be quite good. From these results,
it was concluded that the temperature gradient by the present
method can be measured with an accuracy of approximately
within $\pm$ 4%.

Table N-1

Comparison of Temperature Gradients obtained by Graphical and Analytical Differentiation of the Measured Frost Temperature Profiles.

Temperature ($^\circ$F)	(dT/dx) ($^\circ$F/ft) Obtained by Graphical Differentiation	(dT/dx) ($^\circ$F/ft) Obtained by Analytical Differentiation	% Error $\dfrac{(dT/dx)_G - (dT/dx)_A}{(dT/dx)_G} \times 100$
-215	4.57×10^4	4.635×10^4	-1.402%
-145	2.883×10^4	2.912×10^4	-0.996%
-80	2.267×10^4	2.187×10^4	+3.655%
0	0.889×10^4	0.895×10^4	-0.675%

APPENDIX   O

Evaluation of the Possible Mechanisms for the Transfer

of Fog Particles from a Gas Stream to a Solid Surface

in Early Phases of a Frosting Experiment

As seen in Section V, in early phases of a frosting

experiment, transfer of fog particles control the frost

deposition. The purpose of this appendix is to examine the

various forces acting on a particle suspended in a gas

stream, and to determine which mechanisms are important

in causing the particles to be deposited. The concepts

regarding particle deposition mechanisms developed by

Owen (79), and by Friedlander and Johnstone (45), will be

utilized in examining the deposition of ice particles from

a gas stream onto a frost layer. These concepts are reviewed

below.

1. Previous Study

The fog particles formed in a gas stream can be

transferred to a wall by one or more of the following

mechanisms.

A.   turbulence in the gas stream (45,79)

B.   gravity, if deposition is from above

C.   force due to temperature gradient in the gas stream (95)

D.   electrostatic forces (45)

E.   fluid shear (79)

In their investigation Friedler and Johnstone (45) as

well as Brazinsky (14) concluded that it is gas phase

turbulence which is primarily responsible for transporting

the particles to the wall. ⁻

To corroborate their thesis that the turbulent eddies were responsible for transporting the particles to the wall, Friedlander and Jonstone noted that no particle deposition occurred in the inlet section of pipe where a relatively thick boundary layer existed adjascent to the wall. However, after a length of pipe corresponding to Re_x = 100,000, the position at which the laminar boundary layer is expected to go turbulent (72), deposition of particles onto the pipe wall was clearly observed.

Brazinsky (14) also made two experiments (at Reynolds numbers of 600 and 1,800) in the laminar flow regime to evaluate the effect of turbulence on the particle transfer. He observed that even though there was a considerable amount of fog present in the gas phase, substantially no fog was deposited on the cold wall for at least 37 minutes of the frosting process. He concluded from these results that turbulence in the gas stream plays significant role in the transfer of fog particles from gas to frost surface.

The process of transferring particles by turbulence in a direction transverse to the direction of the gas stream is not completely understood. The investigations of References 45 and 79 have, however, provided some insight into this phenomenon. The details of the mechanism for transporting solid particles through a turbulent gas stream, when molecular transport in the laminar boundary is not important, is also shown in the same references.

Since the experimental set-up for the present thesis is very similar to one used by Brazinsky (14), the calculations similar to one described in References 14 indicate that, in the present study, turbulence in the gas plays a significant role in the transfer of fog particles from gas to frost surface. The details of the calculations is shown in Reference 14.

APPENDIX - P

Contribution of Radiation to the Frost Thermal Conductivity

As mentioned in Section V-A, heat is not only transferred through the frost by conduction through the solid gas network, but also by radiation between ice particles and by water flux through the interior of the frost. In this appendix, the contribution of radiation to the over-all frost thermal conductivity is briefly evaluated.

The warmer ice particles, located at the top of the frost layer, radiate heat to the colder particles located below them. Each layer, in this way, absorbs part of the radiation striking it, and then re-emit radiant heat to the next lower layer. The experimentally measured thermal conductivity, includes this radiation component of thermal conductivity. The value of this radiative component was calculated from the Damkohler equation presented below (30). This equation was obtained from the radiation study in a packed bed onto which a large temperature gradient was imposed.

$$k_r = \frac{0.684}{100} \epsilon D_p (\frac{T}{100}) e_H \qquad (P-1)$$

where, D_p is in ft., T is in $^\circ$R and k_r is in BTU/hr ft $^\circ$F.

In Equation P-1, k_r is the contribution to the over-all frost conductivity made by radiation between the particles. The values chosen for substitution into Equation P-1 were those which would yield the largest possible contribution radiation could make to the frost thermal

conductivity.

The size of ice particles was chosen to be 100 microns
(14). Thus, D_p = 100 micron was substituted into Equation
P-1. The void fraction ϵ chosen for calculating k_r was
taken as 0.94, the largest frost void fraction encountered
in the experiments of present thesis. $32^{\circ}F$ was the temper-
ature chosen for substitution into Equation P-1 as this
is the highest possible temperature that can exist within
the frost layer (In the experiments of the present thesis,
the frost surface temperature never reached $32^{\circ}F$).

Several values of frost emissivity are reported in the
literature (75, 82). Reported values generally vary between
0.082 and 0.098. 0.098 was chosen, as this value represented
the upper limit of the reported emissivities. Using the
values of ϵ, D_p, T and e_H presented above, the value of
k_r was calculated to be 0.000122 Btu/hr ft $^{\circ}F$. Assuming
Damkohler's equation and various assumed values (particul-
arly D_p) are valid, this value of k_r is the highest
possible contribution that radiation can make to the frost
thermal conductivity. Since 0.000122 Btu/hr ft $^{\circ}F$ is
negligible compared with 0.01 Btu/hr ft $^{\circ}F$, the lowest
measured thermal conductivity, it is concluded that
radiation makes a small contribution to the frost
conductivities. Radiant heat transfer is, therefore,
neglected in calculating theoretical values of conductivity.

APPENDIX   R

Table of Nomenclature

a	Constant in Equation I-B1
a	Constant in Equation G-1
A	Cross sectional area for heat and mass transfer
A_v	Cross sectional area of glass vial
A_n	Constants in Equation L-9
b	Constant in Equation G-2
b	Constant in Equation I-B1
c_1	Constant in Equation II-C3
c_A	Concentration of air
c_p	Specific heat of gas
c_w	Concentration of water vapor
c_T	Total concentration of gas
C	Capacity factor as defined in Equation J-1
C_t	Constant in Equation K-13
D_B	Molecular diffusivity
D'_B	Molecular diffusivity in the free convection boundary layers within the frost
D_{eff}	Effective diffusivity
D_H	Hydrolic diameter
D_o	Pipe diameter
D_p	Particle diameter
D_{w-A}	Molecular diffusivity of water vapor in air
D_{1-2}	Molecular diffusivity of component 1 into 2
e_H	Emissivity
E	Energy

f — Friction factor

$f(\beta)$ — Functionality relationship for β

F — Frictional dissipation of energy

F_t — Thermal force

g_c — Gravitational constant

h — Heat transfer coefficient

i — Grid number in direction as shown in Figure E-0

j — Grid number in z direction as shown in Figure E-0

j_D — j-factor for mass transfer as shown in Equation I-C4

j_H — j-factor for heat transfer as shown in Equation I-C4

J — Grid number corresponding to the frost surface

J_s — Mass flux from bulk gas to the frost surface

J_{si} — Mass flux which diffuses in the frost interior

J_{so} — Mass flux allocated to increase the frost thickness

k — Thermal conductivity

k — Boltzmann's constant

k_{excess} — Excess thermal conductivity

k_{fi} — Intrinsic thermal conductivity of the frost

k'_g — Thermal conductivity of air in the free convection boundary layers within the frost

$k_{g,e}$ — Total gas thermal conductivity

k_i — Thermal conductivity of ice

k_{ice} — Thermal conductivity of ice

k_r — Radiative component of thermal conductivity of the frost

k_T — Thermal diffusion coefficient

k'_{excess} — Excess thermal conductivity of frost due to thermal diffusion of ice nuclei

K_g Mass transfer coefficient between bulk gas and the frost surface

K_{g1} Mass transfer coefficient at the start of the frosting process

K_s Ice thermal conductivity

L   Length of a tube   (also width of a duct)

Le   Lewis Number

m   Mass of a particle

m   Mass of a single ice crystal

M   Molecular weight

n   Mass rate of water vapor

n   Mass concentration of ice nuclei

n'   Nuclei concentration per unit volume

N   Number of ice crystals per unit volume

N_d Depletion rate of ice nuclei due to impingement (or trapping)

N_r Nucleation rate

N_s Mass flux of water vapor from bulk gas to the frost surface

N   Concentration of molecules

p   Pressure

p_w Partial pressure at the cold wall (or cold surface)

P   Total pressure

P_{vp} Vapor Pressure

Pr   Prandtl Number

q   Heat flux

q'   Volumetric flow rate

Q	Heat transfer rate
r	Radius
R	Thermal resistance of a zone in a unit cell of the frost structure model
R	Gas constant
Re	Reynolds Number
S	Supersaturation ratio (p/P_{vp})
Sc	Schmidt Number
t	Time for the formation of a smooth frost layer
T	Temperature
T_1	Temperature at the tube entrance
T_2	Temperature at the tube outlet
u	Velocity of the gas
$\overline{U}_a$	Apparent over-all heat transfer coefficient between bulk gas and the cold wall in the frosting conditions
$\overline{v}$	Mean average random velocity of a molecule
v	Volume
V	Velocity
V_t	Thermal diffusive velocity of a solid particle
W	Mass flow rate
x	Dimensionless linear dimension of an ice cube in the frost structure model
x	Distance from the cold wall towards the bulk gas phase
x	Distance from the thermal entrance (Appendix L)
X_*	$2x/Re\ Pr\ D_H$
y	Distance from pipe wall (Appendix L)
Y	Mole fraction of water vapor

z   Dimensionless distance from the cold wall (x/δ)

z   Dimensionless width of the square ice rod in the frost structure model

Greek Letters

α, β, γ Constants used in Equations G-1 and G-2
γ, ψ, ξ

α Constant in Equation H-2

α Thermal diffusion factor

δ Boundary layer thickness

σ Surface tension

σ $p/P_{vp} - 1$

ρ Density

ρ_{ice} Ice density

ϵ Void fraction

ΔH Heat of sublimation

ϵ_H Eddy diffusivity of heat

ϵ_M Eddy diffusivity of momentum

$\varkappa$ Constant in Equation K-5

ψ Constant in Equation K-8

η Viscosity

μ Viscosity

ϵ Constant in Equation K-6

ν Kinematic viscosity

τ_o Shear stress

τ Tortuosity

Δz Grid size in z direction

$\Delta \theta$ Grid size in θ direction

$\Delta(\alpha)$ Differential variation (or increment) in an arbitrary variable α

θ Time

δ Frost thickness

$\dot{\delta}$ Rate of change of frost thickness

λ Mean free path

λ Constants in Equation L-9

Subscripts

g   Gas

s   Frost surface

w   Cold wall

f   Frost

v   Vapor

v   Glass vial

f,s   Frost surface

p   Particle

b   Bulk gas

avg   Average

o   Old value

N   New value

o   Total value

e   Value at the prevailing equilibrium condition

Appendix T

Bibliography

1. Aitken, J., Trans. Roy. Soc. Edinburgh, 32, 293 (1884)

2. Amelin, A. G., "Theory of Fog Condnesation", 2nd ed., edited by B. V. Derjagin, Boston (1968).

3. Arthur D. Little, Inc., "Continant Freeze-out in Heat exchangers", Tech. Rept., No. ASD-TDR-63-508 vol. II, under Air Force Contract No. AF33(657)-8695 (July 1963).

4. A.S.M.E. Research Committee on Fluid Meters, "Fluid Meters, Their Theory and Application", 5th ed., American Society of Mechanical Engineers, New York (1959).

5. Bader, H., R. Haifeli, E. Bucker, J. Neher, O. Eckel and C. Thomas, "Snow and its Metamorphism", U.S. Army, Corps. of Engineers, Snow, Ice and Permafrost Research Establishment Translation No.14, (Jan. 1954).

6. Barron, R. F., "Heat and Mass Transfer to a cryo-surface in Free Convection", Ph. D. Thesis, Mech. Eng., Ohio State University, Columbus, Ohio (1964). Partially reprinted in Barron, R. F. and L. S. Han, Trans A.S.M.E., Series C, Jrl. of Heat Transfer, 87, 499 (1965).

7. Beatty, K. O., E. B. Finch and E. M. Schoenborn, Proc. Gen'l Disc. on Heat Transfer (London), 32-37 (1951).

8. Becker, R. and W. Doring, Ann. Phys., 24, 719 (1935)

9. Bernard, A. I., Proc. Roy. Soc. (London), A220, 132 (1953).

10. Blackman, M. and N. D. Lisgasten, Proc. Roy. Soc. A, 239, 93 (1957).

11. Boelter, L. K. M., D. Young and H.W. Iverson, "An investigation of Air craft-Heaters- XXVII. Distribution of Heat Transfer Rate in Entrance Section of a Circular Tube," N. A. C. A. TN 1451 (1948).

12. Borus, C., Ann. Phys. , 24, 225 (1907).

13. Bradley, R. S., Quart. Rev., 5, 315 (1951).

14. Brazinsky, I. E., "Properties of Water Frost Formed at Cryogenic Temperatures," Sc. D. Thesis, Chem. Eng., M. I. T., Cambridge (1967).

15. Brock, J. R., *J. Colloid Science*, 17, 768 (1962).

16. Brock, J. R., *J. Phys. Chem.*, 66, 1793 (1962).

17. Brock, J. R., *J. Colloid and Interface Science*, 23, 448-452 (1967).

18. Brun, E. A. and K. Feniger, *Compt. Rend.*, 226, 1966 (1948).

19. Buckley, H. E., "Crystal Growth", Chaps. 3, 5, 6 and 12, John Wiley and sons, Inc., New York (1951).

20. Butkovich, T. R., *Trans. Am. Geophys. Union*, 39, 305 (1958).

21. Byers, H. R., "Nucleation in the Atmosphere," a Symposium Sponsored by *American Chemical Society Publications*, Washington D. C. (1967)

22. Cawood, W., *Trans. Faraday Soc.*, 32, 1069 (1936).

23. Chen, M. M., "Heat Transfer in Heat Exchangers Under Frosting Conditions," Ph. D. Thesis, Mech. Eng., M.I.T., Cambridge (1960). Partially reprinted in Chen, M. M. and W. Rosenow, *Trans. A.S.M.E., J. of Heat Transfer*, 86, 334 (1964).

24. Chung, P. M. and A. B. Algren, *Heating, Piping and Air Cond.*, 30, No.9, 171-8, No. 10, 115-22 (1958).

25. Coles, W. D., *N.A.C.A. Tech. Note 3143* (1954).

26. Coles, W. D. and R.S. Ruggeri, *N.A.C.A. Tech. Note 3104* (1954).

27. Corcoran, W. H., F. Page, Jr., W. G. Schlinger and B. H. Sage, "Temperature Measurements in Turbulent Gas Streams," *Industrial and Engineering Chemistry*, 44, 410 (1952).

28. Cunningham, T. M. and R. L. Young, *Adv. in Cryogenic Eng.*, 8, 85 (1963).

29. Cwilong, B. M., *Proc. Roy. Soc. London*, A190, 137 (1947).

30. Damkohler, G., *Der Chemi Ingenieur*, 3, 359 (1937).

31. Deissler, R.G., "Analysis of Turbulent Heat Transfer, Mass Transfer and Friction in Smooth Tubes at high Prandtl and Schmidt Numbers," *N.A.C.A. TN 3145* (1954).

32. Deissler, R. G., "Turbulent Heat Transfer and Friction in the Entrance Regions of the Smooth Passages," <u>Trans</u>. <u>A.S.M.E.</u>, <u>77</u>, 1221 (1955).

33. Deissler, R. G. and J. S. Boegli, <u>Trans. A.S.M.E.</u>, <u>80</u>, 1417 (1958).

34. De Quervain, M. R., "On the Metamorphism of Snow," in "Ice and Snow Properties, Processes and Applications," W. D. Kingery, ed., 377, M.I.T. Press, Cambridge (1962).

35. Derjaguin, B. V. and S. P. Bakanov, <u>Doklady Akademi Nauk, SSSR.</u>, <u>147</u>, No. 1, 139 (1962).

36. Derjaguin, B. V., S. P. Dakanov and J. I. Rabinovich, <u>Proc. of First Nat. Conf. on Aerosols Czech. Acad. Sci.</u>, 197 (1965). Also, cited in Davies, C. N., "Aerosol Science," Academic Press, New York (1966).

37. Derjaguin, B. V. and Ya Yalamov, <u>J. Colloid Sci.</u>, <u>20</u>, 555 (1965).

38. Deveaux, J., <u>Ann. Phys.</u>, <u>20</u>, No. 10, 5-67 (1933).

39. Eckert, E. R. G. and R. M. Drake, "Heat and Mass Transfer," 2 nd. ed. , McGraw-Hill, New York (1955).

40. Farley, F. J., <u>Proc. Roy. Soc. (London)</u>, <u>A212</u>, 530 (1952).

41. Feniger, K., <u>Annex. Bull. Int. Inst. of Refrig.</u>, A39-A47 (1948).

42. Frankel, J., "Kinetic Theory of Liquids," Dovei Publ. Inc. (1955), Sobranie izbrannykh trudov (collected works), vol. <u>3</u> , ch. 7, Izdatel'stvo AN SSSR (1959).

43. Frey, F., <u>Z. Physik. Chem.</u>, <u>B</u>, <u>49</u>, 83 (1941).

44. Friedlander, S. K. and H. F. Johnstone, <u>Ind. Eng. Chem.</u>, <u>49</u>, 1151 (1957).

45. Frossling, N., "Uber die Verdunstung fallender Tropfen," <u>Gerlands Beitr. Geophysik</u>, <u>52</u>, 170 (1938).

46. Fuchs, N. A., "The Mechanics of Aerosols", McMillan Company, N.Y. (1964).

47. Gorring, R. L. and S. W. Churchill, <u>Chemical Engineering Progress</u>, <u>57</u>, 53 (1961).

48. Gray, V. H. and T. F. Gelder, <u>Adv. in Cryogenic Eng.</u>, <u>5</u>, 131 (1960).

49. Grew, K. E. and T. L. Ibbs, "Thermal Diffusion in Gases,"

Cambridge University Press, London (1952).

50. Hardy, J. K., K. C. Hales and G. Mann, Food Investigation Board Spec. Rept. 54, Dept. of Scientific and Industrial Research, H. M. Stationary Office, London (1951).

51. Haselden, G. G., Proc. Phys. Soc. (London), 63 B, 157 (1950).

52. Holten, D.C., "Heat and Mass Transfer to Uninsulated Oxygen Containers," M. S. Thesis, Mech. Eng., Univ. of Colorado (1957). Partially reprinted in Holten, D. C., Adv. in Cryogenic Eng., 6, 499 (1961).

53. Houghton, H. G., "A Preliminary Quantitative Analysis of Precipitation Mechanisms," M.I.T., J. Met., 7, 363 (1950).

54. International Critical Tables, vol. II, McGraw-Hill, New York (1927).

55. Jacobsen, S. and J.R. Brock, J. Colloid Science, 20, 544 (1965).

56. Jeffreys, H., Phil. Mag., 35, 270 (1918).

57. Johnstone, H. F., M. D. Kelley and D. L. Mckinley, Ind. Eng. Chem., 42, 2298 (1950).

58. Kamei, S. et. al., "Research on Frost Formation in Low Temperature Dehumidifiers," Kyoto University, Japan (1950).

59. Kamei, S., T. Mizushina, S. Kifune and T. Koto, Chem. Eng. (Japan), 14, No. 1, 53-60 (1950).

60. Kelvin, W. T., Phil. Mag., 42, 368 (1871).

61. Kennard, E. H., "Kinetic Theory of Gases," McGraw-Hill Company, New York, N.Y. (1938).

62. Kingery, W. D., J. Appl. Phys., 31, 833 (1960).

63. Kossel, W., Ann. Physik., Ser. 5, 21, 455 (1934).

64. Latzko, H., "Heat Transfer in a Turbulent Liquid or Gas Stream," N.A.C.A. TM 1068 (1944). Original in Z. fur angewandte Mathematik und Mechanik, 1, No. 4 (1921).

65. Levy, S., "Heat Conduction Methods in Forced Convection Flow," Trans. A.S.M.E., 78, 1627 (1956).

66. Lodge, O. J. and J. W. Clark, Phil. Mag., 17, 284 (1884).

67. Mason, B. J., "Spontaneous Condensation of Water Vapor in Expansion Chamber Experiments," Proc. Physic. Soc. B, 64, 773 (1951).

68. Mason, B. J., "The Growth of Ice Crystals in a Super-cooled Water Cloud," Imperial College, London, Quart. J. Roy. Met. Soc., 79, 104 (1952).

69. Mason, E. A., "Notes on Thermal Diffusion," Institute of Molecular Physics, Univ. of Maryland, Maryland (1967).

70. Maxwell, J.C., Trans. Roy. Soc. (London), 170, 231 (1879).

71. Maybank, J. and B.J. Mason, "The Production of Ice Crystals by Large Adiabatic Expansion of Water Vapor," Proc. Physic. Soc., 74, 11 (1959).

72. Mcadams, W. H., "Heat Transmission," 3rd ed., McGraw-Hill Book Co. Inc., New York, N.Y. (1954).

73. Mellor, M. and U. Radok, "Some Properties of Drifting Snow," Proc. of Symposium on Antarctic Meteorology, 333-346, Pergamon Press, New York (1960).

74. Mickley, H. S., T. K. Sherwood and C. E. Reed, "Applied Mathematics in Chemical Engineering," 2nd ed., McGraw-Hill Co., New York (1957).

75. Millard, E. B., "Physical Chemistry of Colleges", 7th ed., McGraw-Hill, New York (1953).

76. Mulligan, J. C., H. A. Thompson and H.H. Sogin, "The Effect of Frost Formation on the Heat Transfer to Large Cryogenic Vessels," Boeing Document No. D5-13312, Sept. 18 (1967). It is also reported in Mulligan, J. C., Ph.D. Dissertation, Mech. Eng. Dept., Tulane University (1967).

77. "The Investigation of Heat Transfer and Frost Formation in Humid Air Flowing Across a Plane Surface Held at Sub-Freezing Temperatures," N.S.F. Supported Project at Lousiana Polytechnic Institute, Sept. 1 (1964).

78. Nunner, W., V. D. I. Forschungsheft, 455 (1956).

79. Owen, P.R., "Dust Deposition from a Turbulent Airstream ," in "Aerodynamic Capture of Particles," E. G. Richardson, ed., pp. 8-25, Pergammon Press, New York (1960).

80. Perry, J. H., ed., "Chemical Engineers Handbook," 3rd ed., McGraw-Hill, New York (1950).

81. Pitman, D., "Effective Thermal Conductivity of Snow at -88°C, -27°C and 0°C," Publ. of Smithsonian Astrophysical Observatory, Cambridge, Mass. (1968).

82. Polack, J. A., Sc. D. Thesis, Chem. Eng., M.I.T., Cambridge, Massachusetts (1948).

83. Poppoff, I. G., Industrial Hygiene Quarterly, 15, 145 (1954).

84. Pound, G. M., L. A. Madonna and Sciulli, C., Carnegie Inst. Tech. Metals Res. Lab. Quart. Rept. 5 (1951).

85. Powell, C. F., Proc. Roy. Soc. London, A119, 553 (1928).

86. Prins, L., Kaltetechnik, 8, 160-4, 182-6 (1956).

87. Rau, W., Geofis. Pur. Appl., 28, 201 (1954).

88. Rayleigh, J.W.S., Proc. Roy. Soc., 34, 414 (1882).

89. Richards, R. J., D. K. Edmonds and R. B. Jacobs, Supplement au Bulletin de l'Institute du Froid (1962).

90. Rische, E. A., Chem. Ing. Tech., 29, 603 (1957).

91. Rosenblatt, P. and V. K. LaMer, Phy. Rev., 70, 385 (1946).

92. Ruccia, F. and C. M. Mohr, Adv. in Cryogenic Eng., 4, 307 (1960).

93. Sander and Damkohler, Naturwiss, 31, 460 (1943).

94. Satterfield, C. N. and T. K. Sherwood, "The Role of Diffusion in Catalysis," Addison-Wesley, Reading, Mass. (1963).

95. Saxton, R. L. and W. E. Ranz, J. Appl. Phys., 23, 917 (1952).

96. Schadt, C. F. and R. D. Cadle, J. Phys. Chem., 65, 1689 (1961).

97. Schadt, C. F. and R. D. Cadle, "Thermal Forces on Aerosol Particles in a Thermal Precipitator," J. Colloid Science, 12, 356 (1957).

98. Schaefer, V. J., Science, 104, 457 (1946).

99. Schaefer, V. J., "The Formation of Ice Crystals in Ordinary and Nuclei Free Air," Ind. Eng. Chem., 44, 1300 (1952).

100. Schaefer, V. J., "Ice Crystals Formed Spontaneously by the Rapid Expansion of Moist Air," _J. Colloid Sci_, _2_, 175 (1954).

101. Schneider, P. J., "Effect of Axial Fluid Conduction on Heat Transfer in the Entrance Regions of Parallel Plates and Tubes," _Trans. A.S.M.E._, _79_, 765 (1957).

102. Schropp, K., _Z. ges. Kalte-Ind._, _42_, 81-5, 126-31, 151-4 (1935).

103. Shah, Y. T., A. Dravid, S. T. Meyer and G. Rappe, " Laminar Heat Transfer in Flow between Parallel Plates", Course 10.34 project, M.I.T., Cambridge, Mass. (1968).

104. Sherwood, T. K. and R. L. Pigford, " Absorption and Extraction", 2nd ed., McGraw-Hill Co., New York (1952).

105. Sleicher, C. A. and M. Tribus, "Heat Transfer in a Pipe with Turbulent Flow and Arbitrary Wall-Temperature Distribution", _Trans. of A.S.M.E._, _79_, 789 (May 1957).

106. Sleicher, C. A., "Experimental Velocity and Temperature Profiles for Air in Turbulent Flow in a Pipe," _Trans. A.S.M.E._, _80_, 693 (1958).

107. Sommerfield, R. and J. A. Businger, _J. Geophys. Res._, _70_, 3303 (1965).

108. Sperry, P. R., "The Effect of Additives on the Kinetics of Crystallization of Supercooled Water," Sc. D. Thesis, M.I.T., Cambridge (1965).

109. Stoecker, W. F., "Frost Formation on Refrigeration Coils," _A.S.H.R.A.E. Trans._, _21_, 91 (1960).

110. Tyndall, J., _Proc. Roy. Inst._, _6_, 3 (1870).

111. Volmer, M. and H. Flood, _Z. Physik. Chem. A_, _170_, 273 (1934).

112. Volmer, M., "Kinetik der Phasenbildung- stenkopt", _Dresden un Leipzig_ (1939).

113. Waldmann, L., _Z. Naturf._, _14a_, 589 (1959).

114. Weber, M. E., "Heat Transfer to a Cryogenic Surface Under Frosting Conditions," Sc. D. Thesis, Chem Eng., M.I.T., Cambridge (1964). Partially reprinted in Reid, R.C., P. L. T. Brian and M. E. Weber, _A.I.Ch.E. Jrl._, _12_, 1190 (1966).

115. Whitehurst, C. A., "An Investigation of Heat and Mass Transfer by Free Convection from Humid Air to a Metal Plate Under Frosting Conditions", Ph. D. Thesis,

Agricultural and Mechanical College of Texas, College Station (1962). Partially reprinted in Whitehurst, C. A., _A.S.H.R.A.E. Jrl._, _4_, No. 5, 58 (1962).

116. Whitehurst, C. A., "A Survey of Research Efforts in Heat Transfer through Frost Formation", _A.S.H.R.A.E. Jrl_, _8_, No. 10, 50 (1966).

117. Whitehurst, C. A., O. W. McGregor and J. E. Fontenot, "An Analysis of Turbulent Free Convection Boundary Layer over a Frosted Surface", _Cryogenic Technology, January_ (1968).

118. Wilkey, G. B., "Heat Insulation", John Wiley and Sons., New York (1950).

119. Wilson, C. T. R., _Phil. Trans. A._, _193_, 265 (1899).

120. Woodside, W., _Heating, Piping and Air Cond._, _30_, No. 9, 163 (1958).

121. Woodside, W., _Can. J. Phys._, _38_, 815 (1958).

Biographical Note

The author was born on February 27, 1943 in Bombay, India. He obtained his early education at The Bharda High School, St. Xavier's College and Bombay University, Department of Chemical Technology, all located in Bombay, India.

In September, 1962 he enrolled as a junior in the Chemical Engineering Department of University of Michigan. In June, 1964, he graduated with the degree of Bachelor of Science in Chemical Engineering.

In September, 1964 the author began graduate studies in the Chemical Engineering Department of the Massachusetts Institute of Technology. He received the degree of Master of Science in Chemical Engineering in February 1966 and the degree of Chemical Engineer in February 1967. During the course of his early studies he was teaching assistant for three semesters. During his doctorate thesis the author was supported by Scientific Design and Arthur D. Little Fellowships. He is a menber of Sigma Xi and Phi Lambda Upsilon.

The author attended M.I.T. practice school, at Bound Brook, New Jersey in the Spring of 1966 and 1967. He was Assistant Director of the practise school in Spring 1967. On June 8, 1968 he married the former Mary A. McCumiskey of Dublin, Ireland.